TRANSPORTATION RESEARCH
RECORD

No. 1460

Bridges, Other Structures, and Hydraulics and Hydrology

Structures

A peer-reviewed publication of the Transportation Research Board

TRANSPORTATION RESEARCH BOARD
NATIONAL RESEARCH COUNCIL

NATIONAL ACADEMY PRESS
WASHINGTON, D.C. 1994

Transportation Research Record 1460
ISSN 0361-1981
ISBN 0-309-06067-2
Price: $27.00

Subscriber Category
IIC bridges, other structures, and hydraulics and hydrology

Printed in the United States of America

Sponsorship of Transportation Research Record 1460

GROUP 2—DESIGN AND CONSTRUCTION OF TRANSPORTATION FACILITIES
Chairman: Charles T. Edson, Greenman Pederson, Inc.

Structures Section
Chairman: David B. Beal, New York State Department of Transportation

Committee on General Structures
Chairman: John J. Ahlskog, FHWA, U.S. Department of Transportation
Dan S. Bechly, Amar Bhajandas, Charles H. Bryant, Martin P. Burke, Jr., Frank J. Constantino, Paul F. Csagoly, Donald J. Flemming, Theodore V. Galambos, C. Stewart Gloyd, Frederick Gottemoeller, Richard P. Knight, Clellon Lewis Loveall, Dennis R. Mertz, John Minor, Andrzej S. Nowak, William J. Rogers, Arunprakash M. Shirole, A. J. Siccardi, Paul G. Steinhauser, Dan G. Zollinger

Committee on Steel Bridges
Chairman: Charles W. Roeder, University of Washington
John J. Ahlskog, David R. Anderson, Charles J. Arnold, Mark D. Bowman, William G. Byers, Karen C. Chou, R. Scott Christie, Donald J. Flemming, Dan M. Frangopol, C. Stewart Gloyd, Michael A. Grubb, Tim J. Ingham, Ray W. James, Michael J. Koob, Abba G. Lichtenstein, Ayaz H. Malik, Richard A. Parmelee, Camille George Rubeiz, Robert A. P. Sweeney, John A. Van Lund, Ivan M. Viest, Gerald M. White, Stanley W. Woods, Ben T. Yen

Committee on Dynamics and Field Testing of Bridges
Chairman: Andrzej S. Nowak, University of Michigan
Secretary: Harold R. Bosch, Federal Highway Administration
Baidar Bakht, Michael G. Barker, Ian G. Buckle, Juan R. Casas, James D. Cooper, Bruce M. Douglas, Dan M. Frangopol, Gongkang Fu, Yozo Fujino, Michel Ghosn, Hidayat N. Grouni, Robert J. Heywood, F. Wayne Klaiber, Sudhakar R. Kulkarni, John C. Mathis, Wallace T. McKeel, Jr., Fred Moses, John A. Olandt, Suresh G. Pinjarkar, Mohsen A. Shahawy, Kwok-Nam Shiu, Robert A. P. Sweeney, Sami W. Tabsh, Ivan M. Viest, Ben T. Yen, Robert C. Y. Young

Committee on Structural Fiber Reinforced Plastics
Chairman: Craig A. Ballinger, Craig Ballinger & Associates
Robert J. Bailey, Lawrence C. Bank, Saeed Daniali, Richard Dauksys, Charles W. Dolan, Piyush K. Dutta, Hota V. S. Gangarao, Charles H. Goodspeed, Andrew Green, Srinivasa L. Iyer, Greg T. McCoy, Urs Meier, Aftab A. Mufti, Eric Munley, J. M. Plecnik, Richard D. Roll, Mohsen A. Shahawy, Robert L. Sierakowski, Clinton B. Smith, Abdul-Hamid Zureick

Transportation Research Board Staff
Robert E. Spicher, Director, Technical Activities
D.W. (Bill) Dearasaugh, Engineer of Design
Nancy A. Ackerman, Director, Reports and Editorial Services
Marianna Rigamer, Oversight Editor

Sponsorship is indicated by a footnote at the end of each paper. The organizational units, officers, and members are as of December 31, 1993.

Transportation Research Record 1460

Contents

Foreword

Of the thirteen papers in this volume, eleven were presented in three different sessions sponsored by the Structures Section committees at the 1994 TRB Annual Meeting, and two were submitted for publication only.

The Committee on General Structures and the Committee on Steel Bridges co-sponsored a session at which the first four papers were presented. Burke presents the development of semi-integral abutments for bridges in Ohio that will enable this jointless deck concept to be extended to most bridges in the state. Raju et al. focus on timber bridges and transition rails for glued-laminated bridge decks and describe their development and testing. Weissmann et al. document a factorial analysis of 960 bridges of various types, spans, and design loads to provide inputs for cost allocation procedures. Thippeswamy et al. explain the performance of single-span jointless steel bridges and present the results of a parametric study to help the designer select and optimize superstructure and substructure members.

The next seven papers were presented in two sessions sponsored by the Committee on Dynamics and Field Testing of Bridges. Miller and Parekh describe the destructive testing of a deteriorated prestressed box bridge beam and conclude that lateral instability caused by lateral bending and yielding of the prestressing steel resulted in the sudden collapse of the beam. Pentas et al. describe a field experiment to monitor temperatures, thermal movements, and stresses in a recently constructed composite bridge in Louisiana, as well as the analysis of data and development of a model to predict temperature distribution. Poston et al. present findings of a field investigation of 31 bridges in New Jersey to assess possible deterioration of those constructed in cromite ore processing residue fill. Aktan et al. describe a series of nondestructive and destructive tests on two decommissioned 80-year-old steel truss bridges. Petrou et al. present an evaluation of the fatigue performance of small-scale physical models of noncomposite reinforced concrete bridge decks designed by AASHTO and by OHBDC (Ontario) criteria and loaded by moving wheel and by stationary pulsating loads. Rösler discusses the development of a model of dynamic behavior of bridges and vehicles on the basis of field measurements taken during a systematic test with prescribed dynamic loadings imposed. Roeder et al. describe a research effort undertaken to determine the causes of observed fatigue cracking of single support bar modular expansion joints with 1200 mm of movement capability at each end of the I-90 Lake Washington floating bridge near Seattle.

Shiu and Tabatabai present the measured thermal behavior of the Red River Bridge, a six-span continuous concrete box-girder bridge in Louisiana. In the last paper, Morsi and Larralde discuss the behavior of various types of materials and fasteners and compare the results of tests of reinforced plastic connection fasteners with those of allowable strengths of the various types of fasteners.

Semi-Integral Bridges: Movements and Forces

MARTIN P. BURKE, JR.

For six decades the state of Ohio has been building continuous concrete slab bridges with flexible integral abutments. For three decades it has been building continuous steel beam and girder bridges with flexible integral abutments. Although this type of construction is now routine in Ohio for most bridges, there were a number of exceptions for such applications. For example, bridges skewed greater than 30 degrees, continuous bridges longer than 300 ft (91.4 m), and bridges with abutments on rigid foundations were routinely provided with movable deck joints at abutments. More recently, however, Ohio has conceived and is developing a semi-integral abutment concept that has enabled it to extend the application range of bridges with jointless decks to most bridges—even to those applications with exceptional characteristics. This semi-integral abutment concept is also now being used to retrofit existing end-jointed continuous bridges. Ohio's concept for semi-integral bridges is described, and a number of the peculiarities that should be recognized and provided for are discussed. Properly designed and constructed, this semi-integral bridge concept should extend the application range of bridges with jointless decks to most applications—even to those not normally associated with integral types of construction.

A semi-integral abutment concept has been developed and adopted by Ohio for the design of some new highway bridges and the retrofitting of single-span and multiple-span continuous bridges. However, to understand and appreciate why this type of design has been adopted by Ohio, while the design details and construction procedures are still evolving, will require a brief acquaintance with Ohio's experience with the development and adoption of both end-jointed continuous bridges and continuous integral bridges.

Beginning in the early 1930s Ohio adopted, for most applications, embankments, stub-type abutments, and continuous construction for single- and multiple-span stream crossings and grade separation structures. This was true for bridges of concrete and steel. For the shortest multiple-span bridges and those with span lengths of less than about 50 ft (15 m), continuous concrete slabs were used. Of particular interest is that these original concrete slab designs and most subsequent similar designs used integral abutments, with each abutment supported by a single row of vertical piles. Consequently, with respect to continuous concrete bridges, Ohio has been building fully continuous integral bridges for over 60 years.

For steel bridges, fully continuous members were first achieved in the early 1930s by the use of riveted splices at piers. At the same time, the use of field welding was being perfected and some of the shortest beam bridges were made continuous by the use of field-welded splices at piers. These initial splices consisted of partial butt-welded beams supplemented by fillet-welded cover plates. By the mid-1940s, all field splices of rolled beam bridges with span lengths of up to 84 ft (25.6 m) were field butt welded at piers to achieve continuity.

Burgess & Niple, Limited, 5085 Reed Road, Columbus, Ohio 43220.

Until 1955, steel girder bridges were of riveted construction. In 1955, the first fully welded girder bridges were constructed. Thereafter, all rolled beam and girder bridges were of fully welded continuous construction. In 1963, high-strength bolts were adopted in place of welding for field splices.

In the early 1960s, the first integral details were developed and adopted for steel structures. Since that time, Ohio has been building continuous integral bridges with main members of steel or reinforced concrete.

In summary, Ohio has been building continuous integral concrete slab bridges for over 60 years and continuous integral steel bridges for over 30 years. These bridges were not exceptions. This type of construction was adopted as standard, and most bridges were constructed this way. The primary goal of Ohio designers was the elimination of bridge deck joints whenever practicable.

However, with respect to the application of end-jointed continuous bridges and integral continuous bridges, there were a number of notable exceptions. Bridge decks longer than 600 ft (183 m) were provided with end joints and an intermediate joint. Bridges skewed greater than 30 degrees, those longer than 300 ft (91.4 m), curved bridges, and those bridges with wall-type abutments or stub-type abutments on rigid foundations were still provided with deck joints at abutments. With these few exceptions, almost all of Ohio's other bridges were constructed as fully continuous integral bridges. The others that did not lend themselves to integral types of construction were provided with movable joints at abutments and, except for the bridges with extreme skews, elastomeric joint seals.

If the bridge deck joint sealing systems available to transportation departments had been of a higher functional quality and durability, further interest in expanding the application range of integral types of design probably would have waned. However, the poor quality of these systems and the constant maintenance that they required compelled bridge designers to seek ways to adapt the attributes of integral construction to those bridges still being provided with movable joints at abutments. Figure 1 shows the basic design configuration that has evolved from that search.

The basic features of the semi-integral abutment concept of Figure 1 include the absence of a bridge deck joint; a superstructure that moves longitudinally on elastomeric bearings almost independent of rigid abutment foundations; abutment members, including piling, that can be designed to operate well within the usual allowable stress limits; superstructure end areas that are reduced, resulting in less passive pressure and pressures that are less eccentric with respect to the neutral axis of the superstructure (i.e., lower axial loads and bending moments because of passive pressure); and abutment and end diaphragm configurations that are simple to design, simple to reinforce, and relatively simple to construct.

Note, however, that this design does not eliminate the need for movable joints. In fact, it doubles their number because, in addition

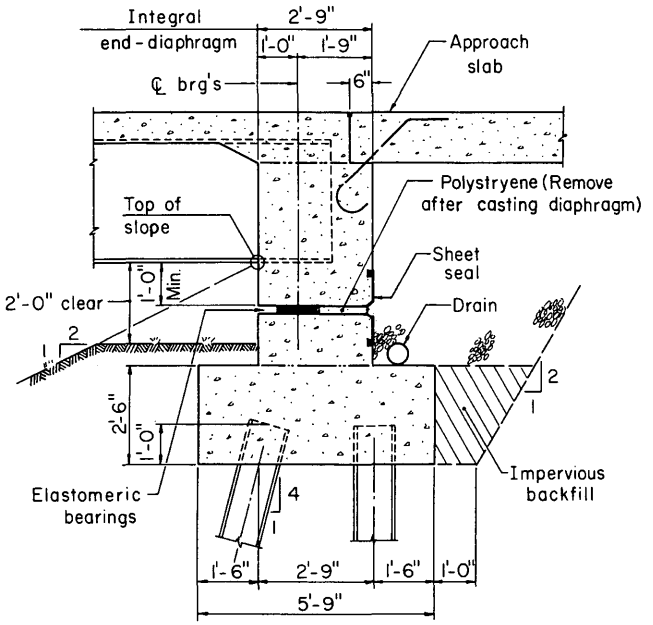

FIGURE 1 Semi-integral abutment concept similar to that of Ohio for single- and multiple-span continuous bridges on rigid supports (spread footings on bedrock, two or more rows of piles, pedestals to bedrock, etc.). This design concept is not recommended for footings on soil or flexible foundations (single row of piles, etc.).

to a movable joint at the level of the bridge seat, another movable joint is needed between the approach slab and approach pavement. However, although it has doubled their number, this design concept has reduced a bridge's vulnerability to substantial maintenance. If these joints fail to function as desired, their failure will not have the damaging consequences that have come to be associated with malfunctioning deck joints and joint sealing systems.

However, a few words of caution. Although it has expanded the application range for bridges without deck joints, the semi-integral design concept described in this paper possesses a number of unusual characteristics that must be recognized and provided for. Otherwise, application of this type of design may result in bridges that do not satisfy all of their functional requirements. A discussion of these characteristics is the primary focus of this paper.

SUPERSTRUCTURE RESTRAINT

Of all the characteristics of the semi-integral bridge concept described in this paper, the longitudinal, lateral, and vertical restraints of the superstructure are the most important. This type of structure should not be considered for design unless its designer is familiar with these characteristics and makes appropriate design provisions to account for them.

Longitudinal Restraint

The details in Figure 1 show that the superstructure that is supported on movable elastomeric bearings moves almost independently of the abutments. That is why this design concept is adaptable to bridges with various types of rigid abutments. For bridges without fixed piers, it receives its longitudinal restraint almost exclusively from sources not normally used in bridge design for this purpose. Longitudinal restraint comes from approach slab-subbase friction, shearing resistance of elastomeric bearings, and the compressive resistance of structure backfill. However, during cold weather, after the superstructure contracts away from the abutments (and away from the backfill), only the shearing resistance of half of the bearings and the frictional resistance of the approach slabs moving relative to the subbase will be immediately available to restrain the superstructure against externally applied longitudinal forces. For this reason, it would be desirable if the granular backfill at abutments could be placed and consolidated during cold weather or at night during hot weather so that the backfill could initially contribute more restraint to supplement that of the approach slabs and bearings for resisting longitudinal forces.

Providing turn-back wingwalls cantilevered from the superstructure in place of straight wingwalls would provide additional longitudinal restraint by mobilizing the resistance of backfill-wingwall friction, or for wingwalls with irregular surfaces, the shearing resistance of the backfill. For longer multiple-span structures, attaching the superstructure to a free-standing pier would be another way of providing additional resistance to longitudinal forces.

Generally, longitudinal resistance provided by approach slabs and bearings should be sufficient to satisfy specification requirements respecting the resistance to longitudinal forces. For moderate earthquake forces, the resistance provided by the consolidated backfill should provide the additional longitudinal restraint needed for moderate-length bridges, even during cold weather. For longer bridges, anchorage to piers can provide the extra longitudinal restraint needed, even for large longitudinal forces.

Lateral Restraint

Figure 2 shows an elevation view of a typical semi-integral abutment. In this view, the superstructure is separated from the abutment by an essentially horizontal movable joint at the bridge seat and vertical movable joints between the superstructure and transverse wingwalls. The horizontal bridge seat joint is shown in Figure 1. The vertical wingwall joints are similar except that only fillers and sealers are provided for unskewed bridges. Consequently, the abutments of this semi-integral bridge concept function essentially as longitudinal guides for the superstructure.

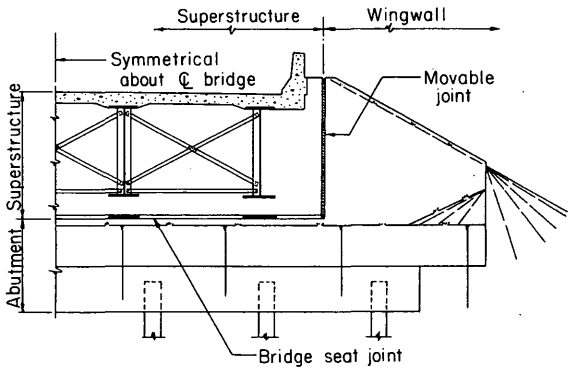

FIGURE 2 Semi-integral abutment with transverse wingwalls.

Vertically, the superstructure is supported by elastomeric bearings in the bridge seat joint. Laterally, the superstructure is supported by the interaction of the superstructure, approach slab, and backfill; to some extent by the compressive resistance of the filler in the lateral joints; and to some extent by the shearing resistance of the elastomeric bearings in the bridge seat joint. For applications in which substantial lateral resistance is necessary [such as skewed structures (described later) or structures exposed to stream flow pressure or earthquake forces], guide bearings are necessary and their use in the wingwall joints or elsewhere between beams is recommended.

For superelevated bridges where bridge seat joints (Figure 2) are sloped parallel to the deck surface and where elastomeric bearings are also sloped, lateral guide bearings are needed to resist the lateral component of the superstructure reaction. Otherwise, support bearings should be set on level bridge seat surfaces. When considering most of the application situations that have to be contended with in the design of semi-integral bridges with characteristics similar to the concept described in this paper, the routine use of guide bearings should be considered as standard for most, if not all, such applications.

Rotational Restraint

On the basis of the analysis given below, superstructures of some skewed semi-integral bridges will, unless restrained by guide bearings, tend to rotate in a horizontal plane. This tendency will be greater for bridges with greater skews. Horizontal rotation will initiate sooner for longer bridges. The characteristics of this behavior are described as follows.

As superstructures of semi-integral bridges expand in response to rising ambient temperatures, superstructure elongation (ΔL) will be resisted by backfill being compressed at abutments (Figure 3). Force is required to compress backfill, and this same force will restrain superstructure elongation by inducing compressive stresses in the superstructure. When considering the relative compressibility of backfill and a reinforced concrete superstructure — even thoroughly consolidated granular backfill—it should be clear that almost all of the expected superstructure elongation will occur as compression of backfill. Only a slight amount of compression will occur in the superstructure, as evidenced by a slight reduction in the amount of superstructure elongation that would have been evident if the elongation had been unresisted. These compressive stresses are shown summarized in Figure 4 as the resultant longitudinal superstructure compressive force $P_p \sec \theta$. The centralized location of this resultant force is based on the assumption that structure backfill is homogeneous and that it would be uniformly compressed throughout the width of the superstructure. The components of this resultant force against the backfill are the normal force as a result of passive pressure P_p and the lateral force $P_p \sec \theta \sin \theta$, or in simpler terms, $P_p \tan \theta$. If lateral guide bearings for the superstructure are not provided and the force $P_p \tan \theta$ is not adequately resisted at the structural backfill interface [by friction of backfill on superstructure end-diaphragms ($P_p \tan \delta$) or by the shearing resistance of backfill ($P_p \tan \phi$)], differential movement at the structural backfill interface will commence. When considering the shearing resistance of backfill ($P_p \tan \phi$) or the frictional resistance of backfill on smooth concrete surfaces ($P_p \tan \delta$), usually the latter force will be found to be the smaller of the two, and it will govern behavior at the structural backfill interface.

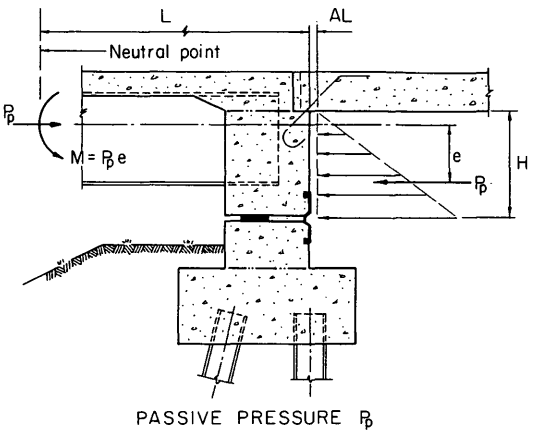

FIGURE 3 Passive pressure development for semi-integral bridges.

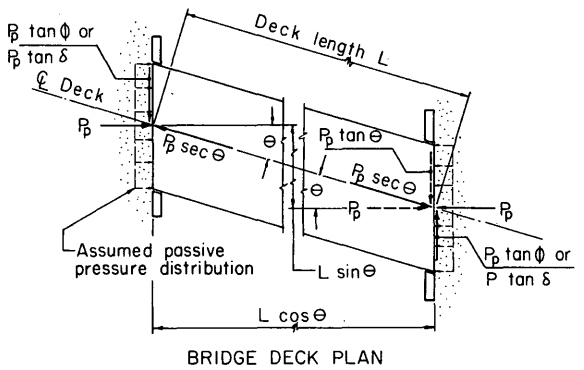

FIGURE 4 Elongation and rotation of semi-integral bridge superstructures before rotation.

Because the external forces act on both ends of the superstructure of a semi-integral bridge (Figure 4), the eccentric longitudinal force component P_p will tend to rotate the superstructure toward the acute corners of the structure or, for the skew shown in Figure 4, in a clockwise direction. The lateral force components on the other hand ($P_p \tan \phi$ or $P_p \tan \delta$) will tend to resist this rotation.

Using the shearing resistance of an idealized granular backfill and the frictional resistance of backfill on the backfill-structure interface surfaces, it can be shown that superstructures of semi-integral bridges skewed greater than about 15 degrees will be unstable unless they are provided with guide bearings at both abutments.

With respect to Figure 4, and the symbols tabulated below, that statement can be justified by a short series of computations as follows:

L = bridge deck length,

θ = bridge skew angle,

P_p = total passive pressure,

FS = factor of safety,

ϕ = angle of internal friction of backfill, and

δ = angle of structural backfill interface friction.

For the superstructure of a skewed bridge to be stable, the force couple tending to resist rotation ($P_p \tan \delta L \cos \theta$) must be equal to or greater than the force couple tending to cause rotation ($P_p L \sin \theta$) or

$$P_p L \sin \theta \leq P_p \tan \delta L \cos \theta \quad (1)$$

Providing a factor of safety against rotation

$$P_p L \sin \theta \leq P_p \tan \delta L \cos \theta / FS \quad (2)$$

Because the weight of attached approach slabs and slab-subbase friction will tend to resist movement, a safety factor of 1.5 seems sufficient for this situation. Inserting this factor in Equation 2 and simplifying yields the following:

$$\sin \theta \leq \tan \delta \cos \theta / 1.5$$
$$\tan \theta \leq \tan \delta / 1.5$$
$$\theta \leq \arctan (\tan \delta / 1.5) \quad (3)$$

Assuming that the angle of friction at the structural backfill interface (δ) is 22 degrees, as discussed in a previous work (*1*, p. 7.2–63) about granular backfill on a smooth concrete surface, Equation 3 suggests that the bridge skew angle θ must be equal to or less than 15 degrees to be stable. For greater skews, it is likely that rotation will be initiated unless guide bearings are provided at both abutments to resist the forces inducing such movement.

Other observations can be made with respect to Equations 1 and 3. Although Equation 1 indicates that some level of passive pressure must be generated to cause rotation, Equation 3 indicates that the skew angle at which rotation will be initiated is independent of both passive pressure and bridge length and directly related to structural backfill interface friction.

What would be the result of the restrained elongation of the superstructure and differential movement at the structural backfill interface? Figure 5 and the speculative analysis described below are offered as an answer for this question.

As before, it is assumed that sliding friction ($P_p \tan \delta$) will govern the behavior at the structural backfill interface. Because the force caused by sliding friction would not be sufficient to resist the lateral force component $P_p \tan \theta$ for bridges with large skews, sliding (rotation) of the superstructure toward the acute corners of the structure will be induced.

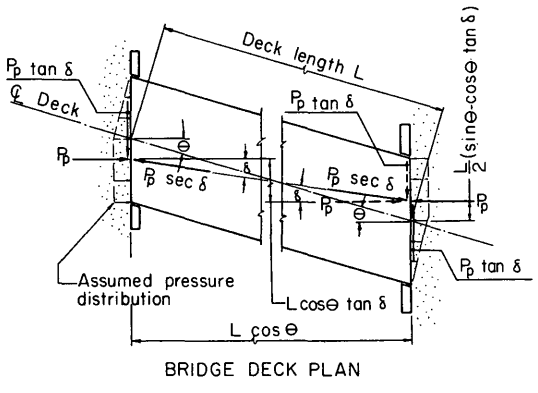

FIGURE 5 Elongation and rotation of semi-integral bridge superstructures after rotation.

Rotation of the flat-ended superstructure will alter the earth pressure distribution within the backfill. As rotation commences, the obtuse corners of the superstructure will move into and compress the backfill while the acute corners will move away from and allow the backfill to expand. The amount of movement into and away from the backfill may appear insignificant when compared with the original movement into the backfill (ΔL) caused by thermal elongation of the superstructure. However, slight movements of soil-retaining structures can have significant effects on soil pressures. Earth pressure research documented previously (*1*, p. 7.2–60; *2*) indicates that a fair amount of structural movement into the backfill (about 5 percent of its height) is needed to achieve full or ultimate passive pressure. On the other hand, only a very small amount of movement away from the backfill (about 0.1 percent of its height) will result in active pressures. On the basis of these relationships of movements to pressure, it is assumed that backfill compression caused by the rotational movement of the obtuse corners into the backfill would only slightly increase passive pressure because this movement is so small relative to the initial superstructure elongation, ΔL. However, at the acute corners, the slight rotational movement of the superstructure away from the backfill probably will result in a drop of soil pressure from the initial passive pressure caused by ΔL to active pressure.

The slight rise in soil pressure at the obtuse corners and the significant drop in pressure at the acute corners of the structure will alter the pressure distributions within the backfill throughout the width of the structure. This change in pressure distribution will be accompanied by a lateral shift of the pressure resultant, identified as P_p in Figure 5 (the designation P_p is actually a misnomer because this pressure resultant is now intended to represent a summation of a whole spectrum of pressures from active pressure near the acute corners through various levels of passive pressure to a maximum passive pressure at the obtuse corners). This shift of the pressure resultant will decrease the lateral distance between the resultants and consequently the moment couple-inducing rotation will diminish.

Figure 4*b* illustrates the condition in which the force components tending to induce sliding ($P_p \tan \theta$) have diminished until they equal the forces caused by frictional resistance ($P_p \tan \delta$). Similarly, the moment couple tending to induce movement ($P_p L \sin \theta$) has diminished to (P_p)($L \cos \theta \tan \delta$) and is in equilibrium with the force couple resisting rotation ($P_p \tan \delta$)($L \cos \theta$).

It is presumed that the movements described were the result of a single increase in the ambient temperature. Subsequently, a temperature drop would be accompanied by a shortening of the superstructure or a movement of the end of the structure away from the backfill. In response to this movement, the backfill would expand and soil pressure would drop to active pressure or less, depending on the composition and state of consolidation of the backfill.

Depending on the amount of backfill reconsolidation that would occur while the superstructure was withdrawn, it is presumed that a similar but more modest superstructure rotation would accompany each cycle of superstructure elongation. Over time, the significant number of thermal cycles that would take place suggests that the superstructures of semi-integral bridges should continue to experience incremental and accumulative rotation until or unless such rotation is terminated by the restraint provided by some other stable part of the structure.

The motions described will be prevented or moderated as a result of approach slab-subbase friction and the shearing resistance of elastomeric support bearings and by the compressive resistance of fillers used in the movable joints between the superstructure and wing-

walls. Depending on the characteristics of the bridge seat joint seal, even this device may offer some resistance to horizontal rotation of the superstructure. When considering these supplemental resistance elements, it seems apparent that for some structures the most susceptible period for rotational movement would occur during construction when the superstructure would be exposed to "at-rest" placement pressures before approach slabs have been placed.

In an Ohio project planned for early construction, there is one site where twin semi-integral bridges with skews of 45 degrees are to be constructed. They are to be provided with removable guide bearings so that after their completion the guide bearings could be removed from one of the bridges. This would provide the opportunity to observe the behavior of essentially similar bridges exposed to the same environmental effects with one bridge with guide bearings and the other bridge without. The construction of these bridges and their early performance under service conditions should provide some of the experience needed to determine with greater certainty the effects of skew on the movement of semi-integral bridge superstructures.

In addition, more formal semi-integral bridge research is being planned by the Ohio Department of Transportation—research that is intended to provide some of the factual background on which the design and construction of future semi-integral bridges can be based.

Earth pressure measurements at the Forks Bridge of Forks, Maine, appear to provide some support for the analysis described. The Forks Bridge is a skewed long span steel rigid frame structure. According to the report (*3*, p. 2)

> Earth pressures were measured at 8 pressure cells on each abutment with measurements on both sides of the abutment centerline and at different elevations. . . . The effect of skew was noticeable during the summer, although the average increase for all cells at El. 583 was 1,200 psf, the increase at the obtuse sides was 1,800 psf, while the increase at the acute sides was 620 psf. . . .

Since pressure measurements at this structure are to continue, the final report for this project should provide valuable background for subsequent pressure research on semi-integral bridges.

The magnitude of guide-bearing reactions is another indication of the potential for superstructure rotation. Because most of the thermal movement of a superstructure will be parallel to the longitudinal axis of a bridge, guide bearings should be placed parallel to this axis. Then on the basis of the lateral force components shown in Figure 4, the guide-bearing reaction, which would be normal to this axis, is given by $P_p \tan \theta \cos \theta$, or in a simpler form, $P_p \sin \theta$. On the basis of this relationship, the required capacity of guide bearings for a structure skewed 30 degrees is equal to $0.5P_p$, or one-half of the total passive pressure. For a 45-degree skew, the required capacity equals more than 70 percent of the total passive pressure. Consequently it is clearly evident that neither the frictional resistance ($P_p \tan \delta$) nor the shearing resistance ($P_p \tan \phi$) of the backfill can resist forces of this magnitude. Consequently, guide bearings should be provided for structures with large skews if a stable superstructure and a fully functional bridge are to be provided.

Vertical Restraint

Because of their jointless construction, many types of integral bridges are buoyant when they become submerged. This is true for many I-beam bridges and some spread-box beam bridges.

The weight of diaphragms and abutments provides some resistance to uplift. But generally, some positive design provisions must be made to ensure that integral bridges have a reasonable factor of safety against flotation. I-beam webs can be pierced near top flanges by holes 3 in. (76 mm) in diameter spaced uniformly throughout the beam length; the space between spread boxes can also be vented by placing horizontal vent ducts 3 in. (76 mm) minimum diameter near the top flange of all beams. These ducts should pass completely through the beams from one web to the other, and they should be placed in concrete diaphragms or be completely encased in concrete to prevent floodwaters from entering beam voids; counterweights could be used but their weight must be taken into account during beam design. Uplift restraints could be provided at pier bearings, or some piers can be integrally constructed with the superstructure to add sufficient uplift restraint to counteract buoyancy.

In place of vent holes, added weight, uplift restraints, or integral pier construction, the use of the most buoyant structures should be restricted to those bridge sites where the highest floodwater levels are well below the superstructure.

DESIGN ASPECTS

Movable Joints

As mentioned earlier, the semi-integral bridge with its attached approach slabs has eliminated bridge deck end joints. In their place, it has incorporated two other joint types: a movable joint at the level of the bridge bearings and one at the pavement end of the approach slab. Although it doubles their number, the design has minimized their significance. Less-than-desirable performance for either of these joints will not have the significantly adverse consequences that have come to be expected with the failure of bridge deck joints. The bridge seat joint and cycle control joint are the two joints that have been provided to accommodate the movement of semi-integral bridges. In addition, one must mention that rigid approach pavements also must be provided with effective pressure relief joints to guard semi-integral bridges from uncontrollable approach pavement growth.

Bridge Seat Joints

In the design shown in Figure 1, the troublesome bridge deck joint has been eliminated. However, in its place, a movable joint has been introduced at the level of the bridge seat. Corrosion-resistant elastomeric bearings are provided so that the superstructure can move longitudinally almost independent of rigid abutments.

The movable bridge seat joint must be provided with a durable elastomeric seal because it is buried in the backfill and consequently is not accessible for repair or replacement. Otherwise its most important characteristic is its ability to prevent backfill from being forced into the joint by compressed backfill. It would be desirable but not absolutely necessary for the seal to be watertight. It must also permit unrestrained differential movement between the abutment and superstructure, even for bridges with large skews, and it must retain these characteristics for many years without the need for repair or replacement.

Although the bridge seat joint seal is an important aspect of the semi-integral bridge design, Ohio has yet to adopt a design that appears to fulfill all necessary functional and durability characteristics. A number of trial designs have been developed and used. Initially, standard compression seals were used. Then it became

apparent that a reinforced elastomeric sheet-type seal was more functionally suitable for square and skewed applications. The sheet seal now being used is nylon reinforced neoprene 3/32 in. (2.4 mm) thick. It is attached to the bridge by various means, including elastomeric anchor rods in formed recesses, steel clamp bars with expansion anchors, washers and masonry nails, or bonding adhesives. It remains to be seen which one or more of these attachment methods will be adopted and perfected by Ohio for this critical joint.

Cycle Control Joints

Semi-integral bridges with attached approach slabs lengthen and shorten in response to temperature and moisture changes. Consequently, for such structures, the boundary between approach slabs and approach pavement should be provided with a cycle control joint to facilitate such movement. Otherwise, longitudinal cycling of both structure and approach slabs can damage both flexible and rigid approach pavements.

At present, standard pavement expansion joints with compressive fillers are being provided for shorter semi-integral bridges. Longer bridges are being provided with pavement pressure relief joints (wide joints filled with asphalt concrete).

Because of the restrained growth of approach pavement it is imperative that semi-integral bridges built adjacent to rigid pavement also be protected from pressures. Effective pressure relief joints should be provided for all semi-integral bridges—even the shortest bridges. Consequently, for bridges adjacent to rigid approach pavement, two types of pavement joints are required: one to facilitate the cyclic movement of the bridge and the other to protect the structure and cycle control joints from the effects of pavement growth. Designs by four transportation departments were illustrated elsewhere (*4*); as noted, all designs in use have their limitations.

For longer integral bridges, Ohio is using wide pressure relief joints to serve both purposes. Because integral bridges and semi-integral bridges are such new conceptions, much additional development is needed if the approach pavement joints adjacent to such structures are to provide all of the necessary attributes that these joints must have to satisfy structural requirements without continuous maintenance.

Backfill

Backfill for semi-integral bridges should not be considered a nuisance that has to be contended with, as is the case with the fully integral bridge on flexible abutments. Instead, backfill should be recognized as an integral and important part of the semi-integral bridge concept. As in the case of a retaining wall supported by spread footings on subsoil, when properly designed the wall will interact compositely with the subsoil and be adequately supported by the soil vertically and laterally. Similarly, the superstructure and backfill of semi-integral bridges form a partially composite interactive structure. In this context, the backfill performs multiple functions. Although rigid abutments provide vertical and lateral support for the superstructure, the backfill supplements this support by providing vertical support for approach slabs and both longitudinal and lateral support for the superstructure. The ultimate success or failure of the semi-integral bridge concept will depend to a great extent on methods and procedures that are developed by the bridge engineering profession to enhance the interaction between the superstructure and backfill. Because backfill is such an integral part of a semi-integral bridge concept, every effort should be made to ensure that it is properly selected, constructed, and maintained.

Backfill should be selected and designed to have characteristics suitable for superstructure-backfill interaction: it should be of a composition that protects it from erosion and it should be protected from above by full-roadway width approach slabs. For bridges with confined drainage (raised curbs, barriers, parapets, etc.) approach slabs must be provided with curbs with a height of at least 6 in. or more to confine roadway drainage and conduct it along bridge approaches and away from the backfill. Approach roadway curb inlets should be considered and provided if necessary to ensure effective drainage control. An effective subdrainage system should also be provided in the backfill above impervious embankments to ensure that the retention of subsurface water is minimized.

Provisions also should be made to intercept subsurface approach roadway drainage and discharge it away from the abutment backfill. Granular subbases should be provided with efficient lateral drains to discharge subbase drainage laterally to embankment side slopes. Roadway underdrains must be terminated beyond the bridge approach slabs and provided with lateral drains to embankment side slopes. Otherwise, underdrain accumulations should be conducted in closed conduits longitudinally through the backfill and abutments.

Finally, bridge maintenance engineers should become familiar with semi-integral bridge characteristics so that they can properly appreciate the importance of backfill superstructure interaction and provide the corrective maintenance that such a structure must have if they are to provide the service life that their design anticipated.

CONSTRUCTION ASPECTS

Unlike their jointed bridge counterparts, the design peculiarities of the semi-integral bridge concept have created concrete placement and curing problems that are unique to this type of design. These problems have to do with the forming for and the placement and curing of second- or subsequent-stage concrete elements of the bridge while attempting to bond them to the first-stage elements that will be moving in response to ambient temperature changes.

End Diaphragms

The integral end diaphragm indicated in Figure 1 is part of the superstructure of semi-integral bridges; consequently it will move both longitudinally and rotationally with the superstructure. However it is cast in forms that are usually fastened to and supported by rigid abutments. In fact, the abutment bridge seat covered by fillers and elastomeric bearings usually serves as a rigid bottom form for the end diaphragm. So while ambient temperature changes during and shortly after end-diaphragm concrete placement, superstructure stringers either will be elongating or shortening in response to those changes, resulting in differential movement between stringers and the rigidly supported end-diaphragm forms. If these movements are appreciable, and occasionally they can be, they can damage freshly placed end-diaphragm concrete. This problem is more acute for the more thermally responsive steel stringers. It is magnified in longer bridges, and it can be compounded in geographical locations where rapid and significant ambient temperature changes can occur during end-diaphragm concrete placement and setting.

Generally, it is not practicable to restrict concrete placement to those days of the year with the smallest temperature range and

consequently to those periods with the smallest potential for large superstructure movements. But for the shorter, more usual moderate-length semi-integral bridges, it is practicable to limit concrete placement to days when large and rapid temperature changes are not expected and to periods during the day when superstructure movement is smallest, generally shortly after the ambient temperature approaches, reaches, and departs from the day's peak temperature. A plan note to provide such control and protection for freshly placed end-diaphragm concrete can be phrased somewhat as follows:

> Concrete for end diaphragms shall be placed during days when sudden temperature changes are unlikely and be completed at least 4 hr before the concrete placement day's peak ambient temperature.

For longer structures where such placement controls may not be sufficient to protect fresh concrete, end diaphragms can be placed in two separate placements. The first placement, up to but slightly below the superstructure stringers, can be placed without concern for superstructure movement. Then, after an appropriate cure time, the stringers and end-diaphragm forms can be attached to and supported by this first placement. Subsequently, this first placement, the end-diaphragm forms, and stringers will move in unison so that the remainder of the end-diaphragm concrete can be placed at any convenient time without regard for ambient temperature changes.

Approach Slabs

Construction of approach slabs is similar to that of the end diaphragms in that slab concrete must be placed on a rigid bottom form (the subbase) while the leading edge of the slab is connected to a moving superstructure. Consequently, similar placement controls can be used for placement of approach slab concrete for the moderate-length semi-integral bridges. A plan note similar to the following can be used:

> Approach slab concrete shall be placed toward the superstructure during days when sudden temperature changes are unlikely and be completed at least 4 hr before the concrete placement day's peak ambient temperature.

To protect approach slab-superstructure connections, an attempt should be made to reduce the force necessary to move the slabs. This can be accomplished by requiring a smooth subbase surface to serve as a bottom form for the approach slab.

For longer semi-integral bridges, it may be necessary to place approach slabs in two placements. The first placement can extend from the far end of the slab to a construction joint located within 3 ft (0.9 m) of the superstructure. Then after this first segment has been placed and cured, it can be connected to the superstructure with several longitudinal tie bars with mechanical connectors, and the remaining portion of the slab can then be placed using a note similar to the one mentioned earlier to protect the freshly placed concrete. If there is superstructure movement, the mechanically connected tie bars should be sufficient to pull the approach slab without stressing the fresh concrete. This will relieve the second-stage concrete placement and connection reinforcement from movement-induced stresses.

Backfill

Because superstructures of semi-integral bridges are restrained in place longitudinally by backfill at abutments and to some extent by the shearing resistance of elastomeric bearings, placement of this backfill needs to be controlled to avoid unbalancing backfill pressures and shifting the superstructure. Therefore, a backfill procedure is necessary to ensure that backfill is placed simultaneously at both abutments.

As mentioned earlier, it would be advantageous to place and consolidate backfill during low-temperature periods to improve confinement of the superstructure. During hot weather, placing backfill at night should be considered.

SUMMARY

The first bridge with semi-integral characteristics similar to those that have been described in this paper was constructed in 1978. This bridge services Ohio's Route 555 and spans the Muskingum River at Zanesville, Ohio. It is an unskewed three-span girder structure 540-ft (164.6-m) long. It uses approach slabs and turn-back wingwalls to engage or embrace the backfill. Since then a number of similar shorter structures have been constructed. The concept has been used most often to retrofit existing end-jointed bridges. A number of other semi-integral bridges are being planned for both new and retrofit applications, some with significant skews. As of this writing, skewed semi-integral bridges with guide bearings have not yet been constructed. The response of local maintenance engineers to these bridges has been good. It is primarily through their continual urging that many of these bridges were built.

For new structures, the main emphasis of the Ohio Department of Transportation is on the construction of fully integral bridges with flexible abutments. However, for those applications where rigid abutments are necessary, the semi-integral bridge concept is now being adapted and used with increasing regularity. The actual performance of these bridges throughout the next several years will influence its further development and ultimately its suitability for further applications.

REFERENCES

1. *Foundations and Earth Structures*. Design Manual 7.2. Department of the Navy, Naval Facilities Engineering Command, Alexandria, Va. 1982.
2. Wu, T. H. *Soil Mechanics*. Worthington, Ohio, 1982, pp. 276–280.
3. Elgaaly, M., T. C. Sandford, and C. B. Colby. *Monitoring of the Forks Bridge to June 6, 1990* (plus Report Supplement 1). University of Maine, Aug. 1992.
4. Burke, M. P. Jr., Bridge Approach Pavements, Integral Bridges, and Cycle Control Joints. In *Transportation Research Record 1113*, TRB, National Research Council, Washington, D.C. 1987.

Publication of this paper sponsored by Committee on General Structures.

Development and Testing of Timber Bridge and Transition Rails for Transverse Glued-Laminated Bridge Decks

PENMATSA R. RAJU, HOTA V. S. GANGARAO, SHEILA RIMAL DUWADI, AND HEMANTH K. THIPPESWAMY

Timber bridge and transition rails for transverse glued-laminated bridge decks were developed and tested. Three timber bridge rails with approach rails on both ends of the timber rail were developed for Performance Level 1, the lowest performance level. Two bridge rails did not have curb rails and one bridge rail had a curb rail. Six crash tests on three bridge rails and one crash test on a transition rail were performed. Each bridge rail was tested with an 817-kg (1,800-lb) small automobile and a 2452-kg (5,400-lb) pickup truck. The transition rail was tested with a 2452-kg (5,400-lb) pickup truck. All of the bridge rails and the transition rail met the crash test requirements as specified by the 1989 AASHTO Guide Specification for Rails and a 1981 NCHRP report. The crash test reports have been submitted to FHWA for review and acceptance.

Recent advances in timber bridge research and development have shown that timber can be a cost-effective and competitive bridge construction material. Timber bridges are being used for low to medium volume and high-intensity traffic conditions and share about 12 percent of total bridges that span 6.1 m (20 ft) or more in the United States (*1*). The present requirement for rail systems to be accepted by FHWA is that the rail system should be satisfactorily crash tested. The acceptance standards are given in AASHTO's 1989 Guide Specifications for Bridge Rails (*2*) and an NCHRP report (*3*). The lack of standard timber bridge rail systems that have been successfully crash tested in accordance with these specifications has limited the use of timber in bridge construction.

The Constructed Facilities Center of West Virginia University (CFC-WVU), was awarded a contract by FHWA to conduct timber bridge research. One task was to develop and crash test timber bridge rails and transition rails suitable for use on transverse timber bridge decks. Other research centers such as SouthWest Research Institute (SWRI) and Midwest Roadside Safety Facility are also involved in similar projects in developing and crash testing timber bridge rails according to the criteria specified in the AASHTO guide specifications for Performance Levels 1 and 2 (PL-1 and PL-2). To date, only one timber bridge rail, tested by SWRI, in 1988, is included in FHWA's approved list of bridge rails for federal-aid projects (*4*). This bridge rail was attached to a longitudinal dowel-laminated bridge deck and successfully crash tested for PL-1 criteria. PL-1 is specified for low-level bridges with light traffic.

P. R. Raju, Michael Baker, Jr., Inc., 420 Rouser Road, Coraopolis, Pa. 15108. H. V. S. GangaRao and H. K. Thippeswamy, Constructed Facilities Center, West Virginia University, Morgantown, W.Va. 26506-6101. S. R. Duwadi, FHWA, McLean, Va. 22101-2296.

BRIDGE RAIL SYSTEMS

Bridge rails are provided to protect vehicle occupants and the traffic. Thus, bridge rails are important elements from a safety point of view. Approach rails are provided on both ends of the bridge rail and consist of both transition rail and guard rail. The transition rail connects the flexible guard rail to the rigid bridge rail.

Bridge rails are commonly made of concrete, steel, aluminum, or timber. The cross section of a bridge rail is a solid wall, a post-beam rail, or a combination of the two. From the functional point of view, bridge rails are classified as traffic rails, pedestrian rails, bicycle rails, and combination rails (*5*).

The main purpose of the traffic rails is to provide safety for the traffic by containing and redirecting the vehicle within the bridge. This is achieved by meeting geometric and strength requirements of the rails for crash testing. The following are important considerations to be taken into account in the design and evaluation of bridge and transition rails:

- Protection of vehicle occupants during collision with traffic rails,
- Protection of vehicle occupants and vehicles on the roadway and near the roadway,
- Replaceability,
- Aesthetics, and
- Cost minimization.

REQUIRED CRITERIA FOR EVALUATING BRIDGE RAIL CRASH TEST

The weight of the test vehicle (W), out-to-out wheel spacing (B), test vehicle center of gravity (CG) above the deck (G), impact angle (θ), and test vehicle velocity (V) are indicated in Table 1 for PL-1 according to AASHTO's guide specifications (*2*). The following are the required criteria for evaluating the bridge rail crash test according to these specifications:

1. The traffic bridge rail must contain the test vehicle without any penetration or without going over the test rail.
2. Debris penetration into the vehicle passenger compartment and hazards to other traffic caused by the crash test vehicle are not permitted.
3. The passenger compartment must show integrity without any deformation or intrusion.
4. The test vehicle must remain upright during and after impact.

TABLE 1 Crash Test Criteria of Bridge and Transition Rail for PL-1 (2,3)

Test Vehicle Description	Bridge Rail		Transition Rail
	Small Automobiles	Pick-up Truck	Pick-up Truck
Weight	817 kg (1.8 kips)	2452 kg (5.4 kips)	2452 kg (5.4 kips)
Out to Out Wheel Spacing	1.68 m (5.5 ft)	1.98 m (6.5 ft)	1.98 m (6.5 ft)
CG of the Vehicle Above the Deck	508 mm (20 in)	686 mm (27 in)	686 mm (27 in)
Distance from CG to Front of the Vehicle	1.65 m (5.4 ft)	(2.59 m) 8.5 ft	2.59 m (8.5 ft)
Impact Angle	20°	20°	20°
Performance Level	TEST VEHICLE SPEEDS		TEST VEHICLE SPEED
PL-1	80 kmph (50 mph)	72 kmph (45 mph)	72 kmph (45 mph)
Note: Permissible Variation in Test Vehicle Speed is +4/-1.6 kmph (+2.5/-1.0 mph) and Impact Angle is +2.5/-1.0 Degree.			

5. Occupant longitudinal and lateral impact velocities must be less than 9.2 and 7.6 mi/sec (30 and 25 ft/sec).
6. Occupant ride down longitudinal and lateral accelerations must be less than 15 *g*.

DESIRED CRITERIA FOR EVALUATING BRIDGE RAIL CRASH TEST

The following are the desired criteria for evaluating the bridge rail crash test according to AASHTO (2):

1. The test vehicle shall be redirected smoothly from the test article.
2. The rear of the test vehicle shall not yaw more than 5 degrees away from the rail during the impact and vehicle exit from the rail.
3. The effective coefficient of friction μ shall be less than 0.35. The smoothness of the rail is assessed by the effective coefficient of friction.
4. The test vehicle exit angle shall be less than 12 degrees.
5. The test vehicle shall not move more than 6.1 m (20 ft) laterally after the bridge rail impact. In addition, the maximum allowable lateral movement of 6.1 m (20 ft) should be maintained within the longitudinal vehicle travel, which is limited to 30.5 m (100 ft) plus vehicle length from the point of impact.

REQUIRED CRITERIA FOR RAIL DESIGN

The height of the rail from the top of the wearing surface to the top of a bridge rail shall be at least 686 mm (27 in.). An overlay thickness of 51 mm (2 in.) needs to be considered for the total height of the rail. Thus for the PL-1 rail system, the total height of the traffic rail shall not be less than 737 mm (29 in.) from the top surface of the deck.

The post setback distance (S) and the maximum clear opening below the bottom rail (C_b) and between the rails shall be determined

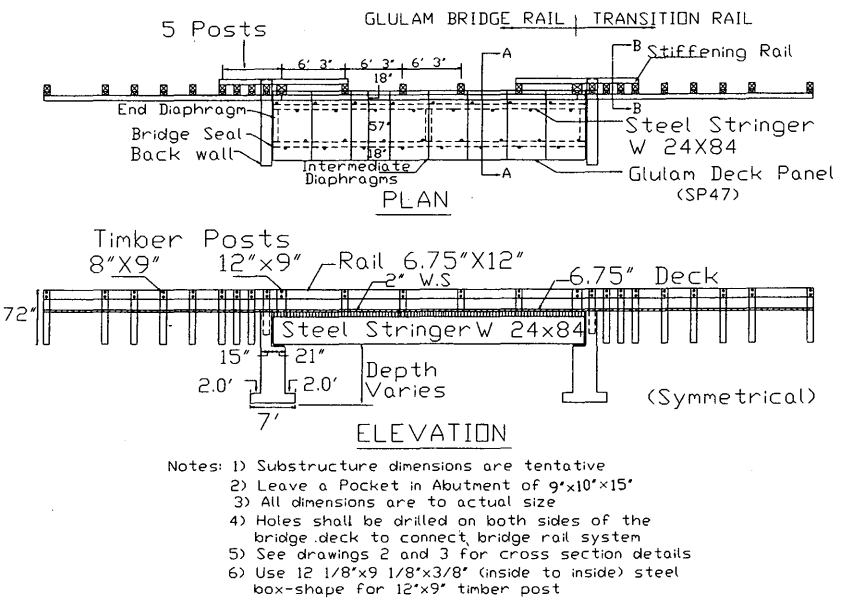

FIGURE 1 Timber Bridge Rail System 1 for PL-1: plan and elevation.

from Figure A 13.1.1-2 of Load Resistance Factor Design (LRFD)draft specifications (*5*). The bottom clear opening (C_b) shall not be greater than 381 mm (15 in.). The post setback distance shall not be less than 25.4 mm (10 in.) to avoid snagging of vehicle ports such as bumpers, wheels, and hood. The traffic face of rails must be continuous and smooth.

DEVELOPMENT OF TIMBER BRIDGE RAIL SYSTEMS FOR TRANSVERSE GLUED-LAMINATED BRIDGE DECKS

The timber bridge rail systems for transverse glued-laminated bridge decks were designed by CFC-WVU to meet the crash test requirements of PL-1. The crash tests were conducted at the Texas Transportation Institute (TTI). Three timber bridge rail systems are indicated in Figures 1 through 9 and listed as follows:

- Bridge Rail System 1: Glued-laminated rail attached to transverse timber deck on steel stringers,
- Bridge Rail System 2: Glued-laminated rail attached to transverse timber deck on glued-laminated beams, and
- Bridge Rail System 3: W-beam rail attached to transverse timber deck on steel stringers.

The following considerations were given while developing and selecting the feasible timber bridge rail systems:

- Ability to meet the strength requirements of AASHTO's 1989 guide specifications, (*2*) and NCHRP Report 230 (*3*),
- Replaceability of rail elements in the event of damage caused by vehicle impact,
- Adaptability to other types of timber bridge decks,
- Availability of material, including hardware,
- Maintainability and constructability,
- Structural integrity with the decks, and
- Cost and aesthetics.

GENERAL FEATURES OF BRIDGE RAIL SYSTEMS

The general features of each system along with the test criteria are indicated in Table 2. The bridge rails span 10 m (33 ft), with approach rails on both ends of the test bridge 7.6 m (25 ft) long. The height of the bridge rail from the top of the 51-mm (2-in.) wearing surface is 686 mm (27 in.) for all systems. The approach rail consists of a transition and a guard rail. All three bridge rail systems were developed for transverse glued-laminated timber bridge decks supported by glued-laminated and steel beams.

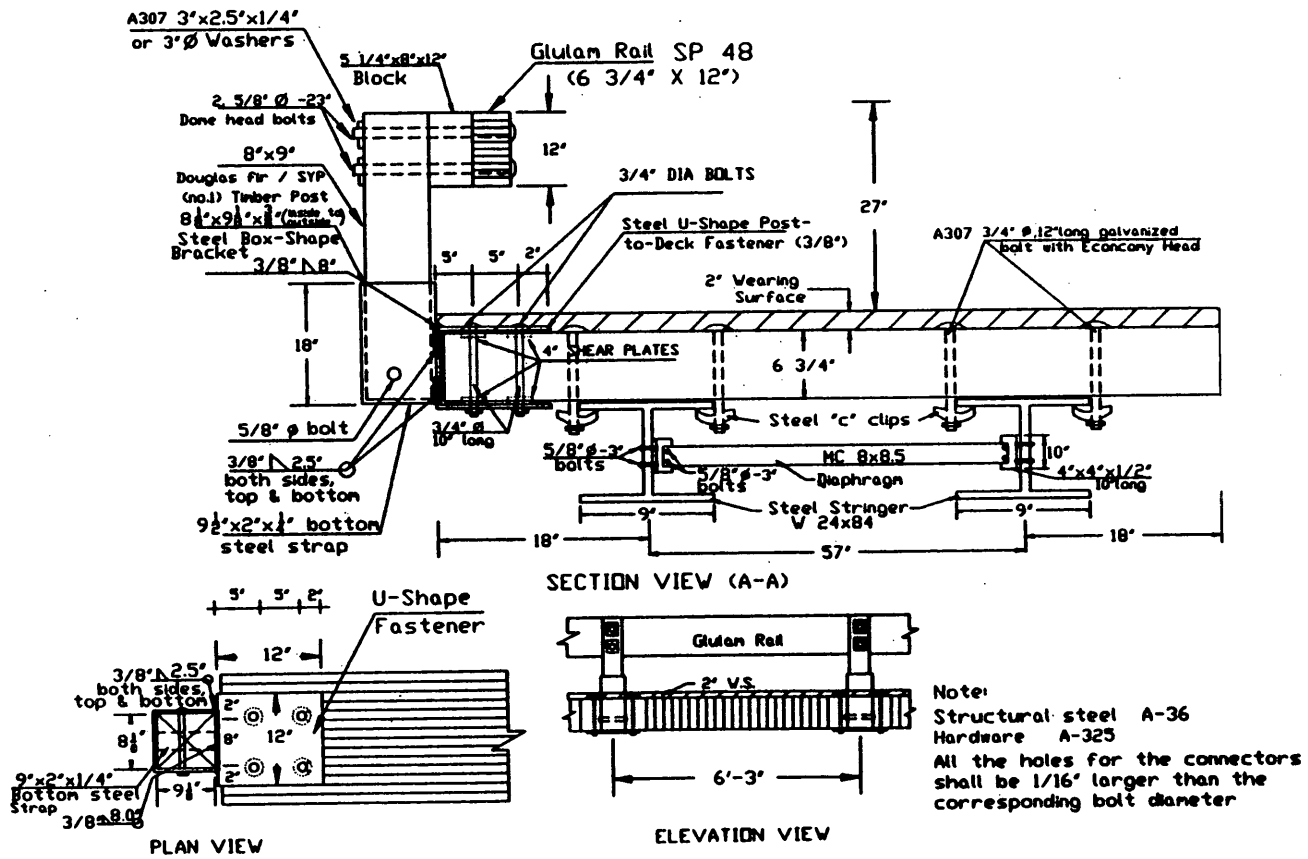

FIGURE 2 Timber Bridge Rail System 1 for PL-1: cross-sectional details of bridge rail.

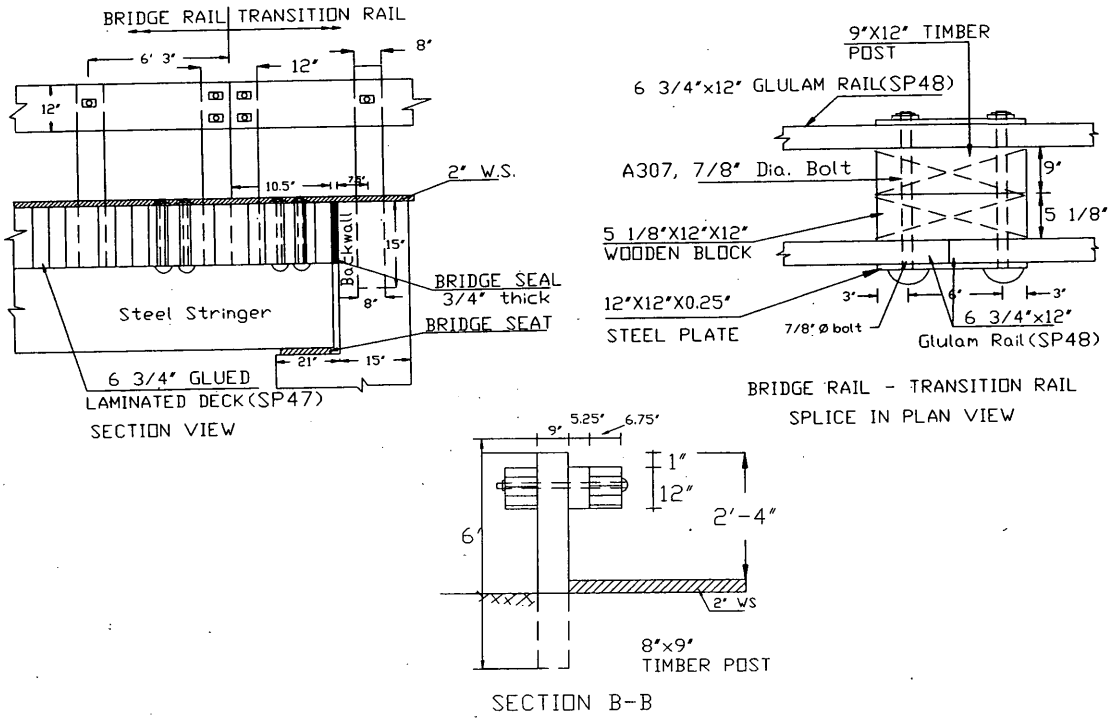

FIGURE 3 Timber Bridge Rail System 1 for PL-1: details of transition rail.

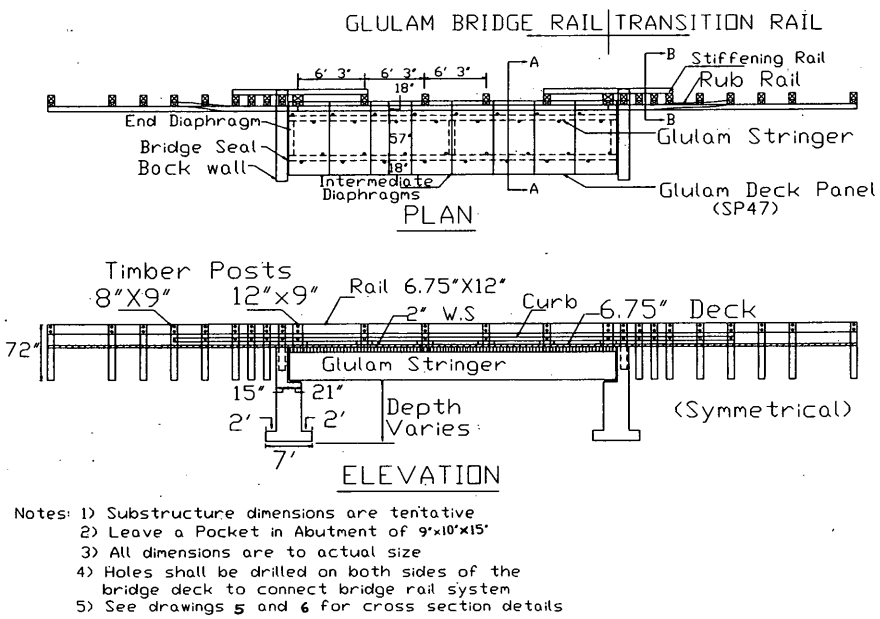

Notes: 1) Substructure dimensions are tentative
2) Leave a Pocket in Abutment of 9"x10"x15"
3) All dimensions are to actual size
4) Holes shall be drilled on both sides of the bridge deck to connect bridge rail system
5) See drawings 5 and 6 for cross section details

FIGURE 4 Timber Bridge Rail and transition Rail System 2 for PL-1: plan and elevation.

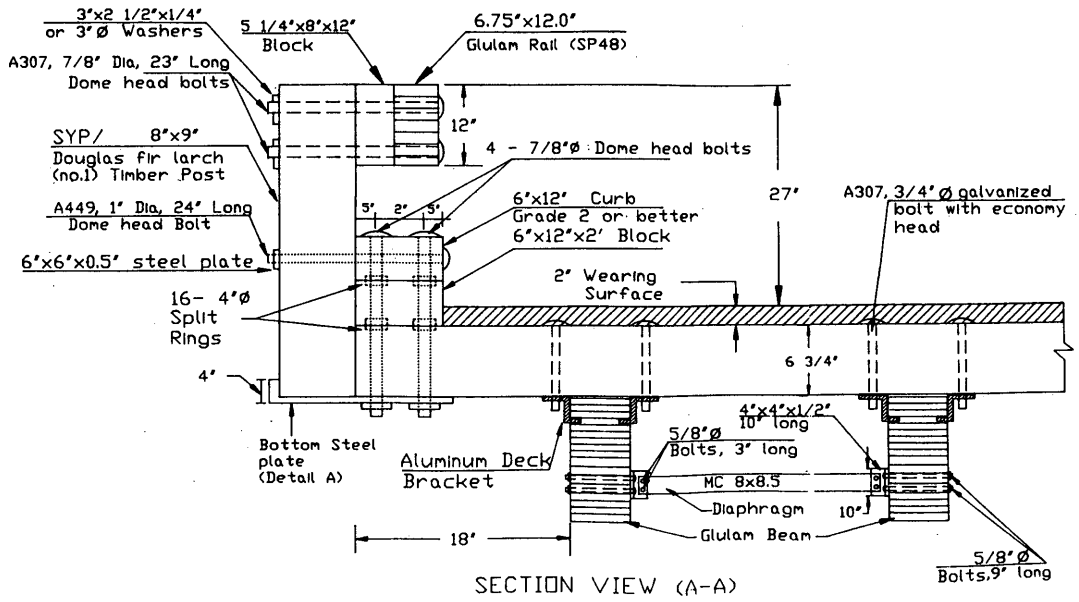

FIGURE 5 Timber Bridge Rail and transition Rail System 2 for PL-1: cross-sectional details of bridge rail.

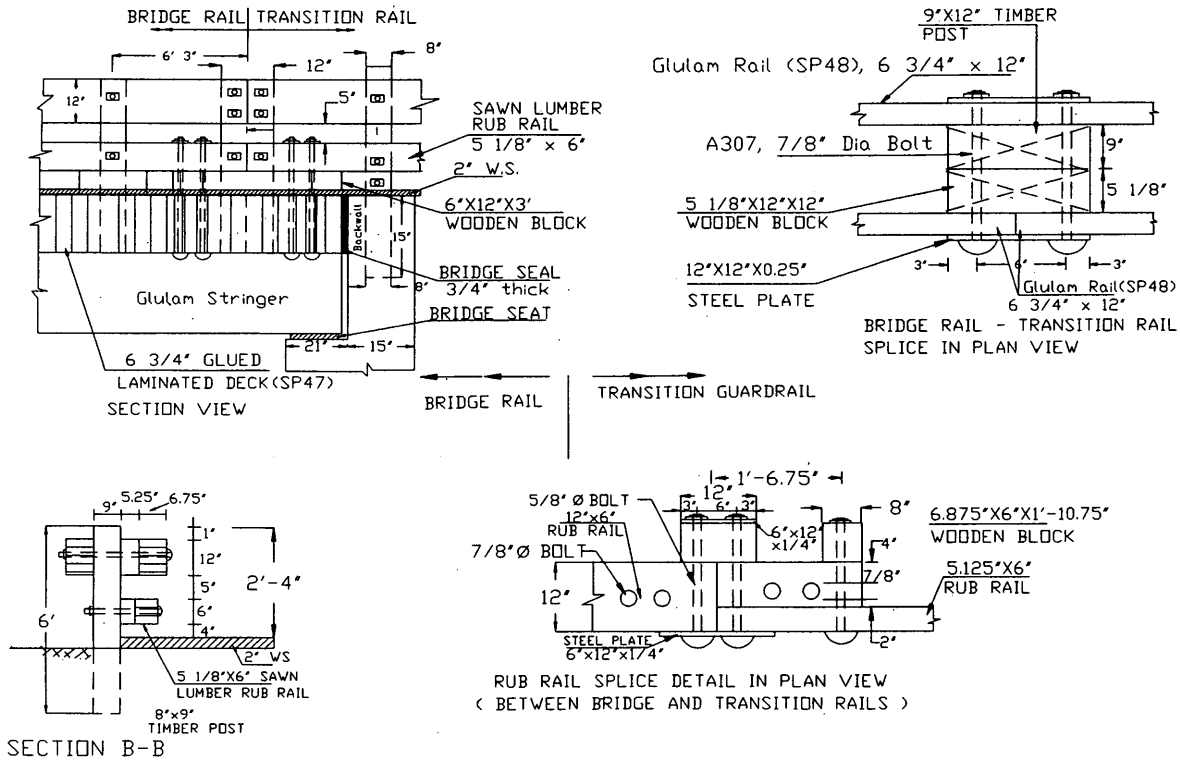

FIGURE 6 Timber Bridge Rail and transition Rail System 2 for PL-1: cross-sectional details of transition rail.

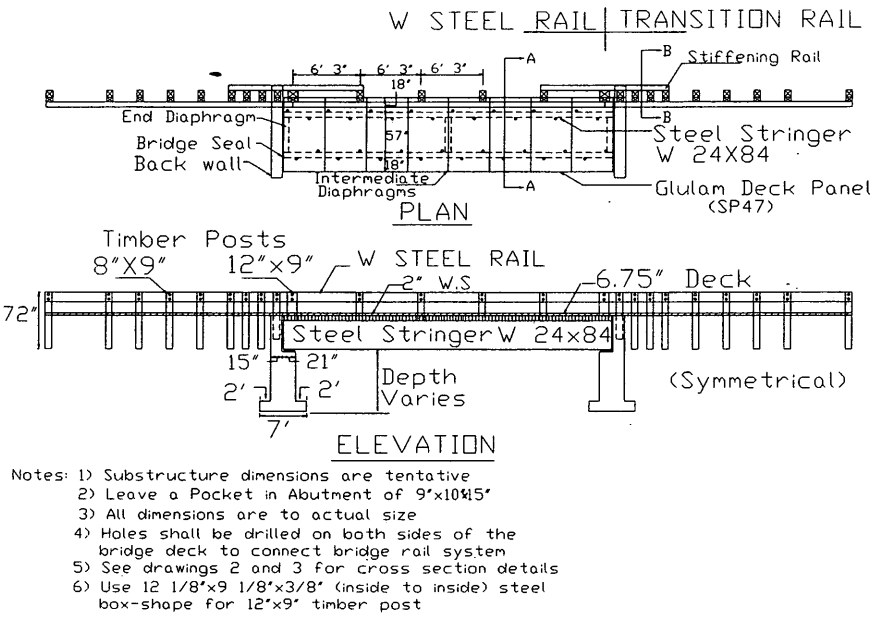

FIGURE 7 Timber Bridge Rail System 3 for PL-1: plan and elevation.

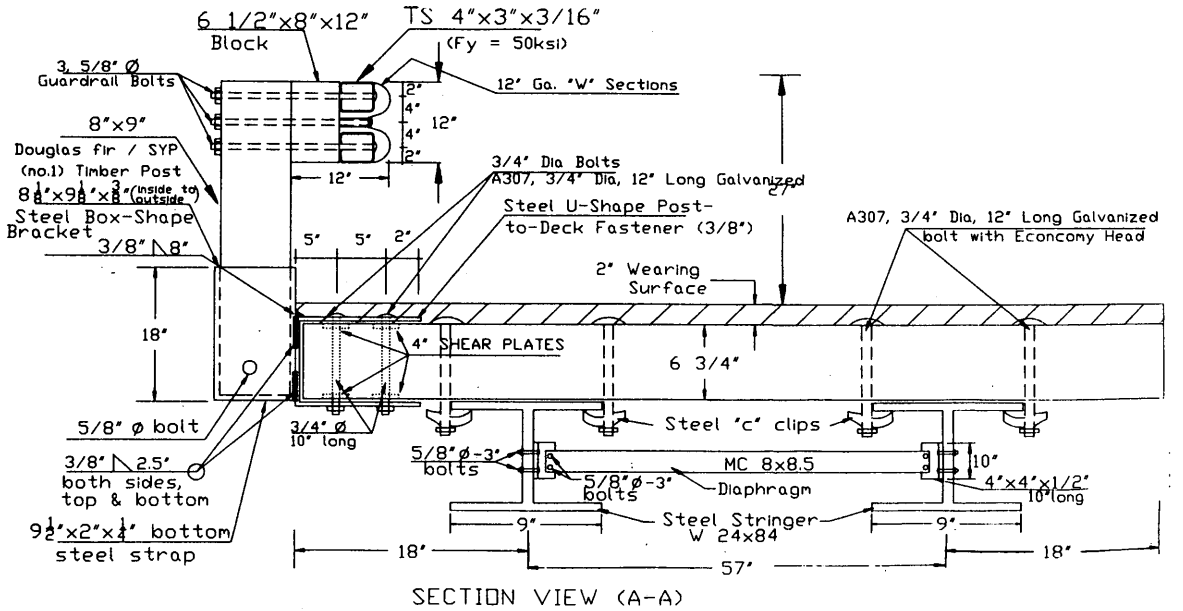

FIGURE 8 Timber Bridge Rail System for PL-1: cross-sectional details of bridge rail.

The deck was fabricated with eight glued-laminated panels; dimensions of each panel are 2.36 m (7 ft 9 in.) long, 1.26 m (4 ft 1.5 in.) wide, and 172 mm (6.75 in.) in depth. The bridge deck panels were connected to the supporting steel beams with "c" clips and to the glued-laminated beams with aluminum brackets. Systems 1 and 3 used two W 24 × 84 steel stringers, and System 2 used two glued-laminated beams 172 × 1029 mm (6.75 × 40.5 in.) to support the transverse glued-laminated bridge deck.

For the bridge rails, solid sawn lumber timber posts [203 × 229 × 927 mm (8 × 9 × 36.5 in.)] were used. These were spaced at 1.91 m (6 ft 3 in.) in all three systems. The post setback distance provided was 305 mm (12 in.) in all three systems. The same post size with varied post spacing was used in the approach rail. The first post in the transition rail closest to the bridge rail post was placed in the abutment, and the rest of the posts in the transition rail were embedded in the soil and compacted thoroughly.

Glued-laminated beam, 171 × 305 mm (6.75 × 12 in.), was used as the bridge rail and the approach rail for both Systems 1 and 2. W-beam mounted on two steel tubes [76 × 102 × 9.5 mm (3 × 4 × ⅜ in.)] was used as the bridge rail and approach rail for System

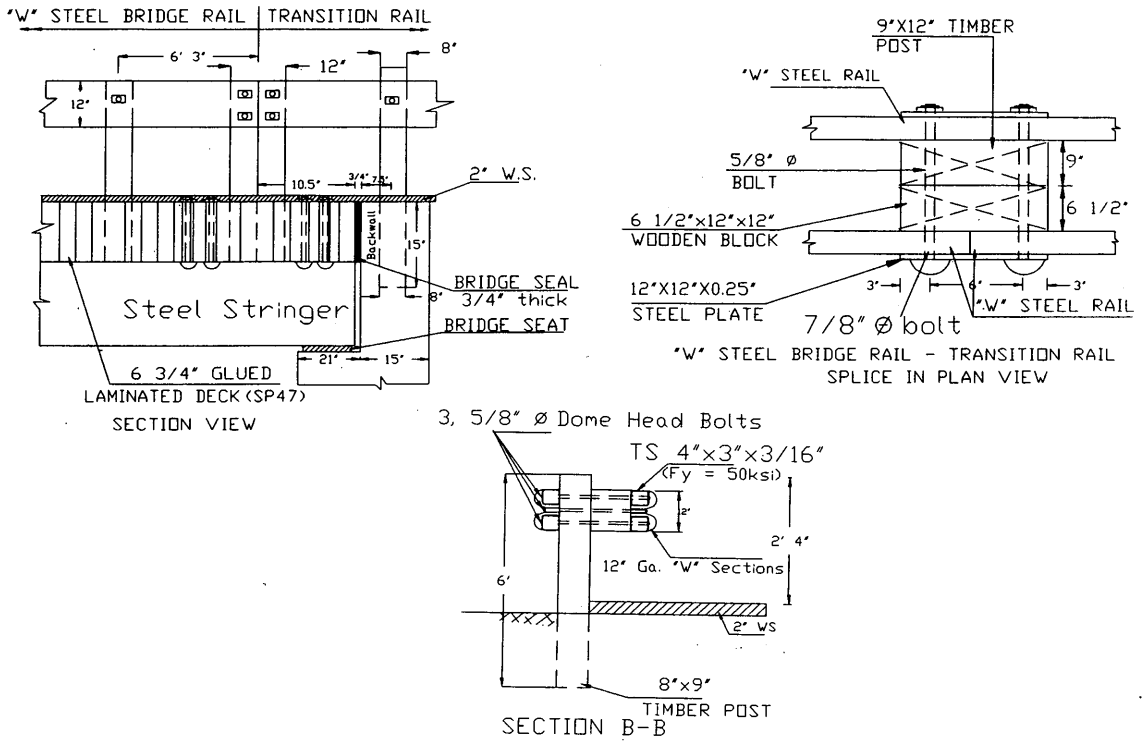

FIGURE 9 Timber Bridge Rail System 3 for PL-1: cross-sectional details of transition rail.

3. Systems 1 and 3 are identical, except that System 1 has a glued-laminated rail, whereas System 3 has a W-beam steel rail. Both Systems 1 and 3 do not have curb rails. The rails, attached to the wooden posts, are placed in box steel brackets. The box steel brackets are welded to steel U-shaped fasteners, as indicated in Figure 2. The steel U-shaped fastener is then connected to glued-laminated deck by four A325 dome head bolts 19 mm (¾ in.) in diameter.

The bridge rail in System 2 has a curb rail. The posts are attached to the curb with bolts 25.4 mm (1 in.) in diameter. The curb is attached to the bridge deck with four dome head bolts 22 mm (⅞ in.) in diameter at each post location. The glued-laminated bridge rail is attached to the posts at the top with A307 bolts.

AASHTO guide specifications recommend an elastic analysis for the design of timber post, rail, deck, and structural connections

TABLE 2 Full-Scale Crash Test Based on AASHTO Load Criteria

Crash Test	Criteria	Test Criteria				Type of Test	Deck Supporting System	Type of Rail
		Type of Vehicle	Weight of Vehicle	Speed	Angle			
1	PL-1 System 1	Small Automobile	817 kg (1.8 kips)	80 kmph (50 mph)	20	Bridge Rail	WF Steel Beam	Timber
2		Pick-up Truck	2452 kg (5.4 kips)	72 kmph (45 mph)	20			
3	PL-1 System 2	Pick-up Truck	2452 kg (5.4 kips)	72 kmph (45 mph)	20	Transition Rail [1]	Glulam Beam	Timber
4		Small Automobile	817 kg (1.8 kips)	80 kmph (50 mph)	20	Bridge Rail		Timber
5		Pick-up Truck	2452 kg (5.4 kips)	72 kmph (45 mph)	20			
6	PL-1 System 3	Small Automobile	817 kg (1.8 kips)	80 kmph (50 mph)	20	Bridge Rail	WF Steel Beam	Steel
7		Pick-up Truck	2452 kg (5.4 kips)	72 kmph (45 mph)	20			

Notes: [1] This transition is compatible with rails in tests 1, 2, 4 and 5.

TABLE 3 Design Forces for Traffic Rails LRFD Recommendations (5)

Design Forces	PL-1
Lateral Force	12258 kg (27 kips)
Longitudinal Force	4086 kg (9 kips)
Vertical (Downward) Force	2043 kg (4.5)
Contact length for Lateral (L_t) and Longitudinal (L_l) forces	1.37 m (4.5 ft)
Contact length (L_v) for vertical forces	5.49 m (18 ft)
Height of Vehicle force (He)	508 mm (20 in)
Minimum height of rail (H) from top surface of the deck	737 mm (29 in)

TABLE 4 Design Values of PL-1 for Pickup Truck

Description	LRFD Draft Specifications	Design values considered by authors
Lateral Load	12258 kg (27 kips)	14528 kg (32 kips)
Contact length	1.37 m (4.5 ft)	1.07 m (3.5 ft)
Height of Rail	737 mm (29 in)	737 mm (29 in)
Recommended wearing surface	51 mm (2 in)	51 mm (2 in)
Vertical opening from bottom of the rail to top wearing surface	381 mm (15 in)	381 mm (15 in)
Height of vehicle force	508 mm (20 in)	584 mm (23 in)

under failure loads. Therefore, draft LRFD code recommendations for strength limit states and applicable load combinations were followed in the design of timber rails.

DESIGN OF BRIDGE RAIL SYSTEMS

The design of timber rails was performed by computing lateral force from a test vehicle using the following formulas according to AASHTO's guide specifications, (2):

$$F_{L.AV} = \frac{W V_I^2 \sin^2\theta}{2g[A \sin\theta - B(1 - \cos\theta) + D]} \quad (1)$$

where

W = gross weight of the vehicle (lb),
V_I = impact velocity in (ft/sec),
θ = impact angle (degrees),
g = acceleration as a result of gravity (ft/sec^2),
A = distance from CG to front of the vehicle (ft),
B = outer-to-outer wheel spacing (ft), and
D = Barrier deflection.

$$F_{L.max} = \frac{\text{II}}{2} F_{L.AV} \quad (2)$$

Lateral forces were computed using Equation 2, and these lateral forces have compared well (±20 percent) with the experimental results. The contact length of 89 mm (3.5 ft) was used to distribute the lateral load (6).

The allowable design stresses were arrived at by taking the recommended design stresses from the National Design Specification (NDS) (7). The recommended design stresses for bending, shear, and compression perpendicular to grain were adjusted with appropriate adjustment factors (Table 2.3.1, NDS)—impact factor and safety factor—as indicated in Equation 3:

$$F_A = C_A C_I C_s F_D \quad (3)$$

F_A = allowable design stress,
F_D = recommended design stress according to NDS,
C_A = appropriate adjustment factors,
C_I = impact factor, and
C_s = safety factor.

The impact factor is taken as 1.65, according to AASHTO's 1989 specifications (2). The factor of safety for ultimate strength to allowable design strength is about four for bending, shear, and compressive stresses. However, in designing the timber bridge rails, the allowable design stresses were multiplied by the factor of safety of two. The actual factor of safety, which is greater than two, was not taken into account intentionally to keep a substantial reserve strength in the material in the event of excessive force inducement by crashing at higher speeds or at heavier vehicle loads.

The design forces considered in the analysis for designing the rail systems are indicated in Table 3. Additional design details recommended previously (5) in Section 13 for bridge rail systems are shown in Table 4. It can be seen from Table 4 that the author's design is conservative by about 15 percent because the lateral force considered by the authors is higher than that recommended in the LRFD bridge design specifications (5). The maximum lateral force from the pickup truck was estimated using Barrier VII (8) and found to be about 12 258 kg (27 kips), which is equal to the lateral force recommended in the LRFD specifications.

Glued-laminated and W-beam steel rails, timber posts, and glued-laminated deck and structural connections are designed for

bending strength, shear strength, and bearing strength. The computed stresses for rail and post of all three systems and allowable design stresses are indicated in Table 5. The computed stresses are lower than the allowable design stresses, except for the shear stress in the post, which is about 50 percent higher than the allowable design stress. The high shear stress in the post is because the factor of safety in the allowable design shear stress to ultimate shear strength is about four. However, in the rail design, a factor of safety of two was used; thus there was twice the reserve strength left to resist the shear stress in the post.

After the construction drawings were prepared for all three systems, the timber bridges were fabricated by Burke, Parsons and Bowlby Corporation of West Virginia. All three systems were fabricated and assembled in about 2½ months. No fabrication and assembly problems were encountered during the construction of the systems. The assembled systems were then shipped to the TTI for

TABLE 5 Stress Levels of Various Components for Different Rail Systems

Description	Components	Stresses (kpa)					
		Bending		Shear		Bearing	
		Computed	Allowable	Computed	Allowable	Computed	Allowable
System 1	Rail (SP48)	24666	30316	2480	3445	2274	6201
	Post (SP)	27422	27216	3927	2067	31418	22392
System 2	Rail (SP 48)	24666	30316	2480	3445	2273	6201
	Post (SP)	27422	27216	3927	2067	6201	6201
System 3	Rail (W-BEAM STEEL)	358348	344500	35277	199810	3445	22396
	Post (SP)	27422	27216	3920	2577	31418	22396

Note: 1 psi = 6.89 kpa

TABLE 6 Evaluation of Crash Tests

Sl. #	Criteria	System One		System Two			System Three		Pass/ Fail
Required Criteria		Test 1 Small Car	Test 2 Pick-up Truck	Test 3 Pick-up Truck	Test 4 Small Car	Test 5 Pick-up Truck	Test 6 Small Car	Test 7 Pick-up Truck	
A	Must contain vehicle	Vehicle was contained in all tests							Passed
B	No debris penetration into passenger compartment	No debris was penetrated into passenger compartment in all tests							Passed
C	No deformation passenger compartment	No passenger compartment deformation was found in all tests							Passed
D	Vehicle must remain upright	Vehicle remained upright in all tests							Passed
E	Occupant longitudinal impact velocity < 9.2 m/sec	5.6	3.8	3.9	4.7	3.4	4.4	4.4	Passed
	Occupant lateral velocity < 7.6 m/sec	5.7	3.8	3.3	5.3	3.3	6.4	4.1	Passed
	Occupant ride down longitudinal acceleration < 15 g's	-1.9	- 8.6	-3.5	-1.0	-3.4	-1.3	-3.7	Passed
	Occupant ride down lateral acceleration < 15 g's	-2.6	-14.7	-6.3	-4.1	-9.0	-5.3	-8.8	Passed
DESIRED CRITERIA									
F	Effective Coefficient of friction μ Assessment 0-0.25 Good 0.25-0.35 Fair > 0.35 Marginal	0.62 Marginal	0.42 Marginal	0.31 Fair	0.32 Fair	0.14 Good	0.34 Fair	0.4 Marginal	Passed

crash testing. The assembled systems were easily erected at the TTI using two fork lifts. The bridge rails were then crash tested for PL-1 with a small automobile weighing 817 kg (1,800 lb) and a pickup truck weighing 2 452 kg (5,400 lb). The transition rail was crash tested with a pickup truck weighing 2 452 kg (5400 lb).

Test 1 with the small automobile and Test 2 with the pickup truck were performed at about midspan of the bridge rail on timber Rail System 1. Test 3 with the pickup truck was performed on the transition rail attached to System 2. Test 4 with a small automobile and Test 5 with a pickup truck were performed at about midspan of the bridge rail on timber rail System 2. Similarly, Test 6 with a small automobile and Test 7 with a pickup truck were performed at about midspan of the bridge rail on timber Rail System 3. All seven tests met the crash test criteria specified in AASHTO's 1989 specifications for rails (*2*) and NCHRP Report 230 (*3*). The bridge rails and the transition rail performed well by containing and redirecting the vehicle with cosmetic damage to the rails. The results of all seven tests are indicated in Table 6.

SUMMARY

1. Three timber bridge rail systems for transverse timber decks (one with a curb and two without curbs) were developed with approach rails on both ends of the bridge for PL-1 according to the requirements of AASHTO's 1989 guide specifications (*2*) and NCHRP Report 230 (*3*).
2. All three rail systems were well instrumented.
3. The test results of the seven tests were within the limits of the specified crash test criteria.
4. The design lateral forces recommended by the LRFD bridge design specifications (*5*) compared well with the experimental values, and the induced stresses were within the allowable limits.
5. The presence of curb rail improves the stiffness of the system and results in better performance of the system.
6. The reports will be submitted to FHWA for its review and acceptance into its list of approved bridge rails for federal-aid projects.

ACKNOWLEDGEMENTS

This research project was sponsored by FHWA, United States Department of Transportation, whose financial support is gratefully acknowledged. The comments offered by the American Forest and Paper Association Special Task Group on Timber Bridges and FHWA during the design, development, and construction stages of Timber Bridge Rail Systems are greatly appreciated.

REFERENCES

1. Ritter, M. A., Timber Bridges—Design, Construction, Inspection, and Maintenance. United States Department of Agriculture. Forest Service, Report EM 7700-8, June 1990.
2. *Guide Specifications for Bridge Railings.* AASHTO, Washington, D.C., 1989.
3. *NCHRP Report 230: Recommended Procedures for the Safety Performance Evaluation of Highway Appurtenances.* TRB, National Research Council, Washington, D.C., 1981.
4. Faller, R. K., M. A. Ritter, J. C. Holloway, C. G. Pfeifer, and B. T. Rosson. Performance Level 1 Bridge Rails for Timber Decks. In *Transportation Research Record 1419*, TRB, National Research Council, Washington, D.C., 1993.
5. *NCHRP Report: Draft LRFD Bridge Design Specifications and Commentary.* Section 13. Modjeski and Masters Inc., TRB, National Research Council, Washington, D.C., 1993.
6. Hirsch, T. J. *Analytical Evaluation of Texas Bridge Rails to Contain Buses and Trucks.* Texas Transportation Institute Report, Texas A & M University System, College Station, Aug. 1978.
7. *National Design Specification for Wood Construction.* National Forest Products Association, Washington, D.C., 1991.
8. Raju, P. R., and H. V. S. GangaRao. *Timber Bridge Rail Testing and Evaluations.* Report 186187188. Constructed Facilities Center, West Virginia University, Morgantown, Submitted for publication, 1994.

DISCUSSION

RONALD K. FALLER
Midwest Roadside Safety Facility, Center for Infrastructure Research, Civil Engineering Department University of Nebraska-Lincoln 1901 "Y" St., Bldg. "C" Lincoln, Neb. 68588-0601.

The authors address an important topic and attempt to develop and test three bridge railings for use on transverse glue-laminated timber bridge decks that could meet PL-1 criteria of AASHTO (*1*). The demand for crashworthy railing systems has become more evident with the increasing use of timber bridge decks on low-volume county and local road systems. Unfortunately, several flaws in the research approach seriously undermine the value of the bridge railings and approach transitions described in the foregoing paper. The following discussion is submitted with respect to several technical issues, such as rail length, impact location, discussion on timber deck damage, and discussion on approach transitions.

The authors reported the length of the bridge deck and rail to be approximately 33 ft. However, the approach transition incorporated a "stiffening rail" or backup rail that extended 7 ft 1½ in. onto both ends of the bridge rail, reducing the actual rail length to only 18 ft 9 in. A bridge rail length of 18 ft 9 in. is neither sufficient nor acceptable for crash testing bridge rails. Testing railings of insufficient length often artificially increases the rail's structural capacity, especially when strong transition and backup rails are incorporated. According to an NCHRP report (*2*), the recommended test length for a bridge rail, excluding terminals, should be at least three times the length in which deformation is predicted, but not less than 75 ft. AASHTO's guide specifications (*1*) follow the guidelines set forth by this NCHRP report (*2*). The new crash testing guidelines found in another NCHRP report (*3*) have similar recommendations for rigid bridge rails, but with the added stipulation that flexible bridge rails should not be less than 98 ft long. One purpose of these minimum bridge rail length recommendations is to ensure that full-scale vehicle crash tests are conducted beyond the strengthening effects of stiff transition designs such as the one incorporated in the foregoing paper.

The lack of sufficient bridge rail length is even more pronounced when it is considered in light of the impact point used for all six full-scale vehicle crash tests conducted on the three bridge rails. The authors used a midspan impact point, which meant that only 9 ft 4½ in. of unstiffened rail remained in front of the vehicle at the time it struck the bridge rail. Crash testing and computer simulation have indicated that the maximum lateral impact forces transmitted to barriers during large automobile and pickup truck impacts are applied 4 or 5 ft downstream from the point of impact (*3*). Thus, the maximum lateral impact forces were applied only 4 or 5 ft from the start

of the stiffened transition section where the bridge rail's strength and stiffness are artificially elevated. Therefore, the short bridge rail length and impact location invalidates all crash test results. The reader should be cautioned against using these bridge rail designs on any bridge longer than 33 ft or without incorporating the stiff transition designs developed under this research effort.

The authors stated that only cosmetic damage occurred to the bridge rails and transition rail. No damage was reported to have occurred to the timber bridge deck panels (i.e., cracking of the timber deck panels). However, from the crash test reports for Systems 1 (*4*) and 2 (*5*), more significant damage in the form of permanent residual displacement of the timber deck was reported to have occurred. For the pickup truck crash test on System 1 (*4*), residual displacement was reported on four of the eight deck panels ranging from 0.5 to 0.75 in. For the minicompact and pickup truck crash tests on System 2 (*5*), the maximum residual displacement of the timber deck panels was 0.25 and 0.5 in., respectively. This bridge deck damage is much more significant than if only small cracks appeared on the surface of the timber deck. The amount of deck damage described in the crash test reports (*4,5*) would be associated with extremely high maintenance and repair costs. Such high maintenance and repair costs are an important consideration when selecting bridge rail systems, even for low-volume roads where accident frequencies are expected to be low.

The authors performed one additional full-scale vehicle crash test on an approach transition attached to System 2. However, no information was provided about the impact location and selection. In addition, design details provided for transitions attached to Systems 1 and 3 would lead the reader to believe that these systems have been successfully crash tested. However, no full-scale vehicle crash tests were performed on the transitions attached to Systems 1 and 3.

On the basis of the insufficient bridge rail length, inappropriate impact location, damage to the timber deck panels, and inappropriate testing or documentation of the transition designs, or both, bridge engineers and designers should use caution when specifying any of the bridge railing and approach transition systems described in the foregoing paper.

REFERENCES

1. *Guide Specifications for Bridge Railings*. AASHTO, Washington, D.C., 1989.
2. Michie, J. D. *NCHRP Report 230: Recommended Procedures for the Safety Performance Evaluation of Highway Appurtenances*, TRB National Research Council, Washington, D.C., 1981.
3. Ross, H. E., Jr., D. L. Sicking, R. A. Zimmer, and J. D. Michie. *NCHRP Report 350: Recommended Procedures for the Safety Performance Evaluation of Highway Features*. TRB, National Research Council, Washington, D.C., 1993.
4. Raju, P. R., K. K. Mak, H. V. S. GangaRao, and D. C. Alberson. *Timber Bridge Rail Testing and Evaluation*. Final Report—Vol. 1. Prepared for the Office of Engineering and Highway Operations—Research and Development, FHWA. Constructed Facilities Center, West Virginia University, Oct. 1993.
5. Raju, P. R., K. K. Mak, H. V. S. GangaRao, and D. C. Alberson. *Timber Bridge Rail and Transition Rail Testing and Evaluation*. Draft Report—Vol. 2. Prepared for the Office of Engineering and Highway Operations—Research and Development, FHWA. Constructed Facilities Center, West Virginia University, Oct. 1993.

AUTHORS' CLOSURE

The discussant's interest in this paper and the unpublished final reports on the crash test results are appreciated. A 33-ft span was selected for study on the basis of analysis and because most timber bridges are short-span bridges in the range of 22 to 44 ft in length. Developing and crash testing a 75-ft bridge rail were not deemed necessary because of timber's good energy-absorbing capability and because it would not represent a typical case were these rails ever to be involved in real accidents.

Each system that was tested included both the bridge rail and the transitions attached to it, which is how an actual system would be built. The transition that was tested in System 2 is designed for use with System 1 as well. All the rails tested performed to the Performance Level 1 criteria set forth in the AASHTO *Guide Specifications for Bridge Railings*. Each system contained and smoothly redirected the test vehicles. There were no debris or detached elements from the bridge rails that could potentially penetrate the occupant compartment. The vehicles remained upright and stable during the collision sequence.

The short length does lead to load sharing between the rail and the transitions. However, the posts that were instrumented show that 65 to 70 percent of the total impact force was taken by the nearest post. There was no pocketing of the rails, and the posts did not fail. The impact location was chosen to be between the posts to study the shear response of timber rails, because timber is weak in shear that is perpendicular to the grain. The rails performed well in the crash tests. If these rails are to be used in bridges with lengths much greater than 44 ft, a case could be made for retesting the bridge rail separately without attaching the transitions.

On deck displacement, ¼ to ½ in. of the deck displacement occurred between the permanent test pavement and the timber deck. It is believed this was because the deck was not rigidly anchored to the abutments. The deck in the test installation is only 8 ft wide as opposed to 20 ft or more in actual applications. The ratio of impact force to bridge deck weight is therefore substantially higher for the test installation. Thus, displacement of the bridge deck may not occur in actual applications.

In conclusion, the authors acknowledge that the length of the bridge rails was shorter than is customary for crash testing bridge rails. This was done to provide a more realistic test condition. The rails met the AASHTO recommendations in that they redirected the vehicle and provided minimal damage to the occupant, vehicle, and rail system. The authors believe the systems developed are adequate for timber bridges with transversely laminated decks of this approximate length.

Publication of this paper sponsored by Committee on General Structures.

Incremental Bridge Construction Costs for Highway Cost Allocation

JOSE WEISSMANN, ROBERT L. REED, AND AHMED FEROZE

The procedures and results of an incremental load analysis of bridge construction costs that consisted of the design and pricing of 960 bridges were documented. These 960 bridge type, load, and span combinations were composed of 11 different bridge types ranging in span from 9 to 72 m (30 to 240 ft) and designed for loads ranging from H2.5 to HS25. The bridge type and span combinations included in this factorial reflect current national design and construction practices, as revealed by statistical summaries obtained from the National Bridge Inventory data base. The incremental bridge cost results are important inputs for the highway bridge cost allocation procedures carried out at the federal and state levels. In addition to the bridge cost results, moment ratios of live load to dead load were recorded during this bridge design exercise. The moment ratios obtained in such an exercise can contribute significantly to policy evaluations—especially those that attempt to define the economic impacts of vehicle size and weight changes on bridges at the highway network level.

Cost allocation studies traditionally have been used to provide a logical basis for relating highway tax structures to highway program costs. There is no doubt that the proper allocation of highway costs is very important in providing adequate resources for the various components of a highway program. One important component of the highway system are the bridges, and the proper allocation of bridge costs relies on the incremental analysis of bridge construction costs.

INCREMENTAL DESIGN OF STRUCTURES

This paper summarizes the results published in a report prepared for an FHWA study, Impacts of Heavy Trucks on Bridge Investment (*1*). The results are aimed at allocating the construction costs of typical bridges to the various vehicle classifications that operate on the nation's highways. The incremental design of highway structure methodology is based on the difference in design costs that results when various classes of vehicles are applied as loadings. In this typical incremental cost allocation approach, as described in FHWA's cost allocation guide (*2*), each of the typical bridges was designed for several AASHTO (H and HS) vehicle configurations representative of the vehicle traffic operating on the nation's highway system. The work reported herein expands considerably on the results previously available for highway bridge cost allocation exercises and documented elsewhere (*3*).

The cost results of this massive bridge design exercise, consisting of 960 bridge type, design load, and span combinations, as summarized by the factorial presented in Table 1, are presented in tabular format in the appendix of the FHWA report (*1*); some of the tables are included in this paper to illustrate the results.

J. Weissmann, Center for Transportation Research, University of Texas at Austin, Suite 200, 3208 Red River, Austin, Tex. 78705-2650. R. L. Reed and A. Feroze, Transtec, Inc., 2630 Exposition Blvd., Suite 10, Austin, Tex. 78703.

RATIOS OF LIVE LOAD TO DEAD LOAD

The FHWA report (*1*) also documents important results on moment ratios of live load to dead load for the various bridge combinations documented in the factorial presented in Table 1. These results are of significant importance for fulfilling one of the main objectives in the study, as quoted from FHWA's specifications for Study DTFH61-92-C-00099 "to improve the analysis of the impacts on bridges of larger and heavier trucks." The lack of simplified ratios of live load to dead load in the National Bridge Inventory (NBI) (*4*) is one of the major limitations in the process of analysis of impacts of larger and heavier trucks. Modeling of bridge impacts in the available literature (*5–8*) has been limited to the comparison of live load bending moments of the larger and heavier trucks with the live load moments of the rating vehicle recorded in the NBI data base (Items 64 and 66 of the NBI). This process could be significantly improved by the addition of the dead load effects to the analysis.

The comparison of bending moments is the key element in applying simplified methods for determining bridge deficiencies to heavier trucks using the NBI. This makes the results reported in the FHWA report (*1*) on ratios of live load to dead load of great importance for the analysis of the impacts of changes in vehicle size and weight on bridges. These ratios are presented in the report for the bridge type, load, and span combinations described in the Table 1 factorial.

FACTORIAL OF BRIDGES TO BE DESIGNED AND PRICED

To design a factorial of bridge combinations that reflects the current bridge design and construction practices nationwide, the entire NBI data base was analyzed—a total of 665,743 bridge records. The NBI analysis involved scanning the complete nationwide NBI data for 1992 and extracting all bridges having spans less than or equal to 72 m (240 ft) (the range of spans required by the FHWA study). In addition, only bridges having a structure type (second and third digits of Item 43 of the NBI structure type) less than or equal to 6 to restrict the bridge types to the ones required by the FHWA study and also the first digit of Item 43 of the NBI (to avoid timber, aluminum, wrought iron, cast iron bridges, etc.) greater than 6 were extracted. This procedure produced a data set of approximately 381,000 bridges.

This nationwide bridge population was categorized into the 15 span lengths required by the study. The main structure types were

TABLE 1 Factorial of Bridge Type and Span Combinations

Reinforced Concrete Slab															
Simple	9	12	15												
Continuous	9	12	15	18											
Prestressed Concrete Slab															
Simple	9	12	15												
Continuous	9	12	15	18	21										
Reinforced Concrete T-Beam (C.I.P.)															
Simple	9	12	15	18	21										
Continuous	9	12	15	18	21	24	27	30							
Prestressed Concrete Beam (Precast)															
Simple	9	12	15	18	21	24	27	30	36	42					
Prestressed Concrete Multi-cell Box Girder (C.I.P.)															
Continuous						24	27	30	36	42	48	54	60	66	72
Steel I-Beam															
Simple	9	12	15	18	21	24									
Steel I-Girder															
Simple			15	18	21	24	27	30	36	42	48	54	60	66	72
Continuous			15	18	21	24	27	30	36	42	48	54	60	66	72

(1 m = 3.3 ft)

categorized using Item 43 of the NBI. The resulting frequency distributions of spans by bridge type are summarized in Table 2 for these 381,000 bridges. From the frequency distributions included in Table 2, it is clear that simply supported slab bridges are typically built with spans up to 15 m (50 ft). The same rationale may be applied to the multibeam concrete simply supported span distribution presented in Table 2 to demonstrate that this type of bridge is built with spans up to 21 m (70 ft).

These frequency distributions were used, in conjunction with experienced engineering judgment, to establish the factorial of bridge type and span combinations to be designed and priced. This factorial, presented in Table 1, establishes a study of incremental

TABLE 2 Distribution of Spans by Bridge Type

	NATIONWIDE BRIDGES FOR SPANS UNDER 72 m (240 ft)																	
Span category (feet)	30	40	50	60	70	80	90	100	120	140	160	180	200	220	240	Cumulative		
(meters)	9	12	15	18	21	24	27	30	36	42	48	54	60	66	72	Percent	Total Bridges	
																per Type (%)	by Bridge Type	
Concrete Slab	81	14	3	1	0	0	0	0	0	0	0	0	0	0	0	100	39,430	
Contin. Concr. Slab	39	27	22	8	3	1	0	0	0	0	0	0	0	0	0	100	25,472	
Prestress Concrete Slab	28	34	24	7	4	1	0	0	0	0	0	0	0	0	0	100	6,786	
Multi-beam Concr.	35	36	20	4	2	1	1	0	0	0	0	0	0	0	0	100	18,386	
Multi-beam Concr. Contin.	24	16	13	14	15	8	5	2	2	1	0	0	0	0	0	100	3,256	
Multi-beam Steel	32	22	14	9	7	5	4	2	3	2	1	0	0	0	0	100	129,844	
Multi-beam Steel Contin.	9	4	6	10	12	12	11	8	12	7	4	2	1	1	0	100	41,470	
Multi-beam Prestress	3	7	12	14	18	14	12	8	9	3	0	0	0	0	0	100	34,638	
Multi-beam Prestress Contin.	0	4	11	14	16	15	13	9	12	5	1	0	0	0	0	100	5,494	
Tee Beam Concr.	27	40	22	9	2	1	0	0	0	0	0	0	0	0	0	100	24,252	
Tee Beam Concr. Contin.	7	10	18	19	18	16	6	3	2	0	0	0	0	0	0	100	7,329	
Tee Beam Prestress Concr.	23	28	19	13	6	4	2	2	2	1	0	0	0	0	0	100	6,025	
Box Beam Concr.	19	20	11	8	10	7	8	4	7	3	1	1	0	0	0	100	2,197	
Box Beam Concr. Contin.	0	0	1	4	11	13	17	14	22	10	4	1	0	0	0	100	5,542	
Box Beam Steel	19	0	3	3	6	6	5	3	5	13	14	7	7	4	1	100	201	
Box Beam Steel Contin.	1	0	2	1	2	4	5	4	18	16	12	16	12	7	1	100	324	
Box Beam Prestress	13	20	21	17	12	6	3	2	2	1	1	0	0	0	0	100	27,417	
Box Beam Prestress Contin.	4	7	10	7	6	5	5	4	12	13	11	8	5	3	1	100	3,157	

Total number of bridges considered in the nationwide bridge population, approximately 381,000 (Source NBI 92)

bridge construction costs for 11 structure types of various span lengths for a total of 80 combinations designed for 10 live loading levels (HS25, HS22.5, HS20, HS17.5, HS15, H20, H15, H10, H5, H2.5) for widths of 11.4 m (38 ft) [two 3.6-m (12-ft) lanes; two 1.8-m (6-ft) shoulders] and, for the lightest live load, designed also for three different widths—11.4, 9.6, and 7.8 m (38, 32, and 26 ft) for a total of 12 load-width combinations. The 12 load-width combinations multiplied by the 80 bridge-type span combinations resulted in 960 bridges to be designed and priced.

METHODOLOGY FOR BRIDGE DESIGN FACTORIAL

The continuous bridges were designed for three equal spans of the span lengths specified in the factorial. The decision to use three span configurations for the continuous bridges was justified by the summary statistics analysis of the NBI nationwide population, which shows that about 80 percent of the continuous bridges nationwide have three or more spans. The detailed documentation of the analysis and design results are available in the files of the contractor for this research study. This documentation includes all tables and handwritten calculations performed by the project team to arrive at the quantities and costs presented in the FHWA report (*1*).

Analysis

For continuous spans, envelopes for the various live load configurations for the moments, shears, and reactions were computed using the program BMCOL51 (*9*), with the results summarized using an electronic spreadsheet. Uniform load values were computed for a distributed load intensity of 15.13 kN/m (1 kip/ft) (also using BMCOL51), and the results were subsequently used for the calculations of the dead load moments, shears, and reactions in an iterative procedure that depended on the weight of the various elements selected by the design engineer. Simple spans were analyzed manually for the dead loads and with the help of BMCOL51 for live loads.

Control Sketches and Bridge Design Details

Sketches showing the details and dimensions of the various types of spans specified in the bridge design factorial were prepared on the basis of the project staff's experience in bridge design. The superstructure sketches showed the details of deck dimensions, beam spacing, and railing for the various bridge types included in the study.

In general, the various dead loads, design moments, and shears for the superstructure were obtained by estimating slab, beam, or girder weights, adding the constant weights distributed equally to each beam/girder and multiplying times the appropriate unit value from the moment, shear, and reaction tables generated in the analysis phase. Live load design moments and shears and reactions were obtained by determining the portion of a lane required to be resisted by one beam/girder/meter of slab, then multiplying by the appropriate value from the moment, shear, and reaction tables.

Section properties for calculating stresses resulting from design moments were computed and tabulated as appropriate. Designs proceeded for the various types of bridges specified in the factorial. The service load method was used for all designs (although other methods were used to check for column adequacy).

Abutment sketches depicted all details except variable dimensions, which were dependent on the beam depths determined during the design procedures. The sketches for the interior bents showed cap size and column spacing for various span lengths.

Sketches for abutments and interior bents established the type of foundation (drilled shaft) and the spacing of columns and drilled shafts. Size and minimum length of drilled shafts were established by experience for the abutments. The size of round columns and drilled shafts for interior bents were established in 15-cm (6-in.) increments for grouped span lengths.

Drilled shaft loads were obtained by multiplying the dead load times the reaction tabulated value and the number of design lanes times the tabulated live load reaction, adding the weight of the interior bent and dividing by the number of columns. Structural adequacy of the proposed sizes was verified, and compatibility with shaft loads was noted.

Drilled shaft lengths were calculated to resist the shaft loads without exceeding allowable soil stresses for point bearing and skin friction.

COST ANALYSIS AND RESULTS

Quantities were calculated on the basis of the design sections and the guidelines outlined by the control sketches and using the methodology presented previously. For reinforced concrete slabs and girders, cubic meters of concrete and kilograms of reinforcing were calculated after the design process was completed. For prestressed concrete slabs and box girders, cubic meters of concrete, kilograms of reinforcing steel, and kilograms of prestressing steel were calculated as the design was completed. For steel I-beams and I-girders, kilograms of beam/girder steel, including miscellaneous steel (diaphragms, shoes, expansion joints) and kilograms of shear connectors were calculated when the design was completed. For abutments, cubic meters of concrete and linear meters of drilled shafts were calculated. The same methodology was applied to interior bents.

After the design was completed, bridge costs were obtained by multiplying quantities by unit costs obtained from the Texas Department of Transportation (TxDOT) using an electronic spreadsheet. All quantities resulting from the design of the 960 bridge span, load, and type combinations are summarized on a bridge-by-bridge basis and are available in electronic spreadsheet format.

The electronic spreadsheet format facilitates updates with the costs originating from a nationwide cost survey carried out by the project. This cost survey could be repeated periodically to maintain the updated results. The initial costs used to perform the calculations (surveyed at TxDOT) reflect the average bid prices for the various items for FY 1992. Because TxDOT uses "mobilization" as a separate bid item, 15 percent of the total cost for the superstructure and substructure was added to the total costs to account for mobilization costs.

Included in the FHWA report (*1*) are 11 tables, one for each bridge type included in the factorial presented in Table 1; these tables summarize construction cost, cost per square meter of deck, and cost ratios in relationship to the HS20 bridge design separated for the superstructure, substructure, and total bridge cost. An example of the results summarized in the report is presented in Table 3. In addition, while the design was being performed, dead load and live load design moments were noted and summarized in

the form of ratios of the live load to the total moment (live load plus dead load).

Plots of total structure cost per square meter versus design live loading revealed a tendency toward linear variation, as observed in Figure 1. This tendency is logical because live load moment variations are linear between HS15 and HS25 and between H2.5 and H20. Any discontinuous results observed were attributed to the designer's selection of discrete sections that would satisfy the stress requirements. Although all cost results may not be economically optimized, the costs reported are considered close enough to establish the proper incremental load cost relationships for the various bridge types and span lengths specified by the factorial described in Table 1.

It appears that all curves resulting from this bridge design and costing exercise could be logically normalized as straight lines between the costs at H2.5 and H20 loads and between the HS15 and HS25 loads or adjusted by regression analysis with no significant effects on the results.

RESULTS OF RATIOS OF DEAD LOAD TO LIVE LOAD

An important by-product of this massive bridge design exercise (960 bridges of various types, loads, and spans) is the ratios of dead load to live load. These ratios were recorded as the design progressed for each of the bridge types. The ratios were calculated using the design moments induced by the dead load and the live load and followed the formulation presented by the following equation:

$$R_{DL} = \frac{M_L}{M_L + M_D}$$

where

R_{DL} = ratio of live load moment to total moment,
M_L = live load moment, and
M_D = dead load moment.

Results were reported in terms of design moments [kN*m (kip*ft)] and in terms of a ratio of the live load design moment to the total design moment (represented by the dead plus the live load effect), as defined by the equation. A sample of the tables available in the FHWA report (*1*) is presented in Table 4.

The AASHTO specifications (*10*) for the design of highway bridges permits a simplified method for obtaining longitudinal moments and shears resulting from live loads. According to this method, a longitudinal girder (or a strip of unit width in the case of slabs) is isolated from the rest of the bridge structure and treated as a one-dimensional beam. This beam is subjected to loads comprising one line of wheels of the design vehicle multiplied by a load fraction S/D, also known in the literature (*11*) as a load distribution factor. S is the girder spacing and D is specified to have a certain value by the AASHTO specifications for each bridge type.

On the basis of this AASHTO methodology, which was used throughout the analysis and design of the 960 bridges of the factorial, one must recognize that the results for the moment ratios reflect the geometry of the bridges used in the incremental cost exercise. This bridge geometry was established by the control sketches. In other words, the moment ratios reported are specific to the load distribution factors determined during the design phase for each bridge type. Nevertheless, these ratios are still a good approximation and very useful inputs for the modeling of economic impacts on bridges, at the network level, of changes on vehicle size and weight.

CONCLUSIONS

The procedures and results of an incremental load analysis of bridge construction costs that consisted of the design and pricing of 960 bridges have been documented. These 960 bridge type, load, and span combinations are composed of 11 different bridge types ranging in span from 30 to 240 ft and designed for loads ranging from H2.5 to HS25. The bridge type and span combinations included in the factorial presented in Table 1 represent the current design and construction practices used nationwide, as reflected by statistical summaries obtained from the NBI data base reported in Table 2.

TABLE 3 Example of Cost Tables for Steel I Girder Bridges (Simple and Continuous) (*1*)

	15 m Span Steel I Girder Simple		21 m Span Steel I Girder Simple		21 m Span Steel I Girder Continuous		30 m Span Steel I Girder Continuous	
Loading	Total Cost ($/m^2)	Total Cost HS20 Ratio	Total Cost ($/m^2)	Total Cost HS20 Ratio	Total Cost ($/m^2)	Total Cost HS20 Ratio	Total Cost ($/m^2)	Total Cost HS20 Ratio
HS 25	308.9	1.049	362.2	1.041	345.9	1.034	398.6	1.035
HS 22.5	305.4	1.038	355.1	1.021	340.2	1.017	392.0	1.018
HS 20	294.3	1.000	347.9	1.000	334.6	1.000	385.1	1.000
HS 17.5	287.0	0.975	340.7	0.979	329.1	0.984	378.7	0.983
HS 15	279.4	0.949	333.4	0.958	323.9	0.968	372.2	0.967
H 20	280.3	0.952	333.9	0.960	330.9	0.989	382.4	0.993
H 15	267.0	0.907	324.2	0.932	318.8	0.953	368.1	0.956
H 10	259.4	0.881	312.8	0.899	306.6	0.916	353.3	0.917
H 5	253.9	0.863	302.6	0.870	294.0	0.879	339.0	0.880
H 2.5(11.4m)	253.1	0.860	296.6	0.852	286.6	0.857	331.7	0.861
H 2.5(9.6m)	267.1	0.764	307.1	0.743	285.4	0.718	333.7	0.730
H 2.5(7.8m)	342.4	0.796	322.4	0.634	301.0	0.616	349.8	0.621

(1 m = 3.3 ft)

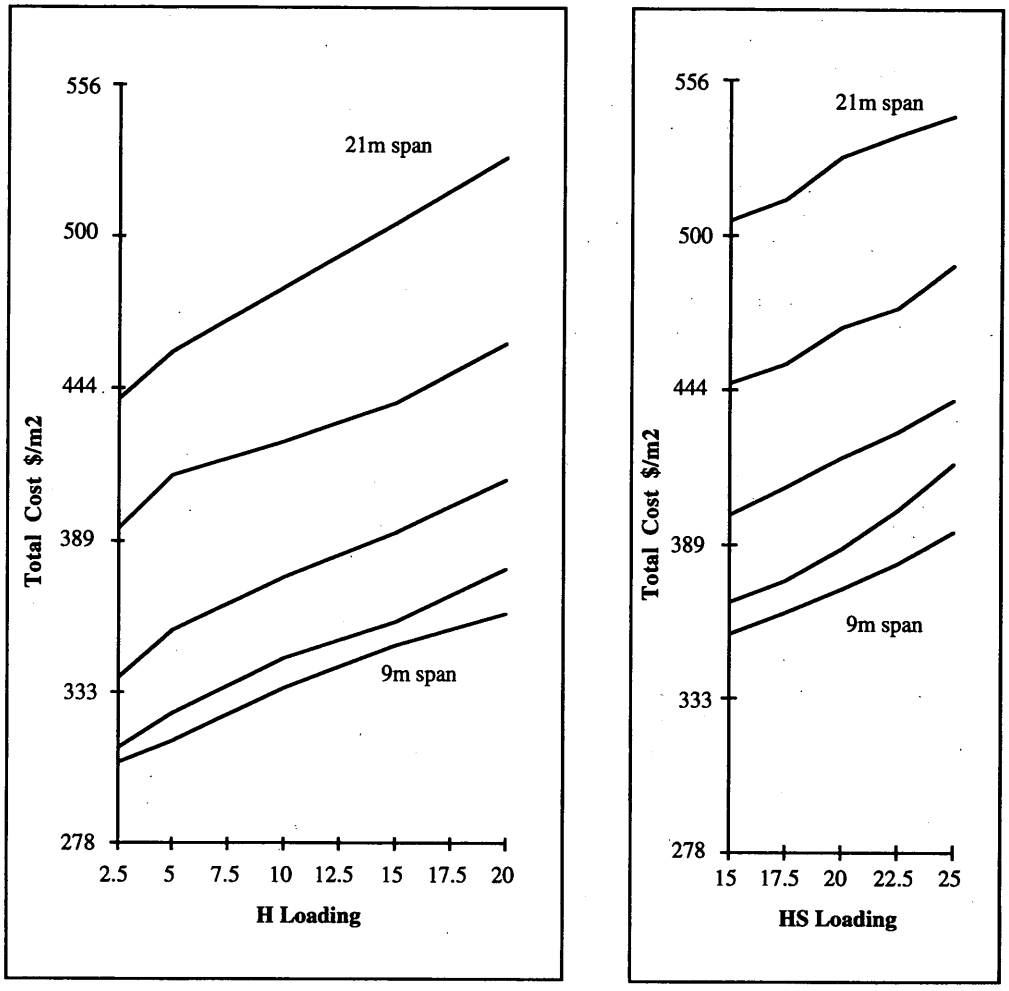

(1 m = 3.3 ft).

FIGURE 1 Incremental cost analysis results for prestressed continuous concrete slabs (1 m = 3.3 ft).

TABLE 4 Moment Ratios for Simple Concrete Slab Bridges (Moments in kN*m)

	Span 9m			Span 12m			Span 15m		
Loading	Moment Dead	Moment Live	Ratio Live/Total	Moment Dead	Moment Live	Ratio Live/Total	Moment Dead	Moment Live	Ratio Live/Total
HS 25	44.95	54.48	0.548	100.79	77.63	0.435	194.77	98.06	0.335
HS 22.5	43.58	49.03	0.529	98.06	69.46	0.415	194.77	88.53	0.313
HS 20	43.58	43.58	0.500	98.06	62.65	0.390	190.68	79.00	0.293
HS 17.5	42.22	38.14	0.475	93.98	54.48	0.367	179.78	68.10	0.275
HS15	39.50	32.69	0.453	91.25	46.31	0.337	179.78	58,57	0.246
H 20	42.22	38.14	0.475	91.25	47.67	0.343	179.78	55.84	0.237
H 15	39.50	28.60	0.420	87.17	35.41	0.289	174.34	42.22	0.195
H 10	35.41	19.07	0.350	84.44	24.52	0.225	163.44	27.24	0.143
H 5	32.69	8.17	0.200	77.63	10.90	0.123	157.99	13.62	0.079
H 2.5(11.4m)	29.96	4.09	0.120	73.55	5.45	0.07	157.99	6.81	0.04
H 2.5(9.6m)	31.33	4.09	0.120	74.91	5.45	0.07	159.35	6.81	0.04
H 2.5(7.8m)	31.33	4.09	0.120	76.27	5.45	0.07	162.08	6.81	0.04

(1 kN*m = 1.375 kips*ft)

The methodological procedures, designed to accommodate the limited resources available for performing the monumental task of designing and pricing 960 bridge combinations, relied heavily on computerized procedures and on the significant bridge engineering expertise available within the project staff. The incremental bridge cost results should support highway bridge cost allocation procedures carried out by FHWA and state agencies.

The results of periodic cost surveys will ensure that the cost data, tentatively reported using Texas costs, reflect the variability of bridge construction costs nationwide.

In addition to the cost results, moment ratios of live load to dead load were recorded during the design phase. These are an important contribution for the policy evaluations of the economic impacts of changes of vehicle size and weight on bridges at the highway network level. If these moment ratios were available, the results of the analysis of longer combination vehicle impacts on bridges, such as those reported elsewhere (*5–8,12,13*), would have been significantly improved. The moment tables reveal how the cost sensitivity to load increments is attenuated by the effect of the dead load.

ACKNOWLEDGMENTS

The authors are grateful to FHWA for providing funding for this study and are especially appreciative of the technical contributions of James G. Saklas and other staff of FHWA. They also thank the staff at the TxDOT Bridge Division, who contributed comments and cost data.

REFERENCES

1. Weissmann, J., R. Reed, and A. Feroze. *Incremental Analysis of Bridge Construction Costs*. Draft Report. FHWA, Washington, D.C., 1993.
2. *State Highway Cost Allocation Guide—Volume 1*. FHWA, U.S. Department of Transportation, Washington, D.C., Oct. 1984.
3. *Incremental Analysis of Structural Construction Costs*. Benito Sinclair and Associates, FHWA, U.S. Department of Transportation, Washington, D.C., April 1981.
4. *Recording and Coding Guide for the Structure Inventory and Appraisal of the Nation's Bridges*, FHWA, U.S. Department of Transportation, Washington, D.C., 1988.
5. Weissmann, J., and R. Harrison. The Impact of Turnpike Doubles and Triple 28s on the Rural Interstate Bridge Network. In *Transportation Research Record 1319*, TRB, National Research Council, Washington, D.C., 1992.
6. Harrison, R., J. Weissmann, and R. Barnhardt. Load Rating Choice and Long Combination Vehicle Impacts on the Rural Interstate Bridge Network. *Journal of the Transportation Research Forum*, Vol. 32, No. 1, 1991, pp. 52–60.
7. Weissmann, J., R. Harrison, and L. Joanes. Estimating Load Impacts on Highway Structures Using the National Bridge Inventory Database. *Proc., 4th International Conference of Microcomputers in Transportation*, ASCE, Baltimore, Md., 1992.
8. Moses, F. Effects on Bridges of Alternative Truck Configurations and Weights. Draft Final Report. TRB, National Research Council, Washington, D.C., 1989.
9. Matlock, H., and T. P. Taylor. *A Computer Program to Analyze Beam-Columns Under Movable Loads*, Research Report 56-4, Center for Highway Research, The University of Texas at Austin, 1968.
10. *Standard Specifications for Highway Bridges*. AASHTO, Washington, D.C., 1989.
11. Bakht, B., and L. Jaeger. *Bridge Analysis Simplified*. McGraw Hill, New York, 1985.
12. *Special Report 225: Truck Weight Limits: Issues and Options*. TRB, National Research Council, Washington, D.C., 1990.
13. *Special Report 227: New Trucks for Greater Productivity and Less Road Wear: An Evaluation of the Turner Proposal*. TRB, National Research Council, Washington, D.C., 1990.

Publication of this paper sponsored by Committee on General Structures.

Parametric Study of Single-Span Jointless Steel Bridges

HEMANTH K. THIPPESWAMY, PENMATSA R. RAJU, AND HOTA V. S. GANGARAO

An engineering explanation for the performance of single-span jointless steel bridges is presented. The performance of jointless bridges is shown to depend on the ratio of superstructure to substructure stiffness, including span length and abutment heights, load types and their combinations, time-dependent creep effects, foundation types, soil properties, and boundary conditions. A finite element analysis program was used to generate moment and deformation data, and the data were then synthesized to develop a better understanding of jointless bridge behavior. The moment and deformation data were also generated for a simply supported jointed bridge to compare with a jointless bridge. The results are presented and discussed for various loading conditions and load combinations. The results of the parametric study serve as a guide to select superstructure and substructure sizes and also to provide a tool for structural optimization. The study found that maximum midspan moment caused by external loads, including time-dependent loads such as creep and shrinkage in a jointless bridge, is about 50 percent of the maximum midspan moment found in a simply supported jointed bridge. The lower midspan moment in a jointless bridge as a result of a combination of all loads explains the superiority of the performance of a jointless bridge over a simply supported jointed bridge. The study also found that the effect of soil settlement and earth pressure is minimal when the jointless bridge has a hinged type of boundary condition at the footing level.

Jointed bridges are extremely common in bridge construction and share about 98 percent of total bridges (*1,2*). Joints are provided to accommodate longitudinal movements in bridges. Longitudinal movements are caused by thermal changes, horizontal earth pressure, soil settlements, and braking forces. Depending on the type of superstructure, span length, and boundary conditions of the bridge, different types of expansion joints and bearings are used in the field. Despite extensive research on expansion joints and bearings, researchers (*3*) have observed that expansion joints and bearings do not serve their intended purpose. In many instances, the major problems in joints and bearings (typical in the case of open joints, sliding plate joints, and open finger joints) encountered are

- Corrosion caused by deicing chemicals leaking through the joints,
- Accumulation of debris and other foreign material restricting the free joint movement,
- Differential elevation at the joints causing additional impact forces, and
- High initial and maintenance costs of joints and bearings.

These problems can lead to costly repair and rehabilitation of jointed bridges. To reduce the cost of bridge maintenance and improve the structural efficiency, transportation departments of various states in the United States have tried to build bridges without joints and bearings. This new approach of integrating bridge superstructure with the abutments and piers has been adopted by as many as 28 states in the United States, with Tennessee taking the lead (*4*). Such a class of bridges is referred to as jointless or integral bridges.

Engineers have observed that integral bridges are performing better than jointed bridges with reduced initial and life cycle costs and also with minimal maintenance problems. Construction of integral bridges is simpler and faster than the construction of jointed bridges because they require fewer parts and less material and are less labor intensive (*5*). Conversion of simply supported bridges into integral bridges has been successful and has been shown to improve the performance of the bridge. The field performance of existing jointless bridges has been well documented by many researchers (*4–10*). Integral bridges also have performed better under earthquake forces than bridges with joints because the continuity between superstructure and substructure develops higher energy dissipation (*11*).

During the design of integral bridges, attention must be given to the following: (*a*) gravity and environmental loads (*5*); (*b*) settlement, temperature variations, and earth pressure (*4*); and (*c*) stability of superstructure and substructure during construction and service. Special attention is required for integral bridges when they are built on skew and curves. The joint between the superstructure and abutment has to be carefully designed and detailed to resist the support moment at the joint by limiting the concrete crack width to avoid reinforcement or steel corrosion.

RESEARCH NEEDS

In spite of the many advantages of jointless bridges over jointed bridges, large numbers of new jointless bridges are not being built and large numbers of jointed bridges are not being converted to jointless bridges. The reasons may be attributed to the following:

- An inadequate understanding of integral bridge behavior under soil settlement, temperature, and earth pressure;
- Limited performance data;
- Inadequate experimental and analytical evaluations;
- A lack of design and construction specifications; and
- A higher cost to convert jointed bridges to jointless bridges.

The design criteria are empirical and are based on observations of the performance of few in-service jointless bridges. For jointless bridges, design and construction specifications are not yet included in AASHTO's Specifications for Highway Bridges (*12*). Consequently, variations in the analysis and design are found from state to state. To properly understand the behavior of integral bridges, analytical data must be developed and carefully interpreted. As a

H. K. Thippeswamy and H. V. S. GangaRao, Constructed Facilities Center, West Virginia University, Morgantown, W.Va. 26506-6101. P. R. Raju, Michael Baker, Jr., Inc., 420 Rouser Rd. Coraopolis, Pa. 15108.

minimum, the following parameters play an important role and should be studied to predict the behavior and performance of integral bridges:

- Effects of superstructure and substructure stiffness in the design of jointless bridges;
- Effects of concrete creep and shrinkage, temperature, and soil settlement in the design of jointless bridges;
- Effect of varying soil properties, types of foundation, and connection details between the foundation and the abutment; and
- Effect of approach slab and its connection with the jointless bridge.

OBJECTIVES

The primary objective of this paper is to present the response of single-span jointless steel bridges by varying the ratios of superstructure to substructure stiffness, load types and their combinations, foundation types, soil properties, and boundary conditions and also to study the time-dependent creep effects of superstructural material on jointless bridge behavior. An additional objective is to explain the superior performance of a jointless bridge over a jointed bridge, particularly in terms of accommodating longitudinal thermal movements.

SCOPE

Research is being conducted at West Virginia University to study the effect of various loads and their combination, including thermal load, earth pressure and soil settlement, spans, heights, foundation types, soil properties, and abutment stiffness. The study addresses the reason for better performance of jointless bridges over jointed bridges. The finite element method that treats the bridge structure as a plane frame has been used to develop data and perform the parametric study on jointless bridge structures. In earlier studies (*13*), due consideration was not given to many influencing parameters, such as superstructure and substructure stiffness ratio, span length, abutment/pier height, and different boundary conditions. Results obtained in the parametric study were compared with those obtained from the simple frame formulas (*14*). The influence of various parameters on bridge behavior is discussed with the help of graphs and tables. Results of time-dependent creep analysis is also presented for one case of a jointless bridge.

PARAMETERS CONSIDERED

Effects of variation in span length, abutment height, ratio of superstructure to substructure stiffness, gravity load, environmental load (temperature), horizontal load (earth pressure and braking), soil settlement, and their combinations have been studied in terms of jointless bridge response. Three types of boundary conditions are considered: hinged, fixed, and partially fixed. Partially fixed boundary conditions are represented by means of rotational springs. Three values are assumed for these rotational springs to represent different types of soils and foundations. Additional details are given in the following sections.

Span Length

The span lengths (L) varied in the parametric study were 9.2, 15.3, 22.9, and 30.5 m (30, 50, 75, and 100 ft). The geometric property of the superstructure was arrived at by considering the full composite action of concrete slab with steel stringer. The moment of inertia (I_s) of the superstructure was arrived at by satisfying the maximum allowable deflection criterion of $L/800$. The superstructure was made of a cast-in-place or a precast concrete bridge deck built composite with steel stringers.

Abutment Height

The abutments were considered to be made of reinforced concrete for varying heights (H), that is, 3.1, 6.1, 12.2, and 18.3 m (10, 20, 40, and 60 ft). The moment of inertia (I_c) of the abutment was varied from 0.2 to 3 times the moment of inertia of the superstructure.

Ratios of Superstructure to Substructure Stiffness

The ratio of superstructure moment of inertia and substructure moment of inertia was varied from 0.3 to 5. The ratio of superstructure to substructure stiffness is a nondimensional parameter represented by stiffness ratio $K = (H/L)\ (I_s/I_c)$. The stiffness ratio was varied from 0.1 to 3, which represents a wide range of practical field cases of jointless bridges.

Gravity Loads

The dead and live loads were considered in the design of concrete deck and steel stringers. The dead load included the weight of slab, wearing surface, parapets, railings, curbs, haunches, and diaphragms. The design live load was arrived at according to AASHTO specifications (*12*). The effect of multiple lanes, wheel load distribution, and impact were also considered in arriving at the maximum design live load.

Horizontal Loads

Horizontal loads are caused by earth pressure and braking force. Earth pressure is assumed to act on one side of the frame, which is a critical case. The Rankine's coefficient of active earth pressure is considered for granular type of backfill, which is commonly adopted (*15*). The total earth pressure is computed using Rankine's theory of active earth pressure, and the total load is assumed to be applied at one-third the height of the abutment from the top of the foundation. The braking force is calculated and applied according to AASHTO specifications (*12*).

Environmental Load (Temperature)

A linear temperature gradient across the depth is assumed to act on the deck and girder system of the jointless bridge model. The temperature gradient varied from 38°C (100°F) at the top of the deck to 21°C (70°F) at the bottom of the stringer. The reference temperature is assumed to be 21°C (70°F). The temperature is selected on

the basis of the AASHTO specifications (*12*) for concrete temperature rise in a moderate climate. The temperature gradient is accounted for in the superstructure design only. The coefficient of thermal expansion used is 6×10^{-6} in./in./°F as specified for concrete by AASHTO (*12*).

Differential Settlement of Soil

The differential settlement of abutments is assumed to be 13, 25, 51, and 330 mm (½, 1, 2, and 3 in.). These discrete values for settlement are considered to simplify the problem of time-dependent settlement of the supporting soil and to establish the tolerable differential settlement limit.

Boundary Conditions

A realistic boundary condition for jointless bridges at foundation level would be somewhere between hinged and fixed conditions, depending on the type of footing and the soil media. Therefore, hinged and fixed (extreme cases) and partially fixed boundary conditions are considered in the parametric study of single-span jointless steel bridges. The partial fixity is achieved in jointless bridge parametric study by providing rotational springs between the abutment and the foundation. Three spring constants [4.6E10, 9.2E10, and 3.5E11 kg-mm/rad (4E9, 8E9, and 30E9 lb-in./rad)] are assumed for partially fixed boundary conditions on the basis of the type of foundation and supporting soil.

Creep and Shrinkage

Time-dependent creep analysis (*16*) under sustained dead load has been conducted for a 15.3-m (50-ft) jointless bridge under consideration. The creep-induced moments are calculated for 10 years.

TABLE 1 Moments for Example Jointed Bridge Under Consideration

LOAD CASE	JOINTED (SIMPLY SUPPORTED) BRIDGE WITH FIXED CONDITION AT ABUTMENT BASE			
	SUPERSTRUCTURE MOMENT (t-m)		ABUTMENT MOMENT (t-m)	
	MIDSPAN	SUPPORT	TOP OF ABUT.	BOTTOM OF ABUT.
LIVE LOAD	87	0	0	0
DEAD LOAD	56	0	0	0
EARTH PRESSURE	0	0	0	-42
TEMPERATURE	0	0	0	0
SETTLEMENT (1")	0	0	0	0
BRAKING	0	0	0	-7
CREEP	0	0	0	0
SHRINKAGE	0	0	0	0
TOTAL	143	0	0	-49

Note: 1 kip-ft = 0.1385 t-mt

The analysis was conducted for creep in the superstructure only. The creep coefficient and the aging coefficient adopted in the analysis are 2.3 and 0.7, respectively. The results of creep analysis are shown in Tables 1 and 2.

Shrinkage analysis was conducted for a 15.3-m (50-ft) jointless bridge (*16*). The shrinkage-induced moments were found for the superstructure at 10 years.

SINGLE-SPAN MODEL

A single-span jointless bridge is modeled as a two-dimensional frame by varying the stiffness ratio of the superstructure and the substructure and boundary conditions. The deck and the stringers are modeled as one-dimensional beam elements assuming full com-

TABLE 2 Moments for Example Jointless Bridge Under Consideration

LOAD CASE	JOINTLESS BRIDGE WITH HINGED-HINGED CONDITION AT ABUTMENT BASE				JOINTLESS BRIDGE WITH FIXED-FIXED CONDITION AT ABUTMENT BASE			
	SUPERSTRUCTURE MOMENT		ABUTMENT MOMENT		SUPERSTRUCTURE MOMENT		ABUTMENT MOMENT	
	MIDSPAN	SUPPORT	TOP OF ABUT.	BOTTOM OF ABUT.	MIDSPAN	SUPPORT	TOP OF ABUT.	BOTTOM OF ABUT.
LIVE LOAD	54.3	-31.8	-31.8	0	52.0	-34.3	-34.3	16.9
DEAD LOAD	28.0	-28.0	-28.0	0	26.3	-29.8	-29.8	14.7
EARTH PRES.	-2.2	-18.0	-18.0	0	-0.8	1.8	1.8	-29.4
TEMP.	15.9 (-15.9)	15.9 (-15.9)	15.9 (-15.9)	0	16.2 (-16.2)	16.2 (-16.2)	16.2 (-16.2)	2.4 (-2.4)
SETT. (1")	0	0	0	0	0	-20.8	-20.8	-20.8
BRAKING	0	5.0	5.0	0	0	1.9	1.9	-3.2
CREEP	-3.1	-3.1	-3.1	0	-3.2	-3.2	-3.2	2.1
SHRIN.	-14.1	-14.1	-14.1	0	-17.4	-17.4	-17.4	3.6
TOTAL	78.8 (47.0)	-74.1 (-105.9)	-74.1 (-105.9)	0	73.1 (40.7)	-85.6 (-118.0)	-85.6 (-118.0)	-18.5 (-13.7)

Note : 1 kip-ft = 0.1385 t-m ; Numbers in the brackets account for winter temperature gradient.

posite action. ANSYS STIF 3 (*17*) beam element is used with 4 degrees of freedom at each node of the element. Partial fixity is simulated by using ANSYS STIF 14 (*17*) spring-damper element, wherein the effect of the damper is suppressed suitably in the input code by giving a zero value for damping coefficient. All the loads are prescribed as individual load cases and the inputs are given accordingly in the ANSYS input data file. Analysis is carried out for each span varying all the parameters discussed above. The results obtained from the ANSYS program were compared with those from other analytical methods (*14*) and found to be correlating with an error of less than 0.5 percent.

RESULTS OF PARAMETRIC STUDY

The results of the parametric study for single-span jointless bridges are summarized in the form of graphs (Figures 1 through 12). Different loads, stiffness (K) values, and boundary conditions were varied in the parametric study. The most important results of the parametric study are discussed herein.

MOMENT AT FOUNDATION LEVEL

Figures 1 through 4 show the moment variation for various boundary conditions at foundation level for varying stiffness ratios. Figures 1 through 4 are developed for live load, environmental load, earth pressure, and various settlement, respectively. The live load moment variation for various system stiffness ratios and for various boundary conditions is shown in Figure 1. The maximum moment of footing level is induced in the case of a fixed boundary condition, when the stiffness ratio is about 0.5. For other stiffness ratios, the moment at the footing level is small. The dead load induced moments also showed a similar trend as exhibited by live load moments. The moment values corresponding to partially fixed conditions lie in between hinged and fixed conditions. Figure 2 indicates that the smaller the stiffness ratio K, the larger is the thermally induced moment at the foundation level. Smaller system stiffness K represents a stiffer abutment and a weaker superstructure. Stiffer abutments resist a larger support moment, thereby transferring a lesser moment to the superstructure. A larger moment at support implies a larger moment at footing level for all boundary conditions except a hinged condition for thermal load (Figure 2). It is obvious and expected that the moment developed at the footing level for hinged condition should be 0 and is observed in Figures 1 through 4 for all values of stiffness ratios K and for all types of loads. Thus, the hinge type of boundary condition at the footing level would not develop undesirable moments that are to be transferred to the soil in the service life of the jointless bridge. The moment at the footing level caused by earth pressure for various boundary conditions is the highest for a system stiffness ratio of 3 (Figure 3) and low for other system stiffness ratios. The moment at the left footing caused by 1-in. settlement of the right footing is shown in Figure 4. The increase in settlement directly increases the magnitude of moment for all boundary conditions except for the hinged boundary condi-

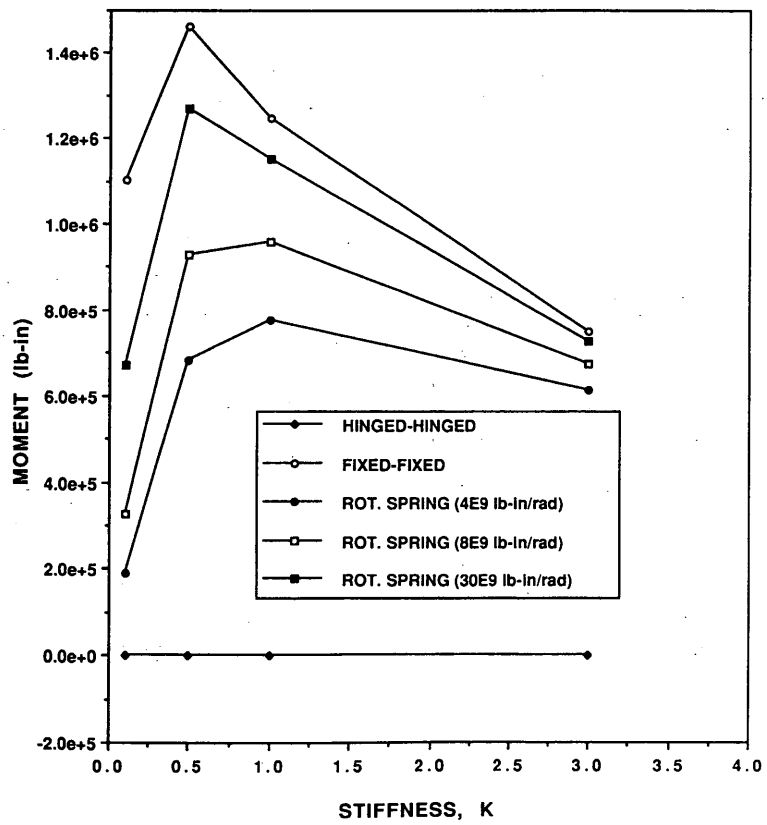

FIGURE 1 Stiffness versus moment at footing due to live load.

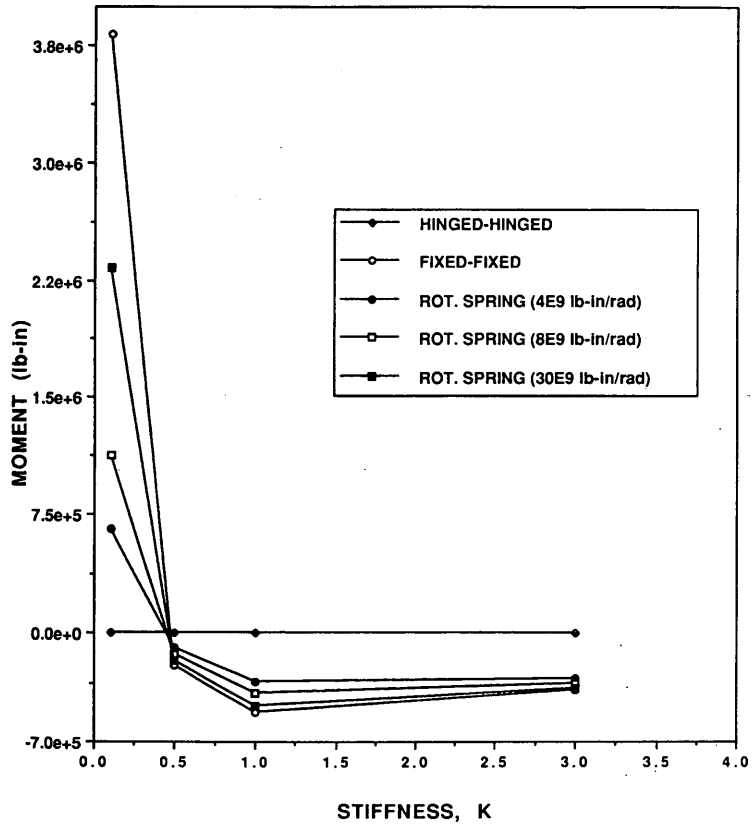

FIGURE 2 Stiffness versus moment at footing due to temperature gradient.

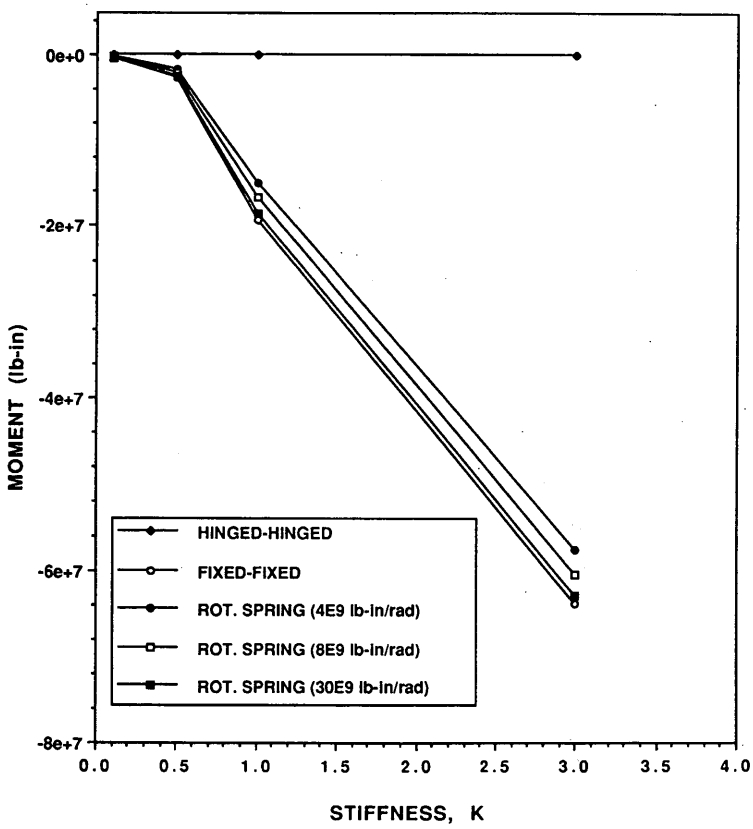

FIGURE 3 Stiffness versus moment at left footing due to earth pressure.

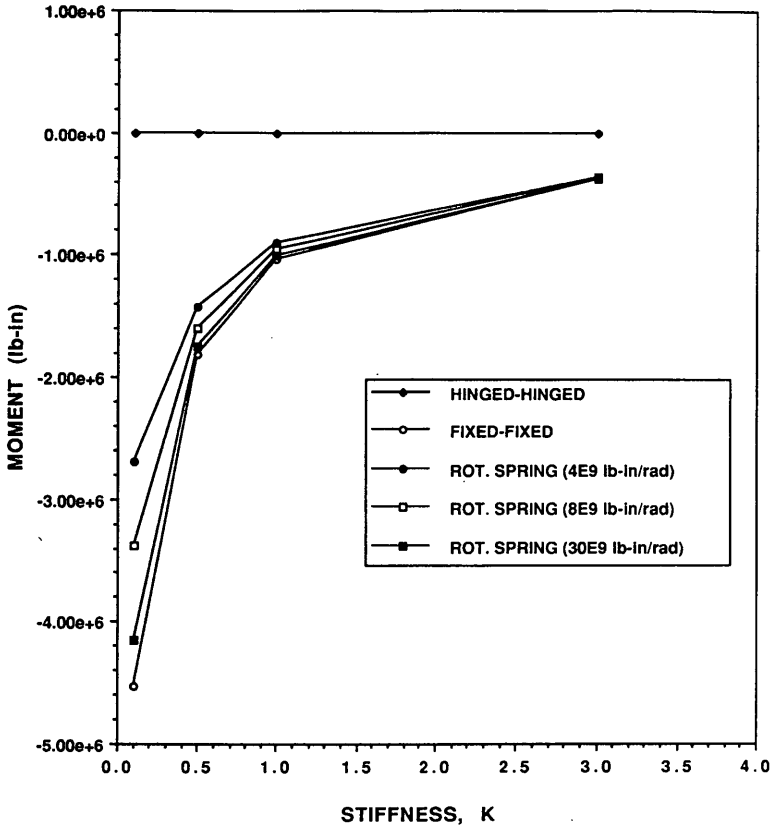

FIGURE 4 Stiffness versus moment at left footing due to settlement of 1 in. at right footing.

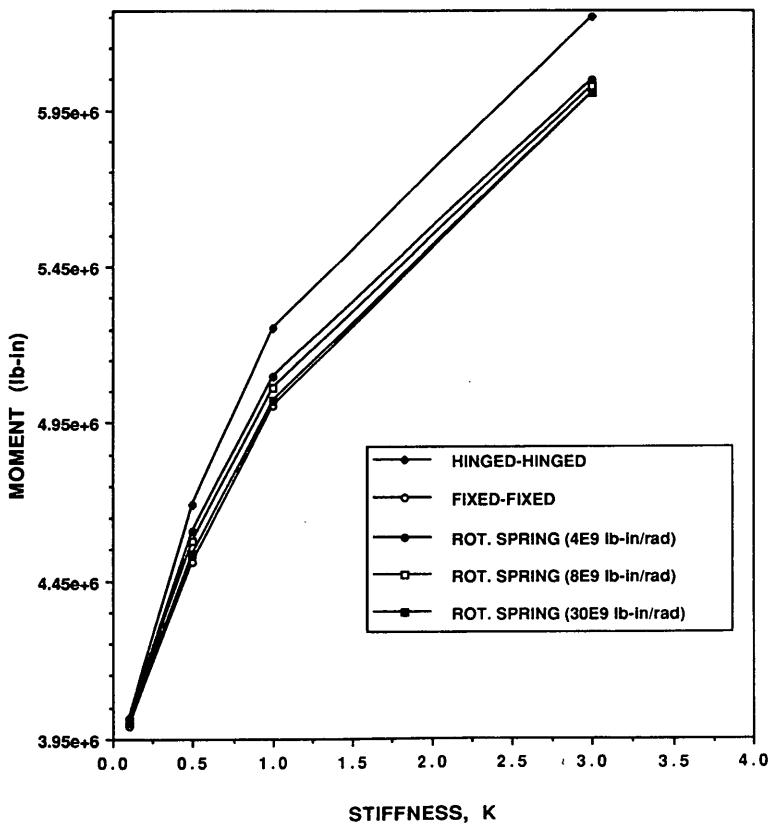

FIGURE 5 Stiffness versus moment at midspan due to live load.

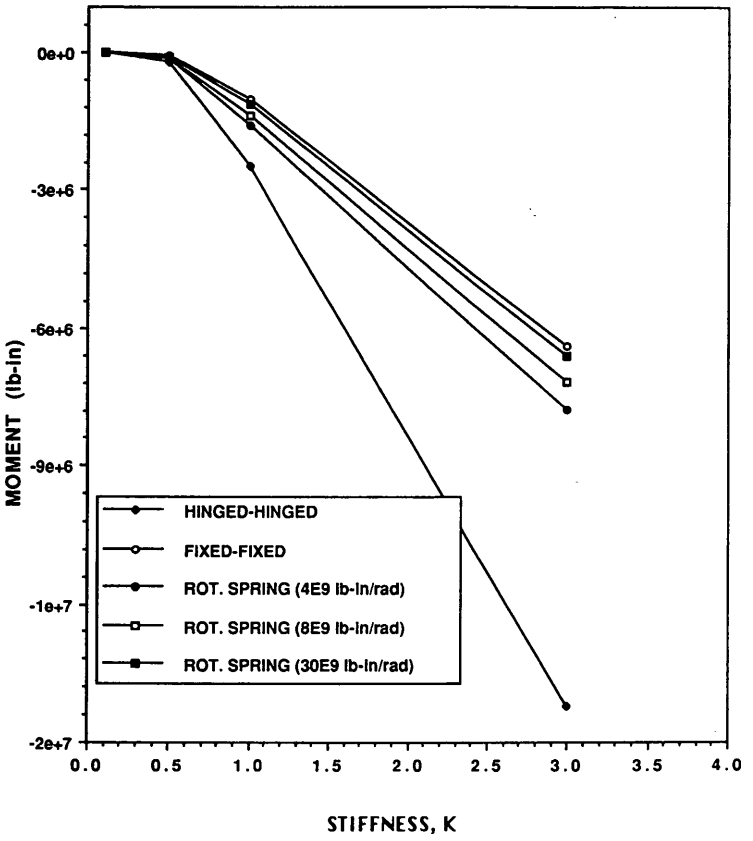

FIGURE 6 Stiffness versus moment at midspan due to earth pressure.

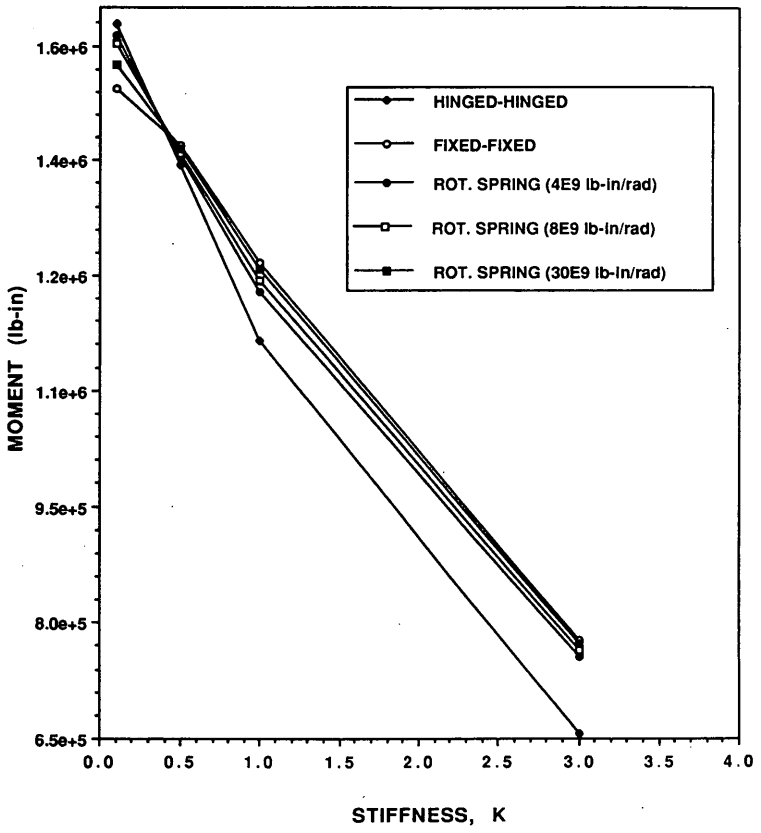

FIGURE 7 Stiffness versus moment at midspan due to temperature gradient.

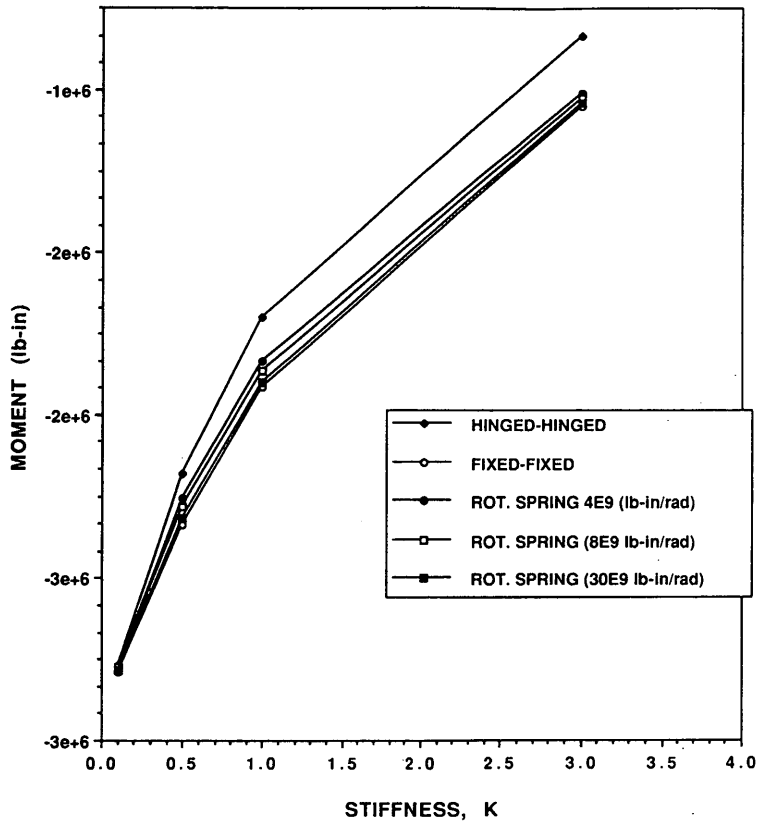

FIGURE 8 Stiffness versus moment at support due to live load.

tion; in addition, the settlement moment at the footing level is higher for a lower stiffness ratio (K).

Moment at Midspan

The effect of higher K would lead to a greater midspan moment in the case of a live load and earth pressure, as indicated in Figures 5 and 6. A similar trend is observed for dead load case. The moment developed as a result of earth pressure causes tension at the top and will reduce the net moment when acting in combination with dead and live loads. Moment caused by temperature gradient at midspan is smaller for increased K values (Figure 7). An increase in stiffness ratio (K) indicates stiffer superstructure and weaker abutment. The stiffer superstructure results in a lower midspan moment. Soil settlement moments are negligible at midspan, and the stiffness ratio K value has little effect on settlement moments.

Moment at Support (Superstructure and Abutment Joint)

The support moment decreases with an increase in K for live load (Figure 8). A similar trend is also observed for the dead load case. The support moment as a result of earth pressure is higher in the case of a hinged-hinged support condition and lower for other boundary conditions as shown in Figure 9. The temperature gradient produces a uniform moment throughout the superstructure. The moment direction and magnitude at midspan and support are the same and can be seen in the Figures 7 and 10. Further, the moment at the left support is the same as the moment at the left footing level in the case of 1-in. settlement of right footing for all boundary conditions.

Horizontal Reaction Due to Earth Pressure

In the parametric study, the height of abutment varied from 3.1 to 18.3 m (10 to 60 ft). The total horizontal force due to earth pressure corresponding to 3.1 to 18.3 m (10 to 60 ft) in height ranged from 4994 to 181 600 kg (11 to 400 kips). Because of this wide range of lateral force associated with earth pressure, it becomes important to study the effect of earth pressure on abutment and superstructure for varied abutment and superstructure stiffness ratio (K). The earth pressure effect on the abutment is indicated in Figure 11. The horizontal reaction caused by earth pressure is smaller at lower values of K and has an increasing trend for increasing K values. The horizontal reaction is 1.5 to 2 times higher for hinged cases over fixed cases for all values of K. The study provides useful information in deciding the system stiffness and boundary conditions to keep the horizontal reaction at a minimum.

Vertical Reaction Due to Earth Pressure

The vertical reactions due to earth pressure are higher for hinged boundary conditions than for fixed or partially fixed conditions. The

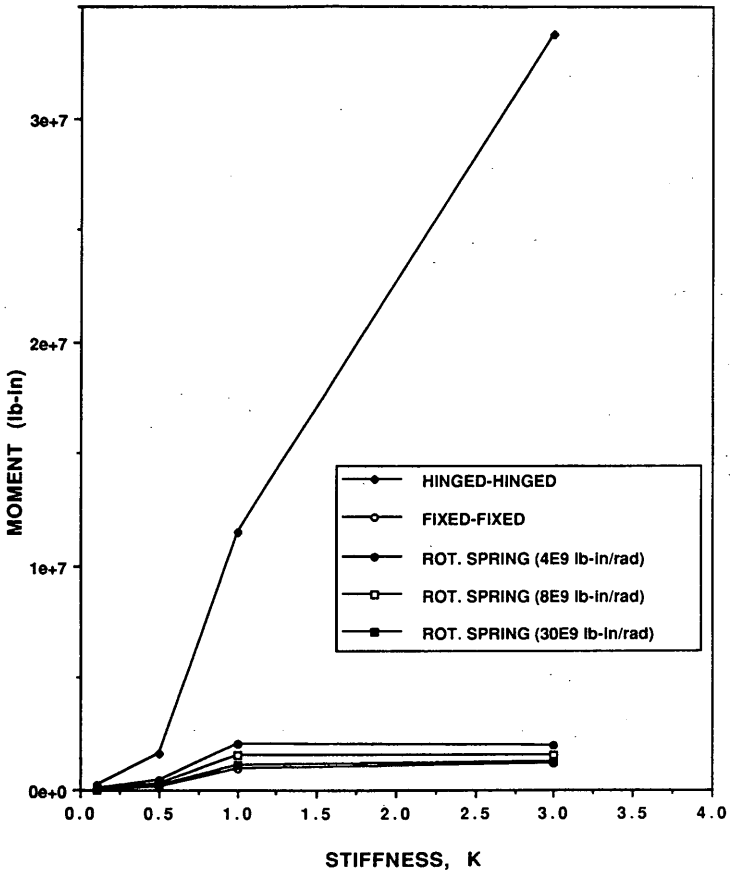

FIGURE 9 Stiffness versus moment at support due to earth pressure.

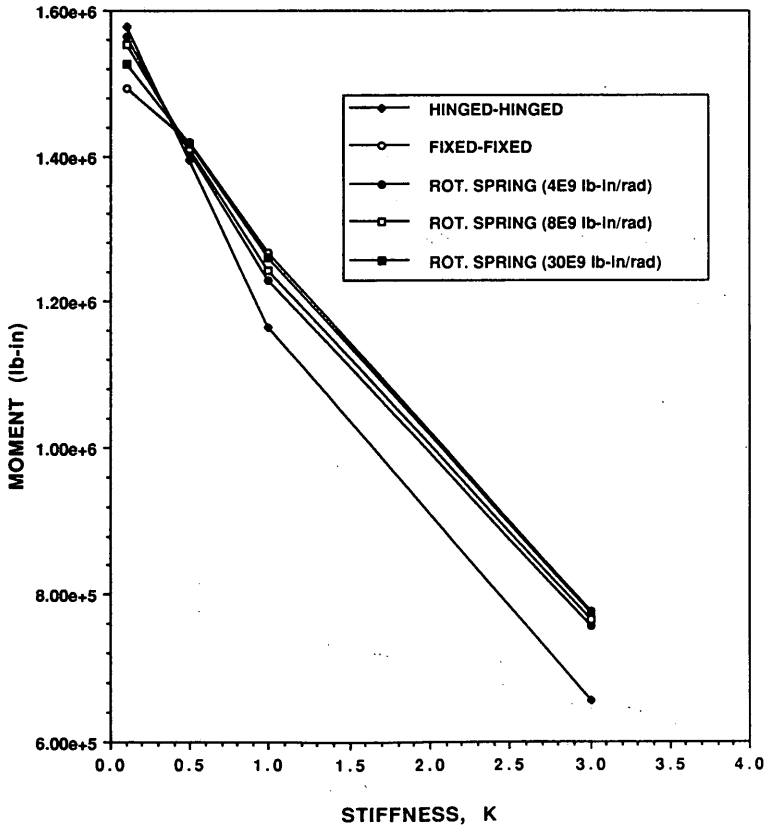

FIGURE 10 Stiffness versus moment at support due to temperature gradient.

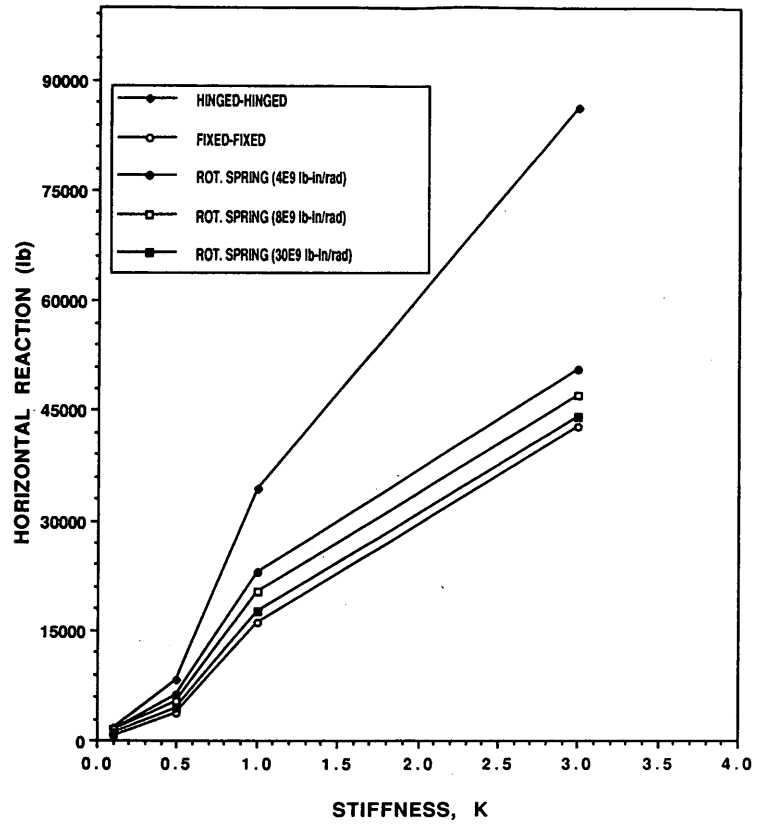

FIGURE 11 Stiffness versus horizontal reaction at right footing due to earth pressure.

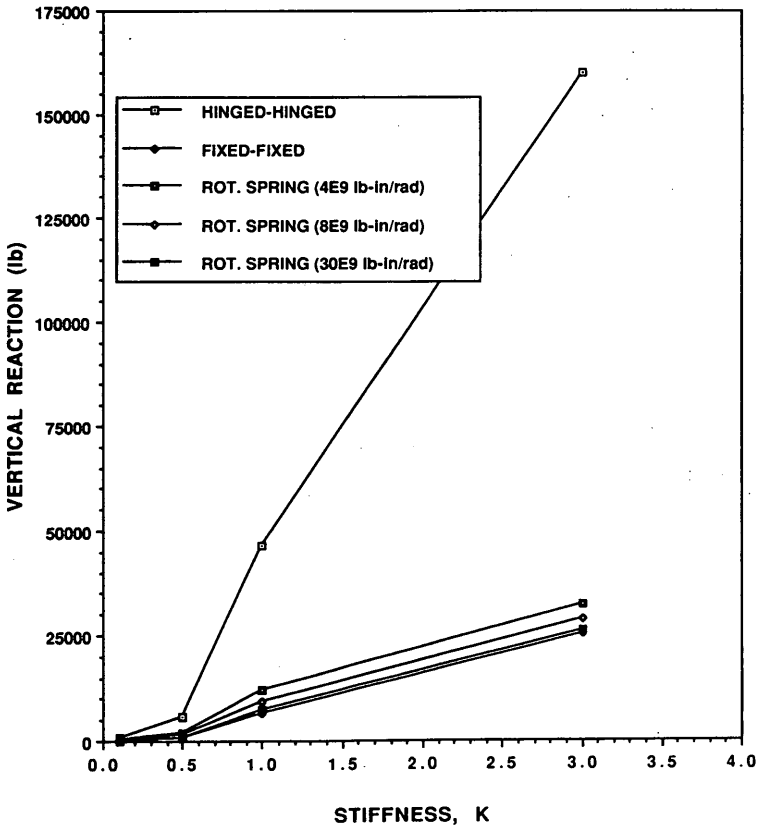

FIGURE 12 Stiffness versus vertical reaction at left/right footing due to earth pressure.

vertical reactions are about 7 to 8 times higher in hinged conditions than in other types when the stiffness ratio K is 3 (Figure 12). This large variation of vertical reactions could lead to differential settlement for large abutment heights.

JOINTLESS BRIDGE VERSUS JOINTED BRIDGE

From the results of the parametric study, a case of a jointless bridge with a system stiffness ratio K of 0.5, a superstructure-to-substructure moment of inertia ratio of 1.25, a span length of 15.3 m (50 ft), and an abutment height of 6.1 m (20 ft) is considered to compare the results with a simply supported jointed bridge with its abutment fixed at the base. Two types of boundary conditions—hinged and fixed—are considered for the jointless bridge. Various load types are applied and the moment developed at the midspan, superstructure, and substructure joint and at foundation level is evaluated. Similar load combination effects in terms of moment are evaluated for a simply supported jointed bridge case, and the results are shown in Tables 1 and 2. In addition, the time-dependent creep-induced moment is also considered in arriving at the total moment. The superstructure and abutment are assumed to act independently in the case of the jointed bridge. The salient points are presented.

- The net moment developed at midspan during summer in a jointed bridge is found to be 1.8 and 1.9 times greater than that of the net moment developed in a jointless bridge for hinged and fixed boundary conditions, respectively. During winter, the net moment at midspan of a jointed bridge is found to be nearly 3 and 3.5 times greater than that of the net moment developed in a jointless bridge for hinged and fixed boundary conditions, respectively. The lower midspan moment in a jointless bridge caused by the combination of all loads explains the superiority of the performance of a jointless bridge over a simply supported jointed bridge.
- The moment transferred to the foundation is 0 when the jointless bridge has a hinged type of boundary condition. Therefore, the foundation and the supporting soils are less vulnerable to soil deformation in the case of a jointless bridge with a hinged type of boundary condition. The moment transferred to the foundation in a jointless bridge with fixed boundaries is 0.3 to 0.4 times that of the moment at the foundation of a simply supported jointed bridge. In the field, the support condition falls between these two extreme cases (partial fixity) and may approach a condition as that of hinged condition with time. So, a choice has to be made about the degree of fixity that may be required at the foundation of a jointless bridge. In addition, orienting the weak axes of the piles normal to traffic flow will further reduce the stresses in the piles and the soils.
- The rigid joint between the superstructure and substructure in the case of a jointless bridge is subjected to high moment, which is nearly the same as that of midspan moment. It becomes necessary to provide adequate section and proper design at the joint.
- Furthermore, connecting the approach slab to the rigid joint will further help redistribute the moment, and the joint may be subjected to a lower moment. A jointless bridge with approach slab may reduce the flexibility against horizontal movement. However, pressure relief methods have been adopted (*4*) to induce flexibility into the system. In a jointless bridge, the backfill seepage has a detrimental effect in terms of weakening the rigid joint and also enhancing the settlement of the approach slab. Provision of a proper drainage system will minimize the effects of backfill seepage.
- For a jointless bridge, the effect of uniform temperature (direct expansion or contraction) on the superstructure of span 15.3 m (50 ft) and height 6.1 m (20 ft) is negligible in terms of the amount of horizontal displacement of the system. However, for longer spans this may be a controlling factor.

CONCLUSIONS

The system stiffness ratio K and the boundary conditions have significant influence on the magnitude of the moments developed in the jointless bridges. The moment at the footing associated with live and dead load is maximum when K is about 0.5. The thermally induced moment at the footing is larger for smaller K values. The moment at the footing associated with earth pressure is the highest for a stiffness ratio of 3. The settlement moment at the footing level is higher for a lower stiffness ratio. The midspan moment is greater for a lower stiffness ratio K in the case of live load, dead load, and earth pressure. Moment caused by temperature loads at midspan is smaller for increased K values. Soil settlement moments are negligible at midspan for all values of K considered in our analysis.

The maximum midspan moment developed for hinged and fixed boundary conditions in a jointless bridge considered is nearly 50 percent lower than that in a jointed bridge. The effect of soil settlement is negligibly small for a hinged case, whereas the moment developed because of 1 in. of soil settlement in a fixed case at support is found to be about 20 percent of maximum moment at support. The effect of earth pressure is significant at the top of the abutment in the case of hinged condition and at the bottom of the abutment in case of a fixed condition. The effect of braking forces in both hinged and fixed jointless bridges is small compared with the maximum moments.

FURTHER STUDY

The analytical data generated for single-span jointless bridges will be compared with the field data. A simple equivalent beam design model with rotational and translation spring constants is being developed for a portal frame. Equivalent rotational and translation spring constants will be arrived at considering the soil stiffness, foundation type, and integral bridge stiffness K. The equivalent beam model indicated in Figure 13 will be solved for a general loading to determine end moments. The beam model would be handy for practicing engineers. The merits and demerits of having an internal hinge between the superstructure and substructure will have to be assessed. The parametric study of two- and three-span bridges with different boundary conditions is being performed by varying the abutment/pier heights, type of foundation, soil conditions, and

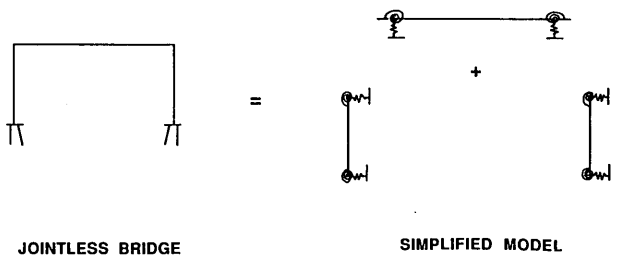

FIGURE 13 Simplified model for jointless bridge.

temperature variations. Length and tolerable movement limits will be established using the data from the parametric study and field.

ACKNOWLEDGEMENTS

The research project was sponsored by the West Virginia Department of Highways and FHWA, U.S. Department of Transportation. Their financial support and suggestions are gratefully acknowledged.

REFERENCES

1. Klaiber, W. F., et al. *NCHRP Report 293: Methods of Strengthening Existing Highway Bridges*. TRB, National Research Council, Washington D.C., 1987.
2. Dagher, J. H., et al. Analytical Investigation of Slab Bridges with Integral wall Abutments. In *Transportation Research Record 1319*, TRB, National Research Council, Washington, D.C., 1991, pp. 115–125.
3. Purvis, R. L., and R. H. Berger. Bridge Joint Maintenance. In *Transportation Research Record 399*, TRB, National Research Council, Washington, D.C., 1983.
4. Wolde-Tinsae, A. M., et al. Performance and Design of Jointless Bridge. *FHWA Final Report*. Department of Civil Engineering, University of Maryland, June 1987.
5. Burke, M. P. Integral Bridges: Attributes and Limitations. In *Transportation Research Record 1393*, TRB, National Research Council, Washington, D.C., 1993, pp. 1–8.
6. Burke, M. P. Integral Bridges. Presented at 69th Annual Meeting of the Transportation Research Board, Washington D.C., Jan. 1990.
7. Loveall, C. L. Jointless Bridge Decks. *Civil Engineering*, Vol. 55, No. 11, Nov. 1985, pp. 64–67.
8. Wasserman, E. P. Jointless Bridges. *Engineering Journal*, Vol. 24, No. 3, 1987, pp. 93–100.
9. Emanual, J. H., and C. M. Taylor. Length-Thermal Stress Relations for Composite Bridges. ASCE *Journal of Structural Engineering*, Vol. 111, No. 4, April 1985.
10. Hulsey, J. L., and J. H. Emanual. Environmental Stresses in Flexibly Supported Bridges. In *Transportation Research Record 664*, TRB, National Research Council, Washington, D.C., pp. 262–270.
11. Lam, P. I. Seismic Design of Highway Bridge Foundations. FHWA *Report RD-86/102*. FHWA, U.S. Department of Transportation, 1986.
12. *Standard Specifications for Highway Bridges*, 14th ed. AASHTO, Washington, D.C., 1989.
13. Hayden, G. A., and M. Barron *The Rigid-Frame Bridge*. John Wiley and Sons, New York, 1950.
14. Kleinlogel, A. *Rigid Frame Formulas*. Frederik Ungar Publishing Co., New York, 1964.
15. Greimann, L. F., et al. *Pile Design and Tests for Integral Abutment Bridges*. Iowa DOT Project 273, Iowa State University, Dec. 1987.
16. Ghali, A., and R. Favre. *Concrete Structures: Stresses and Deformations*. Chapman and Hall, New York, 1986.
17. ANSYS. *Engineering Analysis System User's Manual*. Swanson Analysis Systems, Inc., Houston, Pa., 1987.

Publication of this paper sponsored by Committee on Steel Bridges.

Destructive Testing of Deteriorated Prestressed Box Bridge Beam

RICHARD MILLER AND KETAN PAREKH

A deteriorated prestressed box bridge beam was tested to destruction to determine the effects of deterioration on prestressed beam performance. Three prestressing tendons in one corner of the beam had corroded causing spalling of that corner. One of the tendons had broken and the other two were badly corroded, so only 15 tendons were effective. The resulting tendon pattern was asymmetric. A destructive test was conducted by loading the beam with two point loads. For comparison purposes, an undamaged beam with all 18 tendons intact was cast and tested. The undamaged beam held an applied moment of 2720 kN-m (2005 kip-ft) and did not fail. The deteriorated beam failed suddenly at a total applied moment of 1805 kN-m (1310 kip-ft). This reduction in moment capacity is not totally attributable to loss of tendons or cross section. The deteriorated beam also showed less deflection capacity at the midspan [270 mm (10.7 in.) versus 432 mm (17 in.)], more lateral deflection [28 mm (1.1 in.) versus 0 mm] and more web cracking than the undamaged beam. The final failure of the deteriorated beam appeared to be a lateral instability, which resulted in the sudden collapse of the beam. This lateral instability was caused by the lateral bending and yielding of the steel. It was also found that the AASHTO Code was not conservative for the deteriorated beam. The applied failure moment was 8 percent lower than that predicted by the AASHTO Code.

Bridge elements can be damaged or show signs of deterioration, or both, as a result of traffic and environmental conditions. Engineers frequently are required to determine whether a damaged or deteriorated element may be left in service or should be repaired or replaced. It is difficult to evaluate the strength and serviceability of deteriorated members because clear guidelines and methods often do not exist.

Determination of the strength of a deteriorated prestressed beam is particularly difficult. Deterioration or damage often causes a lack of symmetry in both the cross section and the steel tendon pattern. Under load, the lack of symmetry may cause lateral bending or torsion, or both, which may induce undesirable stresses. The asymmetrical strand pattern of a damaged or deteriorated beam makes evaluation more difficult because there are no standard or simple methods for analysis of asymmetrical prestressed beams. All the usual methods of analysis for prestressed members assume symmetry of the tendon pattern because prestressed beams are almost always manufactured as symmetrical sections to avoid the out-of-plane bowing caused by asymmetry.

There may also be a loss of capacity due to deterioration of the concrete. There is little information on the effect of material damage on the behavior of prestressed members. Therefore any loss of capacity due to material degradation cannot be easily quantified.

One way to determine the effect of deterioration on a prestressed concrete beam is to test a deteriorated beam to destruction while carefully monitoring the response. Information from such a test can then be used to evaluate the various methods of determining the strength and behavior of deteriorated prestressed concrete beams.

R. A. Miller, Department of Civil and Environmental Engineering, University of Cincinnati, P.O. Box 210071, Cincinnati, Ohio 45221. K. Parekh, Moody/Nolan, Ltd., 1776 East Broad St., Columbus, Ohio 43203-2039.

SIGNIFICANCE OF RESEARCH

Prestressed box beams can be damaged by vehicle impact or deterioration mechanisms such as corrosion. Often, the damage will cause a loss of cross section and there may be broken or damaged tendons. One consequence of the damage is that broken tendons result in a loss of prestressing force, which may cause the beam to crack under service loads. There also will be a reduction in ultimate moment capacity due to loss of cross section and tendons. The damaged beam will have an asymmetrical cross section and tendon pattern, and this lack of symmetry may cause lateral bending stresses or torsional stresses under vertical load, or both, which may further reduce the member capacity. Finally, material damage may cause a loss of capacity by limiting material response. By load testing an asymmetrically deteriorated box beam it is possible to evaluate the effect of the damage, loss of cross section, loss of tendons, and loss of symmetry on the beam behavior.

PREVIOUS RESEARCH

Little work has been done on load testing damaged or deteriorated prestressed beams. Shenoy and Frantz (*1*) tested prestressed box beams removed from a bridge. However, these beams were only lightly deteriorated and no tendons were broken or damaged so the beams remained symmetrical. Shenoy and Frantz concluded that, even though slightly damaged, the beams remained sufficiently strong and ductile and that current analysis methods were adequate.

Olson (*2*) tested four 20-year-old AASHTO Type III girders that had been removed from a bridge in Minnesota. These beams were not damaged when removed but were damaged as part of the experimental program to test repair techniques. One beam was tested undamaged, and another was left damaged and was tested without repair as a baseline. (The remaining two beams were damaged, repaired, and then tested.) The undamaged beam was tested under fatigue loading and then tested to failure. Testing of the damaged beam consisted of severing two (of 30) strands on one side of the beam (creating an asymmetrical section) and applying fatigue loads. Fatigue tests were repeated after severing a third and then a fourth strand on the same side of the beam. The beam was then load tested to destruction. The results of Olson's study have three important points. (*a*) Olson observed that the final static load applied at failure was 29 percent lower than that of the undamaged beam. [The flexural capacity was calculated using the 1989 AASHTO Code (*3*) and ignoring the asymmetry in the beam. It was

found that loss of tendons results only in a 15 percent calculated reduction in failure load capacity. Clearly the loss of strength was not only a result of tendon loss.] (*b*) Olson noted that on the damaged side, cracks formed and these cracks propagated back toward the supports. (*c*) Olson also noted that the bottom flange of beam on the damaged side "peeled away" from the web. The impact of these results on this study will be discussed later.

DESCRIPTION OF BEAM

The deteriorated test beam had been a sidewalk support beam in a bridge over the Maumee River in Defiance, Ohio. Because it was a sidewalk beam protected by a high curb, it is unlikely to have seen significant service loads beyond its own dead load. Cast in 1980, the beam was a box section 23.3 m (76 ft 6 in.) long, 0.91 m (36 in.) wide, and 0.84 m (33 in.) high with walls 127 mm (5 in.) thick. (Figure 1). Originally, the beam had 18 prestressing tendons 13 mm (½ in.) in diameter with each tendon having an area of 99 mm^2 (0.154 in.^{2}). At the time of the tests, the prestressing tendons in one corner of the beam had corroded (Figure 2) causing spalling of that corner. In the deteriorated areas, the damage was not uniform along the length and the worst visible damage to the beam occurred 7.6 m (25 ft) from one end of the beam (Figure 2). Examination of the deteriorated corner revealed that one tendon was broken and was missing along almost the entire length of the beam. Two other tendons were still present but were badly corroded. In one corroded tendon, the individual strands were broken at various places. The other corroded tendon was still substantially intact and was still embedded in the concrete in some places. It is not known if either of these corroded tendons was effective. Therefore, it is possible to definitely assume that only 15 of the tendons are still effective, although the test results showed that perhaps one of the corroded tendons also carried some load.

The damage to the beam was first noted during a routine annual inspection of the bridge in the summer of 1989. Since the damaged tendons were in one corner of the box, the remaining tendons in the beam had an asymmetric pattern and the prestressing force became eccentric, which caused a lateral moment in the beam. The deteriorated beam had been tied to another sidewalk support beam as required in the original plans. Before removal, the lateral bending would have been restrained by the attachment to the other sidewalk beam. Therefore, the amount of lateral bending and the associated stresses before removal are not known. Removal of the beam from the bridge occurred in summer 1990. After being removed, the beam was stored until it was tested in summer 1992. The presence of the lateral moment caused by prestressing force eccentricity caused an out-of-plane bowing of the beam that was measured to be about 13 mm (½ in.) at the time of testing.

Originally the beam was designed using 38.5 MPa (5,500 psi) of concrete and 1890 MPa (270 ksi) of prestressing steel. At the time of testing, the concrete was approximately 12 years old. Cores taken after the destructive static test indicated that the concrete strength was approximately 56 MPa (8,000 psi). Tests on the prestressing tendons showed a yield strength of 1645 MPa (235 ksi) and an ultimate strength of 1800 MPa (260 ksi).

To accurately assess the effect of damage on the beam, it was desirable to test an undamaged version of the test beam. Because no such beam was available, an undamaged beam having the same length as the deteriorated beam and the undamaged cross section shown in Figure 1 was cast. Cylinder tests indicated that this beam also had a concrete compressive strength of 56 MPa (8,000 psi) at the time of the test, 21 days after casting. The prestressing steel had a yield strength of 1740 MPa (250 ksi) and an ultimate strength of 1880 MPa (270 ksi).

TESTING SYSTEM

The static, destructive test was conducted on the beams at the ESSROC Prestressed Concrete Products manufacturing facility in Melbourne, Kentucky. This site was chosen because of the presence

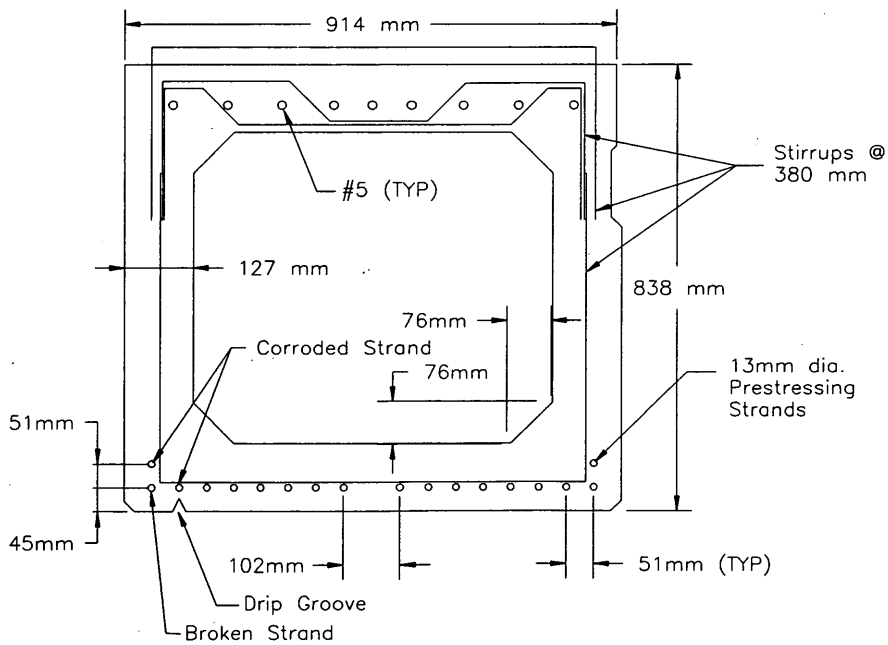

FIGURE 1 Cross section of original beam.

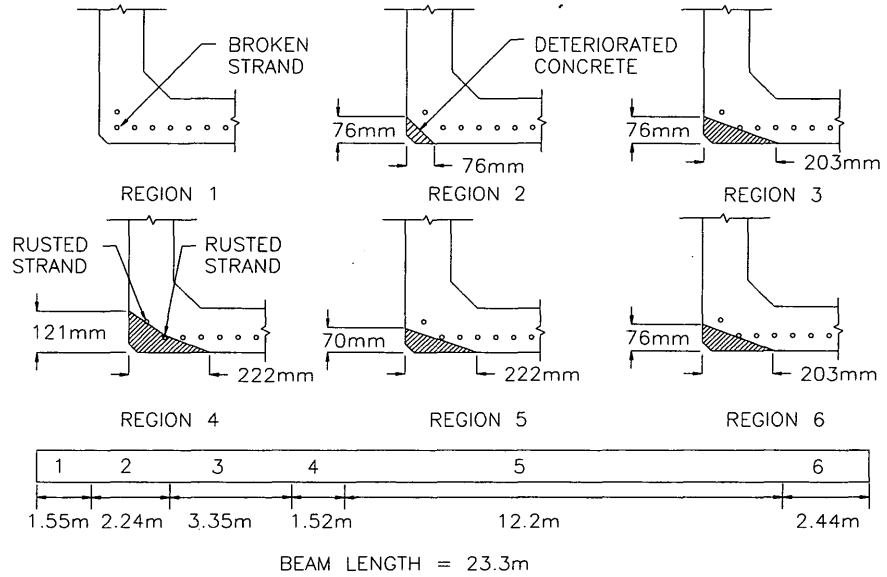

FIGURE 2 Map of damage to deteriorated beam.

of an existing foundation that could be used for securing two testing frames and because equipment for casting the undamaged beam and moving both the deteriorated and undamaged beams was readily available. The beams were loaded with two point loads placed 6.4 m (21 ft) apart, 8.5 m (28.8 ft) from either end. This load position was dictated by the position of existing tie-down plates for the testing frames. Two steel testing frames were fabricated to apply the loads (Figure 3).

Concrete end blocks were cast to provide beam end supports. These blocks were designed to simulate the actual end condition of the original bridge (Figure 4). The beam was doweled into the end blocks, but rather than grouting the dowels, the area around the dowels was packed with wet sand. This was done to allow removal of the beam from the supports after the test.

The Ohio Department of Transportation (ODOT) engineers desired to match field conditions as closely as possible during the test. Because the test beam was an edge beam, the lateral deflection in one direction would be constrained by the presence of other bridge beams. Therefore, during the test a "bumper beam" was placed beside the test beams. For the deteriorated beam, the bumper beam was placed on the side away from the damage since the damage actually occurred on the outside edge of the bridge. The presence of this bumper beam had no effect on the test because neither beam ever touched it. It prevented mapping of the cracks on one side of the beam.

FIGURE 3 Testing frame.

Loads were applied using two capacity servo-controlled hydraulic actuators 1.5 MN (350 kips). A digital controller was used to control the cylinders. The undamaged beam was tested in load control. However, by the time the deteriorated beam was tested the capability for displacement controlled testing had been developed and the test of the deteriorated beam was conducted in displacement control. The system was capable of controlling only one displacement, so a master/slave configuration was used. In this method, the displacement under one load point was used for control and the hydraulic cylinders were linked so that the system supplied the same pressure (load) to each cylinder.

A clevis was installed on the end of each cylinder to transfer the load to the beam. These clevises had bearing plates that were 480 mm (18 in.) square. This size bearing plate spread the load enough to prevent local failure of the box beam top flange. Load was transferred from the clevis plate to the beam by an elastomeric pad 480 mm (18 in.) square to ensure even application of the load.

The undamaged beam was loaded in 18-kN (4-kips) increments and at various points and then unloaded and reloaded so that changes in stiffness could be monitored. The deteriorated beam was loaded in 13-mm (½-in.) displacement increments. At various displacement levels this beam was also unloaded and reloaded. For both beams, after each application of a load or displacement increment, the test was paused and the beam was inspected for cracking. The cracks were marked on the beams.

INSTRUMENTATION

The vertical and horizontal displacements and the angle of twist were measured by wire potentiometers arranged as shown in

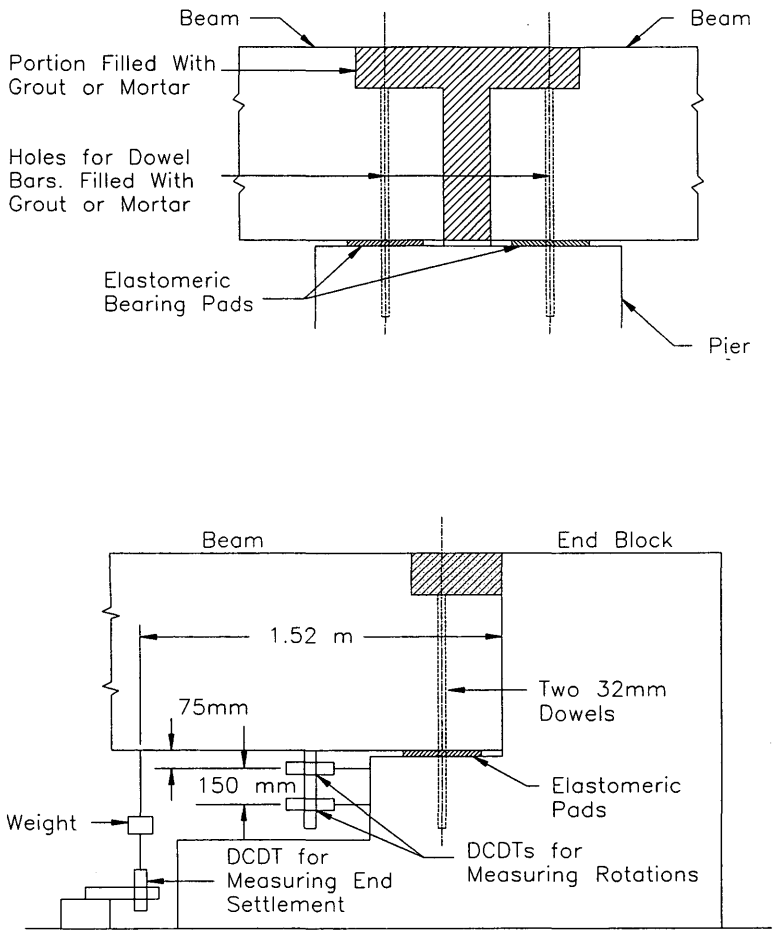

FIGURE 4 Support condition on original bridge and support block and instrumentation for test.

Figures 5 and 6. These instruments were chosen because they had a range sufficient to measure the large beam deflections. Each wire potentiometer had a range of either 254 or 380 mm (10 or 15 in.). Because of the large deflections in both the vertical and lateral directions and because the corners of the beams were moving in two directions at once, the wire potentiometer could not measure vertical and lateral deflection directly. The wire potentiometers basically measure the change in the length of the wire running from the instrument to the beam, so that at any time the distance from the wire potentiometer to the corner of beam was known. Because the distance between wire potentiometers was known, the deflection of the beam in the vertical and lateral directions could be calculated by triangulation. Theoretically, only three wire potentiometers are needed at each point to determine the deflection and rotation of the beam, but five were used to provide for averaging and redundancy.

Linear variable differential transformers were used to measure deflections (support settlement) and rotations of the beam ends as shown in Figure 4. Steel strains were measured by strain gauging the steel tendons. Where necessary, holes were cut into the concrete to expose the prestressing tendons (no holes were necessary where the tendons had been exposed by deterioration) (Figures 5 and 6). Because the tendons were made of seven individual strands, strain gauges were attached to two of these individual strands to measure the steel strain. Strain gauges were installed on the concrete surface to measure concrete surface strains, but several of these gauges failed. However, some concrete strain data were obtained for the deteriorated beam.

TEST RESULTS

The undamaged beam was tested first at an age of 21 days. A plot that shows load versus midspan deflection is indicated in Figure 7. The first cracks were observed at an applied load of 135 kN (30 kips) at each of the two loading points. The test was stopped at an applied load of 258 kN (58 kips) at each load point and a midspan deflection of 432 mm (17 in.) because the deflection capacity of the test frame had been exhausted (i.e., the beam touched the ground). Test results showed that the steel had yielded, but no strands were ruptured. No lateral deflection was noted. Typical crack patterns (Figure 8) show flexural cracks with the characteristic "forking" at the top. In all, the test of the undamaged beam yielded results that were consistent with those of published tests of box beams (*1*).

The results of the deteriorated beam test were different. As loading began, lateral deflection in the direction of the damaged side of the beam was observed. The first cracks occurred at an applied load of 107 kN (24 kips) at each point. Once the beam cracked, the vertical deflection increased rapidly and the load-versus-vertical-

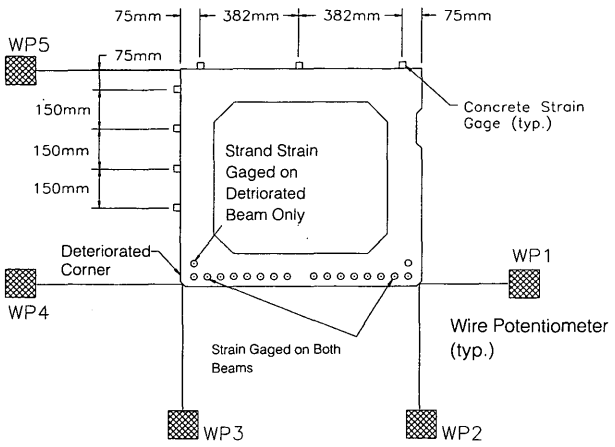

FIGURE 5 Position of instruments on cross section.

midspan deflection curve became flatter than that of the undamaged beam (Figure 7). The lateral deflection also increased significantly after cracking (Figure 9). It was noted that the initial flexural cracks propagated much higher into the web of the deteriorated beam than into the web of the undamaged beam (Figure 10).

At an applied load of 120 kN (27 kips) at each point, the corroded tendon in the bottom layer of steel (Figure 2) ruptured. The other corroded tendon (in the upper layer) remained partially bonded in the concrete but appeared to be pulling loose as the deflection increased. As seen in Figure 2, this tendon was partially exposed in some areas and nearly completely embedded in other areas. As the tendon began to pull loose it caused additional spalling and cracking in the areas where the tendon was still mostly embedded. The most severe spalling occurred near one of the loading points (Figure 10). Under an increasing load, cracks propagated from the area end back toward the support (and the load point) in a fan shape (Figure 10). This spalling and cracking associated with the pull-out and debonding of the corroded tendon seems to indicate that the tendon carried some force during loading. As a result, an assumption that this tendon is ineffective would be conservative.

As the load increased, the flexural cracks propagated high into the web and began to propagate into the top flange (Figure 10). The cracks in the deteriorated beam also are much farther apart than those in the undamaged beam, probably because most of the prestressing steel under this web is missing and the remaining steel is not sufficient to properly distribute the cracks.

At an applied load of 147 kN (33 kips) per load point, the beam failed suddenly and collapsed. At the time of failure, the beam had deflected 270 mm (10.7 in.) vertically and an additional 28 mm (1.1 in.) laterally (the beam already had a 13-mm (½-in.) lateral deflection before the test began).

ANALYSIS OF RESULTS

Figure 7 shows that, before it reaches the cracking load, the deteriorated beam is less stiff than the undamaged beam, but the difference is small. The small difference in stiffness is not unusual because precracking stiffness is largely influenced by gross cross-section properties, and the loss of gross cross-sectional area for the deteriorated beam was small compared with the total gross cross-sectional area.

The cracking load of the deteriorated beam was lower than that of the undamaged beam. Calculations show that the lower stiffness and cracking load of the deteriorated beam can be explained by accounting for the loss of cross section and the loss of prestressing

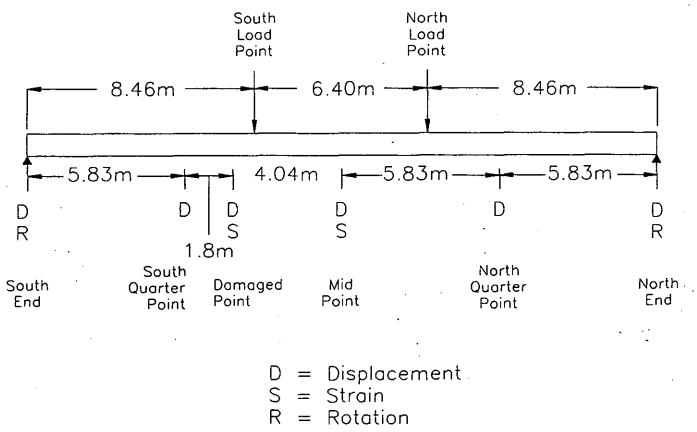

FIGURE 6 Position of instruments along length of beam.

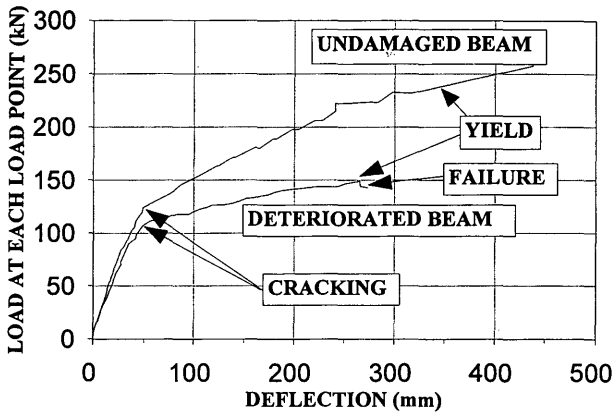

FIGURE 7 Load versus midspan deflection for deteriorated and undamaged beams.

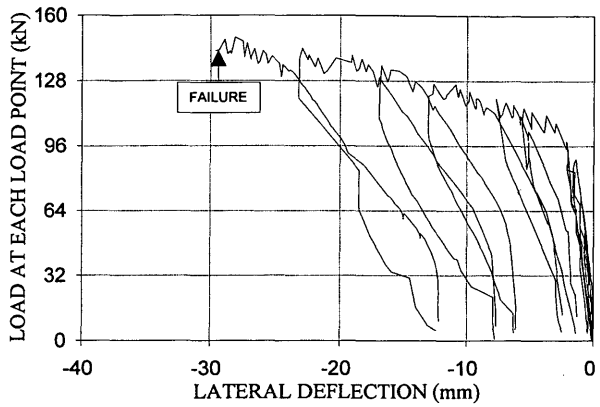

FIGURE 9 Load versus midspan lateral deflection for deteriorated beam.

force in the tendons. The loss of prestressing force was estimated using the provisions of the 1989 AASHTO Code (*3*). These losses were estimated at 10 percent for the undamaged beam and 18 percent for the deteriorated beam. It was the intent of the investigators to determine the actual loss of prestress in the deteriorated beam by strain gauging and severing some of the tendons after the test was complete, but the catastrophic failure of the beam made this impossible.

The loss of prestressing force will be affected by the lateral bending moment caused by the asymmetry of the beam. Once removed from the bridge, the beam was free to deflect laterally because of the eccentric prestressing force. The lateral deflection will increase over time as a result of creep (because the beam was 10 years old at the time of removal, shrinkage was ignored since most of the shrinkage had already occurred). The lateral deflection will cause tendons away from the damaged web to lose prestressing force because they are on the "compressive" side for lateral bending. By the same argument, tendons near the damaged web may gain prestressing force because they are on the "tensile" side. Calculations of these changes in prestressing force, assuming that 50 percent of the ultimate creep had occurred, showed that the prestressing force in a tendon may change by less than 2 percent of the original prestressing force, at most. Also, because the lateral bending is parallel to the tendon line, the change in prestressing force varies linearly along the cross section. When the average loss of prestressing force for the tendon group as a whole was calculated, it was found to be negligible.

The moment of inertia of the deteriorated beam was calculated by assuming the loss of a triangular section 220 × 120 mm (8.7 × 4.7 in.) from the lower corner of the beam. This roughly corresponds to the damage in Region 4 in Figure 2. Using calculated prestressing losses and the normally assumed values of E ($4700 f'^{0.5}_c$ MPa or $57000 f'^{0.5}_c$ psi) and f_r ($0.63 f'^{0.5}_c$ MPa or $7.5 f'^{0.5}_c$ psi), the calculated cracking moment was found to be 1410 kN-m (1035 kip-ft). The actual cracking moment of the deteriorated beam was 1440 kN-m (1060 kip-ft) (applied load + beam weight). The calculated cracking moment is in reasonable agreement with the experiment. Note that measured material properties were used in the calculation. For the undamaged beam, the calculated cracking moment was 1590 kN-m (1170 kip-ft) compared with the measured value of 1625 kN-m (1195 kip-ft), again showing reasonable agreement.

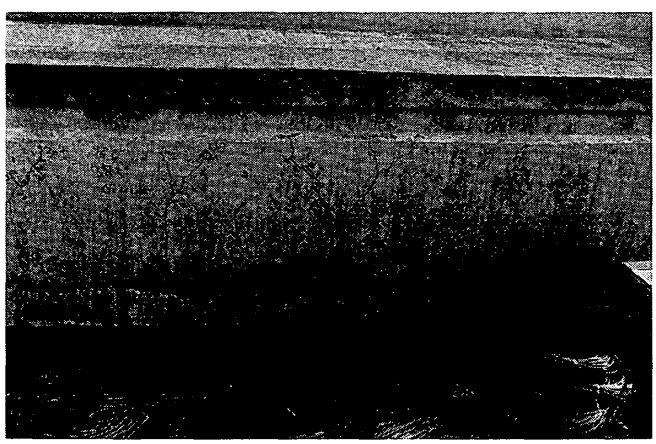

FIGURE 8 Crack pattern for undamaged beam (note: failure notation in photo is incorrect).

FIGURE 10 Crack pattern for deteriorated beam just before failure.

In the postcracking region, the deteriorated beam was significantly less stiff than the undamaged beam (Figure 7). This lower stiffness was caused by the loss of tendons and because once the beam cracked the deteriorated beam showed significantly longer cracks on the damaged web. Because there was no longitudinal mild reinforcing in the web and because three of the prestressing strands under the web were missing, there was little to control web cracking caused by the increased tensile stresses from the lateral moment. This can be seen by comparing the crack patterns for the two beams (Figures 8 and 10). Under a load of 258 kN (58 kips) per point, the cracks in the undamaged beam had propagated only 660 mm (26 in.) from the bottom of the beam. The deteriorated beam had crack lengths that measured 760 mm (30 in.) from the bottom of the beam under a load of 147 kN (33 kips) per load point. The cracks in the deteriorated beam were long enough to penetrate the top flange. It therefore appears that the lateral bending caused much more cracking in the damaged web (note that cracking in the undamaged web could not be observed because of the presence of the bumper beam). This cracking would have reduced the postcracking stiffness. The previously noted cracking caused by pullout of one of the corroded tendons also would have reduced the postcracking stiffness.

It is also of interest to determine whether the provisions of the 1989 AASHTO Code (*3*) will reasonably predict the ultimate moment capacity of the undamaged and deteriorated beams. The calculated capacity of the undamaged beam, using measured material properties, was found to be 2360 kN-m (1735 kip-ft). During the experiment, a total moment (applied load + beam weight) of 2720 kN-m (2005 kip-ft) was applied to the beam and the beam did not fail. This illustrates the conservative nature of the AASHTO Code.

For the deteriorated beam, the AASHTO Code is not conservative. Using the actual material properties and assuming 15 strands to be effective, the calculated moment capacity is 1950 kN-m (1435 kip-ft). The actual failure moment (applied load + beam weight) was 1805 kN-m (1310 kip-ft), about 8 percent below the calculated moment. Note that the calculation of ultimate moment was a lower bound because it assumed that both corroded tendons were ineffective; however, the experimental evidence indicates that one of the corroded tendons may have been at least partially effective. Also note that, since bending capacity is only slightly affected by the concrete compressive strength, the calculated ultimate moment hardly changes if the design concrete strength of 39 MPa (5,500 psi) is used in place of the actual compressive strength of 56 MPa (8,000 psi).

The mode of failure is of great concern. The deteriorated beam failed suddenly as opposed to the undamaged beam, which showed ductile behavior. The exact cause of the final failure is not certain because it occurred suddenly; however, there is a reasonable possibility that the failure is linked to the lateral bending. It was noted that strain in the prestressing steel of the damaged beam was measured at approximately 0.005 at the time of failure. If it is assumed that the prestressing steel was originally stressed to 0.7 f_y (as required by the specifications) and the prestressing losses [calculated by the provisions of the 1989 AASHTO Code (*3*)] were 18 percent, the strain in the steel before the test began would also have been about 0.005. Thus, the total strain (prestressing + applied load) would be approximately 1 percent, which is usually taken as yield in the prestressing steel. It is believed that once the prestressing steel yielded, it was unable to restrain the lateral bending of the beam. Because there was no mild steel in the damaged web and the damaged web was already extensively cracked because of lateral bending, there were no additional mechanisms to prevent a lateral instability. It is therefore believed that the final failure occurred because the beam became laterally unstable. Note that the failure was not a compressive failure since the maximum measured compressive strain in top flange, measured over the undamaged web, was 0.0014—well below the crushing strain.

COMPARISON WITH PREVIOUS TESTS

Comparisons with the box beam tests of Shenoy and Frantz (*1*) show that the effect of losing tendons and cross section is severe. The beams tested by Shenoy and Frantz had no missing tendons or significant loss of cross section. These beams were ductile and had strengths that exceeded the predicted values. In contrast, the beam tested in this work was not ductile and showed values of strength that were lower than predicted.

When comparing this test with that of Olson (*2*), there are several similarities. As previously noted, comparisons of the failure loads of Olson's damaged and undamaged beam showed that the damaged beam failed at a much lower live load and that the reduction in live load capacity cannot be easily explained by loss of tendons. Similar results were obtained in this study. A comparison of the load/deflection for Olson's beams reveals that the damaged beam also was much less stiff in the postcracking region. Olson gives no data about lateral deflections. Finally, Olson noted that the damaged side of the beam had cracks that propagated back toward the supports and that the bottom flange on the damaged side of the beam appeared to "peel away" from the web. These were believed to be caused by tensile stresses from the lateral moments caused by the lack of symmetry. Olson reported a compressive failure of the beam, and the effect of any tensile stress generated by the asymmetric nature of the cross section on the I-girder is not clear from Olson's report.

CONCLUSIONS

1. A prestressed box beam that had lost 3 of 18 tendons to corrosion was tested to failure. For comparative purposes, a similar, undamaged beam was also tested. The deteriorated beam exhibited a slightly lower precracking stiffness when compared with the undamaged beam. The deteriorated beam also exhibited a lower cracking load. However, the lower precracking stiffness and lower cracking load in the deteriorated beam can be explained by accounting for loss of prestressing force, loss of cross section, and loss of tendons in the deteriorated beam.

2. The deteriorated beam showed significant lateral deflection under load. This lateral deflection was caused by the fact that the deterioration caused a lack of symmetry in the tendon pattern and concrete cross section. Before testing, the beam exhibited 13 mm (0.5 in.) of lateral deflection because of the asymmetry of the cross section. At failure, the beam had deflected an additional 28 mm (1.1 in.) in the lateral direction. This lateral deflection is believed to have significantly influenced the postcracking and failure behavior.

3. In the postcracking range the deteriorated beam was much less stiff than the undamaged beam. Some of this loss of stiffness is attributable to the loss of three tendons. However, the lateral moments caused by the lack of symmetry raised the tensile stresses in the damaged web. As a result, when the deteriorated beam was compared with the undamaged beam, it was found that the cracks

in the damaged web propagated further into the web. The cracks in the deteriorated beam were also spaced further apart because there was no prestressing steel in this area to distribute the cracking. Additional cracking also occurred because a corroded tendon had pulled out. The additional cracking caused by lateral bending and tendon pull-out contributed to the reduction in postcracking stiffness.

4. The undamaged beam held a total moment (applied load + beam weight) of 2720 kN-m (2005 kip-ft) and did not fail. The deteriorated beam failed suddenly at a total moment of 1805 kN-m (1310 kip-ft). The lower failure moment of the deteriorated beam is not totally attributable to the loss of tendons and cross-section area.

5. The ultimate moment for the deteriorated beam was 8 percent lower than that predicted by the AASHTO Code, showing that the AASHTO Code was not conservative for the deteriorated beam. Of more importance is that the deteriorated beam failed suddenly.

6. The final failure of the deteriorated beam was a sudden collapse of the beam. It is believed that the lateral bending contributed to this failure. At the time of failure, strain gauges on the prestressing steel showed that the steel had just reached yield. It is believed that as the steel yielded, the beam became laterally unstable and failed. Normally, box beams in bridges are tied together by transverse posttensioning. Because lateral deflection contributed significantly to the failure of the beam, this transverse posttensioning may help prevent premature failure of deteriorated box beams.

ACKNOWLEDGMENTS

This research was funded by ODOT and FHWA. The authors thank William Edwards, Vik Dalal, David Hanhilammi, Berkeley Hill, and Maher Girges, all from ODOT, for their support in this project. The authors also thank ESSROC Corp. of Melbourne, Kentucky, and Prestressed Services of Decatur, Indiana, for their assistance with this project.

REFERENCES

1. Shenoy, C., and G. Frantz. Structural Tests of 27-Year-Old Prestressed Concrete Bridge Beams. *PCI Journal*, Vol. 36, No. 5, Sept.–Oct., 1991, pp. 80–90.
2. Olson, S. A. *Impact Damage and Repair of AASHTO Type III Girders*. Ph.D. thesis, University of Minnesota, Minneapolis, April 1991.
3. *Standard Specifications for Highway Bridges*. AASHTO, Washington, D.C., 1989.

Publication of this paper sponsored by Committee on Dynamics and Field Testing of Bridges.

Field Study of Bridge Temperatures in Composite Bridges

HERODOTOS A. PENTAS, R. RICHARD AVENT, VIJAYA K. A. GOPU, AND KEITH J. REBELLO

An experimental and analytical investigation was conducted to obtain thermally induced movements and bridge temperatures of a newly constructed bridge in central Louisiana. The instrumentation, field monitoring, and temperature data analysis are described. On the basis of a measured distribution of temperatures through the depth of the bridge sections, a model to predict this distribution was developed. The model is accurate and easy to use and can be easily adopted and applied as thermal loading in finite element programs predicting thermal movements and stresses in bridges.

Highway bridges generally require expansion joints between sections of the deck or between the deck and the approach roadway. The current practice for the design of expansion joints for Louisiana highway bridges (*1*) is based on elementary strength of materials formulas, and these may not accurately predict actual joint movements in modern bridges. Therefore an experimental research project was conducted on an actual bridge in central Louisiana to obtain longitudinal movements and bridge temperatures. The purpose of this paper is to describe the instrumentation, field monitoring, and data analysis as related to bridge temperatures. A detailed description of instrumentation and presentation of results pertaining to longitudinal movements appears elsewhere (*2*).

RELATED STUDIES

Reynolds and Emanuel (*3*) have written a concise summary of relevant research conducted in this area between 1957 and 1970. They concluded that relating environmental conditions to bridge movements is extremely complex. Mortlock (*4*) investigated various types of instruments used to obtain bridge movements and temperatures. He considered measuring devices that could be left at a bridge site for continuous field monitoring and concluded that the following should be used: (*a*) thermocouples placed in the slab during construction to obtain the variation of temperature through the slab depth, (*b*) linear variable differential transformers (LVDTs) mounted across the expansion joint to measure the joint movements, and (*c*) a Kipp solarimeter to measure the solar radiation of the slab. Combinations of these measuring devices were placed at seven bridge sites in England and Wales. The data obtained were compiled and analyzed by Emerson (*5*). A major conclusion was that the instrumentation had functioned satisfactorily. From the gathered data, a coefficient of thermal expansion for each bridge was developed. It was finally concluded that, with certain limitations, it is possible to estimate the extreme range of movements likely to occur during the life of a bridge if the shade temperatures are known. Dillon and Kissane (*6*) summarized the movements of prestressed concrete girders located throughout New York State over a 2-year period. This information was compared with that from climatic records, and it was concluded that the actual temperature ranges were greater than the design ranges; however, the average annual end movement was not significantly different from design values. Emerson (*7*) describes a method for determining the effective temperatures in composite bridges when shade temperatures and bridge movements are known. The method was applied on two bridges in England. Thermocouple wires were used to measure the temperature in the bridge slab and the ambient temperature. The method of prediction was based on these measurements, and the results were reasonably accurate. Abdul-Ahad (*8*) developed a theoretical method of calculating thermally induced stresses and movements in continuous bridge structures. The experimental monitoring was done on a composite box girder bridge. The bridge was 2,700 ft long with 29 spans and no expansion joints except at the abutments. The experimental and analytical results were close; however, the experimental data were limited and no generalized conclusions could be drawn.

OBJECTIVES AND SCOPE

The purpose of this paper is to describe the experimental procedures and associated instrumentation and to discuss the general behavioral characteristics of a specific bridge as related to thermal gradients. Reported here are the results of a systematic study of bridge temperatures and temperature distributions. An upcoming paper will address the thermal joint movements. The study was focused on a newly constructed bridge on US-190 over the Atchafalaya River at Krotz Springs, Louisiana. The bridge was instrumented using LVDTs, thermocouples, and optical devices. The objective was to study the thermal characteristics and temperature distribution through the depth of bridge sections.

BRIDGE DESCRIPTION

The bridge to be investigated is the east approach of US-190 over the Atchafalaya River at Krotz Springs, Louisiana. It consists of cast-in-place concrete slabs acting compositely with either Type IV AASHTO prestressed concrete girders or steel plate girders. This superstructure is supported by twelve bents, as shown in Figure 1. The abutment is labeled Bent 1 and the rest of the bents are numbered in ascending order from east to west. Five expansion joints are provided to allow for bridge movements. These joints are num-

H. A. Pentas, Dames & Moore, Inc., Baton Rouge, La. 70809. R. R. Avent and V. K. A. Gopu, Department of Civil Engineering, Louisiana State University, Baton Rouge, La. 70803. K. J. Rebello, Gulf Engineers and Consultants, Inc., Baton Rouge, La. 70809.

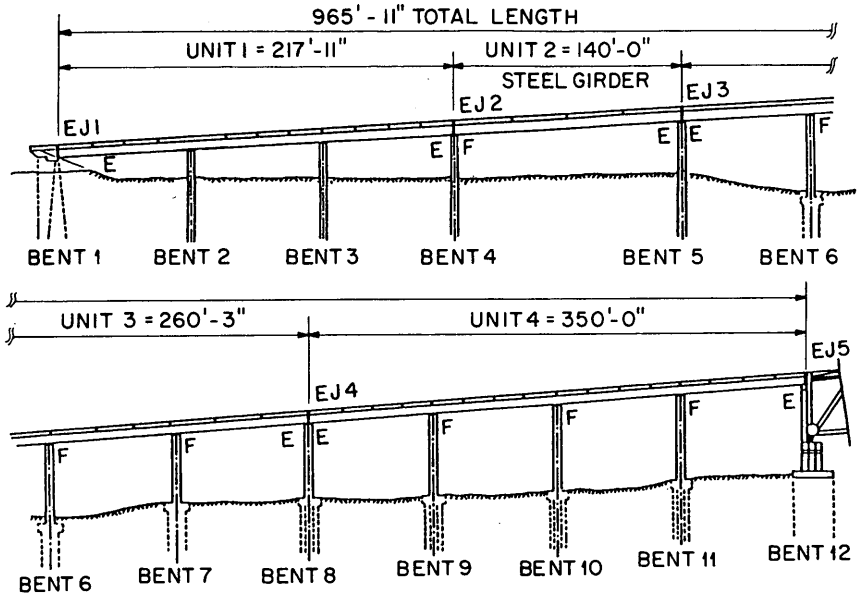

FIGURE 1 North elevation of the east approach of the U.S. 190 bridge at Krotz Springs, Louisiana.

bered 1 through 5 in consecutive order from east to west as well. Joints 1 through 4 are membrane seals, whereas Joint 5 is a toothed type. The bridge continues over the river as a steel through truss.

Unit 2 is the longest single span of the approach at 140 ft. It consists of a cast-in-place slab 8½ in. thick acting compositely with four steel plate girders 72 in. deep. The other three sections of the approach (Units 1, 3, and 4) consist of a slab 7½ in. thick acting compositely with five Type IV AASHTO prestressed concrete girders.

The supporting Bents 2 through 5 consist of concrete caps poured at the top of precast concrete piles 30 in.[2]. Bents 2 and 3 each have four precast concrete piles supporting a level cap. Bents 4 and 5 each have five piles supporting the cap. The cap is stepped to allow the top of the steel girders to match flush at the same level as the top of the concrete girders. The supporting Bents 6 through 11 consist of level concrete caps poured at the top of two cast-in-place concrete columns 54 in. in diameter. Bent 12 consists of two cast-in-place concrete columns 30 in. in diameter anchored to a bridge pier. This pier also supports the end rocker bearings of the river crossing truss. The ends of the girders at the expansion joints and at continuous joints over the bents were placed on neoprene bearing pads of the standard type used in Louisiana.

At continuous joints, the girders were connected to the bent cap by imbedding a dowel into the cap extending into the continuous joint. At some expansion joint locations, the girders were pinned to the bent cap. The connection consists of a steel angle-shaped bracket bolted to both the girder and the cap. The bolt holes do not allow for any longitudinal movement between the cap and the girders. At some expansion joint locations, the girders were allowed to slide on the cap. This roller type of connection consists of a steel angle-shaped bracket with slotted holes, which allows for movement. The location of each type of joint connection is shown in Figure 1. Pinned joint connections are denoted by the letter F, whereas joints allowed to move are denoted by the letter E. Additional information and bridge design details appear elsewhere (*2*). The bridge was already under construction at the beginning of this research project (October 1986). The supporting bents had been erected and the girders were already in place. It was during that period of construction that the first instrumentation was installed. At that time the decks were also constructed. On October 27, 1988, construction was completed and the bridge was opened to traffic.

INSTRUMENTATION

LVDTs were chosen to obtain the joint movements. A theodolite was chosen to obtain the bent sway, and thermocouples were used to obtain all temperature measurements. The LVDTs and thermocouples were wired to the monitoring station where they would be connected to a Hewlett Packard microcomputer and data acquisition system. The computer would store the readings for later processing. Electrical power for the system was supplied through a portable generator.

Thermocouple wires type PP20TX were used to measure the temperatures of the Krotz Springs bridge; three advantages made them the choice for this investigation. The thermocouples were placed along the depth of the section to detect the temperature variation. Each array consisted of six thermocouples located on both slab and girder. The location of these arrays is shown in Figure 2. The slab thermocouples were placed near the top, center, and bottom of the slab at the time of pouring. The girder thermocouples were placed at a later time. These were bonded on the outer surface of the concrete girders using epoxy and a layer of hydraulic cement to ensure a more consistent thermal conductivity. Two additional thermocouples were placed hanging under the slab to record the ambient temperature. All thermocouples were run under the bridge to the data acquisition system of the microcomputer at the monitoring station.

LONG-TERM THERMAL BEHAVIOR

The mechanism of bridge joint movements is very complex. The strains that influence joint movements are caused by a variety of factors, including thermal changes, time-dependent creep and

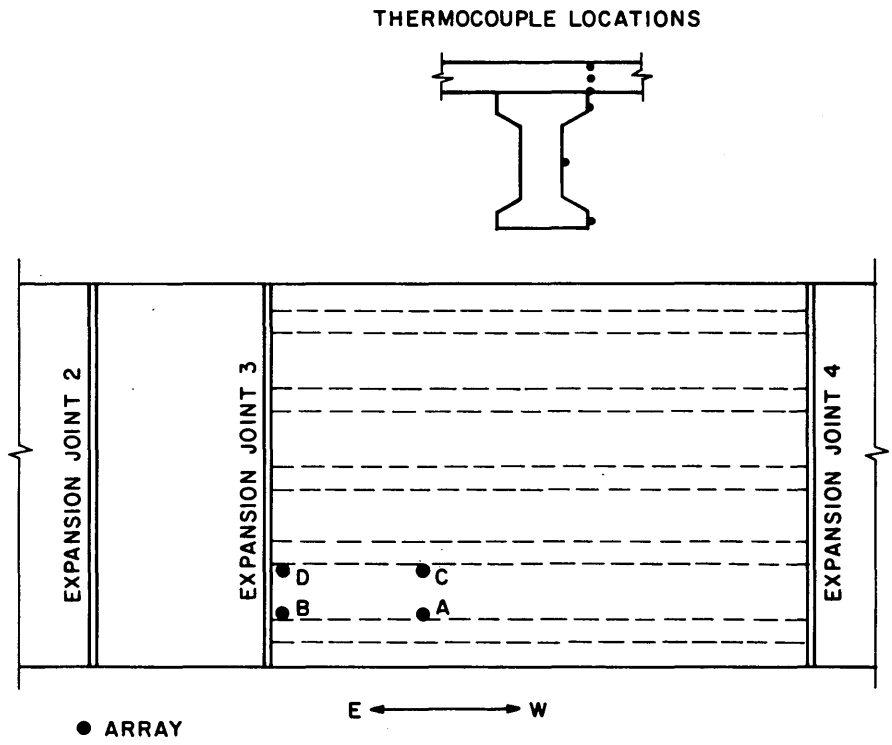

FIGURE 2 Plan view of bridge showing location of thermocouple arrays.

shrinkage, loss of prestress, and applied live loads. Furthermore the movements caused by thermal changes are greatly affected by the profile of temperature distribution through the depth of the cross section. A change in temperature, which varies linearly over the cross section of a simply supported bridge, produces no stresses. However, when the temperature variation is nonlinear, the same bridge will be subjected to stresses, because any fiber, being attached to other fibers, cannot exhibit free temperature expansion. These thermal stresses in the cross section are referred to as the self-equilibrating stresses. When the temperature variation is nonlinear, the strain distribution over the cross section hypothetically would be nonlinear, but because plane cross sections tend to remain plane, the actual strain distribution is linear. (*9,10*) The difference between the hypothetical and actual strain curves represents expansion or contraction, which is restrained by the self-equilibrating stresses.

The bridge was monitored over an approximate 2-year period. It was not practical to provide continuous monitoring over such an extended time. Instead, the bridge was monitored once per month continuously for a 24- or 12-hr period. The monitoring time was alternated between 12 and 24 hr on a month-to-month basis. The results of these intermitent cycles of monitoring are summarized in Figures 3 and 4. Actual temperature measurements were taken at the top, center, and bottom of both the slab and concrete girder, respectively. The results were a relatively narrow band of temperature variations for slab and girder, respectively, with the band of girder temperatures generally a step lower than the slab temperatures during the heat of the day but similar during the nighttime hours. The plots in Figures 3 and 4 are limited to the band width of slab and girder temperatures. Also shown is the variation of ambient temperature during the same periods. Figure 3*a* and *b* shows the temperatures recorded at Locations A and B, whereas Figure 4*a* and *b* gives the temperatures recorded at Locations C and D. The bottom slab thermocouple at Location C did not function properly, however, and readings recorded by it were discarded.

It can be seen from Figures 3*a* and *b* and 4*a* and *b* that there is a small variation between the temperatures recorded at Locations A, B, C, and D. For example, on the coldest day, December 16, 1987, the highest slab temperatures recorded at Locations A, B, C, and D were 57°F, 53°F, 57°F, and 55°F, respectively. Similarly for the hottest day, May 16, 1988, the highest slab temperatures recorded at Locations A, B, C, and D were 113°F, 108°F, 113°F, and 110°F, respectively. It can also be seen from the figures that, with the exception of January 12, 1988, and January 5, 1989, the slab temperatures rose higher than the girder temperatures during the heat of the day, with the ambient temperature falling somewhere in between. Again this is because the slab was exposed to the sun and solar radiation while the girders were in the shade. The largest differential between slab and girder temperatures was about 20°F and occurred during the hottest monitoring days of April 15, May 16, June 10, and August 25, 1988. A large temperature differential through the depth of the bridge section as well as a large maximum and minimum temperature differential was of particular significance for future studies of expansion joint movements in bridges of this type.

To better illustrate the long-term temperature trends of the composite system, the maximum and minimum values of the average slab and girder temperatures as well as ambient temperatures are plotted in Figure 5. Only the values from the 24-hr continuous monitoring periods are shown with lines connecting points for clarity in reading the trends. Because this bridge is located in a temperate climate (only 1 day with below-freezing temperatures), the trends reflected here do not necessarily apply to colder climate conditions.

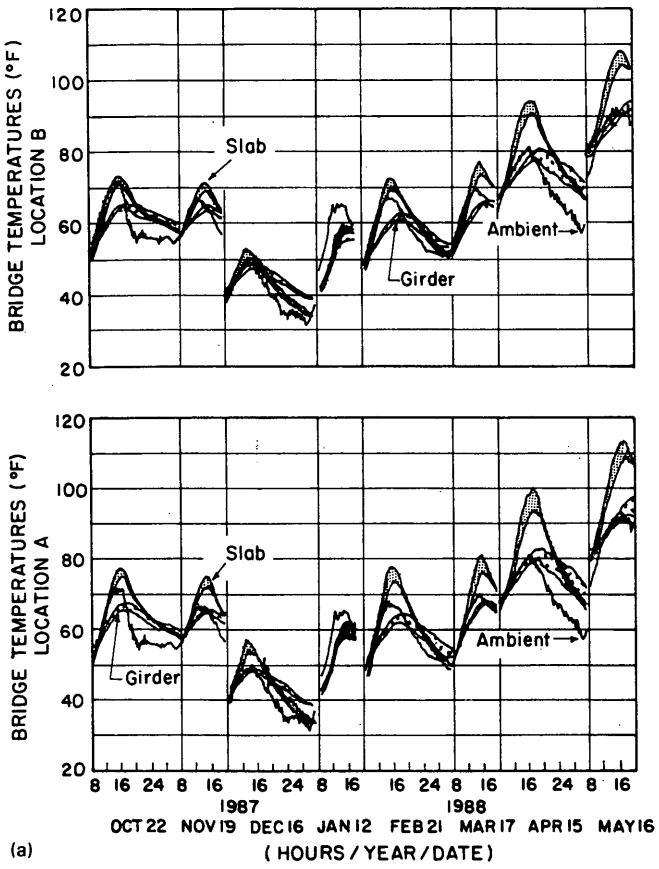

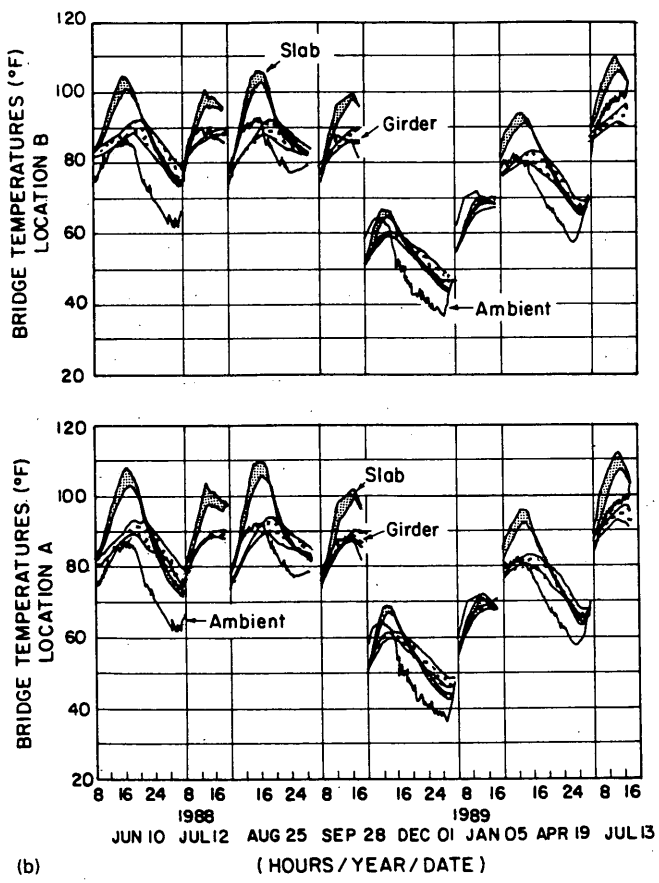

FIGURE 3 Bridge temperatures obtained from thermocouples at locations A and B.

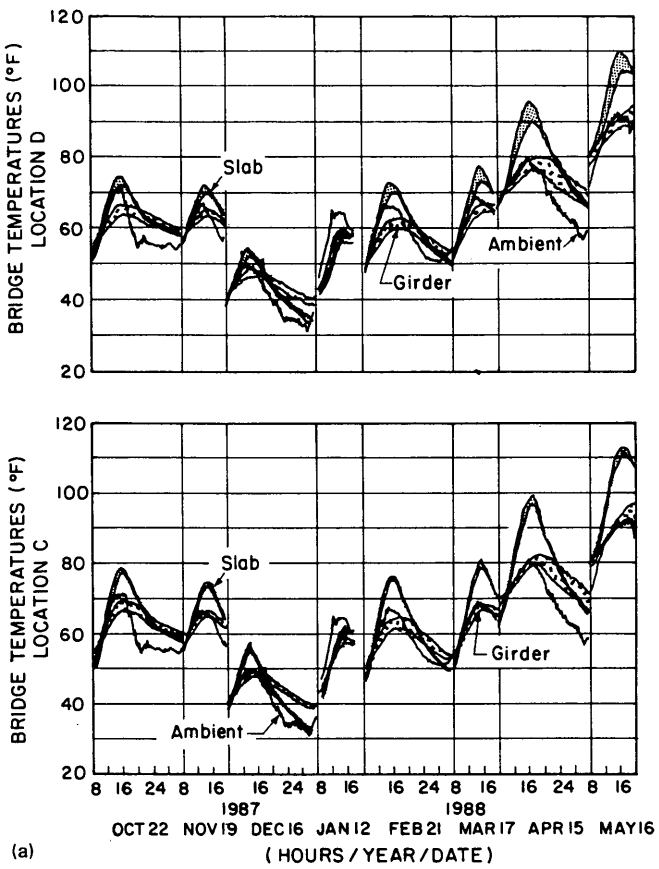

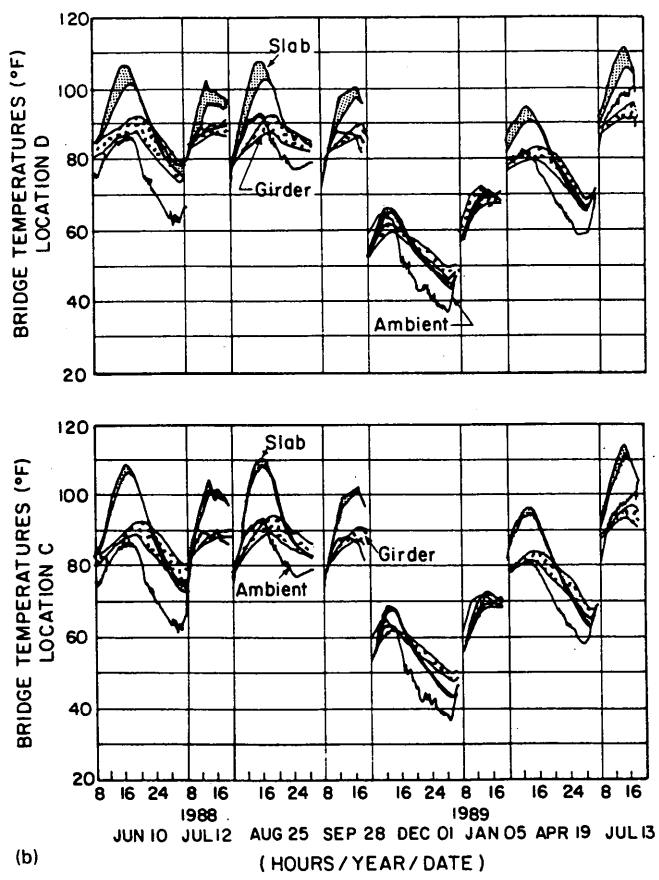

FIGURE 4 Bridge temperatures obtained from thermocouples at locations C and D.

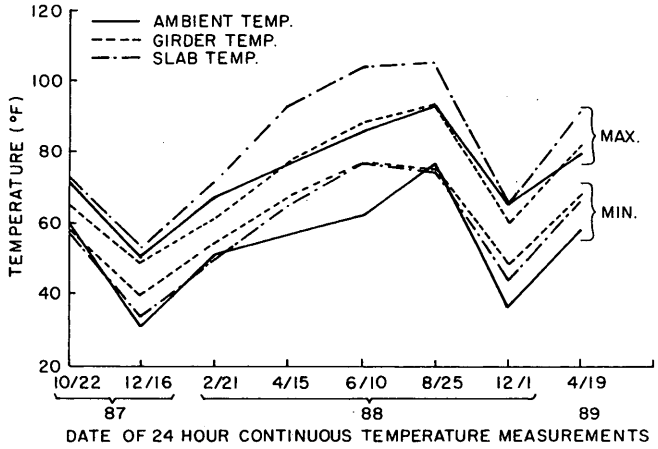

FIGURE 5 Seasonal variation in extreme temperatures for slab, girder, and ambient (slab and girder temperatures are average values).

The maximum average temperature in the girders closely followed the maximum ambient temperature (although with a phase shift as seen in Figures 3 and 4). However, usually the minimum average temperature of the girders was somewhat higher than the minimum ambient temperature. Thus the girders often did not reach temperature equilibrium with the ambient before reheating with the next day's temperature rise.

For the slab the same trends occurred except when the maximum ambient temperature began to exceed 70°F. At these higher temperatures, the solar radiation effect serves to magnify the slab temperatures in a somewhat linear manner. For example, a linear least-squares curve fit (slightly rounded to whole numbers) relating maximum average temperature in the slab, T_s, to maximum ambient temperature, T_a, is

$$T_s = T_a \quad \text{For } T_a \leq 70$$

$$T_s = 2T_a - 70 \quad \text{For } T_a > 70 \qquad (1)$$

TEMPERATURE VARIATIONS THROUGH DEPTH

The data obtained during the 24-h monitoring days were used to further study the temperature distribution. For these days, the temperature distribution through the depth of the bridge section is plotted at 4-hr intervals starting at 8:00 a.m., as indicated in Figures 6 through 9. The dashed line indicated in the upper left plot of each figure represents the temperature distribution at the end of the 24-hr cycle or 8:00 a.m. the next day. The ambient temperature is also given in each plot for relative comparison. Figures 6 through 9 indicate that the thermal profiles follow a certain path over time. In particular, the slab temperatures generally are lower than, or close to, the girder temperatures during the morning hours, then rise higher than the girder temperatures, reaching their peak values around 4:00 p.m. Finally, during the evening hours the slab and girder temperatures converge again while falling to their lowest values over night.

Thermal stresses are known to cause considerable damage in bridges. Although current bridge specifications such as those of

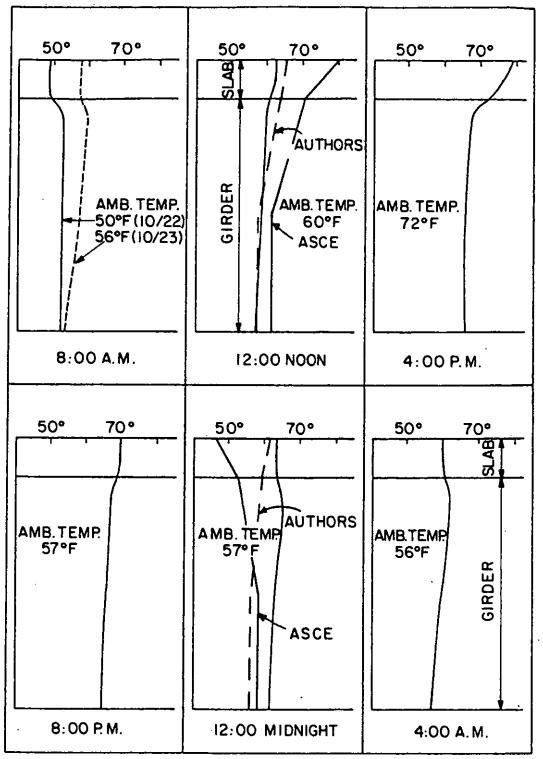

FIGURE 6 Temperature distribution through the depth of the section for October 22, 1987.

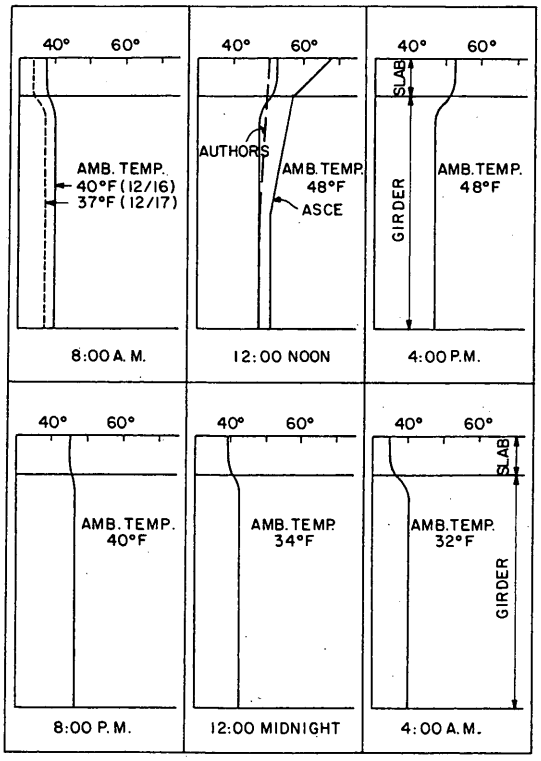

FIGURE 7 Temperature distribution through the depth of the section for December 16, 1987.

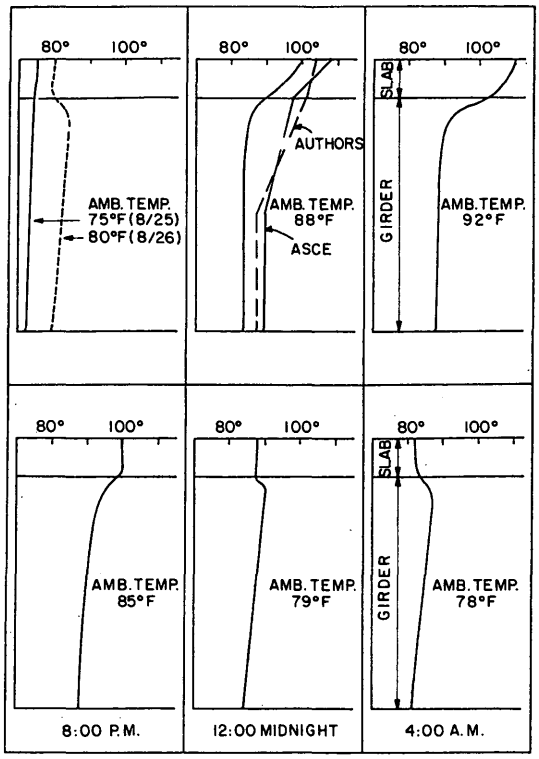

FIGURE 8 Temperature distribution through the depth of the section for August 25, 1988.

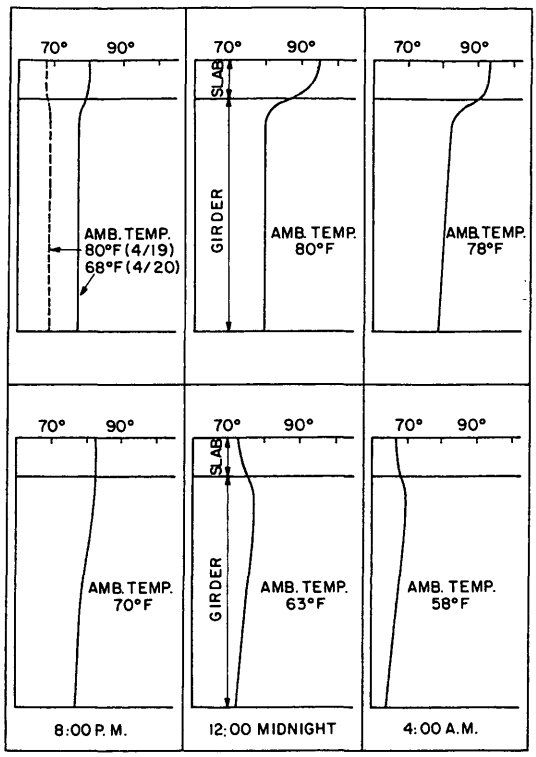

FIGURE 9 Temperature distribution through the depth of the section for April 19, 1989.

AASHTO (*11*) recognize the existence of thermal expansion and thermal forces, they are vague about values. In particular AASHTO recommends a range of temperature variation in bridges to account for the expansion movements; however, it does not provide guidelines about the vertical temperature distribution through the depth of the section. Several analytical and experimental studies have been conducted in relation to the vertical temperature distribution through the section depth of concrete and composite concrete slab-on-steel beam bridges. (*12–15*) Although many complex factors, such as solar radiation, ambient temperature, wind velocity, conductivity, and evaporation come into play, many researchers tried to obtain a simple but reasonable method of predicting the temperature distribution of bridge sections. The work of Imbsen et al. (*13*) has been incorporated into the AASHTO Guide Specifications. However, the approach was to develop maximum temperature differentials to be expected for a bridge at a given location. No relationship was developed that relates the slab/girder temperatures to the ambient temperature. Therefore a direct comparison cannot be made between the model developed here and Imbsen's work. However, a comparison can be made with another widely recognized model. The Committee on Loads and Forces on Bridges, ASCE, (*16*) recommends as thermal loading a temperature distribution through the depth of the section on the basis of the ambient temperature variation. The temperature distribution is recommended as a positive thermal loading for concrete bridges. The temperature at the top and bottom of the deck is found by adding 20°F and 10°F, respectively, to the ambient temperature and is assumed to vary linearly in between. The bridge temperature is assumed to vary linearly from the bottom of the deck to the middle of the girder where the bridge temperature is taken equal to the ambient temperature. The temperature from midgirder to the bottom of the girder is also taken equal to the ambient temperature. Similarly, ASCE provides a negative thermal loading for dropping temperatures. In this profile, the temperature at the top and bottom of the slab is found by subtracting 10°F and 5°F, respectively, from the ambient temperature.

On the basis of the experimental data a modified profile is developed by the author that is both accurate and easy to use. Polynomials of various degrees were used to curve fit the temperature data obtained from the thermocouples. On the basis of the calculated sum of the squares of the residual, a second-order polynomial is deemed to be both accurate and simple. A different curve fit is used to predict the bridge temperatures at the top of Deck T_1, the bottom of Deck T_2, and the middle and bottom girder Temperature T_3. These curve fits are indicated in Figure 10. The horizontal axis of the figure represents the ambient temperature T_a, whereas the vertical axis represents the bridge temperatures T_1, T_2, and T_3. The approach used to analyze these data was to first select a series of ambient temperatures over the range of 30°F to 90°F degrees (14 were used). Then the eight 24-hr continuous monitoring periods (Figures 3 and 4) were used to select all slab temperatures associated with each of the selected ambient temperatures. The number of data points associated with each slab temperature typically ranged between 5 and 10 per selected ambient temperature location. These data points were grouped and averaged for illustrative purposes. Each data point shown in Figure 10 represents this averaging process. The least-squares curve fit was thus based on all points and corresponds to approximately 75 data points per curve. Once T_1, T_2,

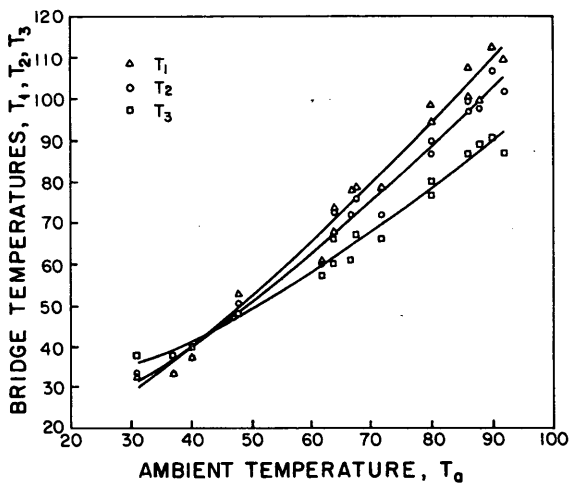

FIGURE 10 Bridge temperatures as a function of ambient temperature.

and T_3 are found the thermal profile is obtained by assuming a linear temperature variation between T_1, T_2, and T_3. The values of T_1, T_2, and T_3 can also be calculated from the following equations:

$$T_1 = 0.095 + 0.832\,T_a + 0.004\,T_a^2 \quad (2)$$

$$T_2 = 6.63 + 0.648\,T_a + 0.005\,T_a^2 \quad (3)$$

$$T_3 = 23.88 + 0.206\,T_a + 0.006\,T_a^2 \quad (4)$$

The model was developed on a bridge constructed of concrete slab on Type IV AASHTO girders, which is a common type of construction in Louisiana and elsewhere. It should be applicable also to concrete bridges of similar construction using Types II and III AASHTO girders. The developed thermal profile is compared with the experimental measurements and the ASCE profile on 3 typical days in various seasons, as shown on Figures 6 through 8. Figures 6 and 7 (October 22, 1987, and December 16, 1987) indicate that when the ambient temperatures are low the author's experimental and analytical results agree very well, whereas ASCE'S profile differs in the range of 30 to 40 percent in the slab. On August 25, 1988, however, when the ambient temperatures were high, both the authors' and ASCE'S profiles overestimated bridge temperatures by approximately the same amount of 5 to 10 percent.

The temperature distribution predicted by the model is also compared to the experimental measurements obtained at the Boone River Bridge (*17*). Figure 11 shows the temperature distribution through the depth at the time of the highest temperature as well as the author's distribution corresponding to the recorded ambient temperature of 103°F. The figure shows that the author's model overestimated bridge temperatures by approximately 10 percent at the top of the slab and 20 percent at the bottom of the girders. The large difference at the girder bottom is because at the Boone bridge the girder thermocouples were placed at the center of the girder and during a hot day when the temperature was rising quickly there is a time lag between girder center and surface temperatures. In addition, the model's accuracy decreases at high ambient temperatures because it was developed using data corresponding to ambient temperatures of up to 92°F.

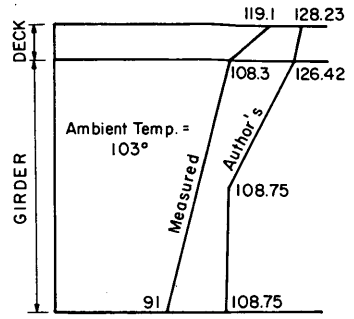

FIGURE 11 Comparison of author's temperature distribution model with Boone River Bridge measurements.

CONCLUSIONS

A composite concrete deck-girder bridge (typical of the type constructed in the southeast and much of the United States) was experimentally studied to determine thermal distributions in both deck and girders. Periodic observations over a 2-year period were used to evaluate long-term trends. Each observation was conducted continuously for 12 or 24 hr to also evaluate short-term behavior. The following conclusions and observations are of some significance.

1. For the 8½-in. concrete deck, the temperature variations through the thickness were relatively small, rarely exceeding 8°F and usually less than 5°F.
2. Temperature variations through the depth of the 72-in. prestressed concrete girders were also relatively small and seldom exceeded 10°F.
3. On the basis of the average temperature values in both the slab and girder, long-term trends indicated that (*a*) girder temperatures closely follow the maximum ambient temperature over the range of 50°F of 95°F (with a phase shift), (*b*) for the same temperature the minimum girder temperatures often remain 5°F to 10°F higher than the lowest ambient temperatures, and (*c*) slab temperatures follow the same trend as girders except when the maximum ambient temperature exceeds 70°F, in which case solar radiation magnifies the slab temperature in a somewhat linear manner.
4. The distribution of temperatures through the depth of the slab and girders varied significantly. On the basis of the measured distribution of temperatures through the depth of the bridge sections, a model to predict this distribution was developed. The model relates the temperatures at the top and bottom of the slab as well as the girder temperatures to ambient temperatures.
5. The developed model provides a good description of thermal profiles through the depth of the slab and girder. For the low ambient temperature range, the values obtained from the model are almost identical to the actual temperature measurements and are more accurate than those of the ASCE profile. For the high temperature range, the model varies only 5 to 10 percent and is similar to that of the ASCE profile. The use of such a model in a finite element program that predicts thermal movements and stresses in bridges should give more realistic results and significantly aid the design of bridge expansion devices.
6. The developed model is applicable to both positive and negative temperature distributions (rising or falling temperatures) and

can be easily adopted and used as thermal loading in finite element programs.

REFERENCES

1. *Bridge Design Manual*, 3rd ed. Louisiana Department of Transportation and Development, Baton Rouge, 1987.
2. Pentas, H. A. *Experimental Investigation of the Longitudinal Movements Associated with Highway Bridge Joints*. Ph.D. dissertation. Louisiana State University, Baton Rouge, 1990.
3. Reynolds, J. C., and J. H. Emanuel. *Thermal Stresses and Movements in Bridges*. ASCE *Journal of Structural Division*, Vol. 100, No. 1, 1974, pp. 63–78.
4. Mortlock, J. D. *The Instrumentation of Bridges for the Measurement of Temperature and Movement*. TRRL Laboratory Report 641. U.K. Transport and Road Reasearch Laboratory, Crowthorne, Berkshire, England, 1974.
5. Emerson, M. *Thermal Movements of Concrete Bridges: Field Measurements and Methods of Prediction*. Joint Sealing and Bearing Systems for Concrete Structures. ACI Special Publication SP-70, Vol. 1, Detroit, 1971, pp. 77–102.
6. Dillon, E. W., and R. J. Kissane. *Annual End Movements of Prestressed Concrete Bridges*. Final Report. U.S. Department of Transportation, FHWA, New York, 1978.
7. Emerson, M. Bridge Temperatures for Setting Bearing and Expansion Joints. TRRL Supplementary Report 479. U.K. Transport and Research Laboratory, Crowthorne, Berkshire, England, 1979.
8. Abdul-Ahad, R. B. *Effects of Restrained Thermal Movement in a Continuous, Prestressd Concrete Bridge Without Interior Expansion Joints*. Ph.D dissertation. University of Tenessee, Nashville, 1981.
9. Ghali, A., and R. Favre. *Concrete Structures: Stresses and Deformations*. Chapman and Hall, New York, 1986.
10. Will, K. M., C. P. Johnson, and H. Matlock. *Analytical and Experimental Investigation of the Thermal Response of Highway Bridges*. Report 23-2. Center for Highway Research, The University of Texas at Austin, 1977.
11. *Standard Specifications for Highway Bridges*, 13th ed. AASHTO, Washington, D.C., 1983 (with interim specifications, 1984, 1985, 1987–1988).
12. Kennedy, J. B., and M. H. Soliman. Temperature Distribution in Composite Bridges. ASCE *Journal of Structural Engineering*, Vol. 113, No. 3, 1987, pp. 475–482.
13. Imbsen, R. A., D. E. Vandershaf, R. A. Schamber, and R. V. Nutt, *NCHRP Report 276: Thermal Effects in Concrete Bridge Superstructures*. TRB, National Research Council, Washington, D.C., 1985.
14. Churchward, A., and Y. J. Sokal, Prediction of Temperatures in Concrete Bridges. ASCE *Journal of Structural Engineering*, Vol. 107, No. 11, 1981, pp. 2163–2176.
15. Zuk, W. Thermal Behavior of Composite Bridges—Insulated and Uninsulated. In *Highway Research Record 76*, HRB, National Research Council, 1965, pp. 231–253.
16. Committee on Loads and Forces on Bridges. Recommended Design Loads for Bridges. ASCE *Journal of Structural Engineering*, Vol. 107, No. 7, 1981, pp. 1161–1213.
17. Girton, D. D., T. R. Hawkinson, and L. F. Greimann. Validation of Design Recommendations for Integral-Abutment piles. ASCE *Journal of Structural Engineering*, Vol. 117, No. 7, 1991, pp. 2117–2134.

Publication of this paper sponsored by Committee on Dynamics and Field Testing of Bridges.

Evaluation of Bridges Constructed in Chromite Ore Processing Residue

RANDALL W. POSTON, A. RHETT WHITLOCK, CHRISTOPHER L. GALITZ, AND KEITH E. KESNER

A field investigation was conducted to assess the structural and durability implications of bridges constructed in chromite ore processing residue (COPR) fill. The findings are based on visual inspection and various testing of 31 bridges, located in known chromium and nonchromium sites in and around Hudson County, New Jersey. Various types of observed deterioration of the concrete bridge substructures are documented for each of the study bridges. Of the 31 bridges, approximately half (15) of the bridges underwent more extensive nondestructive testing, including determination of chloride ion content and pH, determination of the presence of alkali-silica reactivity, impact-echo for assessment of integrity, and measurement of half-cell corrosion potentials where exposed reinforcement was available to document the causes of observed deterioration. On the basis of the study results, it is concluded that observed deterioration of the bridges is a result of classical causes, such as chloride-induced corrosion and alkali-silica reactivity and clearly not a result of exposure to COPR.

From the turn of the century until the early 1970s, several industrial concerns in and around Hudson County, New Jersey, operated chromite ore processing facilities. A by-product of the kiln firing of chromite ore was a soil-like material similar in appearance and properties to a brown sandy silt soil with pebble-sized particles but with a lower density than soil. Because of its similarity to soil, this by-product material, commonly referred to as "slag" or "mud," was used by builders and public agencies as a fill material for reclamation of swamp lands known locally as the meadowlands (*1*).

Chromium, like other metals, may exist in several physicochemical states. Trivalent chromium [Cr(III)] is a naturally occurring stable form of chromium. Hexavalent chromium [Cr(VI)], less stable, generally is not naturally occurring but is produced by industrial processes. Total chromium refers to the total amount of chromium in all valent forms including Cr(III) and Cr(VI). A particular site has been informally deemed to be a chromium site in New Jersey if the Cr(VI) concentration in soil is 10 ppm or greater or the total Cr concentration is in excess of 500 ppm, or both.

In 1984, the U.S. Environmental Protection Agency classified Cr(VI) as a respiratory carcinogen to humans. Hexavalent chromium has been found at various sites in the Hudson County area where chromite ore processing residue (COPR) has been used as fill. More recently, the New Jersey Department of Environmental Protection and Energy and the New Jersey Turnpike Authority have alleged that COPR causes structural deterioration of roadways, bridges, and other structures in contact with COPR (*2*). Even though no specific mechanisms have been identified for deterioration of highway structures as a result of chromium exposure, the postulated mechanism apparently is related to crystallization of chromium salts.

KCI Technologies, Inc., 8832 Rixlew Lane, Manassas, Va. 22110.

This paper reports the results of a research study that was conducted to obtain data related to performance of bridges in Hudson County, New Jersey. This included a literature search to identify previous research and knowledge of any deleterious effects of chromium on construction materials and structural behavior. To assess the possible deleterious structural and durability implications of COPR fill on bridge structures in Hudson County, New Jersey, a comparative evaluation of bridges constructed both within and outside of chromium sites was conducted. The comparative evaluation was based on visual inspection of selected bridges augmented by nondestructive testing of bridge substructure components that included determination of chloride ion content and pH, determination of the presence of alkali-silica reactivity, and measurement of half-cell corrosion potentials. In addition, impact-echo testing was conducted to assess the overall structural integrity of selected bridge piers.

PROJECT DESCRIPTION

The study bridges were of two principal types of structural systems. Most bridge superstructures were conventional multigirder, steel or concrete, with a composite reinforced concrete deck supported on concrete pier bents. The other major superstructure system was steel truss with a concrete deck supported by steel stringers. The truss bridges were also supported on concrete pier columns or bents.

The exposure of the pier bents of the study bridges varied, depending on the site, from relatively dry fill and groundwater at depth to more brackish groundwater for those bridges in low-lying marsh areas. In all cases, the study bridge decks have likely been subjected to chemical deicers as evidenced by staining at expansion joints and drains.

FIELD INVESTIGATION

Initially, a reconnaissance of bridges located on and over major highways in Hudson County and surrounding areas was conducted. This was done to identify potential sites to be included in the overall survey. On the basis of this reconnaissance, 31 bridges, representing a broad range of structural systems and ages, were selected for study in the overall evaluation. The bridges generally were 40 plus years of age, as determined from date markers at the site and historical factors, such as bridge type and on which highway they were located. Table 1 summarizes the 31 bridges included in the overall evaluation and their general location in the northern New Jersey area.

TABLE 1 Summary of Bridges Included in Study

Bridge	Location	Description	Approx. Age
1	Western NJTP near Exit 18W	Welded plate girders with concrete pier cap and 2 column pier bents	40
2	Eastern NJTP near Exit 17	Welded plate girders with concrete pier cap and 2 column pier bents	40
3	Western NJTP near Rt. 506	Welded plate girders with concrete pier cap and 4 column pier bents	40
4	Eastern NJTP near Rt. 508	Riveted plate girders with concrete pier caps and 2 column pier bents	50
5	Eastern NJTP near Rt. 506	Riveted plate girders with concrete pier caps and 2 column pier bents	50
6	Eastern NJTP near Hackensack River	Riveted plate girders with concrete piers and 2 column pier bents	50
7	Eastern NJTP	Riveted plate girders with hammerhead wall piers	50
8	Pulaski Skyway	Steel arch bridge with diagonally braced concrete, 2 column piers	60
9	Pulaski Skyway	Steel arch bridge with diagonally braced concrete, 2 column piers	60
10	Pulaski Skyway	Steel arch bridge with diagonally braced concrete, 2 column piers	60
11	Pulaski Skyway	Steel arch bridge with 4 column piers	60
12	Pulaski Skyway	Steel arch bridge with 2 column piers	60
13	Pulaski Skyway	Steel arch bridge with concrete wall piers	60
14	Pulaski Skyway Viaduct	Concrete arch bridge with 4 column piers	60
15	NJTP Hudson County Extension	Welded plate girders with 2 column hammerhead piers	40
16	NJTP Hudson County Extension	Welded plate girders with 2 column hammerhead piers	40
17	NJTP Hudson County Extension	Welded plate girders with steel pier caps and 2 column pier bents	40
18	NJTP Hudson County Extension	Riveted plate girders with steel pier caps and 3 column pier bents	50
19	NJTP Hudson County Extension	Welded plate girders with concrete pier caps and 2 column pier bents	40
20	NJTP Hudson County Extension	Rolled steel girders with concrete hammerhead wall piers	40
21	NJTP Hudson County Extension	Riveted plate girders with concrete hammerhead wall pier	50
22	NJTP Hudson County Extension	Welded plate girders with 2 column hammerhead pier	40
23	NJTP Hudson County Extension	Riveted plate girders with concrete pier cap and 2 column pier bents	50
24	NJTP Hudson County Extension	Riveted plate girders with concrete pier cap and 2 column pier bents	50
25	NJTP near Exit 12	Welded plate girder with concrete pier cap and 2 column pier bents	40
26	NJTP near Exit 11	Welded plate girder with concrete hammerhead pier	40
27	Garden State Parkway near Exit 137	Riveted plate girders with concrete wall piers	50
28	NJTP Hudson County Extension	Riveted plate girders with concrete pier cap and 2 column pier bents	50
29	NJTP Hudson County Extension	Riveted plate girder with steel pier cap and 3 column piers	50
30	NJTP Hudson County Extension	Welded plate girder with concrete pier cap and 2 column pier bents	40
31	Western NJTP near Hackensack River	Welded plate girder with concrete pier cap and 2 column pier bents	40

For each of the 31 bridges included in the study, a limited visual condition survey was conducted from the underside of the bridge, with particular emphasis on the condition of the supporting pier substructures in direct contact with the soil. Various forms and signs of distress and deterioration, such as cracking, efflorescence, presence of corrosion products, delamination, spalling, and freeze-thaw damage were documented and recorded for each bridge.

After completing the initial limited condition evaluation of the 31 selected bridges, 15 bridges (approximately half the total) were selected for more in-depth evaluation and nondestructive testing. The testing of these 15 sites was conducted to assess the general integrity of the supporting piers at selected locations and to determine the probable cause of visible distress and deterioration. Nondestructive testing is testing that does not require any significant invasive probing or sampling of structural materials. At each site, soil samples were collected at approximately 0.3 m below grade adjacent to selected bridge piers. These soil samples were tested for total and hexavalent chromium concentrations, chlorides, sulfates, pH, and the percentage of solids in the soil. On the basis of prevailing health-based guidance levels of 10 ppm Cr(VI) and 500 ppm total Cr, 7 of these 15 bridge sites would be classified as chromium sites.

A summary of the various types of nondestructive testing conducted at selected bridge piers of the 15 specific sites follows.

Alkali-Silica Reactivity

The visual survey of the 31 bridges indicated that in some cases observed cracking and distress in concrete bridge piers may have been caused by alkali-silica reactivity (ASR). ASR reaction products form in concrete when sufficient alkalis, such as potassium and sodium, in the cement react with silica and silicates in the aggregates. In the presence of moisture, ASR gel reaction products expand, which may lead to cracking.

The presence of ASR was determined using the uranyl acetate fluorescence method (*3*). This procedure was developed in the recent government-sponsored Strategic Highway Research Program (SHRP), which focused on the development of advanced technology for improving and rehabilitating the nation's highway infrastructure. The results from each ASR test were classified into one of four categories—none, meager, moderate, and abundant—depending on the amount of gel reaction products and brilliance of the background fluorescence.

Chloride Ion and pH

Concrete powder samples from select piers of the 15 bridges were obtained by percussion drill and subsequently analyzed for chloride ion (Cl^-) content and pH. This testing was conducted to assess the susceptibility of the embedded reinforcing steel to chloride- and carbonation-induced corrosion.

The generally accepted chloride corrosion threshold, the value above which corrosion of reinforcing steel will occur in the presence of sufficient amounts of oxygen and moisture, is 300 ppm. In addition, corrosion will not likely occur as long as the concrete maintains a pH in excess of 12 (*4*). If pH is reduced to below 11 by the presence of high chloride levels or if calcium hydroxide (CaOH) is converted to calcium carbonate ($CaCO_3$) by the presence of

atmospheric carbonation (CO_2), corrosion can occur if oxygen and moisture are available (*4*).

The Cl^- content in the concrete powder samples taken from selected bridge piers at each of the 15 sites was measured by the recently SHRP-developed procedure, which uses direct reading in a chemical digestion solution using a specific chloride ion probe (*5*). The pH was determined by using an analytic chemistry procedure of placing a pH electrode in solution.

Half-Cell Corrosion Potentials

Measurement of corrosion potentials was possible only on bridge piers at two sites where reinforcing steel was already exposed because of deterioration. Corrosion potentials were measured using a copper/copper-sulfate half cell following the standard ASTM method (*6*). Half-cell potential measurement does not provide information about corrosion rate but does provide an indication of on-going corrosion activity; half-cell corrosion potentials more negative than –350 mV indicate ongoing active corrosion.

Impact-Echo Testing

The initial reconnaissance revealed the presence of pier cracking on some of the study bridges. In some cases, the cracks have been epoxy injected presumably to restore integrity. At other study sites, the concrete piers had little if any signs of distress or deterioration despite being in service for more than 40 years. To quantify to some degree the present structural condition of selected bridge piers at the 15-in.-depth study sites, as well as to assess the extent of cracking beyond that which could be visually observed, impact-echo testing was conducted. In addition, impact-echo testing was conducted to be able to directly compare the integrity of selected piers constructed in chromium and nonchromium sites. The theory, experimental, and field techniques using the impact-echo method for testing platelike (slabs) and beamlike (beams, columns, and bridge piers) concrete structures are well documented (*7–10*).

In the impact-echo technique, a transient stress pulse is introduced into the test object by mechanical impact on the surface. The stress pulse propagates into the object along spherical wavefronts as *P*- and *S*-waves and along the surface of the object as an *R*-wave. The *P*- and *S*-waves are reflected by internal cracks or interfaces and by the external boundaries of the object. The arrival of these reflected waves at the surface where the impact was generated produces displacements that are monitored by a transducer. If the transducer is placed close to the impact point, the waveform is dominated by displacements caused by *P*-wave arrivals.

In plates, wave reflections from the side boundaries do not have a significant effect on the response. In contrast, transient wave propagation in linear (barlike) elements, such as bridge piers, subjected to transverse elastic impact is more complex because the effects caused by the close proximity of the side boundaries are significant. The response of a linear member subjected to transverse impact is dominated by cross-sectional modes of vibration set up by multiple reflections of waves in a cross section (*9*). The geometry and dimensions of a cross section determine the shape and frequency of each cross-sectional mode. The length is not a factor as long as it is greater than about three times the width. The presence of a flaw within a linear element disrupts the frequency pattern created by the cross-sectional modes.

RESULTS

Literature Review

A review of the technical literature related to effects of chromium on concrete found few papers on the subject. One reference (*11*) referred to a 1969 study by Craig (*12*) in which potassium chromate was used as a corrosion inhibitor. Although Craig (*12*) reported that concrete compressive strength decreases with increasing levels of admixed potassium chromate, it is important to emphasize that a careful review of the data shows some scatter. Moreover, the strength decrease is related to the percentage of chromate salt, but it is not time dependent. In other words, for a given percentage of admixed chromate salt, the strength does not decrease with time.

Mehta (*13*) reports a possible deterioration mechanism of porous materials subjected to sulfate salts. He states that crystallized salts inherent in the pores of materials in critically saturated solutions may create stresses large enough to cause cracking. However, Mehta (*13*) does not specifically mention that chromium salts cause this type of deterioration.

The possible deterioration mechanism identified by Mehta (*13*) is analogous in effect to deterioration associated with freeze-thaw cycles. Porous concrete that is critically saturated can freeze and an associated expansion can occur. If the tension stresses developed from the expansion exceed the tensile strength of the concrete, cracking can occur. Thus, concrete that might be susceptible to deterioration from crystallization of salts would likely also be susceptible to deterioration by freeze thaw.

Visual Survey

The visual survey of the study bridges revealed that the concrete bridge substructures exhibited classical signs of deterioration associated with age and prolonged exposure to deicer chemicals, moisture, and freeze-thaw cycles. Figure 1 illustrates some of the more aggressive forms of deterioration observed on concrete bridge substructures of the study bridges. Table 2 documents the deterioration observed on the study bridges.

As described in Table 2, much of the deterioration is associated with corrosion, water penetration, and freeze thaw. This observed deterioration tended to be focused at the pier caps and upper por-

FIGURE 1 Freeze-thaw deterioration on pier.

TABLE 2 Summary of Visual Study

Bridge Site #	Description of Observed Deterioration and Distress
1	Cracks with efflorescence on pier cap and piers, 0.3 - 0.8mm in width; epoxy injection on pier caps and piers; rust stains on pier caps.
3	Good condition; rust stains on pier caps and piers from steel girders.
4	Cracks with efflorescence, spalls; cracking on pier caps and piers; corrosion products evident.
5	Cracks ; cracking on corners of piers. Piers in good condition otherwise.
6	Small cracks with efflorescence. Piers in good condition.
7	Cracks on pier cap, previous patching; cracks w/ efflorescence below bridge bearing shoes, patches on piers.
8	Heavy cracking with corrosion products and efflorescence; epoxy injection on piers; previous repair work.
9	Cracking with corrosion products and efflorescence; epoxy injection on piers; cracks with corrosion products and efflorescence; previous repair work.
10	Heavy cracking with corrosion products and efflorescence; epoxy injection on pier bases.
11	Cracks and spalling concrete on piers, staining on piers; cracks and spalls with corrosion products and efflorescence, previous repairs.
12	Cracks with efflorescence and corrosion products, epoxy injected cracks.
13	Cracks with efflorescence and staining; many epoxy injected cracks.
14	Cracks and spalls with exposed rebar, previous patches.
15	Cracks and spalls on pier caps; cracks with corrosion products; chipped out spalls; patches w/ efflorescence.
16	Stains from corrosion products; previous repairs with cracks; corrosion products.
17	Incipient spall on pier cap; staining and corrosion products on pier caps.
18	Cracking with corrosion products on pier cap; epoxy injection on concrete pier cap; corrosion on steel pier cap; staining.
19	Stains from corrosion products; stains around bridge shoes on pier caps.
20	Cracks with corrosion products and efflorescence on pier faces; incipient spall on pier face.
21	Heavy corrosion products at cracks, previous patches.
22	None
23	Cracks with corrosion products on pier cap bottoms.
24	Cracks with corrosion products and efflorescence on pier caps, incipient spalls on pier caps.
25	Cracks with corrosion products and stains on pier caps, previous patches.
26	Stains on piers, freeze-thaw damage.
27	Cracks with efflorescence; cracks with efflorescence below bridge shoe.
28	Incipient spalls on pier caps, previous repairs on pier caps.
29	Incipient spalls and cracks on piers, epoxy injection on piers, steel pier cap corrosion visible.
30	Spalled concrete on piers, corrosion and efflorescence present, epoxy injected areas.
31	Cracks and staining; vertical cracks in piers, corrosion products on piers.

Note: Site 2 did not have good access for visual survey and, therefore, is not included.

tions of the pier columns. This deterioration is likely caused by almost direct exposure of water and deicer chemicals through expansion joints in the bridge deck.

There were numerous cases in which it was apparent that observed cracking in pier bents had been previously epoxy injected. This cracking, which was generally prevalent throughout the entire pier, was likely caused by ASR, corrosion, or possibly sulfate attack. Clearly, because it was located well removed from any direct or indirect contact, this cracking could not have resulted from exposure to COPR.

For the piers examined in the 31 bridges included in the study, there was no visual indication of structural distress from foundation displacement or from vehicular impact.

Soil Sampling

Table 3 summarizes the results of the chemical analysis of the soils collected from the 15 bridge sites included in the more in-depth study. Of the 15 bridges 7 are considered to be chromium sites on

TABLE 3 Chemical Analysis of Soils from Sites of 15 Bridges Included in More In-Depth Study

Bridge Site #	Sample #	% Solids	Sulfates (ppm)	Chlorides (ppm)	Cr(VI)[1,2] (ppm)	Total Cr[1] (ppm)	pH
1	A	90.6	113	80	< 4.0	18.4	7.84
	B	90.0	113	70	< 4.0	15.5	7.84
5	A	90.7	48	370	14.0	125.0	8.69
6	A	67.3	640	4500	< 6.0	21.3	7.14
7	A	83.3	9	69	< 5.0	18.0	7.86
9	A	-	-	-	< 2.5	2600.0	-
10	A	-	-	-	< 2.5	570.0	-
	B	82.8	1350	51	< 5.0	141.0	7.53
11	A	87.7	420	190	< 5.0	54.2	8.15
14	A	96.3	20	5	< 4.0	9.3	8.48
22	A	84.9	20	110	< 5.0	26.0	9.28
	B	83.7	32	260	< 5.0	41.6	8.88
25	A	90.3	47	700	< 4.0	9.7	8.75
27	A	90.0	180	12	< 4.0	17.2	5.17
28	A	74.3	51	200	12.0	132.0	7.71
29	A	93.1	620	3000	45.0	6680.0	8.25
	B	87.8	480	19000	32.0	2620.0	8.11
30	A	79.2	750	36000	248.0	2170.0	8.67
31	A	86.9	180	240	11.0	527.0	8.75

Notes:

1. Shaded cells indicate chromium sites based on health-based guidance levels in New Jersey of 10 ppm Cr(VI) and 500 ppm total Cr.
2. A < sign indicates concentrations less than the detection limits of the laboratory procedure.

the basis of the prevailing health-based guidance levels for Cr(VI) and total CR concentration in New Jersey.

The measured sulfate, chloride, and pH values in the sampled soils are shown in Table 3. There is no apparent trend between measured sulfate, percent solids in soil, pH, and chromium concentration.

A review of the chloride contents of the soil at the 15 bridge sites revealed some extraordinarily high chloride contents at two locations classified as chromium sites. It was assumed that these values were caused by outside chloride sources, such as chemical deicers, and not from the chromite ore processing residue apparently used as fill at these sites. Chemical deicers contain chlorides and are present in runoff water from the bridge decks that drains to the soil below through drains and expansion joints. To verify the validity of this assumption, the chloride and chromium contents from the bridge sites were compared with samples collected from a plant site where COPR was produced and used as fill. Results showed the plant site samples to have mean and median chloride contents of 236 and 50 ppm, respectively, with a standard deviation of 500. For the bridge site samples, the mean and median chloride contents were 3,815 and 200, respectively, with a standard deviation of 9,486. These results show that the chloride content of soil at bridge sites is substantially higher than that of known COPR fill. Therefore, the assumption of an external chloride source is valid.

Figure 2 presents the measured chloride and total chromium concentrations of the soil at the bridge sites included in this study and that measured at plant sites where COPR was used as fill. The data shown in Figure 2 reflect the higher chloride concentrations at bridge sites and clearly indicate no correlation between chloride concentration and chromium concentration.

Concrete Chemical Analysis

The results from the various chemical analyses of selected bridge pier concrete are provided in Table 4. Several general trends are evident. At 13 of 15 sites, the Cl^- levels of at least one of the concrete samples exceeds the generally accepted chloride corrosion threshold of 300 ppm. Concomitantly, the pH of the concrete is generally less than 12. Both these factors suggest that steel reinforcement in the piers is at high risk to corrosion in the presence of moisture and oxygen.

The ASR testing revealed the presence of some ASR. Only in cases designated "moderate" and "abundant" is observed cracking

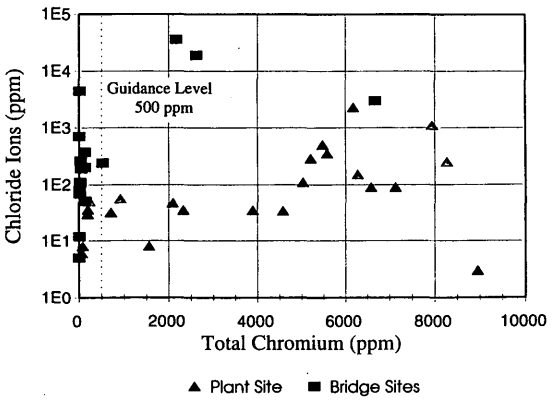

FIGURE 2 Comparison of chloride and total chromium concentration at bridge and plant sites.

directly attributable to ASR. This is the case for 8 piers of the over 30 examined at 15 different sites.

Corrosion Potentials

Half-cell corrosion potentials were measured at Sites 14 and 30 on piers in which there was exposed reinforcing steel. The measured corrosion potentials of the pier of Site 14, a nonchromium site, were between –60 and –280 mV, which indicates low probability of ongoing corrosion activity.

The corrosion potentials on the pier at Site 30 were measured around the pier at an area approximately 3 to 5 m off the ground. Electrical contact was made at an area of exposed reinforcing steel. On the basis of visual observations, there clearly had been past corrosion activity on the steel reinforcement. The measured corrosion potentials were between –450 and –575 mV, which indicated active corrosion. This area of exposed reinforcing steel and aggressive concrete deterioration of the concrete pier at this chromium site was well removed from possible contact with the COPR. In fact, the observed deterioration was in the trajectory of an open drain from the bridge deck above.

Impact-Echo

A summary of the impact-echo test results is also presented in Table 4. Many of the piers have flaws that generally were found to be at shallow depth, indicating that there is a basic core of concrete that is unaffected. A review of Table 4 indicates that the detected flaws are independent of whether the structure is located in a chromium or nonchromium site. This is the case because observed cracking is caused mainly by chloride-induced corrosion.

EVALUATION AND IMPLICATIONS

Raghu and Heieh (*11*) state that Mehta (*13*) offers a possible cause of the deterioration of concrete subjected to COPR as the pressure of crystallization of salts in pores of the concrete presumably caused by migration of chromium into the concrete. Mehta (*13*) discusses concrete deterioration caused by crystallization of salts but does not discuss chromium. In fact, Mehta's (*13*) discussion relates to sulfate salts inherent in the constituent concrete materials and not from ingress from external sources.

In other field investigations the authors observed deterioration by salt crystallization in masonry that contains surface glazing or a relatively impervious dye skin. This deterioration is caused by naturally occurring salts in the masonry units or mortar. There was no evidence in the present study that the observed deterioration in concrete, often well removed from contact areas of the chromium fill, could be related to salt crystallization. Moreover, as has been observed in masonry structures, if deterioration of concrete is caused by crystallization of salts inherent in the material, salts are clearly visible. There was no evidence of salts or salt residue at locations of deterioration on the bridges even though salts were clearly visible on the soil surface of some of the sites with COPR fill.

CHROMIUM VERSUS NONCHROMIUM SITES

The results presented in Table 3 reveal that 7 of the 15 sites included in the more in-depth study could be classified as chromium sites by the health-based guidance levels informally promulgated in New Jersey. Other sites adjacent to these chromium sites with bridges of similar age and structural system permitted direct comparison of the field investigation results.

Figures 3 and 4 are from Sites 10 and 11, which are on the Pulaski Skyway. As indicated in Table 3, Site 10 is classified as a chromium site, whereas Site 11 is not. Most of the deterioration of the large concrete piers was present just below the deck slab where water could accumulate and subsequently drip. The measured Cl^- levels in the concrete (see Table 4) were above the chloride corrosion threshold, indicating that much of the deterioration is caused by corrosion; this observation is supported by visible rust stains that emanate from cracks.

At both sites the large concrete piers also exhibited vertical cracks, generally on all four sides of the pier, rising a substantial height. These cracks tended to be near the center of the pier, indicating that they could be related to shrinkage early in the life of the structure. However, impact-echo results did not indicate that the cracks went through the entire section, a condition that could compromise the load capacity and thus the integrity of the piers.

Direct comparison of results was also possible between Sites 5 (chromium site) and 6 (nonchromium site) because they were adjacent to each other on the New Jersey Turnpike. In general, the concrete pier bents at these two sites were in fair condition, with limited signs of the usual cracking caused by reinforcing steel corrosion on the pier caps and at corners of piers. In both cases, the Cl^- levels in the concrete were above the threshold level, indicating that the observed cracking was likely caused by chloride-induced corrosion.

It was observed that the cracking in one of the piers examined at Site 6 was more extensive and pronounced. As noted in Table 4, the ASR test result for this pier was classified as "abundant," indicating that cracking was likely caused by ASR.

A comparison of test results between chromium and nonchromium sites reveals some general trends. For example, the average Cl^- contents in both chromium and nonchromium sites typically are above the generally accepted chloride corrosion threshold, indicating that the reinforcement in the piers is susceptible to corrosion in both chromium and nonchromium sites.

Analysis of the test results from Site 30 provides the most convincing evidence that observed deterioration is clearly not related to exposure to chromium. The soil data in Table 3 indicate that Site 30 is a chromium site. As indicated in Figure 5, many of the bridge piers at Site 30 are mounded by COPR: the visible pier cap in Figure 5 was previously epoxy injected, presumably to restore integrity.

TABLE 4 Chemical and Physical Analysis of Concrete from Selected Piers at 15 Bridges Included in More In-Depth Study

Bridge Site #	Sample	Chlorides(ppm)	pH	ASR	Impact-Echo
1	A	84	11.7	none	Solid
	B	311	11.7	meager	N/A
5	A	1958	12.2	meager	Solid
	B	4381	11.8	meager	Flaw
6	A	435	11.2	abundant	N/A
	B	1329	12.3	meager	N/A
7	A	808	12.0	meager	Solid
	B	334	11.9	meager	Flaw
9	A	2701	11.8	meager	Solid
	B	1585	11.8	moderate	N/A
10	A	1188	11.9	moderate	Solid
11	A	535	11.9	meager	Flaw
	B	1061	11.9	meager	Flaw
14	A	613	10.7	meager	Solid
	B	217	11.3	meager	Flaw
22	A	130	11.0	meager	Flaw
	B	208	11.9	moderate	Flaw
25	A	719	11.5	meager	Solid
	B	1976	11.7	meager	Solid
27	A	154	11.9	meager	Flaw
	B	208	11.3	meager	N/A
28	A	1922	12.1	none	Solid
	B	478	12.0	none	N/A
29	A	2826	11.4	moderate	Flaw
	B	898	11.9	meager	Flaw
30	A	417	11.2	meager	Flaw
	B	1144	11.7	meager	Flaw
	C	495	10.8	moderate	N/A
	D	1041	11.8	moderate	N/A
31	A	1373	12.1	moderate	Flaw
	B	1150	12.1	none	Solid

N/A - Not Available

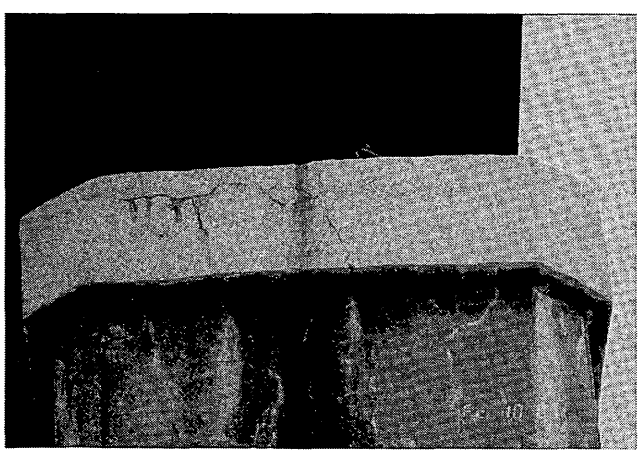

FIGURE 3 Observed deterioration of pier at Site 10 (chromium site).

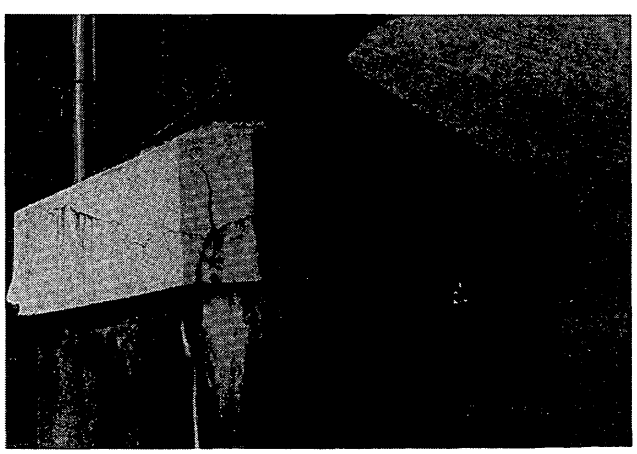

FIGURE 4 Observed deterioration of pier at Site 11 (nonchromium site).

This pier cap was directly under an expansion joint in the bridge deck, and the observed deterioration was clearly corrosion related, as evidenced by rust stains that emanated from the cracks.

Figure 6 indicates aggressive deterioration of the piers, approximately 3 to 5 m above grade, where cracking along the longitudinal corner bar of the pier and signs of previous epoxy injection occurred. Cl^- Sample B from Site 30 in Table 4 was taken from the location shown in Figure 6. This high Cl^- level concomitant with measured half-cell corrosion potentials up to –575 mV clearly indicates that the observed deterioration is from chloride-induced corrosion. There is no indication that the deterioration, by any measure, is related to contact with COPR.

It is again noted that the soil taken from Site 30 (see Table 3) indicates a high level of chloride as well as chromium. As previously discussed, the chlorides in the soil are in all probability from bridge deck runoff, which contained chemical deicers.

SUMMARY AND CONCLUSIONS

An evaluation of 31 selected bridges in and around Hudson County, New Jersey, was conducted to investigate the general condition of the structures as related to structural integrity and durability and to assess the causes of observed deterioration. The visual survey of these 31 bridges was followed by more in-depth testing of 15 of these bridges. Seven of the bridges are located in chromium sites as determined by measured Cr(VI) or total Cr concentration in the surrounding soil, exceeding health-based guidance levels in New Jersey. Testing of selected concrete bridge piers at 15 sites included determination of Cl^- content and pH, impact-echo testing to assess general structural integrity, determination of the presence of ASR, and, where possible, measurement of half-cell corrosion potentials.

On the basis of visual survey and results from the various types of nondestructive testing, it is concluded that deterioration of the concrete bridge substructures is clearly independent of site soil conditions and, in particular, the concentrations of Cr(VI) and total Cr. The general forms of observed deterioration were cracking and spalling caused by corrosion and freeze-thaw deterioration. There was also evidence of cracking at some piers caused by ASR.

The more salient specific conclusions from the investigation are summarized as follows:

1. A previously purported concrete deterioration mechanism associated with chromium is believed to be incorrect (*11*). That postulated mechanism, related to crystallization of salts, is believed to be appropriate for naturally occurring salts in the constituent materials of porous products such as masonry and, to a lesser degree, concrete. The migration of chromium from the surrounding soil into the concrete to a level associated with crystallization of salts and subsequent generation of tension stresses from expansion as a result of crystallization to a degree to cause cracking and deterioration is highly improbable. In any case, no deterioration was observed on the bridge structures included in this study that could be associated with this type of deterioration mechanism. Moreover, visible signs of chromium salt residue on the concrete, which would suggest that there had been chromium migration and deterioration caused by stresses generated by salt crystallization, were not present.
2. There is no evidence in the study bridges that crystallization damage associated with chromium intrusion into concrete has occurred in the concrete bridge substructures in contact with the soil. Even if chromium migration has occurred, it is evident from the lack of visible deterioration associated with crystallization that the pore size and pore structure of the substructure concrete accommodated any crystallization that occurred on evaporation at or near the surface of the concrete.
3. A comparison of the test results clearly indicates that most of the observed deterioration of the concrete piers was related to corrosion of embedded reinforcement, independent of soil conditions. On average, the measured Cl^- content in the concrete bridge piers in both chromium and nonchromium sites exceeded the chloride corrosion threshold. This is clear evidence that there has been significant Cl^- ingress over 40 years or more of service from salt water spray and runoff from the use of deicer chemicals on the bridge decks. This is also the reason for the relatively high Cl^- levels measured in some bridge site soil samples.
4. The observed deterioration of the concrete piers at the site with the highest concentrations of Cr(VI) (Site 30) was determined to be from chloride-induced corrosion. Chloride levels in some samples exceeded 1,000 ppm, and half-cell potentials on the order of –575 mV were measured.
5. To a lesser degree, some of the observed deterioration can be attributed to ASR. In several cases, the ASR was severe enough to cause cracking in the piers.

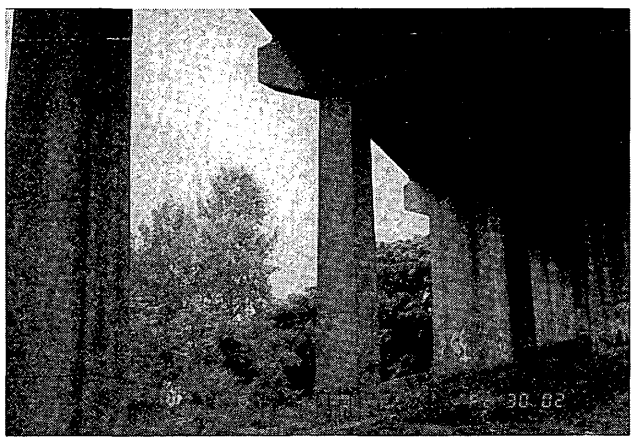

FIGURE 5 Site 30 showing piers mounded by COPR.

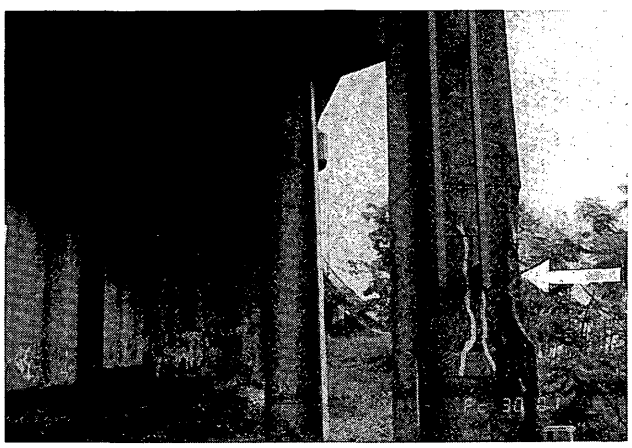

FIGURE 6 Corrosion-related deterioration of bridge pier at Site 30.

6. Neither distress nor deterioration that could be related to foundation displacement was observed in the bridge piers.

7. There was no evidence that observed deterioration of the bridge piers selected for study was severe enough to be of immediate structural concern. This was substantiated to a degree by the results from the impact-echo testing, which indicated that flaws were not deep rooted, leaving a basic core of sound concrete.

REFERENCES

1. Sheehan, P. J., D. M. Meyer, M. M. Sauer, and D. J. Paustenback. Assessment of the Human Health Risks Posed by Exposure to Chromium-Contaminated Soils. *Journal of Toxicology and Environmental Health*, Vol. 32, 1991, pp. 161–201.
2. Wyckoff, P. L. Turnpike Is Gearing Up to Sue Firms Over Decades-Old Chromium Taint. *New Jersey Star-Ledger*, March 31, 1993.
3. Stark, D. *Handbook for the Identification of Alkali-Silica Reactivity in Highway Structures*, SHRP-C/FR-91-101. Strategic Highway Research Program, National Research Council, Washington, D.C., 1991.
4. Mindess, S., and J. F. Young. *Concrete*, Prentice-Hall, Englewood Cliffs, N.J., 1981.
5. Cady, P. D. *Condition Evaluation of Concrete Bridges Relative to Reinforcement Corrosion—Volume 8: Procedure Manual.* SHRP-S-330. Strategic Highway Research Program, National Research Council, Washington, D.C., 1992.
6. *Standard Test Method for Half-Cell Potentials of Uncoated Reinforcing Steel in Concrete, C876.* American Society for Testing and Materials, 1991.
7. Sansalone, M., and N. J. Carino. *Impact-Echo: A Method for Flaw Detection in Concrete Using Transient Stress Waves.* NBSIR 86-3452. National Bureau of Standards, Gaithersburg, Md. Sept. 1986.
8. Sansalone, M., and N. J. Carino. Detecting Honeycombing, the Depth of Surface-Opening Cracks, and Ungrouted Ducts Using the Impact-Echo Method. *Concrete International*, April 1988, pp. 38–46.
9. Lin, Y., and M. Sansalone. Detecting Flaws in Concrete Beams and Columns Using the Impact-Echo Method. *Materials Journal of the American Concrete Institute*, July–Aug. 1992, pp. 394–405.
10. Sansalone, M., and R. W. Poston. Detecting Cracks in the Beams and Columns of a Post-Tensioned Parking Garage Structure Using the Impact-Echo Method. *Proc. Conference on Non-Destructive Evaluation of Civil Structures and Materials*, Boulder, Colo., May 1992.
11. Raghu, D., and H. Heieh. Performance of Some Structures on Chromium Ore Fills. ASCE *Journal of Performance of Constructed Facilities*, Vol. 3, No. 2, May 1989, pp. 113–120.
12. Craig, R. J. Physical Properties of Cement Paste with Chemical Corrosion Reducing Admixtures. M.S. thesis, Purdue University, West Lafayette, Ind., 1969.
13. Mehta, P. K. *Concrete: Structure, Properties and Materials*, Prentice-Hall, Englewood Cliffs, N. J., 1986.

Publication of this paper sponsored by Committee on Dynamics and Field Testing of Bridges.

Destructive Testing of Two 80-Year-Old Truss Bridges

A. E. AKTAN, K. L. LEE, R. NAGHAVI, AND K. HEBBAR

Two decommissioned 80-year-old steel truss bridges were subjected to a series of nondestructive and destructive tests. The trusses had built-up members that were rigidly connected by rivets at the gusset plates. The floor system, many truss members, and the connections exhibited considerable deterioration. The bridges were retrofitted at critical connections by welding A36 plates on the pre-A7 steel. Both bridges exhibited acceptable performance during the tests at all the limit states. One bridge yielded initially at 371 tons and failed at 415 tons. The other bridge yielded initially at 458 tons, and failure could not be induced under as much as 622 tons because of displacement limits in the loading equipment. The test results revealed that serviceability, damageability, and failure behavior of steel truss bridges possessing built-up members rigidly connected by rivets at the gusset plates are not adversely affected by local deterioration. The built-up members and the connections possessed adequate deformability permitting extensive redistribution. Connection retrofit by welding plates was feasible and successful.

A large number of steel truss bridges constructed before the 1930s continue to serve the public, although many are classified as deficient because of geometric obsolescence, deterioration, aging, increasing truck weights, and traffic volumes. Because of scarce financial resources and budget priorities, many deficient bridges may remain posted for a considerable period until they are replaced. A number of historic bridges, such as the John Roebling Bridge in Cincinnati, the Brooklyn Bridge in New York, and the Golden Gate Bridge in San Francisco, must be preserved regardless of cost or functional limitations. A rational, reliable, and quantitative method for assessing deteriorated bridge condition and strength is needed for their effective management and preservation.

Some steel truss bridges have been rehabilitated or upgraded, or both (*1*). Most reported examples of truss bridge retrofit have included complete or partial replacement of the floor system, replacement of the deteriorated truss members (*2*), posttensioning of the existing elements (*3*), addition of missing elements, and replacement of rusted connection plates and rivets with new plates and bolts. Whether it is possible to effectively and simply upgrade a steel truss bridge by welding plates on existing elements and connections has not been appropriately investigated to the knowledge of the writers, and because of a lack of guidelines, most bridge practitioners are hesitant to weld new materials onto older steels.

This paper reports the results of a series of nondestructive and destructive tests conducted on two 80-year-old steel truss bridges (Figure 1). Both bridges were extensively instrumented by over 150 transducers each to capture all of their important global and local responses. The nondestructive tests included diagnostic truck load tests and modal testing. Destructive tests were carried out by loading the bridges using hydraulic actuators reacting against rock anchors, following their retrofit at some of the critical connections.

A. E. Aktan and K. L. Lee, Cincinnati Infrastructure Institute; R. Neghavi and K. Hebbar, Department of Civil and Environmental Engineering, University of Cincinnati, Cincinnati, Ohio 45221-0071.

OBJECTIVES

The principal reasons for steel truss bridge collapses are typically failure because of fatigue or deterioration at the critical locations of nonredundant designs (pin failure in eye bar trusses), bearing failure, abutment and wing-wall instability; accidents that are often the result of functional limitations such as inadequate vertical clearance; and aging and deterioration. Therefore, given this opportunity to test two steel truss bridges that exhibited signs of extensive deterioration, the first objective is to evaluate whether many bridges that remain from the early 1900s and have similar design and construction characteristics may pose a public safety hazard. The second objective is to explore cost-effective and unobtrusive methods of upgrading deteriorated steel truss bridges with attributes similar to those tested.

The third objective follows from problems related to condition assessment: (*a*) limitations in detecting damage and deterioration in obscure or hidden components and (*b*) the lack of a rational procedure for reliable analytical modeling. A reliable analytical model should simulate all the important resistance mechanisms and the effects of any existing damage and deterioration on these mechanisms. Therefore, it is intended to explore truss bridge behavior by nondestructive and destructive tests and to correlate the experimentally measured responses with corresponding analytical predictions. An earlier destructive load test of a truss bridge in Iowa (*4*) and diagnostic tests on truss bridges in Ontario (*5*) had revealed unexpected reserves of strength; however, the reasons could not be clearly understood because of a lack of sufficient instrumentation.

Cognizant of some of the difficulties in exploring aged bridge behavior and the effects of the bridge conditions on the latter, the writers explored dynamic testing and structural identification as a condition assessment tool. They used static shakedown tests with extensive instrumentation for an identification of the actual limit states, important load distribution mechanisms, and the effect of deterioration on bridge behavior at all the limit states, including failure.

TEST SPECIMENS AND CONDITIONS

The first bridge (Figure 1*a*) was an eight-panel Pratt through truss bridge (the Pratt), with a span of 46.4 m and a roadway width of 6.1 m. Truss members were fabricated with built-up riveted members. Bottom chords consisted of four angles. Top chords consisted of two channels and a plate. Verticals were made of two laced chan-

(a) Pratt Truss Bridge

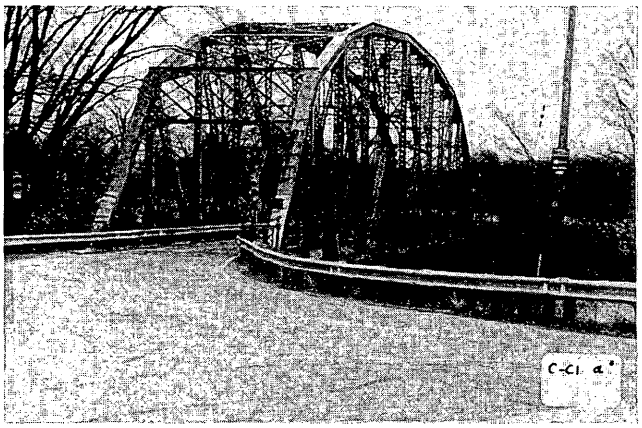

(b) Camelback Truss Bridge

FIGURE 1 Test bridges.

(a) Rust Pocket in Truss Member

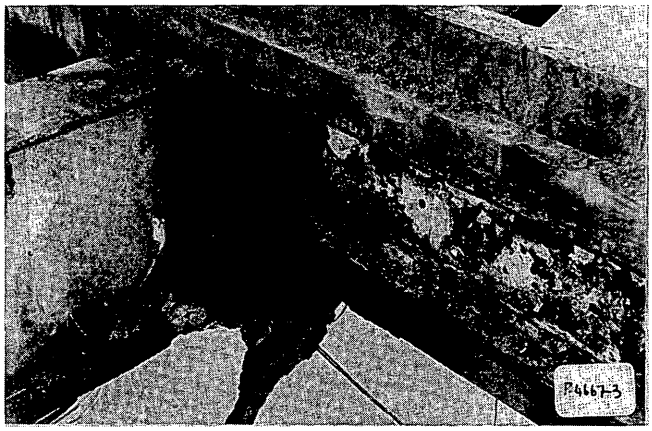

(b) Connections of Floor Beam and Exterior Stringer

FIGURE 2 Examples of deterioration effects.

nels, and diagonal members were fabricated from four angles and a plate. The truss connections were constructed by gusset plates 8 mm thick and rivets 19 mm in diameter. The floor system consisted of main transverse girders, longitudinal stringers, and a wood deck. Interior stringers were I-sections 46 cm deep spaced 122 cm center to center. Exterior stringers were built up of angles and plates. Transverse floor girders were I-beams 76 cm deep. The truss was supported by rollers and hinges bearing on reinforced concrete abutments faced with sandstone.

The second bridge (Figure 1*b*) was a 12-panel Camelback through truss bridge (the Camelback) 12 m high at the midspan, with a span of 76.2 m and a roadway width of 6.1 m. The construction of the Camelback was similar to that of the Pratt, with the exception that gusset plates were 11 mm thick and rivets were 22 mm in diameter.

Arms-Length Inspection

A hanging scaffold system was constructed along the lower chords and a cherry picker was used to reach the upper chords to enable visual inspections at close range. The inspections served to (*a*) verify that construction matched the available shop drawings; (*b*) document existing deterioration and damage on the members, connections, supports, and foundations; and (*c*) identify any past repair/retrofit. On the basis of the inspection results, analytical studies were carried out to predict possible influence of the observed damage on capacity and to identify other important parameters that may affect capacity. Results of these analytical studies were then used for design of retrofit and the loading system for dynamic and static tests.

Condition of Bridges

Both bridges were found to be in fair to poor condition. Existing member sizes, details, and geometries matched almost perfectly with the drawings with the exception of minor discrepancies at two connections. The abutments were in good condition with no apparent settlement or distress. The rollers appeared not to have functioned for many years because of accumulated rust. The timber deck was generally in good condition with no evidence of infestation or rot. Truss members were in good condition above the deck level; however, several members had accumulated rust pockets at the deck level (Figure 2*a*). The rust pockets considerably decreased the effective cross-sectional area of inflicted truss members. Paint on the bridges was in poor condition overall and was flaking from many elements. Both bridges were last coated with lead-based paints in

1982. The most relevant damage specific to each bridge is discussed in the following sections.

Pratt

Bottom chords and the gusset plates had considerable rust at connections to the bearings. At the northeast bearing, 50 percent of the gusset plate cross section was gone. Interior stringers were in satisfactory condition, with less than 5 percent loss caused by rusting of the overall cross sections. Several interior stringers were not bearing on the abutment walls at both ends; however, connections to floor girders were satisfactory. Exterior stringers suffered from extensive rust and deterioration. Damage was caused by atmospheric effects accelerated by poor slope and deicing salts. Webs of stringers at both ends of panels had lost almost 100 percent of their cross sections (Figure 2*b*). Apparently, these stringers had lost all their load-carrying capacity and were held in place by the timber decks. Floor girders, in general, were in good condition, except for the end connections to trusses, where girders had lost 50 percent of the web area with missing or corroded rivets.

Camelback

Bottom chords on both trusses had lost some lacings at end panels. Rust was noticeable on the tips of built-up angles of bottom chords. The maximum area reduction caused by rust was approximately 15 percent of the total cross section. Interior stringers were in good condition, with less than 5 percent cross-section reduction caused by rust. Stringers were in satisfactory shape at the connections to the floor girders. Exterior stringers, however, were so deteriorated that they had lost more than 80 percent of their cross sections at the connections. Both ends of the floor girders exhibited considerable rust at connections to the trusses so that the loss of effective web and rivet cross-sectional areas was about 40 and 30 percent, respectively.

RESEARCH PROCEDURE

The research procedure was designed to fulfill the objectives while maintaining an acceptable cost. A considerable investment was already made in data acquisition and signal conditioning equipment, loading actuators, and servo-control systems in conjunction with an earlier study that incorporated nondestructive and destructive testing of a reinforced concrete slab bridge (*6*). To attain the main objective it was necessary to load the main trusses to extensive yielding and if possible, failure, while simulating progressively increasing truck loading. This required retrofit and a load transfer system. The retrofit was needed to prevent premature failures of floor girders and truss connections. The load transfer system was needed to transfer applied static loads generated by hydraulic actuators (up to 728 tons) through floor girders to truss members. It was desired to accomplish this while simulating single as well as multiple one-lane truck loading. One-lane loading was considered more probable for the test specimens and asymmetric failure modes were expected to be more critical than symmetric ones.

Material Properties

Some of the deteriorated and nonfunctional lower wind-bracing elements and plates were removed to fabricate material samples. Coupons were tested to determine the mechanical characteristics of the pre-A7 material. Average values for the yield stress (Fy = 248 MPa), the modulus of elasticity (E = 207 GPa), as well as the yield plateau, strain-hardening characteristics, and the elongation capacity were found to be comparable to those for A7 steel. Microstructural evaluation of the material was carried out on polished and etched samples using the scanning electron microscopy technique. Tests on the mechanical characteristics of the material were followed by welding tests to explore the weldability of A36 plates of comparable thickness to the bridge material. The microstructure of the welds was then investigated by various coupon tests to verify deformability and strength.

Nondestructive Dynamic Tests

Modal tests were carried out for structural identification and for exploring whether bridge flexibility obtained by processing modal test results serves as a condition and damage index (*7*). The structural identification studies served as a basis for designing the loading and instrumentation. Damage-detection studies, summarized elsewhere, verified that flexibility may serve as a damage-sensitive and objective structural condition index (*8*).

Loading System

To simulate one-lane truck loading (*9*), a loading system that was capable of applying loads of any proportion to four consecutive girders was used (Figure 3). The servo-controlled electro-hydraulic system consisted of a pump, four actuators, four servo-valves, and a four-channel digital controller (Figure 4). Each double-action actuator had a capacity of 182 tons and 30.5 cm of total stroke. Rock anchors embedded 24.4 m into the bedrock under the riverbed provided reactive force. Actuators could be individually or simultaneously controlled in force or displacement modes. The tests were conducted by prescribing master-slave relationships to actuator forces while commanding a master actuator in terms of either force or displacement. Actuator forces and strokes were respectively monitored by calibrated pressure transducers and wire potentiometers.

Load Transfer System

The load transfer system shown in Figure 3 was designed to ensure safe transmission of loads to trusses at all the limit states while maintaining similitude with single or multiple one-lane truck loading (*10*). Four girders were fabricated from W27 × 84 beams running on top of and parallel to the floor girders. Each girder had four vertical legs that were bolted to floor girders. In addition to transmitting load to the floor girders, the ends of the loading girders also transmitted approximately 20 percent of the load directly to the verticals of the trusses using roller bearings. In this manner, the truss adjacent to the loaded lane was transferred about 70 percent of the total load (in the linear limit states) while avoiding a premature failure in the participating floor girder-to-truss connections.

Retrofit Design and Application

Design of the loading system necessitated an upgrade of the affected girder-to-truss connections to avoid premature failures in these con-

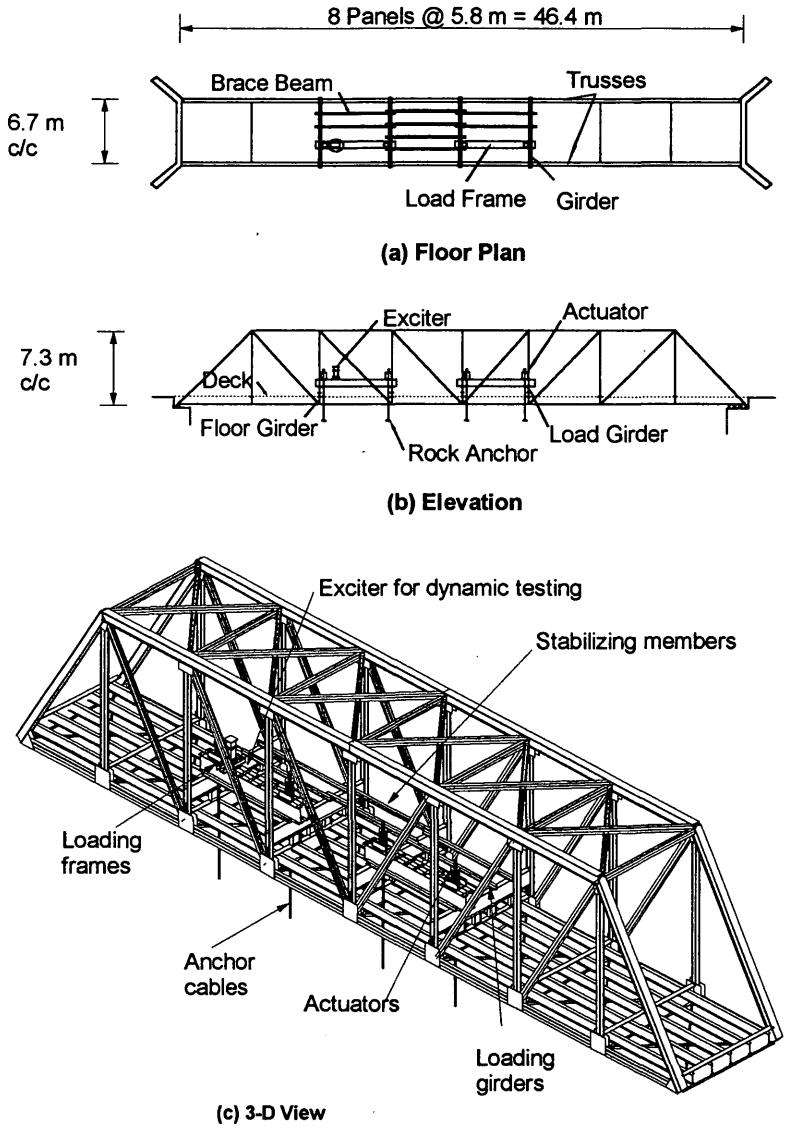

FIGURE 3 Set-up of loading system for Pratt bridge.

nections as a result of high-magnitude concentrated loads. The bridge retrofit was designed considering possible maximum forces that the loading system could transmit to the affected connections (Figure 5), also accounting for the existing conditions of the members, gusset plates, and rivets at the connections. Although necessitated by the loading scheme, the retrofit also created an opportunity to explore effective and feasible manners of treating extensive deterioration or upgrading similar steel truss bridges, or both, with minimal change on the aesthetics. A simple solution to all these problems was to add A36 plates to the affected connections by some simple fillet welds, as shown in Figure 5. This design did not require removal of any rivets, it was unobtrusive, and finally it did not alter the original appearance of the exposed joints. The low cost of the retrofit with welding (approximately a few thousand dollars per connection) and its successful performance during destructive tests indicated that a possibly superior alternative to retrofit with bolting/riveting may be found in welding.

Instrumentation

The responses that were measured in the static tests included the following: (*a*) the global vertical and horizontal displacements at each truss connection at the lower chords, including the horizontal and vertical displacements at the bearings, in which the vertical displacements were measured by wire potentiometers using reference posts embedded in the creek while bearing movements were measured by linear voltage differential transformers (LVDTs); (*b*) local strains and axial distortions along selected members and connections, such that the force distribution at each connection could be completely established by the forces computed from measured member strains and equilibrium [clip gauges (30.5-cm gauge length), LVDTs (measuring member axial distortions over gauge lengths of up to 6.1 m using piano wire), and strain gauges welded on steel were used for these]; (*c*) variations in elongation along the length of critical members as well as strain distributions within built-

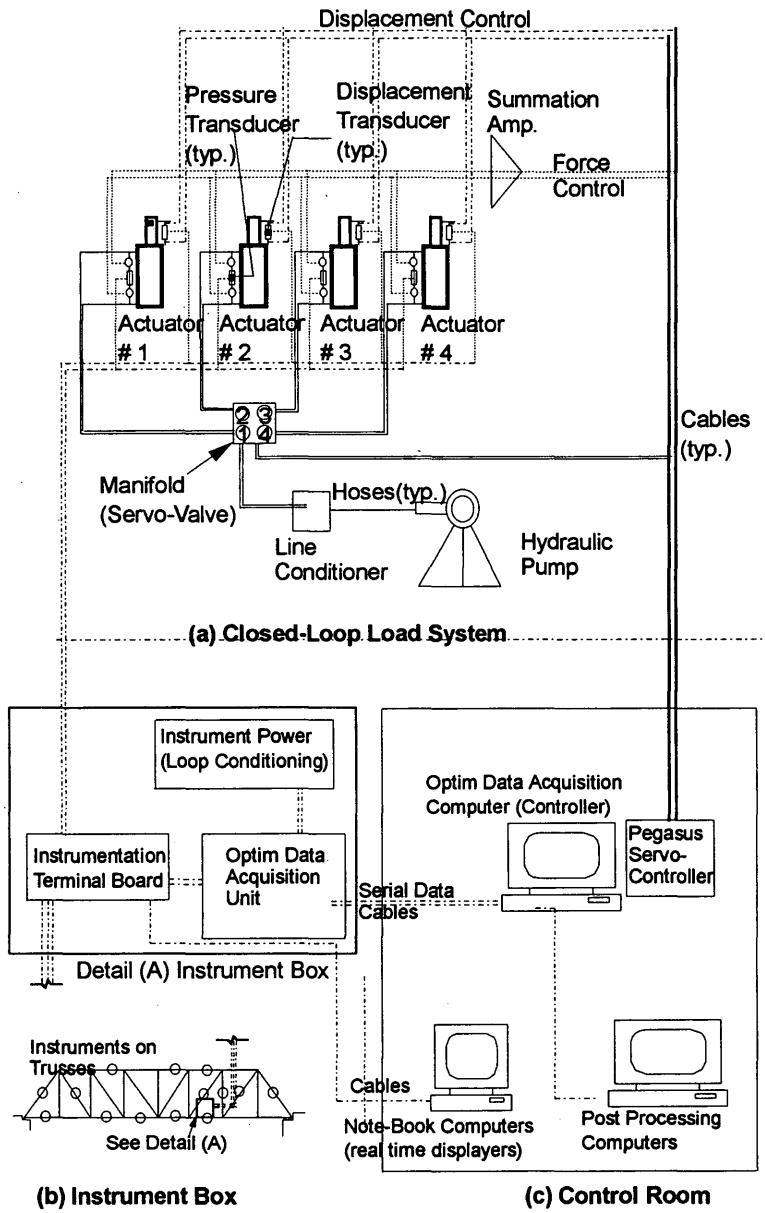

FIGURE 4 Loading and data acquisition system.

up cross sections; and (d) ambient and bridge temperatures, using thermocouples. More than 150 gauges were installed on each bridge.

The instruments and their calibration, installation, and protection schemes were selected on the basis of experience from prior field and laboratory tests and pilot studies in the field at the preliminary stages of the research. A comprehensive study that included the mechanical calibrations of each type of transducer was essential for evaluating properties such as sensitivity, linearity, repeatability, hysteresis, and drift.

Because of limitations in signal conditioning and data acquisition (only 80 channels could be monitored at one time at high scan speed), several data sets of 80 instruments were grouped for monitoring at various phases of the nondestructive and destructive tests. In this manner, all of the measurement objectives were satisfied during the linear limit states, and a final set of 80 instruments was selected for monitoring during the destructive tests. An instrumentation box was installed on the bridge to house data acquisition, connection slots, power, and current stabilizer (Figure 6). A high-speed communication cable transmitted the data to a control center in a field trailer next to the test bridge.

Data Acquisition and Postprocessing

A high-speed data acquisition, signal conditioning, and recording system (OPTIM Megadac 2210C) was used to record bridge responses during truck load tests and static tests conducted with the actuators. Data could be recorded in real time on buffered tape cartridge or at a rate of 20,000 samples/sec on the hard disk of a portable personal computer (PC). High-speed data acquisition incorporating a large number of averages is important even in

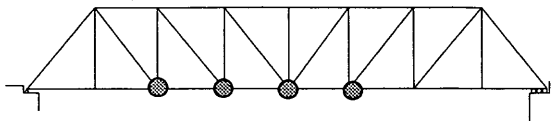

(a) Pratt Bridge Elevation Showing Retrofitted Joints

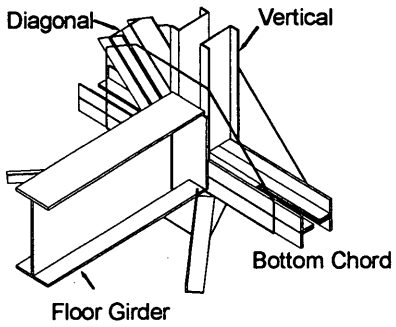

(b) Before Retrofit

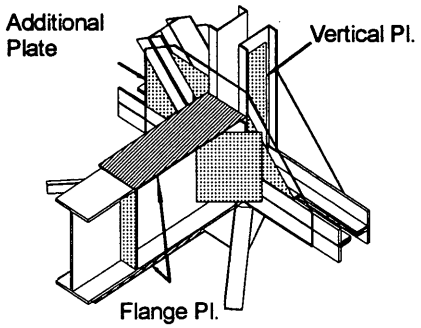

(c) After Retrofit

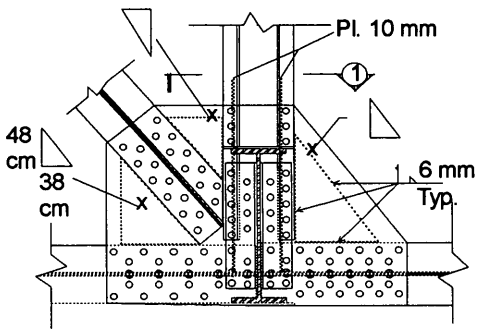

(d) Joint 3 (Elevation)

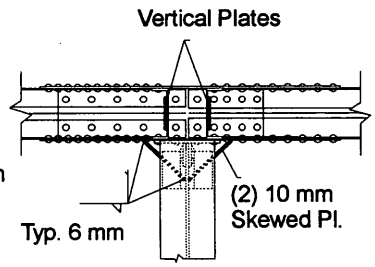

(e) Section 1 (Plan)

FIGURE 5 Typical joint retrofit.

quasi-static tests to minimize noise and random errors, for synchronous measurement of loads and responses, and to minimize test time and therefore any drift caused by changes in the ambient conditions.

During tests a portable PC was used to communicate with the OPTIM system and control data acquisition from the control room (Figure 7*a*). Real-time digital plotting software was used for instantaneous feedback of actuator loads, strokes, and critical global and local-member responses (Figure 7*b*). This system revealed the loading condition and critical responses and was essential for decision making while maintaining a reasonable pace of the test. In addition, a PC software was developed to postprocess all of the measured responses within only a 15-min intermission during a test. This permitted visually verifying the reliability of the data from applied load versus measured response plots to perform preliminary correlations with analytical predictions to check for any anomalies. A large number of loading-unloading excursions (10 to 20) to load levels of up to 20 trucks could be confidently executed within several hours once the test control and data reduction systems were debugged.

LOADING PROGRAM AND PRELIMINARY TEST RESULTS

Truck Load Tests

Following instrumentation, bridge responses were measured after positioning two loaded trucks weighing 18 tons each in several configurations. Because the bridges had been posted to 9 tons, these tests served for diagnostics and proof loading. It was possible to investigate and verify (*a*) global and local response for a study of behavior under service loads, (*b*) instrument and data acquisition performance, and (*c*) flexibility for correlating with the flexibility obtained from modal tests.

Truck positions, global displacement responses, and local responses for one of the critical truss elements in the Pratt (upper chord element labeled BC3) are summarized in Figure 8. The displacement responses indicate differences in the truss stiffnesses and that the bridge is stiffer than analytically predicted. The reason for the latter was because of frozen rollers and the effect of the floor system and the gusset plates, which increased the effective stiff-

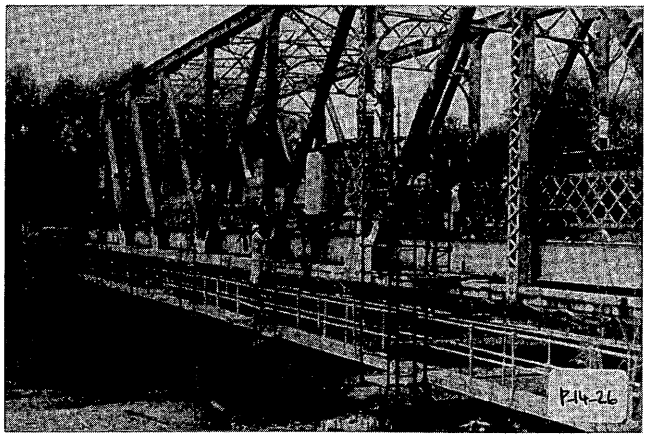

(a) Pratt Showing Scaffolding and Instrument Box

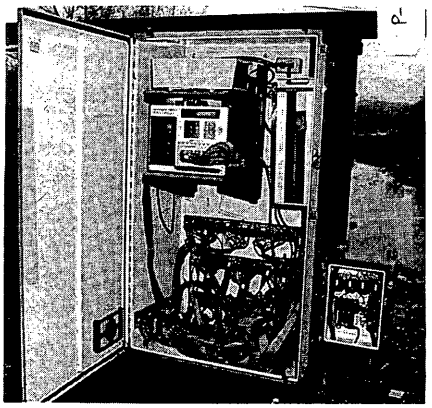

(b) Instrumentation Box

FIGURE 6 Scaffolding and instrumentation box.

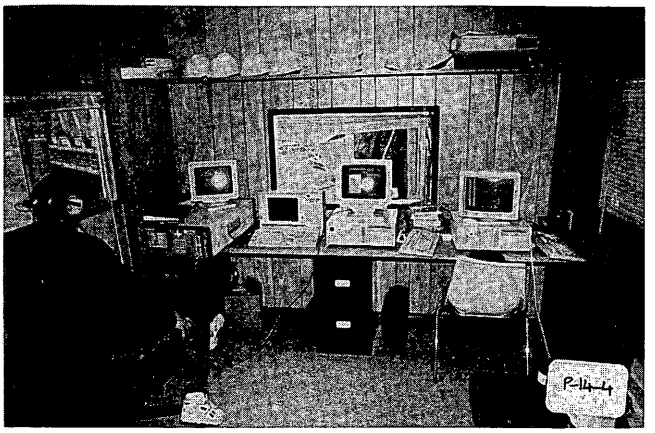

(a) Control Room

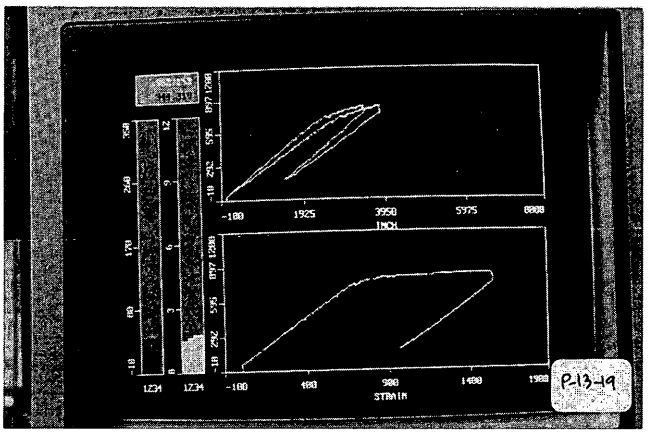

(b) Real-Time Display

FIGURE 7 Test control and data acquisition.

nesses of the members. Under the proof-load level caused by two trucks, the most critical truss strain was observed to correspond to less than 20 MPa stress. Moreover, a variance of almost 25 percent was observed in the strains measured at various locations of the same cross section, revealing the nonuniform strain field in the built-up member. This points to the need for careful and extensive instrumentation for reliable conduct of any type of diagnostic test on truss and other types of bridges.

Static Tests by Actuators

The static test programs were designed in the form of shakedown loading with loading-unloading cycles. The peak load in a cycle could be varied to simulate multiple rating trucks. The peak loads attained in testing the Pratt and the Camelback corresponded to 12.8 HS 20–44 trucks and 20 Hs 20–44 (*9*) trucks, respectively. These peak loads were attained after applying typically more than 60 load cycles, progressively reaching higher levels. An important variable in the tests was the loading patterns—the ratio of load in each actuator. By changing the load pattern it was possible to simulate various single-lane load configurations and therefore change the critical elements.

The four different inelastic limit states that were induced by loading the Pratt with various load patterns are indicated in Figure 9. These limit states corresponded to the yielding of the diagonal element at Node 6; buckling of the diagonal element at Node 4; yielding of the diagonal element at Node 3, as well as the upper chord element labeled BC2; and rupturing of the lower chord connection to the upper chord and the pin bearing at Node 1. The peak loads at which these events occurred in the truss adjacent to the loaded lane (the other truss remained linear) are indicated in Figure 9.

The total applied load versus the vertical displacement at the midspan of the truss (B5) adjacent to the loaded lane is plotted in Figure 9, revealing how the occurrence of each of the inelastic limit states affected the global response. The corresponding local responses of the diagonal element labeled BT7 and the upper chord element labeled BC2 are also shown in the same figure. Although these local strain responses of less than 1 percent were measured at element midpoints, it was later assessed that longitudinal strains in the vicinity of rust pockets and at lower gusset-plate connections were much greater than 1 percent and at some locations reaching perhaps 10 percent. The failure occurred when the roller bearings that were displacing with significant resistance because of rust slipped, leading to a sudden surge in the lower-chord tension. The lower-chord connection at the pin-bearing ruptured in a brittle man-

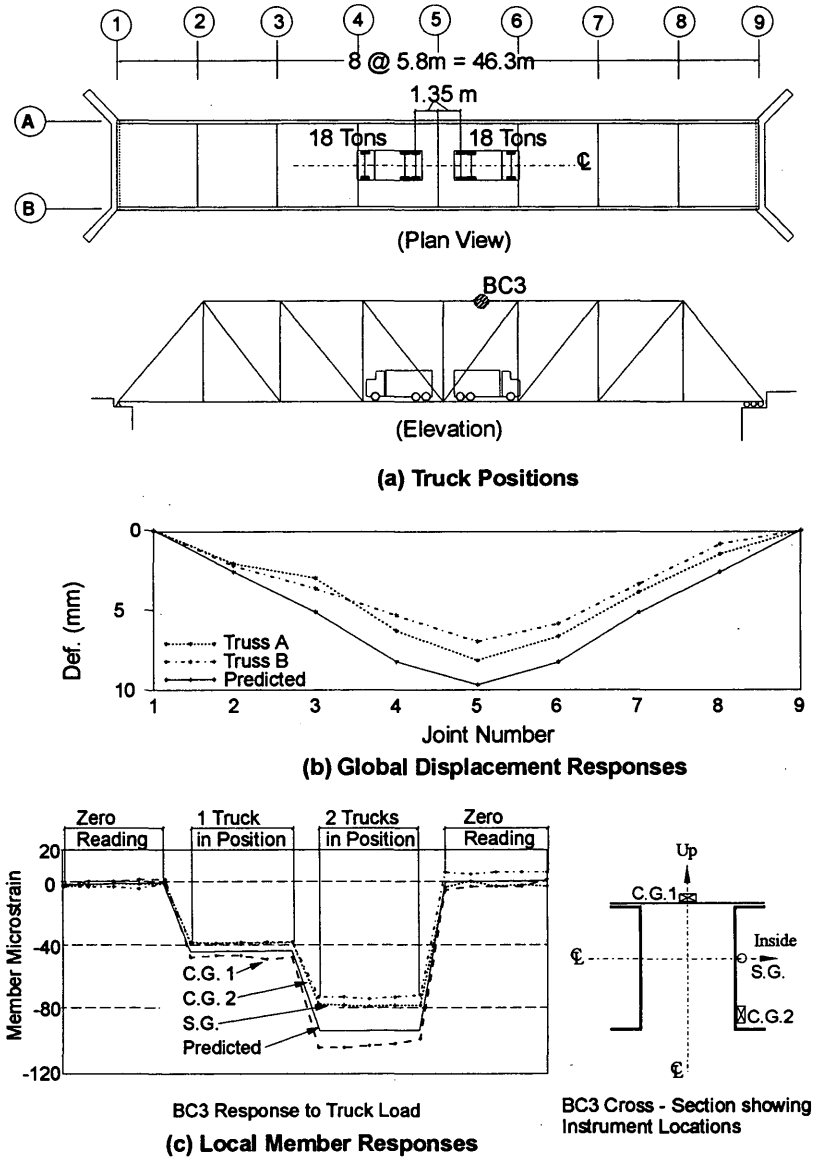

FIGURE 8 Nondestructive truck-load testing.

ner because of the surge. However, the bridge did not collapse and the test equipment could be salvaged after cribbing the failed truss.

Figure 10 shows the global and local responses at the final phases of destructive tests of the Camelback. The test setup for the Camelback was similar to that of the Pratt, and 91 loading cycles were applied to this bridge. The member labeled BT8 yielded initially at a load of 458 tons. The local responses of this member indicate that elongation at the midpoint along a 30.5-cm gauge length reached 1.3 percent, whereas the elongation measured along the complete length of the member exceeded 1.6 percent. In spite of such local strains, a failure could not be induced with the available displacement capabilities of the loading system, and the bridge did not reveal any obvious signs of distress other than two members of a portal strut buckling at 622 tons (19 equivalent HS 20–44 trucks). Particularly interesting is the nature of hardening of the Camelback responses at both the member and the structural levels in Figure 10. The member and structural responses appear to have been more affected by the local yielding of the lacing and the rivets than yielding of the material in the main components of the built-up members.

DISCUSSION AND CONCLUSIONS

Public Safety

Even though some members and connections experienced rusting and deterioration, the truss capacities of the test bridges were not adversely affected by this deterioration at the serviceability, damageability, and failure limit states. Therefore, it is possible to conclude that simply aging and scattered surfacial rusting of the trusses that are constructed with built-up members connecting together by gusset plates and rivets should not constitute an immediate public safety hazard if the bearings, abutments, and floor members are sound.

The writers have to qualify that in the test only the principal girders of the floor system were loaded. There may be cases in which secondary elements of a floor system may govern load capacity. More important, a number of trusses with eye-bar connections are still in service. The most relevant conclusion that the writers can extract from this research is that in view of the successful performance of the test specimens, it is important to differentiate between the segment of truss bridge inventory and the desirable characteristics of the test specimens and assign the highest program priority to those aged truss bridges that do not possess the rigid gusset-plate connections or other sound design and construction attributes of the test specimens.

Bridge Behavior Mechanisms

The tests confirmed that the important parameters that affect the capacity of the test bridges are far more complex than just local deterioration. Through-truss bridges are externally nonredundant; however, if the supports are sound, engineers should take advantage of the internal redundancy provided by the built-up and rigidly connected truss elements, the floor system, and portal bracing. Clearly, bridge behavior cannot be accurately modeled by just decreasing the cross-sectional properties by an amount corresponding to the corroded portions of members. The exact amount of corrosion cannot be identified easily, and the effects of various levels of deterioration are unknown. Moreover, deep pockets of corrosion (randomly distributed) did not influence bridge capacity because the remaining material provided adequate elongation capacity until structural failure was precipitated by other mechanisms.

The measured responses indicated that the roller bearings of both bridges had not been functioning for some time as ideal rollers. Because of this, the bridges were acting as arches, a phenomenon that alters truss behavior. The frozen rollers did not transfer tension to the lower chords particularly close to the supports. This mechanism stiffened the trusses and accumulated more energy in the

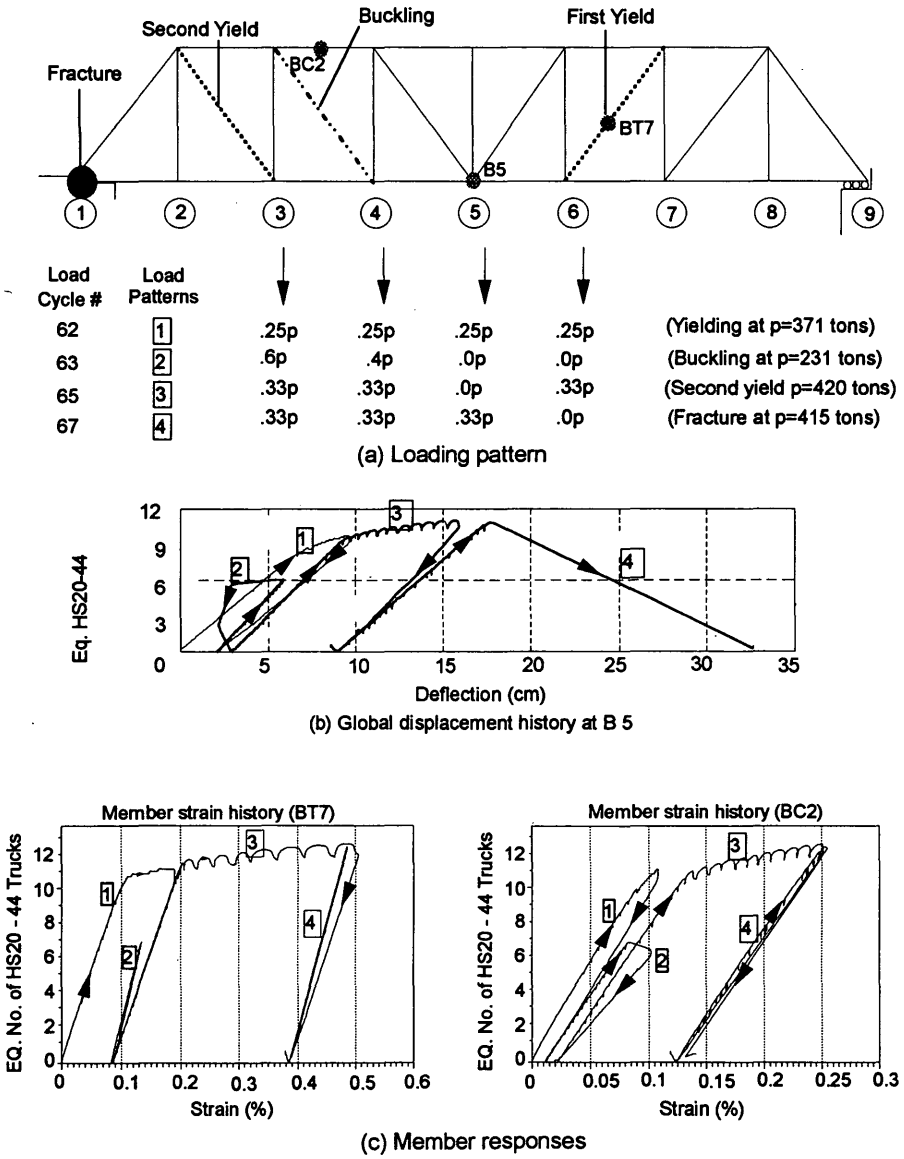

FIGURE 9 Pratt bridge: behavior and failure modes.

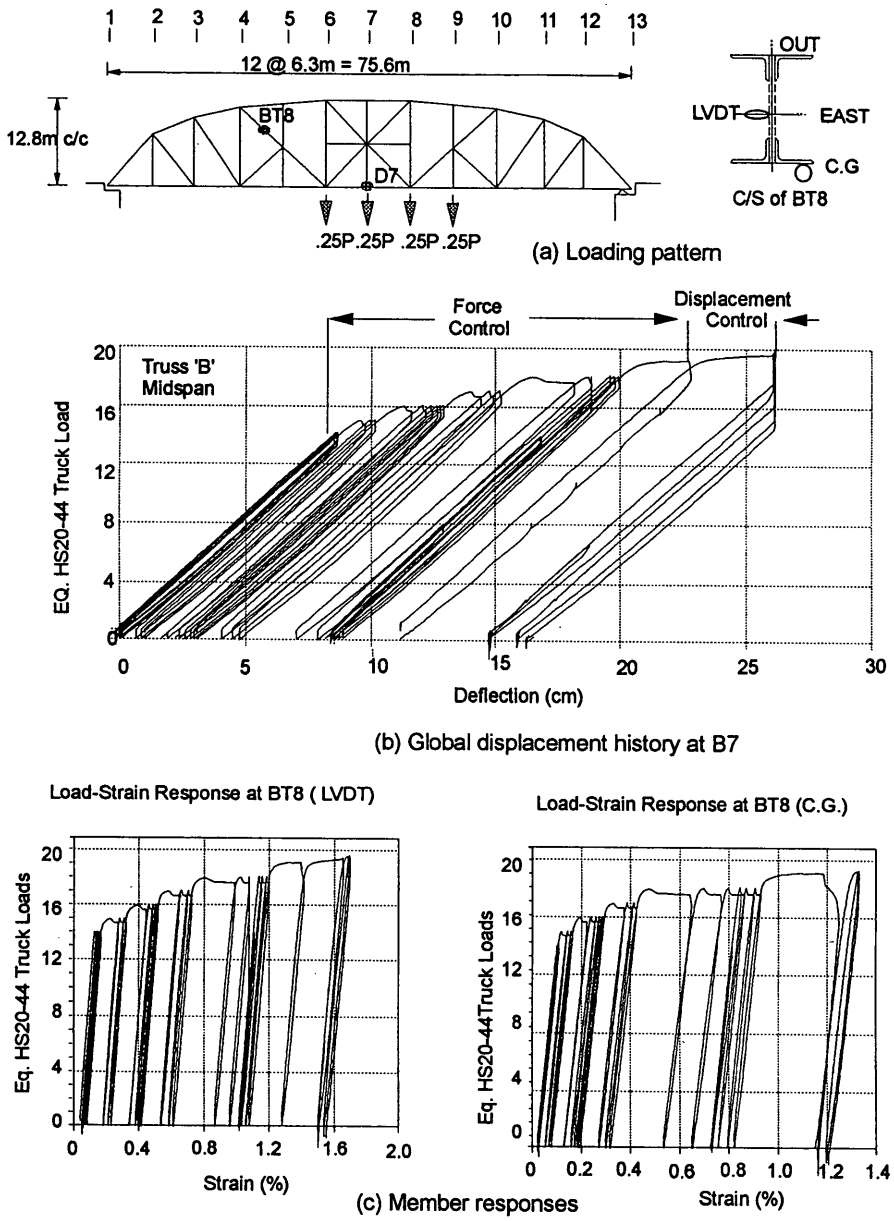

FIGURE 10 Destructive test responses of the Camelback Bridge.

upper chord than if the rollers could move freely. When the applied loads reached a critical level of over 12 rating trucks, the rollers of the Pratt started to move freely, and some of the energy that accumulated in the upper chord was suddenly released. This mechanism caused brittle failure of the Pratt. In the case of the Camelback, the roller movement was limited by the abutment at load levels exceeding 10 rating trucks. The abutment confined the rollers, and because it could develop sufficient lateral reaction, a sudden energy release did not happen.

On the basis of the experiences during the destructive tests, bridge performance at the advanced limit states would be more desirable if the rollers were free to slide as envisioned in their design. Therefore, in maintaining through-truss bridges it is recommended that the rollers be clean to ensure their free travel.

Analytical Predictions

Actual behavior and limit states of the deteriorated test bridges could not be predicted even though they possessed simple structural configurations. Although the forces in some of the members could be estimated in truck load tests, forces in the lower chord elements were overestimated and the predicted deflections were off by about 15 percent. The stiffnesses were off because of the frozen rollers,

effects of the floor and portal bracing systems, and the gusset plates, which reduced the effective length of the members. The capacities of the test bridges could not be predicted without conducting the experimental studies. Failure modes (the brittle failure of the Pratt and buckling of strut members of the Camelback) and some important mechanisms (variations in the strain field within a cross section, variation of post-yielding strains along the deteriorated members, post-yield hardening in built-up latticed members caused by lattice yielding) could not be predicted without destructive testing.

Fastening the timber floor system to the steel beams not only considerably increased the vertical stiffness of the deck but also significantly contributed to the lateral stability of the bridge at the deck level. Such a floor system could eliminate the need for bottom x-bracings. Elimination of x-bracings is a valuable consideration because typically these are the most deteriorated elements of older truss bridges.

Retrofit

The Pratt and Camelback resisted total loads equivalent to 12.8 and 19 HS20-44 trucks, respectively. After completion of each destructive test, no evidence of distortion or failure was found at the connections that were retrofit. The effectiveness of the retrofit was demonstrated under the heavy concentrated loads that the connections experienced during destructive testing. Therefore, it is concluded that it should be possible to retrofit similar bridges up to acceptable levels of safety with minimal effort and cost. Truss connections may be upgraded easily by inserting properly designed triangular plates that are welded to truss members behind the existing gussets. This method maintains the aesthetics and the original appearance of the joints while providing the extra strength needed to assist deteriorated rivets and gusset plates. In the case of rivet deterioration alone, lines of simple fillet welds between a healthy gusset and the truss member may be sufficient to compensate for rivet (fastener) losses.

The bottom chords of most older trusses are designed to be slimmer than the top chord, and they are generally more vulnerable to deterioration because of their geometric position and tensile strain. To reduce the risk of failure in a deteriorated bottom chord, additional redundancy would be desirable. High-strength cables posttensioned alongside and parallel to the bottom chord may provide redundancy. In the Pratt, only the end panels of the bottom chords were posttensioned by cables. A continuous posttensioned cable extending all the way along the bottom chord would have been more effective.

ACKNOWLEDGMENTS

Research has been conducted at the Cincinnati Infrastructure Institute with support provided by the Ohio Department of Transportation (ODOT), FHWA, the National Science Foundation (NSF), and the Franklin County Engineer. The writers express their appreciation to Messrs Edwards, Dalal, Hanhilammi, and Barnhart of ODOT, Mr. Sherman of Franklin County, Mr. Shamis of Ohio FHWA, and Dr. Chong of NSF for their encouragement and support. Corporate assistance was provided by GOETTLE, OPTIM Megadac, SCHENK-PEGASUS, and PCB Piezotronics. Excellent support was provided by CII research support personnel and many graduate students.

REFERENCES

1. Sessions, L., B. Blanchard, and J. Locke. Over the Hill Bridges. *Journal of Modern Steel Construction*, Vol. 33, No. 2. American Institute of Steel Construction, Feb. 1993.
2. Klaiber, F. W., K. F. Dunker, T. J. Wipf, and W. W. Sanders, Jr. Methods of Strengthening Existing Highway Bridges. In *Transportation Research Board 293*, TRB, National Research Council, Washington, D.C., 1987.
3. *Special Report 222: Bridges on Secondary Highways and Local Roads, Rehabilitation and Replacement.* TRB, National Research Council, Washington, D.C., 1980.
4. Klaiber, F. W., W. W. Sanders, and H. A. Elleby, *NCHRP Report 607: Ultimate Load Test of a High-Truss Bridge.* TRB, National Research Council, Washington, D.C., 1976.
5. Bakht, B., and L. G. Jaeger. Bridge Testing: A Surprise Every Time. ASCE *Journal of Structural Engineering*, Vol. 116, No. 5, 1990.
6. Aktan, A. E., M. J. Zwick, R. A. Miller, and B. M. Shahrooz. Nondestructive and Destructive Testing of a Decommissioned RC Slab Highway Bridge and Associated Analytical Studies. In *Transportation Research Record 1371*, TRB, National Research Council, Washington, D.C., 1993.
7. Aktan, A. E., K. L. Lee, and V. Dalal. Multireference Modal Testing For Bridge Diagnostics. *Proc., Structural Materials Technology, NDT Conference, New Jersey DOT and FHWA*, Feb. 1994.
8. Aktan, A. E., K. L. Lee, C. Chuntavan, S. Hosahalli, and T. Aksel. Modal Testing For Structural Identification and Condition Assessment of Constructed Facilities. *Proc., 12th International Modal Analysis Conference*, Honolulu, Hawaii, Jan. 1994.
9. *Standard Specifications of Highway Bridges*, 14th ed. AASHTO, Washington, D.C., 1989.
10. *Guide Specifications for Strength Evaluation of Existing Steel and Concrete Bridges.* Washington, D.C., 1992.

Publication of this paper sponsored by Committee on Dynamics and Field Testing of Bridges.

Fatigue Behavior of Noncomposite Reinforced Concrete Bridge Deck Models

MICHAEL F. PETROU, PHILIP C. PERDIKARIS, AND AIDONG WANG

The fatigue performance of the AASHTO and Ontario Highway Bridge Design Code (OHBDC) designs for noncomposite reinforced concrete bridge decks was studied on the basis of tests conducted on small-scale physical models. The type of fatigue loading has a profound influence on the fatigue behavior of the decks. Under a moving constant wheel-load, the initial two-way deck slab action changes to a one-way slab action, whereas under a stationary pulsating load the two-way action is maintained until failure. The bridge decks subjected to a stationary pulsating load exhibited a flexural radial cracking; those under a moving constant wheel-load exhibited a flexural gridlike pattern similar to the grid of the bottom steel layer. For a given applied fatigue load level, the decks subjected to a stationary pulsating loading regime exhibited higher fatigue life than those subjected to a moving constant wheel-load. On the basis of an exponential curve fit of the fatigue data in this study, the 2.5 million load cycle deck fatigue strength under a stationary pulsating load ranges between 0.47 and 0.54 P_u (safety factor against a 2.5 million load cycle fatigue failure of 5 to 12), where P_u is the measured static ultimate strength. On the other hand, the 2.5 million wheel-load passage deck fatigue strength under a moving constant wheel-load is estimated to be between 0.21 and 0.28 P_u (safety factor of 3 to 4). If the efficiency of the deck fatigue design is determined by the number of wheel-load passages on the deck at a given moving wheel-load level ratio (P/P_u) without deck failure, the OHBDC deck design appears to be more efficient than the AASHTO design.

Current AASHTO Code provisions (*1*) require concrete bridge decks to be orthotropically reinforced. They are designed as beams transverse to the traffic direction supported on the steel girders and carrying the traffic loads in flexure. On the basis of the AASHTO deck design, a concrete deck of a steel stringer bridge is reinforced for flexure transversely to the steel girders with a steel ratio of about 0.7 percent in each top and bottom steel layer and longitudinally (traffic direction) with a steel ratio of about 0.35 percent for each steel layer. This approach does not take into account the two-way slab action in the bridge deck and the enhancement of its flexural and shear ultimate strength caused by membrane compressive action (*2–9*).

Since the early 1960s, the lack of adequate understanding of the fatigue behavior of concrete deck slabs has started to be alarming in view of the ever-growing intensity of traffic and the serious deterioration of the highway bridge system. It is becoming increasingly important to determine the effect of moving wheel-loads on the fatigue structural response of reinforced concrete decks, including the cracking pattern and failure mode. Extensive studies on the failure mechanism of small-scale reinforced concrete bridge deck models subjected to static and stationary pulsating concentrated loads were performed at Queen's University at Kingston, Ontario, Canada (*8–11*), University of Petroleum and Minerals, Dhahran, Saudi Arabia (*2*), and the University of Texas at Austin (*12,13*) and Case Western Reserve University (*3–7,14,15*) in the United States. On the basis of the results of the full-scale and small-scale tests performed under static and stationary pulsating loads at Queen's University, an "isotropic" steel reinforcement pattern with equal amounts of steel reinforcement of 0.3 percent in the transverse and longitudinal directions (each top and bottom steel layer) was adopted in the Ontario Highway Bridge Design Code [OHBDC, (*16*)]. This steel reinforcement arrangement reduced the reinforcement content in the deck by up to 60 percent, considerably increasing the durability of such decks because of better protection of the top steel layer and undoubtedly lowering their construction and maintenance cost.

Tests performed in Japan (*17,18*) showed that the flexural and shear rigidity of the deck slab under a "stepwise" moving wheel-load are dramatically reduced compared with that under a stationary pulsating load. One passage of a stepwise moving wheel-load consists of applying a single concentrated load in sequence at a set of preselected equally spaced points on the deck along the loading path. A loading setup was designed and constructed at Case Western Reserve University to simulate a moving constant wheel-load in an extensive experimental program funded by the Ohio Department of Transportation (ODOT) and FHWA (*3,4,14*). Fatigue studies under moving load were also performed in Japan at Osaka City University (*19,20*). The preliminary experimental results by Perdikaris and Beim (*3,14*), Perdikaris et al. (*4*), and Sonoda et al. (*20*) indicated a substantial reduction in the bridge deck's fatigue life if the decks were subjected to a moving wheel-load instead of a stationary pulsating load. In the former research study (*3,4,14*), "isotropically" reinforced OHBDC decks and "orthotropically" reinforced AASHTO decks were fatigued under moving wheel-loads equal to 60 percent of their static ultimate strength to determine their fatigue strength under overload conditions. The OHBDC decks exhibited longer fatigue lives than the AASHTO decks under this high fatigue load level.

The objective of this paper is to present selected results on the fatigue response of noncomposite reinforced concrete bridge deck models and compare the fatigue performance of the AASHTO and OHBDC deck design.

EXPERIMENTAL SETUP

Full-Scale Bridge Structure

The prototype highway bridge structure represents a simply supported noncomposite reinforced concrete deck-on-steel girder bridge with a span of 15.24 m (50 ft) and a thickness of 21.6 cm

M. F. Petrou, Department of Civil Engineering, University of South Carolina, Columbia, S.C. 29208. P. C. Perdikaris and A. Wang, Department of Civil Engineering, Case Western Reserve University, Cleveland, Ohio 44106.

(8.5 in.). The deck slab is supported on four W36 × 150 steel girders spaced at 2.13 or 3.05 m (7 or 10 ft). Two deck designs are studied in this paper. According to the AASHTO design provisions, the deck slab is assumed to be orthotropically reinforced with No. 6 Grade 60 deformed steel rebars [d = 19 mm (0.75 in.)]. This orthotropic flexural steel reinforcing arrangement (AASHTO) corresponds to steel ratios of about 0.7 and 0.35 percent in each steel layer. The isotropic steel reinforcing pattern (OHBDC), on the other hand, consists of transverse and longitudinal flexural steel ratio of 0.3 percent for each top and bottom steel layer.

Bridge Deck Model (1/6.6 Scale)

The full-scale W36 × 150 steel girders were modeled by M6 × 4.4 steel I-beams. Diagonally braced L-shaped steel struts sized 25.4 × 12.7 × 3.2 mm (1 × ½ × ⅛ in.) were used to model the transverse bridge diaphragms between adjacent steel girders, as shown in Figure 1. The deck slab thickness is 36 mm (1.4 in.). The deformed steel wire used as model steel reinforcement has a nominal diameter of 2.8 mm (0.11 in.) and a cross-sectional area of 6.1 mm^2 (0.0095 in.^{2}). The dimensions of the model bridge specimen for a 2.13-m (7-ft) full-scale girder spacing are indicated in Figure 1. The forms for the concrete deck specimens were made of Plexiglas, which is an adequately stiff, lightweight, and reusable material. No steel shear studs were used because only noncomposite deck behavior was studied.

Each deck specimen was divided transversely into three "lanes." Each lane, which is the part of the deck between two adjacent steel girders with a length equal to the deck's length and a width equal to the girder spacing, is labeled east (E), center (C), and west (W) and divided longitudinally into three regions labeled north (N), center (C), and south (S), as indicated in Figure 1. Thus, nine deck regions (SW, CW, NW, SC, CC, NC, SE, CE, and NE) were tested under a static or a stationary pulsating load and three lanes were tested under a moving wheel-load.

For the OHBDC deck models, the steel reinforcement wires were spaced at about 56 mm (2.2 in.) in both directions (top and bottom steel layer). In the case of the AASHTO deck models, the deformed steel wires were spaced transversely and longitudinally at about 24 and 48 mm (0.94 and 1.88 in.), respectively. The concrete cover was about 4 mm (0.15 in.) for the top steel layer (longitudinal) and 8 mm (0.3 in.) for the bottom steel layer (transverse).

Materials

The prototype material behavior of concrete and steel reinforcement is properly modeled (*21*) by scaling the aggregates for the model concrete and using deformed wire for the model reinforcement. The measured average uniaxial cylinder concrete compressive strength is about 44 MPa (6,400 psi), as indicated in Table 1. The measured average concrete tensile strength based on splitting tension cylinder tests is 5.7 MPa (830 psi) for the cylinders 5.1 × 10.2 cm (2 × 4 in.) and 4.5 MPa (650 psi) for the cylinders 10.2 × 20.4 cm (4 × 8 in.).

The assumed full-scale steel reinforcement of No. 6 Grade 60 deformed steel bars [d = 19 mm (0.75 in.)] with a yield strength of 413 MPa (60 ksi) and modulus of elasticity of 199,810 MPa (29,000 ksi) is modeled with D-1 steel wire deformed in the models laboratory. The deformed steel wire was annealed for 2 hr at 580°C (1,076°F) to lower its yield strength to the desired level of about 413 MPa (60 ksi) and increase its ductility (strain of about 20 percent at failure). The nominal diameter of the model steel reinforcement is about 2.8 mm (0.11 in.).

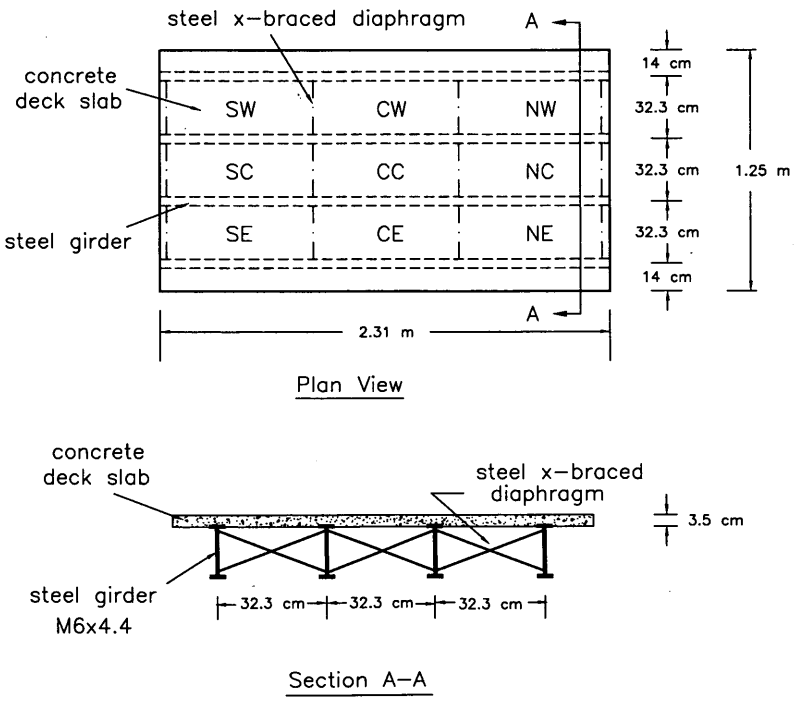

FIGURE 1 Dimensions of the 1/6.6-scale bridge deck model with a prototype girder spacing of 2.13 m (1 m = 3.28 ft and 1 cm = 0.394 in.).

TABLE 1 Experimental Program for 1/6.6-Scale Bridge Deck Models (1 m = 3.28 ft, 1 cm = 0.394 in., and 1 MPa = 0.145 ksi).

Deck Specimen	Full-scale Girder Spacing (m)	Flexural Steel Reinforcement Pattern	Average Compressive Strength, f_c' (MPa)		Number of Tests		
			5.1x10.2 cm Cylinder	10.2x20.4 cm Cylinder	Static Load	Pulsating Load	Moving Load
BI3-7SP(1)	2.1	Isotropic[a]	-	-	5	4	-
BI3-7SPM(2)			-	-	2	1	2
BI3-7M(3)			41.8	-	-	-	4
BI3-10SP(1)	3.0	Isotropic	50.0	48.0	6	3	-
BI3-10M(2)			49.5	48.0	-	-	3
BI3-10SPM(3)			42.4	44.6	1	2	2
BI3-10PM(4)			40.1	40.1	-	3	2
BO-7SPM(1)	2.1	Orthotropic[b]	45.6	45.9	2	2	2
BO-7PM(2)			39.7	37.1	-	3	2
BO-10SP(1)	3.0	Orthotropic	48.3	41.1	6	3	-
BO-10M(2)			-	-	-	-	3
BO-10M(3)			42.2	-	-	-	3
BO-10PM(4)			39.5	-	-	2	3

Notes:
[a]Isotropic: ρ_l =0.003 (longitudinal) and ρ_t=0.003 (transverse); top and bottom-Ontario design.
[b]Orthotropic: ρ_l =0.0035 (longitudinal) and ρ_t=0.007 (transverse); top and bottom-AASHTO design.

Loading Setup

The loading setup used for the static and stationary pulsating load tests is a steel reaction frame bolted to the floor and a 222.5-kN (50-kips) hydraulic actuator with a maximum stroke of 15.2 cm (6 in.). The wheel-load is applied to the deck specimen at specific locations through a rubber pad 9.5 mm (3/8 in.) thick bonded to a steel plate 91.4 × 38.1 × 9.5 mm (3.6 × 1.5 × 3/8 in.), which models a representative full-scale 61 × 25.4 cm (24 × 10 in.) contact area of a pair of truck tires. The stationary pulsating load tests were performed using load control at an average frequency of 7 Hz. The loading frequency of 7 Hz for the 1/6.6-scale models corresponds to a frequency of about 1 Hz for the full-scale bridge deck structure. A truck traveling speed of 88.5 km/hr (55 mph) for a 15.24-m (50-ft) span bridge corresponds to a loading frequency of about 1.7 Hz for any point of the deck. The pulsating load varied sinusoidally with a minimum load level of about 2.2 kN (500 lb) and a maximum load level equal to that selected for each test.

A moving constant wheel-load setup was developed in the first phase of this study (*3,4,14*). As shown in Figure 2, it consists of a moving steel trailer bolted to a hydraulic jack that applies a constant wheel-load to the deck specimen through a steel reaction frame attached to the floor. The wheel-load is applied to the deck through a steel wheel coated with polyurethane attached to the bottom of the jack by a steel yoke. A pressure accumulator enables the applied load to be controlled within a variation of about ±3 percent. The hydraulic actuator with a 15.2-cm (6-in.) stroke has a capacity of 133.5 kN (30,000 lb). The jack-wheel assembly, powered by a hydraulic motor, moves back and forth at a maximum speed of about 61 cm/sec or 2.2 km/hr (2 ft/sec or 1.4 mph). Similitude requirements demand the traffic speed in the full-scale deck to be the same as in the models. Thus, because the model speed is far lower than a reasonable "design" speed of 88.5 km/hr (55 mph), the results of this study on the fatigue response under a constant moving wheel-load do not include any possible dynamic effects present at normal traffic speeds.

Experimental Program: Parameters, Instrumentation

The experimental program discussed in this paper is shown in Table 1. The bridge deck models were subjected to concentrated static load, stationary pulsating, and moving constant wheel-load (*22,23*). Only the experimental results on the fatigue behavior (cracking patterns and failure modes) for the 1/6.6-scale bridge deck models (reinforced according to AASHTO and OHBDC specifications) under stationary pulsating and moving constant wheel-load are discussed. Full-scale girder spacings of 2.13 and 3.05 m (7 and 10 ft) were considered. The boundary conditions of the deck, which affect the deck restraint level, varied from "simply supported" (bridge deck panel models, which are not presented here) to "continuous" (central region of the bridge deck models).

The instrumentation used for the tests included displacement transducers (DCDTs), load cells, and strain gauges. For acquiring

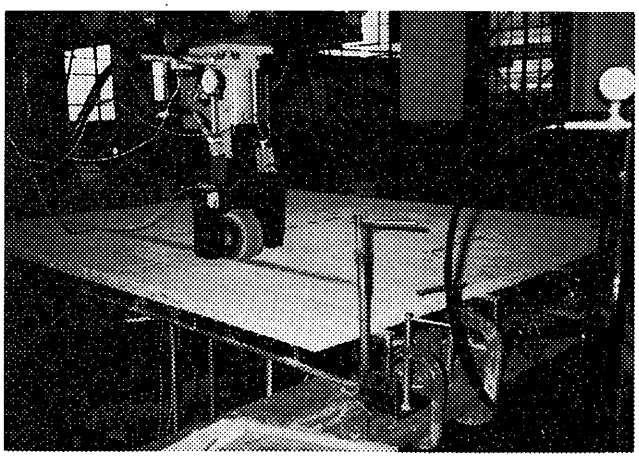

FIGURE 2 Moving constant wheel-load setup.

the global structural response of the bridge deck and assessing the induced static and fatigue damage in the concrete deck slab, three DCDTs were used to measure the vertical displacement of two adjacent steel girders and the deck midway between the two girders at a specified section along the deck. Epoxy-bonded electrical resistance foil-backed strain gauges were used to measure the axial strains in the steel reinforcement at selected locations of the top and bottom steel layer, flexural strains in the steel girders, and strains on the concrete deck surface.

DISCUSSION OF EXPERIMENTAL RESULTS

Effect of Load Level

The log of the number of load cycles to failure under stationary pulsating load, $\log N_{cf}$, and the log of the number of wheel-load passages to failure under moving constant wheel-load, $\log N_{pf}$, are presented as a function of the applied model load and the ratio of applied model load to deck static ultimate strength in Figures 3 through 6. The fatigue data correspond to a punching deck failure at a specific deck region subjected to a given stationary pulsating or moving constant wheel-load level. In the case of the moving wheel-load fatigue tests, a deck lane will fail sequentially at various locations, whereas the test is usually continued until a punching deck failure eventually occurs in the vicinity of midspan (usually the second or third consecutive failure). This means that for a given moving wheel-load fatigue level there could be a maximum of three fatigue strength data points.

Stationary Pulsating Load

For unrealistically high stationary pulsating concentrated load levels that are more than 60 percent of the deck's measured static ultimate strength, P_u, the deck fatigue strength appears to be less than 10,000 load cycles. The primary deck failure mode at this high fatigue load level is punching but for a load level lower than 0.6 P_u, the primary fatigue failure in the deck occurs in a combined flexural-punching mode. Usually the lower the applied load level the more primary the flexural failure. For bridge decks subjected to static loads or high

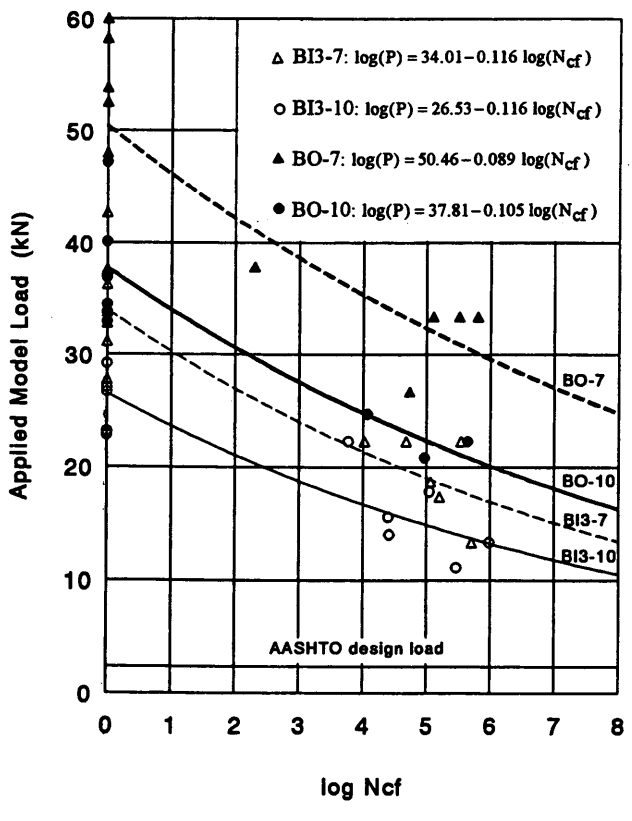

FIGURE 3 *S-N* fatigue curves under stationary pulsating load in terms of the applied load level versus log N_{cf} (1 kN = 225 lb).

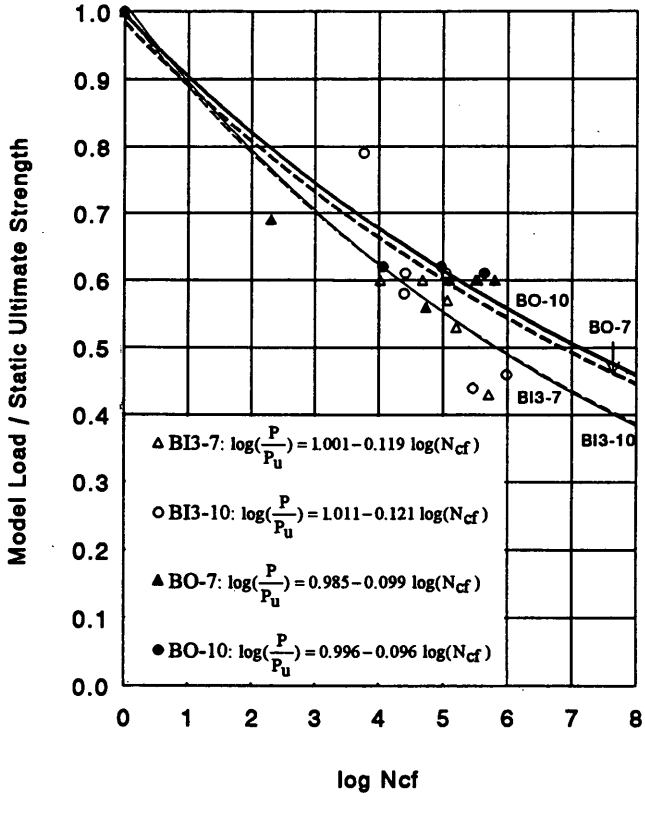

FIGURE 4 *S-N* fatigue curves under stationary pulsating load in terms of the ratio of applied load to static ultimate strength versus log N_{cf}.

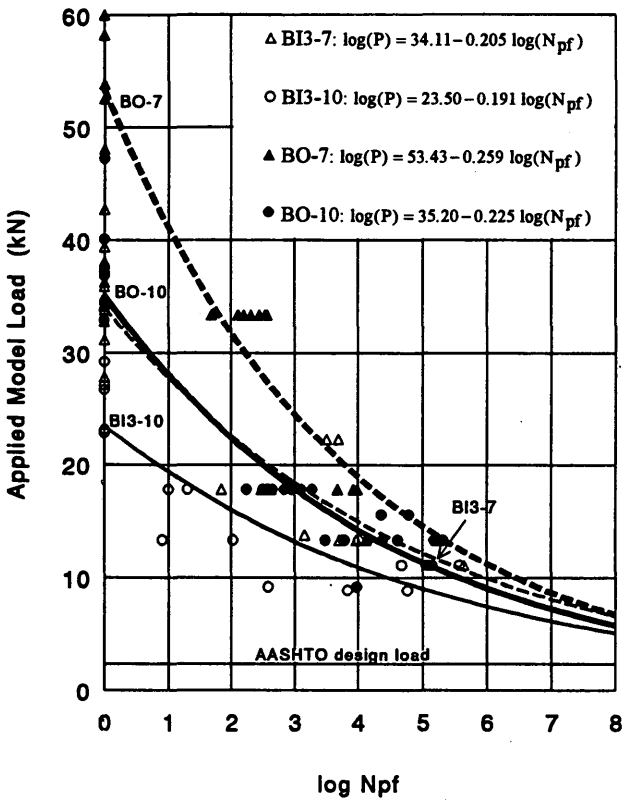

FIGURE 5 *S-N* fatigue curves under moving constant wheel-load in terms of the applied load level versus log N_{pf} (1 kN = 225 lb).

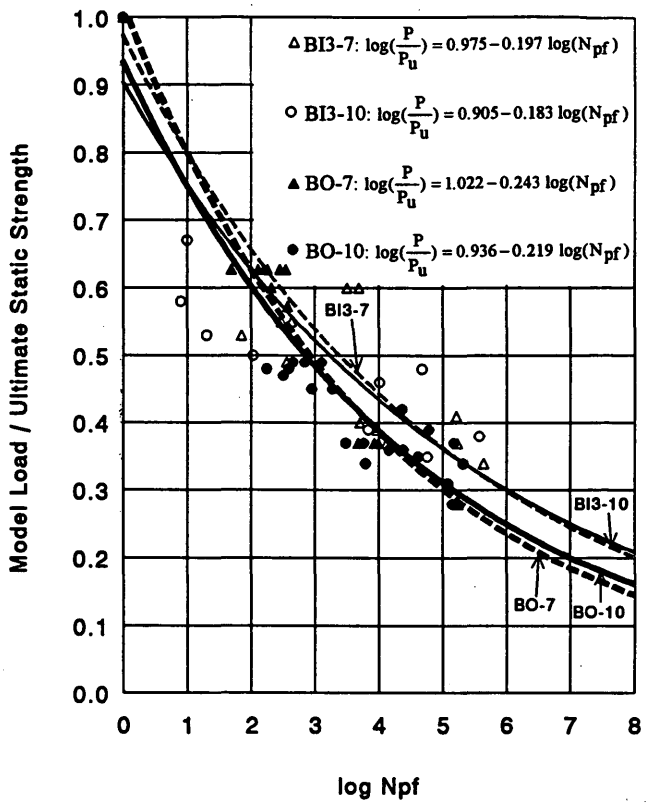

FIGURE 6 *S-N* fatigue curves under moving constant wheel-load in terms of the ratio of applied load to static ultimate strength versus log N_{pf}.

fatigue load levels, failure occurs suddenly without yielding of the steel reinforcement beyond the loaded area, whereas for bridge decks under low fatigue load level extensive yielding of the steel reinforcement is necessary for failure to occur. Further discussion of this behavior will be presented in another paper.

The estimated fatigue strength values in terms of the static ultimate strength and maximum measured AASHTO deck static ultimate strength ratios are presented in Table 2 for 1,000, 2.5 million, and 100 million load cycles. The safety factors against fatigue failure after 2.5 million load cycles presented in Table 2 are based on a model design load of 2.3 kN (525 lb). The model design load is determined by dividing the full-scale AASHTO design load of 92.6 kN (20.8 kips), including an impact factor of 1.3, by S_l^2, where S_l is the length scale factor. The fatigue strength levels are estimated on the basis of the following expression:

$$\log P \text{ or } \log\left(\frac{P}{P_u}\right) = A + B \cdot \log N_{cf} \qquad (1)$$

where A and B are constants estimated by the least-squares method (see Figures 3 and 4). The exponential curve fitting of the experimental data points presented in Figure 3 (P versus $\log N_{cf}$) is based on Equation 1 and corresponds to correlation coefficients between 0.71 and 0.86. In Figure 4 (P/P_u versus $\log N_{cf}$), the exponential curve fitting of the data points corresponds to correlation coefficients between 0.92 and 0.98.

The predicted bridge deck fatigue strength at 2.5 and 100 million load cycles under stationary pulsating concentrated load ranges from 0.27 to 0.48 P_a and 0.22 to 0.41 P_a, respectively, where P_a is the largest measured AASHTO deck static ultimate strength. The predicted safety factor against fatigue failure in the deck under a stationary pulsating load for the 2.5 million load cycle limit is about 5 to 7 for the OHBDC design and 8 to 12 for the AASHTO design (see Table 2). The predicted deck fatigue strength at 2.5 million load cycles expressed in terms of the deck's static ultimate strength is at least twice the cracking load level and ranges between 0.47 and 0.54 P_u, as indicated in Figure 4 and Table 2. This value is close to the generally accepted 2.5 million load cycle fatigue strength of plain concrete and consistent with that of 0.5 P_u according to Batchelor et al. (*11*) and slightly lower than 0.6 P_u according to Azad et al. (*2*). The AASHTO decks exhibited higher fatigue strengths than the OHBDC decks when they were subjected to the same load level, the same ratio of load to static ultimate strength, or the same ratio of load to maximum measured AASHTO static ultimate strength.

On the basis of steel reinforcement strain measurements (*22,23*) under a stationary pulsating load, there is a two-way action in the deck slabs. The observed cracking pattern is similar to that produced by a static concentrated load. On the top deck surface, the damage around the loaded area is minor. A fan-shaped pattern of radial positive cracks emanating from the load application point is observed at the bottom deck surface under the loaded region. The radial bottom flexural cracks open and close as the applied pulsating load varies from the minimum to the maximum value. The reinforcing flexural bars blunt the cracks, and larger deformations in the flexural steel reinforcement are required for the cracks to propagate in the deck. As soon as the steel reinforcement yields, the

TABLE 2 Predicted Fatigue Strength of Reinforced Concrete Bridge Decks Based on Exponential Curve Fitting of Experimental Data

Specimen	Predicted Fatigue Strength (P/P_a and P/P_u)												Safety Factor	
	Stationary Pulsating Load (number of load cycles, N_{cf})						Moving Constant Wheel-load (number of wheel passages, N_{pf})							
	1,000		2,500,000		100,000,000		1,000		2,500,000		100,000,000		Pulsating	Moving
	P/P_a	P/P_u	P/P_a	P/P_u	P/P_a	P/P_u	P/P_a	P/P_u	P/P_a	P/P_u	P/P_a	P/P_u	N_{cf}=2.5 mil.	N_{pf}=2.5 mil.
BO-7	0.64	0.73	0.48	0.52	0.41	0.45	0.41	0.49	0.17	0.21	0.11	0.14	12.2	4.4
BO-10	0.58	0.74	0.41	0.54	0.35	0.46	0.38	0.48	0.18	0.23	0.12	0.16	8.3	3.6
BI3-7	0.40	0.70	0.27	0.47	0.22	0.39	0.31	0.54	0.15	0.28	0.11	0.20	6.9	3.9
BI3-10	0.40	0.70	0.27	0.47	0.22	0.38	0.28	0.52	0.15	0.28	0.11	0.21	5.4	3.0

Notes:
P = Applied load.
P_a = Largest static ultimate strength of "AASHTO" decks.
P_u = Static ultimate strength.

cracks propagate rapidly, and the cumulative damage of the deck increases. This explanation is supported by the fact that yielding of the steel reinforcement underneath the loaded area occurs at a load level of 0.4 to 0.6 P_u, which is similar to the 2.5 million load cycle fatigue strength range under a stationary pulsating load. At this point, the total and the per-cycle (static "load-unload" cycles) peak deck deflection versus the number of load cycles increase rapidly. After the deck damage reaches a critical level, the deck collapses.

Moving Constant Wheel-Load

The deck fatigue life is extremely short at less than 10 wheel-load passages under wheel-load levels higher than 0.7 P_u, as shown in Figure 6. The fatigue failure in the deck is sudden and is caused by punching shear. For lower wheel-load levels, flexure becomes the primary failure mode. The fatigue strength of the decks subjected to moving wheel-loads is consistently lower than that under stationary pulsating loads of the same magnitude or the same ratio of load to static ultimate strength. Because of time constraints, the fatigue tests performed under a moving load resulted in far fewer than 2.5 million wheel-load passages to failure. The highest number of wheel-load passages to failure recorded was 439,204 for the west-lane deck of B13-7SPM(3) subjected to a moving constant wheel-load of 11.1 kN (2,500 lb).

The moving wheel-load setup used in this study did not allow wheel-loads lower than 8.9 kN (2,000 lb). However, fatigue tests under model wheel-loads of 8.9 to 11.1 kN (2,000 to 2,500 lb), which give a good indication of the fatigue strength of the bridge decks, were performed. The estimated fatigue strength in terms of the static ultimate strength and largest measured AASHTO static ultimate strength is presented in Table 2 for 1,000, 2.5 million, and 100 million wheel-load passages. The safety factors against fatigue failure for the 2.5 million wheel passage limit are presented in the same table. The fatigue strength values presented in Table 2 are estimated using an exponential expression similar to that of Equation 1 (see Figures 5 and 6). The exponential curve fitting of the experimental data points presented in Figure 5 (P versus $\log N_{pf}$) corresponds to correlation coefficients between 0.74 and 0.88. In Figure 6 (P/P_u versus $\log N_{pf}$), the exponential curve fitting corresponds to correlation coefficients between 0.92 and 0.98.

The predicted bridge deck fatigue strength level at 2.5 and 100 million wheel-load passages under a moving wheel-load is about 0.16 P_a and 0.12 P_a, respectively (see Table 2). The predicted safety factor against fatigue failure in the deck under a moving constant wheel-load for the 2.5-million wheel passage limit is about 3 to 4 for the OHBDC and the AASHTO deck design. In terms of the measured deck static ultimate strength, the 2.5-million wheel-load passage limit fatigue strength of all decks is estimated at 0.21 P_u to 0.28 P_u, which is similar to the average cracking load level of 0.26 P_u. The cracking load level corresponds to the static concentrated load reached at the end of the linear elastic region of the load-deflection response curve of a deck. If the efficiency of a deck design is determined by the number of wheel-load passages on the deck at a given moving wheel-load level (percentage of the static ultimate strength) without deck failure, the OHBDC design appears to be more efficient than the AASHTO deck design. The deck slenderness has a minor effect on the efficiency of the two deck designs with respect to their fatigue behavior.

Fatigue under moving wheel-loads results in a gridlike bottom flexural cracking (transverse and longitudinal) matching the steel reinforcement pattern (*22,23*). Initially, a major longitudinal flexural crack forms at the bottom surface of the deck along the wheel-path midway between the two adjacent steel girders supporting the deck. As the moving wheel-load causes the opening and closing of this major longitudinal crack and forces it to propagate upwards, additional longitudinal cracks appear at the bottom of the deck. The longitudinal cracks open wider and wider with an increasing number of wheel-load passages, and transverse bottom flexural cracks (perpendicular to the steel girders) also form practically at the same spacing as that of the bottom transverse flexural steel reinforcement. Although the bottom longitudinal cracks open and close (flexural mode) as the wheel-load moves back and forth on the bridge deck, the bottom transverse cracks in addition to opening and closing (flexural mode) also slide up and down (shearing mode) causing continuous rubbing of the crack interfaces. This "reversing" shear

movement of the transverse crack surfaces causes degradation of the interface shear transfer mechanism. This also results in debonding along the steel reinforcement because the cracks in both directions form usually close to the bottom steel reinforcement in a gridlike pattern.

Cracking appears to be the major reason for fatigue failure of a bridge deck subjected to a moving wheel-load. This is supported by the fact that the 2.5-million wheel-load passage limit fatigue strength of the decks under moving wheel-load is similar to the average cracking load level under a concentrated static load. Therefore, although the necessary condition for fatigue failure under stationary pulsating load is yielding of the flexural steel reinforcement, the necessary condition for fatigue failure under moving wheel-load is flexural transverse and logitudinal cracking.

Effect of Type of Loading: Pulsating versus Moving

The development of the OHBDC for deck design was based on stationary pulsating load tests conducted on 1/8-scale composite bridge deck models (*11*). The fatigue strength at 2.5 million load cycles of those bridge decks was determined to be about 0.5 P_u for the orthotropic (AASHTO) and isotropic (OHBDC) designs. These findings, based on the AASHTO design load, correspond to safety factors against fatigue failure of 8 to 10. These results are consistent with the stationary pulsating load test findings in the present research study. One major difference, however, in the two testing programs is that the tests by Batchelor et al. (*11*) were conducted on composite bridge decks, whereas the present study dealt with the response of noncomposite bridge decks.

It is known that membrane compressive action in a laterally restrained concrete bridge deck slab is the major mechanism carrying the applied concentrated load. Membrane compressive forces are induced by the restraining action of the supports and the deck region surrounding the loaded area. This deck region, however, cannot provide the same membrane action if it is damaged during fatigue. Indeed, this is what probably happens in the case of fatigue under a moving wheel-load. Every loaded section in the deck along the load path is surrounded (at least in the longitudinal direction) by damaged regions that become less and less capable of providing the membrane compressive forces that a nondamaged region could have provided. This results in a gradual transition from a two-way to a one-way slab action. The wheel-load is eventually transferred primarily in the transverse direction (perpendicular to traffic), and the bridge deck becomes a series of parallel transverse beams linked together mainly by the steel and supported on the steel girders. If the concrete bridge deck is designed to transfer most of the wheel-load in the transverse direction (AASHTO design), the transformation of the two-way deck slab action into a one-way will probably be accelerated because of the already existing orthotropy in the deck.

CONCLUSIONS

1. For a given load level, decks subjected to a stationary pulsating concentrated load exhibited much higher fatigue strength than those fatigued under a moving constant wheel-load. The stationary concentrated pulsating load tests are not adequate in predicting the fatigue strength of concrete bridge decks subjected to traffic load.
2. The estimated fatigue strength of the reinforced concrete bridge deck models under a stationary pulsating load at 2.5 million load cycles is 0.47 to 0.54 P_u (P_u = measured static ultimate strength). These values correspond to safety factors against fatigue failure of about 5 to 12 [assuming a scaled model design load of 2.3 kN (525 lb)]. The 2.5-million wheel-load passage limit fatigue strength for the bridge decks subjected to a moving constant wheel-load is estimated to be about half of their fatigue strength under a stationary pulsating load. On the basis of an exponential curve fit of the experimental fatigue data, a fatigue strength of 2.5 million is predicted to be in the range of 0.21 to 0.28 P_u. This range of fatigue strength corresponds to safety factors against fatigue failure of about 3 to 4.
3. The predicted fatigue strength of the bridge decks under a moving constant wheel-load for 2.5 million wheel-load passages is in the same range as the average flexural cracking load level of the decks of $P_{cr} = 0.26\ P_u$. The predicted fatigue strength of the decks under a moving constant wheel-load for 100 million wheel-load passages ranges from 0.14 to 0.21 P_u, which is slightly lower than the average flexural cracking load level. It appears that the fatigue design specifications should not allow flexural cracking in concrete decks. The effect of shrinkage cracking has not been studied. On the other hand, under a stationary pulsating load the fatigue strength of the decks appears to be related to the yielding load level of the decks.
4. Bridge decks subjected to a stationary pulsating load exhibited flexural radial cracking (on the bottom deck surface) similar to that observed in the static load tests. However, the cracks at the bottom surface of the bridge deck models subjected to a moving constant wheel-load formed a gridlike pattern similar to that of the bottom steel layer. On the top deck surface, longitudinal negative cracks eventually formed above the steel girders adjacent to the deck region being tested and crushing of concrete occurred along the wheelpath, especially for the higher deck slenderness and lower steel ratio.
5. For a bridge deck subjected to a moving constant wheel-load, the initial two-way deck slab action is transformed to a one-way transverse slab action as deck failure is approached. For a similar deck subjected to a stationary pulsating load of equal peak value, the initial two-way slab action is maintained until deck failure occurs, usually because of punching.
6. If the efficiency of a deck design for fatigue is determined by the number of wheel-load passages on the deck at a given moving wheel-load level ratio (P/P_u) without deck failure, the OHBDC deck design appears to be more efficient than the AASHTO design. The deck slenderness has a minor effect on the efficiency of the two designs regarding the fatigue deck behavior.

ACKNOWLEDGMENTS

This research was funded by ODOT and FHWA. Their support is greatly appreciated. Special thanks are due to Steve Marine of the Structures Laboratory, who was a major contributor in the design and construction of the wheel-load setup, and Lindberg Heat Treating Co., Solon, Ohio, for kindly donating time for the annealing of the model steel reinforcement wires.

REFERENCES

1. *Standard Specifications of Highway Bridges*, 14th ed. AASHTO, Washington, D.C., 1989.

2. Azad, A. K., M. H. Baluch, M. Y. Al-Mandil, and M. S. Al-Suwaiyan, Static and Fatigue Tests of Simulated Bridge Decks. Experimental Assessment of Performance of Bridges. *Proc., of ASCE Convention*, Boston, Mass., Oct. 1986, pp. 30–41.
3. Perdikaris, P. C., and S. R. Beim, *Design of Concrete Bridge Decks*. Final Report FHWA/OH/RR-88-004. Ohio Department of Transportation, Aug. 1988.
4. Perdikaris, P. C., S. Beim, and S. Bousias, Slab Continuity Effect on Ultimate and Fatigue Strength of R/C Bridge Deck Models. *ACI Structural Journal*, Vol. 86, No. 4, July–Aug. 1989, pp. 483–491.
5. Perdikaris, P., and M. Petrou, Code Predictions Versus Small-Scale Bridge Deck Model Test Measurements. In *Transportation Research Record, 1290*, TRB, National Research Council, Washington, D.C., 1991, pp. 179–187.
6. Petrou, M. F., and P. C. Perdikaris, Small Scale Model Tests: Arching Action in Reinforced Concrete Bridge Decks. *Proc., 3rd International Conference on Short and Medium Span Bridges*, Toronto, Ontario, Canada, Aug. 1990.
7. Petrou, M. F. *Behavior of Concrete Bridge Deck Models Subjected to Concentrated Load-OHBDC vs. AASHTO*. M.S. thesis, Case Western Reserve University, Cleveland, Ohio, May 1991.
8. Hewitt, B. E. *An Investigation of the Punching Strength of Restrained Slabs With Particular Reference to the Deck Slabs of Composite I-Beam Bridges*. Ph.D. dissertation. Queen's University at Kingston, Ontario, Canada, March 1972.
9. Hewitt, B. E., and B. deV. Batchelor. Punching Shear Strength of Restrained Slabs. ASCE *Journal of the Structural Division*, Vol. 101, ST9, Sept. 1975, pp. 1837–1853.
10. Batchelor, B. deV., and B. E. Hewitt. Are Composite Bridge Slabs Too Conservatively Designed? Fatigue Studies. *Fatigue of Concrete, ACI Special Publication SP4-15*. 1974, pp. 331–346.
11. Batchelor, B. deV., B. E. Hewitt, and P. Csagoly. An Investigation of the Fatigue Strength of Deck Slabs of Composite Steel/Concrete Bridges. In *Transportation Research Record 664*, TRB, National Research Council, Washington, D.C., 1978, pp. 153–161.
12. Fang, I-K. Behavior of OHBDC-Type Bridge Deck on Steel Girders. Ph.D. dissertation. University of Texas at Austin, Dec. 1985.
13. Fang, I-K., J. Worley, N. H. Burns, and R. E. Klingner. Behavior of Isotropic R/C Bridge Decks on Steel Girders. ASCE *Journal of Structural Engineering*, Vol. 116, No. 3, March 1990, pp. 659–678.
14. Perdikaris, P. C., and S. Beim. RC Bridge Decks Under Pulsating and Moving Load. ASCE *Journal of Structural Engineering*, Vol. 114, No. 3, March 1988, pp. 591–607.
15. Wang, A. Fatigue Behavior of Small-Scale R/C Bridge Decks Subjected to Pulsating and Moving Loads. M.S. thesis. Case Western Reserve University, Cleveland, Ohio, May 1992.
16. *Ontario Highway Bridge Design Code*, 2nd ed. Ontario Ministry of Transportation and Communications, Downsview, Canada, 1983.
17. Okada, K., H. Okamura, and K. Sonoda. Fatigue Failure Mechanism of Reinforced Concrete Bridge Deck Slabs. In *Transportation Research Record 664*, TRB, National Research Council, Washington, D.C., 1978, pp. 136–144.
18. Sonoda, K., and T. Horikawa. Fatigue Strength of Reinforced Concrete Slabs Under Moving Loads. *Proc., IABSE Colloquium, Fatigue of Steel and Concrete Structures*, Vol. 37, Lausanne, Switzerland, 1982, pp. 455–462.
19. Hayashi, H., M. Okino, S. Matsui, and K. Sonoda. Reliability of a Repairing Method for Cracked and Damaged RC Slabs of Bridge Deck. *Proc., Pacific Concrete Conference*, New Zealand, Nov. 8–11, 1988, pp. 613–624.
20. Tanihira, T., K. Sonoda, T. Horikawa, and H. Kitoh. Low Cycle Fatigue Characteristics of Bridge Deck RC Slabs Under the Repetition of wheel-loads. *Proc., Pacific Concrete Conference*, New Zealand, Nov. 8–11, 1988, pp. 381–392.
21. Sabnis, G. M., H. G. Harris, R. N. White, and M. Mirza. *Structural Modeling and Experimental Techniques*, Prentice-Hall, Englewood Cliffs, N.J., 1983.
22. Petrou, M. F. *Fatigue Performance of AASHTO and OHBDC Design for Non-Composite Reinforced Concrete Bridge Decks*. Ph.D. dissertation. Case Western Reserve University, Cleveland, Ohio, Aug. 1993.
23. Perdikaris, P. C., M. F. Petrou, and A. Wang. *Fatigue Strength and Stiffness of Reinforced Concrete Bridge Decks*. Final Report FHWA/OH-93/016. Ohio Department of Transportation, March 1993.

The contents of this paper reflect the views of the authors, who are responsible for the findings and conclusions presented herein, and do not necessarily reflect the views of ODOT or FHWA.

Publication of this paper sponsored by Committee on Dynamics and Field Testing of Bridges.

Dynamic Interaction Between Bridge and Vehicle

MICHAEL RÖSLER

An interactive behavior between a bridge and a vehicle periodically stimulated by road roughness was observed through systematic testing. Periodic roughness was stimulated by using wooden planks placed at various distances across the road. The vehicles, two 7.5-ton trucks, were run across the bridge with varying loads and at varying speeds. The test bridge was a two-span prestressed concrete pedestrian structure on which many sensors were placed. A complete model was developed on the basis of separate components, including excitation, vehicle, and bridge. These components were linked in the final calculating step. Particular attention was paid to determining the stiffness of the superstructure.

Increasing improvements in construction materials and calculation methods have resulted in an increasing reliability level of structures. Major benefits are material saving and slimmer components, which increase the ratio of live load to dead load and change the dynamic behavior of structures. Therefore, there is a need for adequate dynamic analysis methods. Traditionally, the dynamic part of the load is associated with the static load through a dynamic load factor. The basic theory was developed around the turn of the century for the construction of steel railway bridges.

A bridge live load caused by heavy trucks entails a strong dynamic character conditioned on the vehicle dynamic properties. However, one major source of vibration for vehicles is the surface roughness. Therefore, it is necessary to consider a complex dynamic system composed of three components: surface roughness, vehicle, and bridge.

The objective of this study was to investigate the dynamic behavior of the whole system by undertaking a series of systematic tests. The parameters considered included frequency of excitation, vehicle speed, and vehicle mass.

SURFACE ROUGHNESS

The vehicle may undergo vibrations as a result of outside effects. Surface roughness of the road is an important source of vibration that directly influences the vehicle through tire contact. It is important to determine and quantify related parameters.

To describe roughness, the power spectral density function is used. In general, the amplitude decreases as the wavelength increases. The relationship between the vibration frequency of the vehicle body and axles, vehicle speed, and the wavelength of the road roughness is indicated in Figure 1.

Institute of Structural Engineering, Technical University of Berlin, Berlin, Germany.

DESCRIPTION OF VEHICLE

The bridge load caused by heavy vehicles can be divided into two categories: static and dynamic. The static part of the load is constant, but it has a variable position. The dynamic part of the load maintains the same position but is time dependent. It is defined by the dimensionless dynamic load increment. Its size depends on the natural frequency of the bridge and the vehicle, the surface roughness, the speed, and other outside effects.

The three major components of the system (surface, vehicle, bridge) determine the dynamic properties of the vehicle-bridge system. Not only the maximum amplitude of the load increment but especially its distribution over the frequency spectrum is important. Different types of vehicles, body and axle masses, and springs and dampers have a considerable influence on the dynamic properties.

DESCRIPTION OF BRIDGE

Tests were carried out on a research bridge in Berlin. Its design characteristics and static behavior are important factors for the evaluation of the dynamic experiments and developement of a calculation model. Other parameters considered include geometry, cross-section values, reinforcement, material properties, and especially the response of the bridge under a static test load. As a result of the test load, cracks occurred in the superstructure, which caused a change in its stiffness; this had to be included when developing the model.

The research bridge is an asymmetric, two-span concrete pedestrian structure with partial prestressing without bond. The spans are 27.6 and 23 m, and the superstructure consists of a double T-girder with a depth of 1.1 m and a width of 4.8 m. The prestressing reinforcement material is made of a high-strength composite (fiberglass) with seven tendons.

A total of 360 sensors were placed on the superstructure to measure the strain in concrete, stirrups, longitudinal reinforcement at the bottom and top of the girder, as well as the concrete and air temperatures. In addition, the forces in the tendons and the bearings could be measured.

For the dynamic tests, the results of the deflection measurement, cracks documentation, and strain of the reinforcement during a former static test load had to be considered because together they determine the actual stiffness. This value was needed for the developement of the model and provided important information for the selection of the points of measurement.

DYNAMIC INVESTIGATIONS

The dynamic tests were carried out to clarify what the influence of the surface-related excitations has on the vehicle and bridge systems

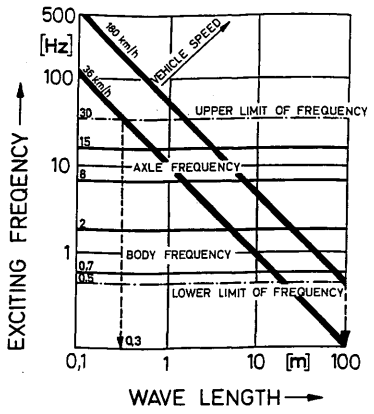

FIGURE 1 Relationship between exciting frequency and wavelength of roughness.

and on their interaction to specify the resulting bridge load. Periodic and impact excitations were chosen.

For the periodic excitations, a quasi-stationary mode was selected. This mode allowed for a parallel form of vibration in both systems, which is particularly important for the analysis of frequency and resonance effects. The impact excitation was used to investigate the influence of the speed. For vehicles, the body mass was changed in three steps and the speed was varied.

The sensors used on the bridge included four measurement bearings, eight strain gauges, and four measuring cylinders for the prestressing force. Nine accelerometers were installed on the superstructure as well.

Two different 7.5-ton test trucks with 200-l water containers for ballast were used for the dynamic tests. Each vehicle was equipped with four accelerometers, which were placed on the front and rear axles and on the front and rear areas of the body to be able to distinguish the different kinds of movements in the vibration modes. The vehicle and the measuring device were connected by a cable that allowed for a simultaneous recording of the bridge and vehicle signals.

Planks 5 cm thick and 25 cm wide were positioned in such a way that the front and rear axles went over the planks at the same time. This led to a harmonious up-and-down movement of the vehicle. Exciting frequencies between 0.5 and 8 Hz were observed. The vehicles were driven at speeds between 10 and 40 km/hr.

Evaluation in Time Domain

Evaluation in the time domain provides the basis for determining the dynamic increments and the exact exciting frequencies. The predetermined parameters include the average speed between the two end points of the bridge, the exact speed over the planks, the static part of the measured amplitude, the extreme amplitudes of the dynamic part, the corresponding frequency when counting the peaks, and the exciting frequency of the vehicle.

The frequencies counted from the time curves provided necessary additional information about the frequency spectra. Because of the variable location of the vehicle mass, the natural frequencies of the coupled system changed. Within the frequency spectrum, the effects appeared to be nonlinear and, therefore, no definite interpretation was possible. Only after consideration of the results in the time and frequency domains did all of the information become available. The first three natural frequencies of the bridge are 2.4, 4.5, and 9.6 Hz.

First, the amplitudes of the dynamic part were evaluated while taking into account the frequency for the periodic excitation. To make the resonance effect clear, even the test runs with various loads were put together in one diagram per point of measurement (Figure 2) to determine the reaction of the bridge. It is clear that the amplitudes in the area of 1.5 to 3.5 Hz are significantly higher than those at other frequencies. This shows that there is a resonance between the vehicle and the bridge.

The measured amplitudes did not indicate, however, the differences in the individual load levels, as expected. The largest value was even measured for the empty vehicle. One explanation may be that the laminated spring could not take advantage of the friction effect that resulted from a sufficiently loaded vehicle. In this case, the friction between the segments of the spring was so strong that the spring effect was reduced. This led to a higher axle impact and therefore to larger dynamic amplitudes.

Evaluation of Dynamic Increments

Figure 3 (*left*) indicates for the vehicle periodically in vibration the relationship between the dynamic increments in the reinforcement and the exciting frequency. In the other diagram in Figure 3 (*right*), the relationship between these increments and the speed for the vehicle excited by a plank 2 m wide and 5 cm high for impact excitation is shown. The dynamic increments increase as the load of the vehicle decreases. During the periodic vibration, these differences appear clearly at frequencies at which resonance occurs, between 1.5 and 3.5 Hz.

During the test runs with the fully loaded vehicle, the dynamic increment increased from 75 to 150 percent in the resonance field. These observations were also confirmed when using the plank. However, resonance effects at certain speeds were not found. The dynamic increment increases at an almost steady rate as the speed increases.

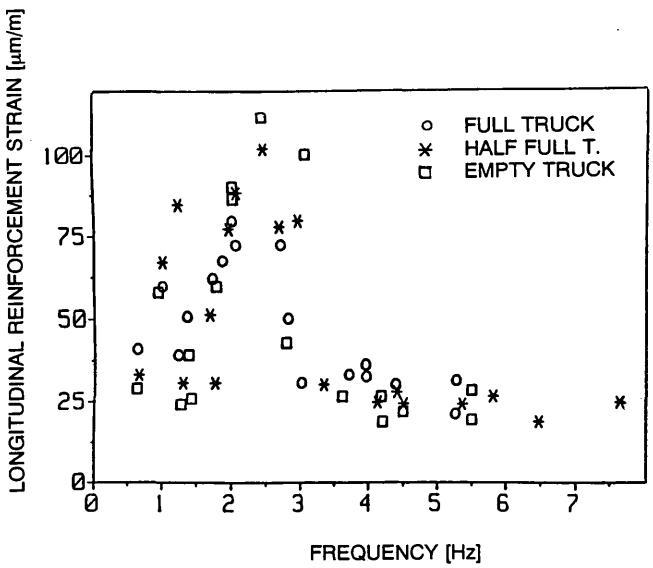

FIGURE 2 Dynamic amplitude for periodic excitation.

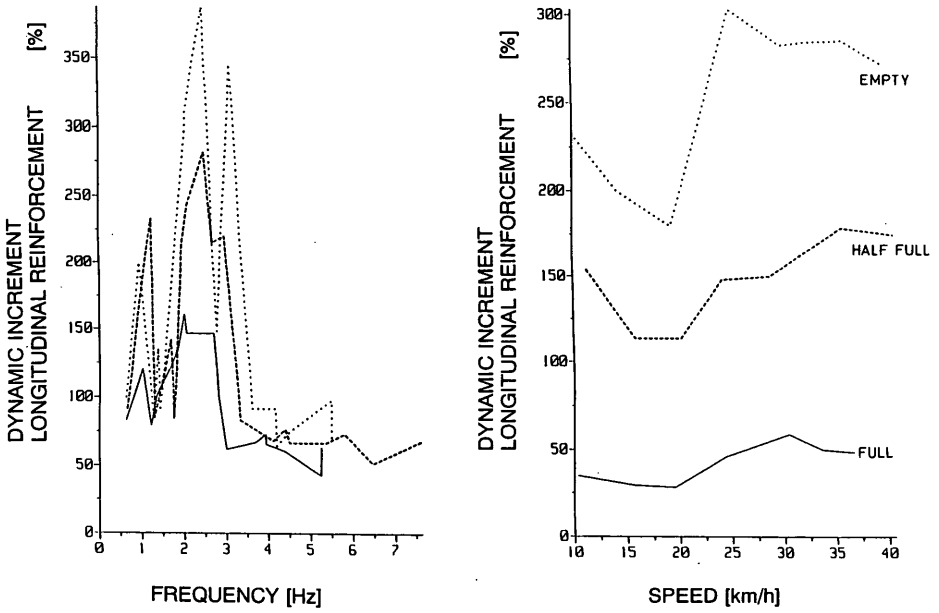

FIGURE 3 Dynamic increments.

Frequency Spectra of Bridge

For the evaluation in the frequency domain the data were transformed using Fast Fourier Transformation. Figure 4 demonstrates that the peaks of the frequency spectra for the runs with periodic vibration are always particularly high when the response and the stimulating frequencies are in tune, as in the case of resonance. Frequencies between 1.5 and 3.5 Hz are especially easily obtained.

In Figure 4*a*, all the values on the graph were in the resonance area or on one of the lines having stimulating frequency/response frequency rates between 0.5 and 3 Hz. In the three-dimensional graphs, the highest amplitudes are found in the resonance field, whereas the smaller amplitudes correspond with the higher frequency rates. Stimulating frequencies of more than 3 Hz, even in the resonance field, lead to small peaks. These observations imply the existence of a resonance rectangle that is limited by stimulating frequencies of up to 3 Hz and by response frequencies between 1.5 and 3 Hz.

Frequency Spectra for Vehicle

The three-dimensional view of the vehicle's reactions (Figure 5) is presented in the same way as the overview of the bridge. The axles are easily excited over all the frequency areas and respond with frequencies between 2 and 15 Hz. The body shows a concentration in the lower frequency range at stimulating frequencies under 2 Hz and response frequencies of up to 5 Hz. However, the truck body vibrates less when the stimulating frequencies go up to 6 Hz and the response frequencies reach 12 Hz. The top view shows the vibrations of the body to be between 1 and 5 Hz and those of the axles to be between 9 and 14 Hz.

For a fully loaded vehicle, there is a noticeable concentration within the resonance rectangle with a 2-Hz stimulating frequncy and a 2.5-Hz response frequency. However, the resonance field for

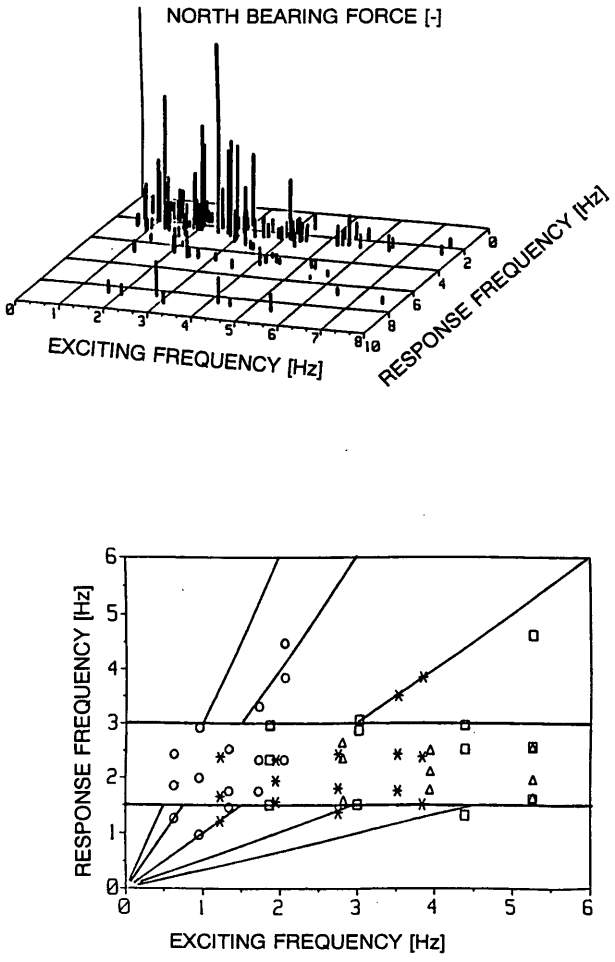

FIGURE 4 Spectral behavior of bridge.

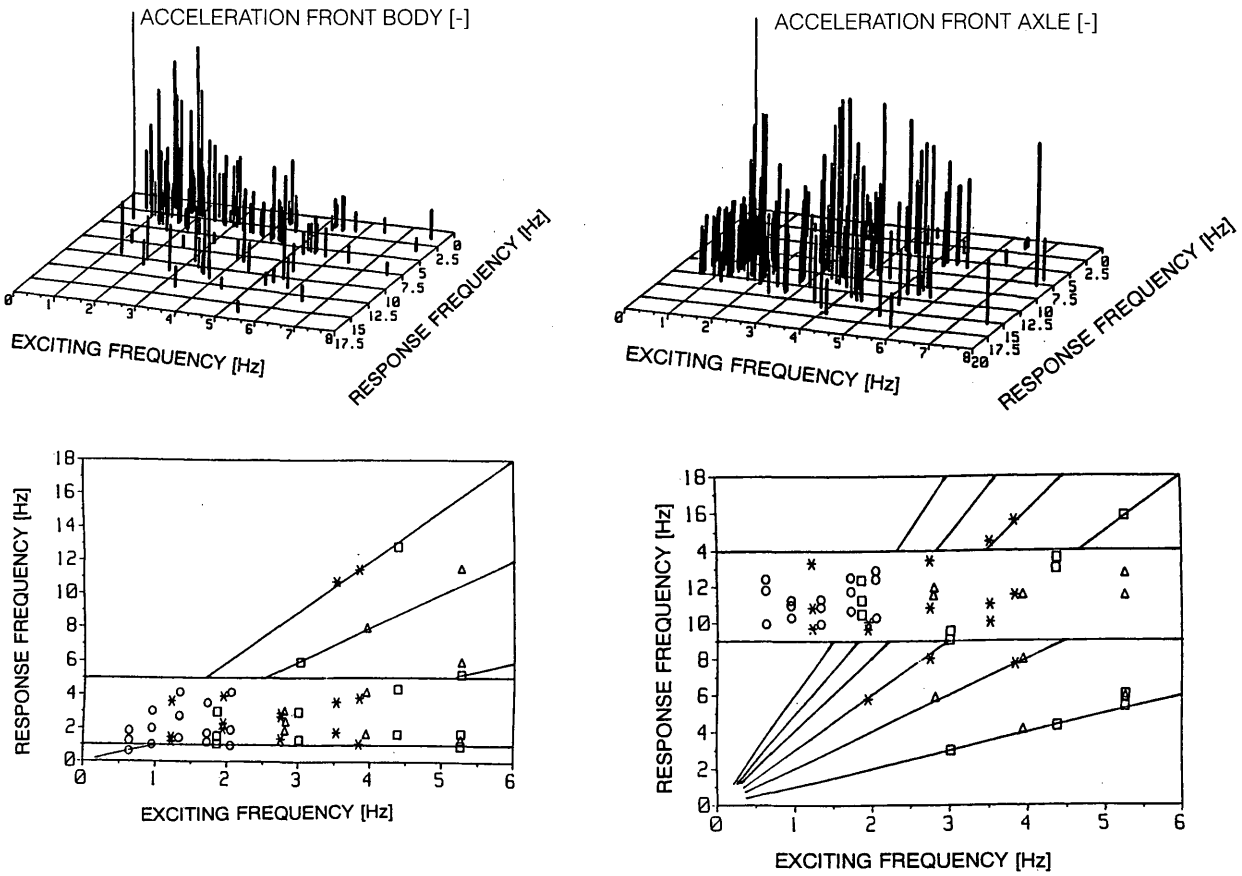

FIGURE 5 Spectral behavior of vehicle.

a less loaded vehicle is not as easily identifiable. The empty vehicle responds with considerable amplitudes of up to 10 Hz. This behavior cannot be explained by the presence of a higher natural frequency of the body. The cause is probably to be found in the nonlinear behavior of the vehicle's springs.

Cross-Power Spectra

To consider the interaction between the vehicle and the bridge, the cross-power densities between the signals of the vehicle and the bridge were calculated. This means that the frequencies that appear in both spectra were amplified, whereas the others were almost nonexistent. The cross-power spectra (CPS) were calculated between the bridge signals on one side and the axles and the body signals on the other.

The three-dimensional view in Figure 6 shows the clear differences between the axles and the body CPS. The axle CPS cause interactive responses with high peaks of up to 12 Hz. Noteworthy peaks of only up to 2.5 Hz appeared in the body CPS. Observation of the stimulating frequencies shows that the body CPS can be amplified only up to 3 Hz, whereas the differences between the lower and the higher stimulating frequencies are less clearly distinct at the axle CPS. A resonance field manifests itself clearly for the body CPS and is limited by stimulating frequencies of 3 Hz and response frequencies of 2.5 Hz.

In the top view, plotted points were most often found on the lines showing the proportional rates of 1, 2, and 3 for the axle crosses and on those of 1, 0.5, and 2 for the body crosses. It was observed that 83 percent of the peaks are located within a 10 percent range from the proportionality lines, with 40 percent of the values located within 10 percent of the resonance Line 1. This proves that the load on bridges is frequency dependent.

Development of Analytical Model

By using the knowledge obtained from the static and dynamic investigations it became possible to model the interactive relationship for other parameters by using a finite elements program with frame elements. Particular emphasis was placed on the adaptability to various forms of stimulation and different types of vehicles and bridges. It was necessary to consider and optimize separately each component of the dynamic system.

The model includes the forces resulting from the mass, dampers, and springs of the vehicle and bridge systems. The stimulating function is locally fixed and was calculated by combining the surface roughness of the test road with the speed.

The direct calculation of the system under a moving dynamic load can, if necessary, be approximated by using dynamic influence lines. Their calculation is similar to the determination of the static influence lines by replacing the moving static load by a vibrating

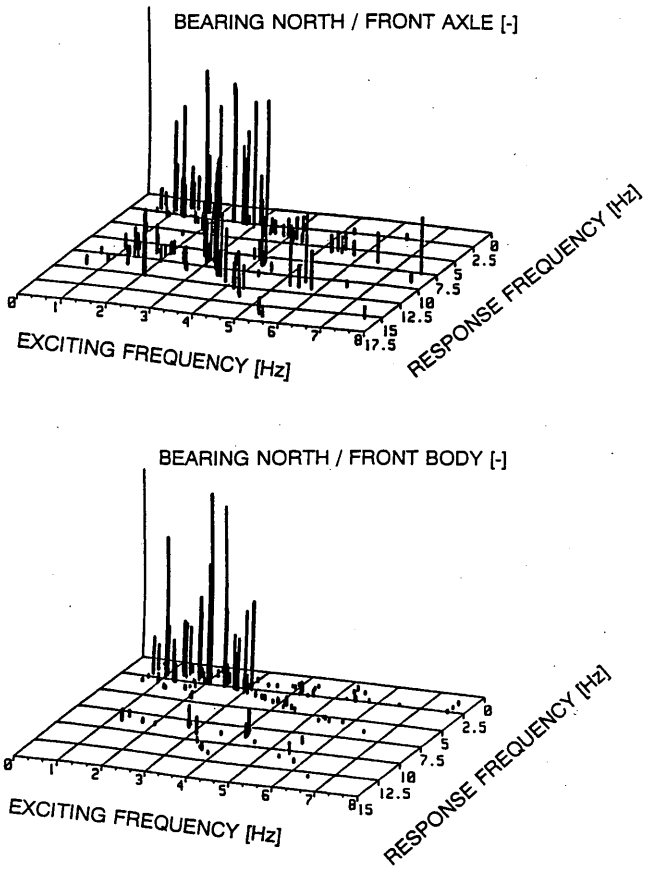

FIGURE 6 Spectral behavior of interaction.

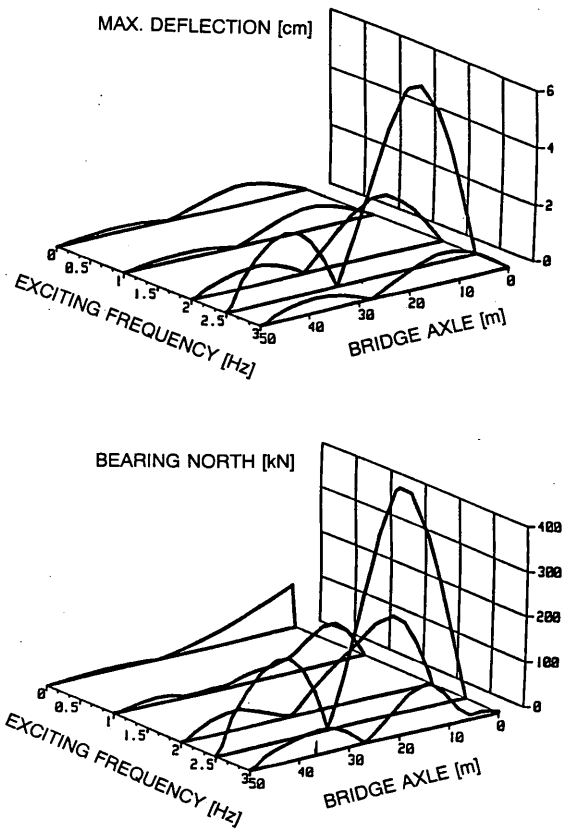

FIGURE 7 Dynamic influence lines.

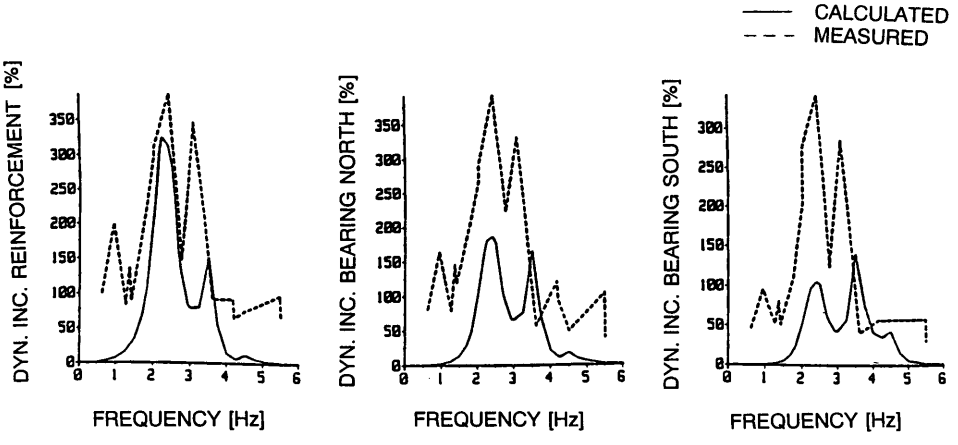

FIGURE 8 Comparison of calculated and measured results.

force whose effect on the system can be evaluated at any point. In Figure 7, a static and four dynamic influence lines are shown at various stimulating frequencies for a standard load of 100 kN. The deflections, bending moments in the middle of the long field, and the forces of the supporting points are also shown. The dynamic influence lines are primarily differentiated according to the size of their amplitudes, depending on their closeness to the stimulating frequency and the natural frequency of the bridge. Their construction, however, is different from that of the static influence lines, whose amplitudes are located at a stimulating frequency of 0 Hz.

For each vehicle load, a specific calculation for each frequency is necessary. To simulate a test run on a computer, a variable connection between the vehicle and the bridge is necessary. The whole system responds to the movement of the truck by changing its natural frequencies. A direct comparison of frequencies and amplitudes obtained by analysis and tests is shown in Figure 8. Although the

calculated values were slightly above those measured for the fully loaded vehicle, for the half-loaded vehicle it was the other way around. For the empty vehicle, the amplitudes measured at least for both supporting points were clearly above those calculated. Outside the resonance fields, a basic value for the dynamic increments remained that fundamentally did not appear in the theoretical model. In general, the measured and the calculated values were satisfactorily similar.

In the frequency domain, a good conformity could be observed as well. The global structure of the main masses of the vehicle and the bridge emerged for both values. The developed model can be used for the analysis of the effect of variable road surface, various types of bridges, and for special types of vehicles carrying variable loads.

SUMMARY AND CONCLUSIONS

An interactive behavior between a bridge and a vehicle periodically stimulated by road roughness was observed through systematic testing. The evaluation of the bridge's reactions showed a clear increase in the response amplitudes at stimulating frequencies between 1.5 and 3 Hz and at response frequencies that were multiples of the excitation frequency. Thus, resonance fields are important in the bridge spectral behavior. Their limits are a stimulating frequency of up to 3 Hz and a response frequency between 1.5 and 3 Hz.

The vehicle frequency behavior was found to be similar to that of the bridge. The resonance fields are limited differently because of the presence of the axle frequencies. However, the obvious influence of the natural frequencies of the individual elements remains.

To investigate the interaction, the CPS between the bridge and vehicle signals were calculated as a function of the stimulating frequencies. Resonance fields whose limits were dependent on the natural frequencies of the systems involved were also observed.

It is clear that the load magnitude depends on the parameters related to the vehicle and bridge frequencies. They include primarily the natural frequencies of the components of the dynamic system. The stimulating frequency is the most significant effect that results from the road roughness and the speed.

For the design of bridges subjected to dynamic loads, the classical dynamic load factor does not affect the natural frequency behavior of the bridge, vehicles, speed, and road roughness. For the design of dynamically sensitive bridges, further dynamic calculations are necessary.

For the maintenance of existing bridges, it can be concluded that more attention should be paid to the level of the road roughness at the approach and on the bridge. The surface roughness is the major cause of the dynamically related damages to the bridge. It is suggested that a catalog of limit values for various types of surfaces be established and become a part of the design and construction code.

Publication of this paper sponsored by Committee on Dynamics and Field Testing of Bridges.

Fatigue Cracking in Modular Bridge Expansion Joints

CHARLES W. ROEDER, MARK HILDAHL, AND JOHN A. VAN LUND

Single support bar modular expansion joints with 1200 mm of movement capability were used at each end of the Third Lake Washington Bridge between Seattle and Mercer Island on Interstate 90. Within 18 months after the bridge was open to traffic, cracks were observed in the tubular centerbeams of these large modular systems. Additional cracks have occurred since that date. Research was performed to determine the causes of the observed cracking and included an evaluation of existing methods for fatigue design of modular joint systems, finite element analyses of the large modular joints, and correlation of the results with observed behavior. The results show that the cracking is caused by fatigue due to repeated wheel loading. However, existing design methods may not be reliable indicators of the fatigue behavior because the behavior is influenced by the stiffness and dynamic response of the individual joint system. The variable span lengths complicate the evaluation process. The edge centerbeams have the longest and shortest alternating spans and have the highest percentage of fatigue cracks. The dynamic response of the modular joints is complicated because hundreds of vibrational modes contribute to the response, but theory suggests that the response is affected by joint type and loading. The single support bar system amplifies horizontal loads that are applied slowly, but it amplifies vertical loads through a wide range of vehicle speeds. The 1200-mm movement joints will require replacement before the expected design life of 25 to 30 years is achieved.

The Washington State Department of Transportation (WSDOT) uses modular expansion joints on bridges whose expected movements are larger than 127 mm. The Third Lake Washington Bridge has two 1200-mm modular expansion joints at opposite ends of 1.75 km of floating pontoons. These joints, which were open to traffic in June 1989, are believed to be the largest modular expansion joints in the world (*1*). As shown in Figure 1, these joints use the single support bar swivel design, which was developed in Germany. Steel tubes were substituted for the I-shaped centerbeams used in the original design because domestically produced centerbeams were unavailable and FHWA's Buy American steel requirements for federally funded bridge construction would not permit the use of foreign steel. Figure 2 shows the extruded steel rail that was welded to the top of the tubes to grip the strip seals.

Approximately 6 months after the bridge was opened to traffic, WSDOT received complaints of expansion joint noise. Inspection of the joints showed that some elastomeric bearings used to cushion the traffic impact between the centerbeams, stirrups, and support bars were loose. Shims were added, but within a year cracks in the tubular centerbeams were observed. Most of these cracks started at the toe of the stirrup to centerbeam fillet weld and progressed through the centerbeam, as shown in Figure 3. One crack occurred at the end of a reinforcing bar. The manufacturer repaired seven of these cracks in April 1991 by rewelding the cracked metal. Additional cracks were noted in the centerbeams after this first repair, and seven more cracks were repaired in November 1991. Additional cracks were noted after this second repair, and some of the previously repaired cracks reappeared.

WSDOT had concerns about the observed cracking and initiated two courses of action. First, a specification was developed to improve the quality and durability of bridge modular expansion joints. This specification requires fatigue design and testing of joint components to a minimum of 100 million cycles (*2*). Second, a research study was started to evaluate the cause of cracking because there were many special conditions for the Third Lake Washington Bridge, such as substitution of the tubular centerbeams, loss of precompression in the elastomeric springs, heavy traffic, effect of roadway grade, changing lake levels, and long expansion distance (*3*).

REVIEW OF PREVIOUS WORK

In the United States there has been little study of the fatigue life of modular expansion joints. Modular joints are complex because they have many members that move and interact with one another. Each modular system has unique (often patented) features developed by the manufacturer, and these features further complicate the load distribution and evaluation process. However, a relatively simple fatigue limit states design method has been proposed elsewhere (*4–6*). First, the loads on the bridge and the expansion joint are determined. The design limit states fatigue wheel loads, including impact proposed (*4–6*) are a vertical downward load of +91.0 kN and a minimum vertical rebound load of –27.3 kN and a horizontal load of +18.2 kN. The horizontal loads include the effects caused by traffic acceleration and braking. These design limit states fatigue loads are based on field measurements from several bridges in Europe (*6–8*).

By using these loads, the stresses are calculated at critical locations to determine the maximum computed stress range, $\Delta\sigma_{max}$. The centerbeams are treated as continuous beams, and the elastomeric springs and bearings are treated as rigid supports for determination of the moments and the stress level. For normal conditions, each centerbeam carries approximately 50 to 60 percent of the wheel load with a 1.8-m wheel spacing because the wheel distributes the load to more than one centerbeam. Note that the primary loading considered in the design method produces compressive stress in the same area as the fatigue cracking on the Third Lake Washington Bridge. Fatigue design practice historically has focused on the total stress range, and mean stress is ignored (*9*).

From laboratory fatigue tests, separate S-N curves were determined for each critical component or location. Pattis (unpublished data) conducted one fatigue test on the as-built tubular centerbeam

C. W. Roeder and M. Hildahl, Department of Civil Engineering, University of Washington, Seattle, Wash. 98195. J. A. Van Lund, Office of Bridge and Structures, Washington State Department of Transportation, Olympia, Wash. 98504-7340.

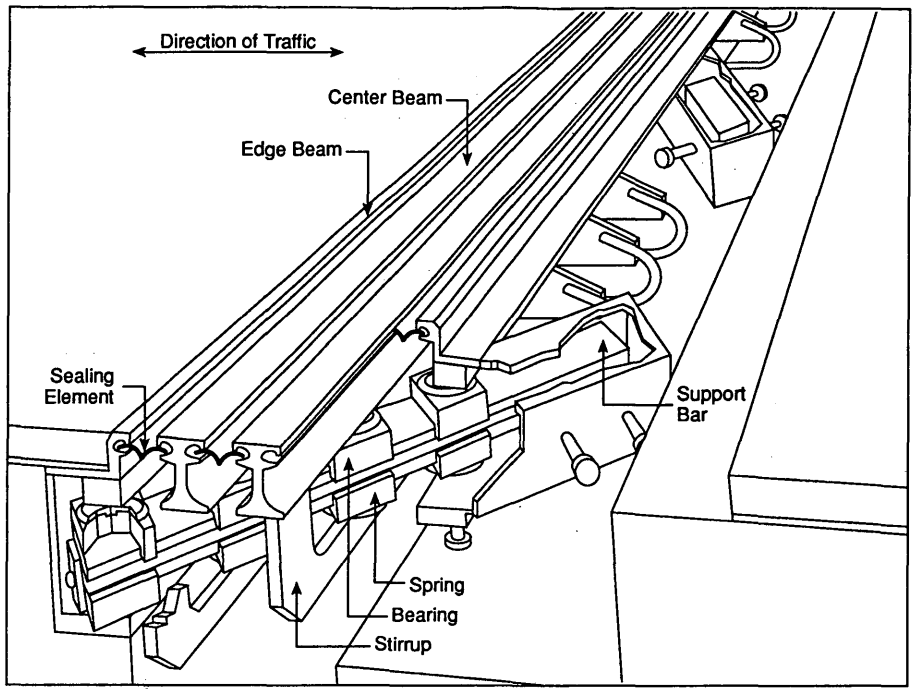

FIGURE 1 Partial plan single support bar swivel expansion joint.

to stirrup welded connection used in the Third Lake Washington Bridge. Figure 3 shows the S-N curve generated from this single test result. The S-N curve is constructed with a slope of –0.33 on the log-log S-N curve for a stress range of less than 5 million cycles and a slope of –0.20 for a stress range between 5 million and 100 million cycles. The intercept at 100 million cycles is the theoretical endurance limit, $\Delta\sigma_L$, proposed elsewhere (*4–6*), but all tests are performed at 2 million cycles or less. Using the proposed fatigue design loads (*4–6*), a fatigue life of 10 million cycles of total truck loading was predicted.

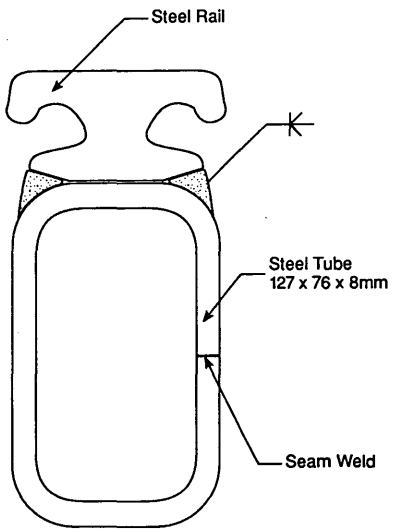

FIGURE 2 Tubular centerbeam with welded rail.

The maximum calculated stress range is compared with the theoretical endurance level from the S-N curves developed from experimental results. The comparison considers the full load spectrum and the accumulation of damage attributable to variable amplitude loading through the combination of Miner's rule and the load spectrum (*6*). The design comparison is made by

$$\frac{\Delta\sigma_{max}}{2} < \Delta\sigma_L \quad (1)$$

where $\Delta\sigma_{max}$ is the calculated stress range on the basis of the defined range of wheel loads, and $\Delta\sigma_L$ is the limit states fatigue stress range at 100 million cycles, as projected from the fatigue tests. The maximum calculated stress range is divided by 2 because of the partial

FIGURE 3 Crack in centerbeam at toe of stirrup weld.

safety factors γ_{Mf}, and α, where α accounts for accumulated fatigue damage by Miner's rule.

There are reasons for questioning the validity of the Tschemmernegg procedure. Koster (*10*) states that the elastic deformation of the system affects the stress distribution and the fatigue potential and contends that deformability of the joint is desirable because it may spread the load and possibly reduce the critical fatigue stress. However, the elastic deformation and stress distribution may not occur because of the very short duration of the wheel loads.

Agarwal (*11*) performed a series of field measurements on a modular expansion joint on a bridge in Ontario, Canada. These field measurements suggested that the loads and load spectrum recommended by Tschemmernegg may not be universally applicable. Large horizontal forces noted by Tschemmernegg (*6*) were not detected and the load range and spectrum were different. However, the centerbeam instrumentation that Agarwal used may not have been adequately located or sensitive enough to detect horizontal loads on the joint.

ANALYSIS OF MODULAR JOINT

The modular joint at the west end of the eastbound lane of the Third Lake Washington Bridge was analyzed with the SAP90 finite element analysis computer program (*12*). As indicated in Figure 4, a global model was analyzed first and the results were used to evaluate local effects near fatigue cracking. The centerbeams, support bars, and stirrups were modeled with beam elements. The geometry, member properties, and stiffness were based on information obtained from the contract shop drawings. The elastomeric springs and bearings were modeled as compression and shear springs, where the spring stiffness was determined by typical models of elastomeric bearing stiffness (*13*). The shop drawings did not specify the elastomer stiffness, and a study was performed to determine the sensitivity of the computed response to variations in the elastomer stiffness. Modest variations in bending moments, deflections, and deformations were noted when the spring stiffness was doubled or when divided by two. The elastomeric spring stiffness did not have a dramatic effect on the bending moments, but other aspects of the behavior noted with elastomeric springs were different from those noted when rigid connections between the support bars and centerbeams were used.

The initial global analyses were performed with a standard, vertical, 71.2-kN wheel load with a 1.8-m wheel spacing. No horizontal load or impact was applied during the initial analyses but was included in later calculations. The static load was distributed to several support beams in the ratio of 25, 50, and 25 percent as proposed by Tschemmernegg (*6*) when the joint opening is in the midrange position.

Bending moment diagrams were computed for the various centerbeams, with vehicle wheel loads passing over four different truck travel paths across the joint. Only one-half the bridge required analysis because the joint is nearly symmetric around the center line. This variation produced the full variation in stress states expected with traffic loading. Figure 5*a* shows the moment diagram of an edge centerbeam (CB13) and its stirrups. The figure shows that the bending moment in the centerbeam was large near the stirrup weld, and it produced tensile bending stress in the centerbeam

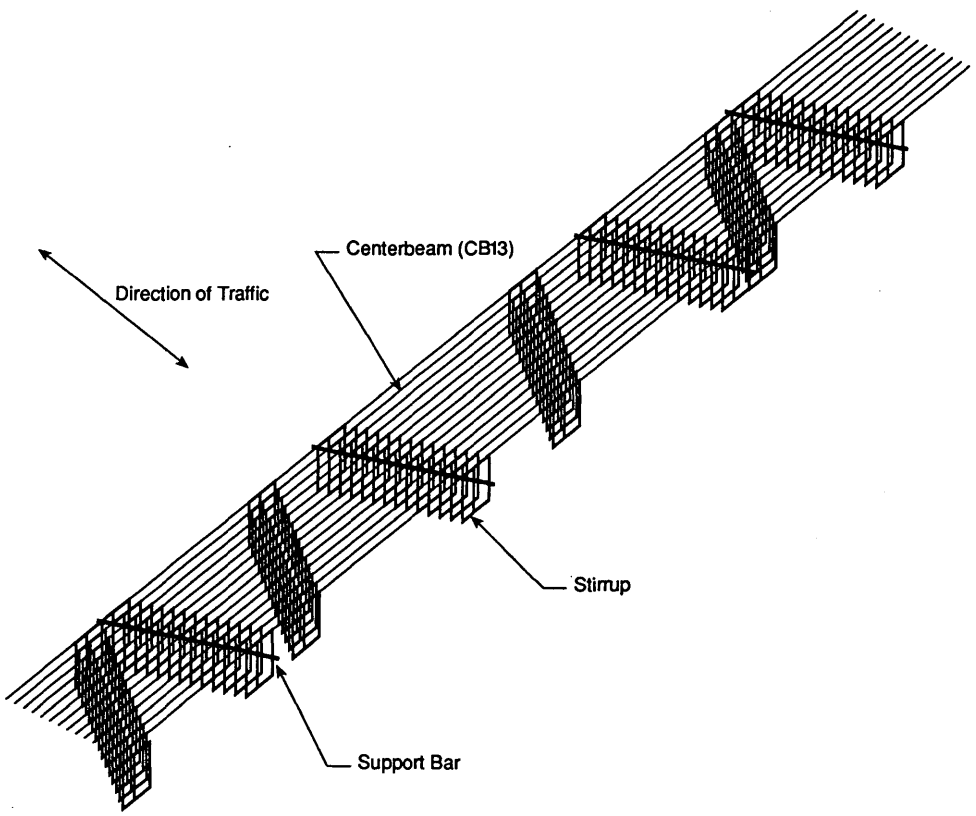

FIGURE 4 Finite element model of entire modular expansion joint LM line.

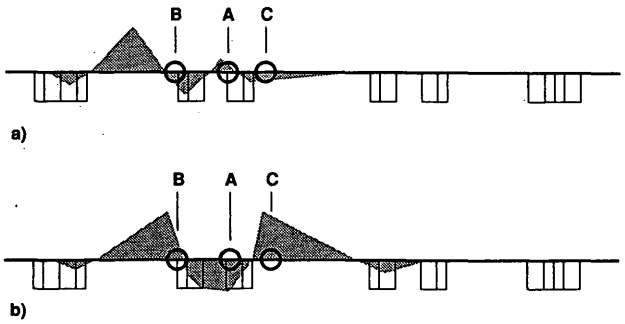

FIGURE 5 Moment diagram for edge centerbeam with (a) truck wheels in outside lane and (b) truck wheels in adjacent lane.

at the stirrup weld at critical Location A and compressive bending stress at the weld of critical Location B. Figure 5*b* shows the same centerbeam with the wheel loads simulating a truck in an adjacent intermediate lane position. The bending moment with this load position produced a sign reversal for the bending moment at all three critical locations. Comparison of Figure 5*a* and *b* shows that the largest stress range may be achieved because wheels are placed in different traffic lanes. AASHTO regards 2 million repetitions of the AASHTO truck loadings as an appropriate number of design load cycles for bridge fatigue. For expansion joints, the number of cycles depends on the number of axles crossing the joint and the number of cycles and the stress range may increase because trucks sequentially pass in adjacent lanes since the largest stress range is caused by this combination.

Similar behavior was noted for other centerbeams, but the bending moments and nominal stress ranges were smaller when the load was placed on interior centerbeams than on edge centerbeams because edge centerbeams had alternating long and short spans and interior centerbeams had more uniform span lengths. The more uniform spans reduced the range of the stress and the bending moments at the critical stirrup locations. Thus, the edge centerbeams experience earlier fatigue cracking than the interior centerbeams.

Global analyses also were performed with horizontal loads applied to the joint. Torsional deformation and weak axis bending of the centerbeams resulted when these horizontal loads were applied at the top of the centerbeam rail. Horizontal loads varying between 5 and 40 percent of the nominal 71.2-kN wheel load were applied and distributed to the centerbeams by the same proportions as those used for the gravity load. The system was surprisingly stiff against these horizontal loads because horizontal deflections of the centerbeam were no more than approximately 8.9 mm with the largest horizontal loads if slip of the elastomeric springs is avoided. The minor axis bending stress at the critical stirrup location was approximately 1.7 MPa when the lateral wheel load was 5 percent of the 71.2-kN gravity load and approximately 13.8 MPa with a 40 percent horizontal loading. Complete reversals were noted when the truck wheels were placed in alternate positions, as noted earlier in the gravity load analysis. The maximum stresses were increased to –49.0 and 59.3 MPa for the load paths of Figure 5*a* and *b*, respectively, when a 40 percent horizontal load was combined with the vertical load. Bending moments for both weak axis and strong axis bending were larger at locations other than the stirrup connection, but fatigue cracks were not likely to form at these other locations because they were not fatigue-sensitive details.

Local Finite Element Analyses

The global analyses showed the bending moments, forces, and deflections of the joints under a wide range of loadings. However, the analyses did not provide a complete picture of the state of stress in the critical stirrup location. The centerbeam and the stirrup were modeled with a detailed local model. The centerbeam was modeled with shell elements, and the stirrups were modeled with three-dimensional brick elements. The loads at the ends of the tube and the spring loads attributable to the elastomeric springs were obtained from the global computer analysis results. Note that the mesh used in this local analysis was appropriate for determining local stress and deformation but was not fine enough to determine stress concentrations or crack initiation conditions.

Local deformations had an impact on the stirrup connection location. The local analysis performed with gravity loads showed only considerable local bending deformation of the walls of the tube near the stirrup weld. The bending stresses caused by these plate bending moments were computed, and the stresses at the critical location were found to be approximately the same magnitude as the basic beam bending stress described earlier in the global analysis. These bending stresses varied from tension to compression through the thickness of the wall of the tube and caused increasing stress (tensile) on the inside of the tube and decreasing stress on the outside of the tube near the stirrup weld in the absence of precompression in the elastomeric springs. If the springs were precompressed, the local bending moments changed somewhat. This change in local bending moments could change the magnitude of the plate bending moment at some locations and ultimately might cause tensile bending stress at the outside of the tube at the critical location.

CORRELATION OF COMPUTED STRESS TO FATIGUE CRITERIA

Efforts were made to correlate the computed stress ranges with existing fatigue criteria. The stresses were computed at the critical stirrup location (Location A on CB-13) because of the large tensile and compressive stresses. More than 60 percent of the visible cracks observed during an inspection of the joints in January 1993 were in similar locations.

Normal AASHTO fatigue design is based on 2 million repetitions of the HS-20 truck loading. The stress range is the difference between the maximum stress caused by the load and its impact and the unloaded condition. The welded stirrup to centerbeam detail is somewhat analogous to Detail 17 in the AASHTO Specifications (*14*) in which attachments are welded to a longitudinally loaded member with short fillet welds. Detail 17 indicates fatigue Category D or E. Two million truck passes will cause far more than 2 million cycles of wheel loading. Category D of the AASHTO Specifications (*14*) requires a maximum stress of 48.3 MPa if more than 2 million cycles is used, and no more than 31.1 MPa is permitted for Category E. However, the existing joint of the Third Lake Washington Bridge has not experienced 2 million cycles of HS-20 wheel loading in the short time it has been in service. This suggests that either the detail is closer to the more critical Category E condition, or the wheel load is larger than 71.2 kN, or the dynamic amplification of the stress range is large.

Different stresses occur at the critical stirrup location when the truck axle passes over a different line of travel, and complete stress reversals are possible when the cyclic stress is caused by these alternate truck path loadings. A stress range of 45.5 MPa, neglect-

ing local bending effects, should be expected with a 71.2-kN wheel load without horizontal load or impact caused by these alternate lane loads. If 30 percent impact is added to this stress range, the range becomes 59.3 MPa. Thus, dynamic amplification clearly raises the stress range to a level well above the fatigue limit for AASHTO Categories D and E.

The analyses were performed with the modular joint in its midrange position. If the joint is opened to its maximum width, the resulting stress ranges are 30 percent larger than those noted earlier. Local bending effects likely play a role in the fatigue cracking, but Category D would predict only several hundred thousand cycles of alternate lane loading when local bending effect is neglected. These ranges do not include any horizontal load. In addition, the stress range used in this evaluation requires passage of two trucks. The trucks do not pass simultaneously, but they pass over the joint in different lanes. It is reasonable to expect up to one cycle of this higher stress range with each truck passage. Additional smaller-amplitude cycles can be expected with each wheel passing over the joint, and this accumulated damage would further reduce the number of cycles of severe loading that the joint could sustain.

Using the proposed Tschemmernegg fatigue design loads and the S-N curve shown in Figure 6, a fatigue life of 10 million cycles of total truck wheel loading was predicted for the as-built stirrup-to-centerbeam connection. As indicated in Figure 7, this estimate is different from the AASHTO (*14*) and AASHTO LRFD (*15*) life estimates because it includes the total number of truck passings and an estimate of accumulated damage. The accumulated damage estimate is based on a design wheel load spectrum proposed for expansion joints in Europe. Fatigue cracks were noted approximately 18 months after the bridge was opened to traffic, and 10 million cycles would require approximately 18,000 axles for one lane of traffic per day. A traffic count performed in 1990 found that the westbound lanes of the bridge experienced approximately 6,720 axles of bus and truck traffic during the busiest 12-hr period of a normal work day. When the traffic was distributed over three lanes and the lighter weekend traffic was considered, the accumulated traffic was less than 20 percent of the fatigue life estimate proposed by Pattis (unpublished data). Further, the cracks obtained in the laboratory fatigue test were quite different than those observed on the Third Lake Washington Bridge. The initial and predominant cracking in the laboratory test was longitudinal cracking along the edge of the stirrup to center beam weld. This cracking is different from the transverse-through-depth cracking seen on the Third Lake Washington Bridge and illustrated in Figure 3. No longitudinal cracking has been noted on the Third Lake Washington Bridge. Transverse cracking was eventually noted on the test specimen, but it occurred only after the longitudinal crack had grown large and it did not progress through the depth of the centerbeam (Pattis, unpublished data). This observation suggests that the Tschemmernegg procedure may not be applicable for all joints.

Although the Tschemmernegg method does not duplicate the fatigue cracking noted in the Third Lake Washington Bridge, the stress ranges predicted by the test may be fairly realistic. The reason for the approximate accuracy of the S-N curve is that the modular joint details are likely to always be close to AASHTO Category D or E because the weld detail is similar to that of AASHTO fatigue Details 9 and 17. The detail may be closer to Category D or even Category C if the modular joint is less susceptible to fatigue and closer to Category E if it is more susceptible. However, it is clear that the load history is most important for establishing a fatigue design criteria.

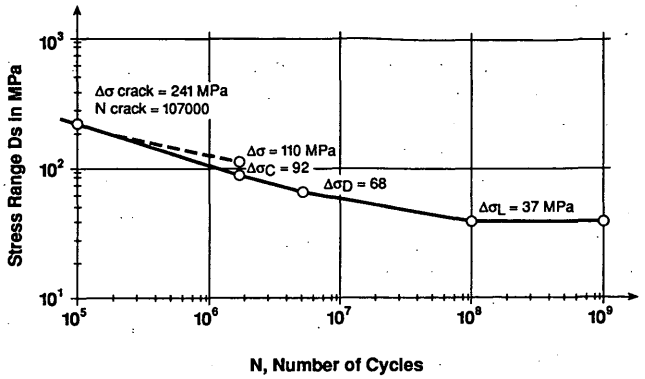

FIGURE 6 S-N curve proposed for tubular centerbeams (Pattis, unpublished data).

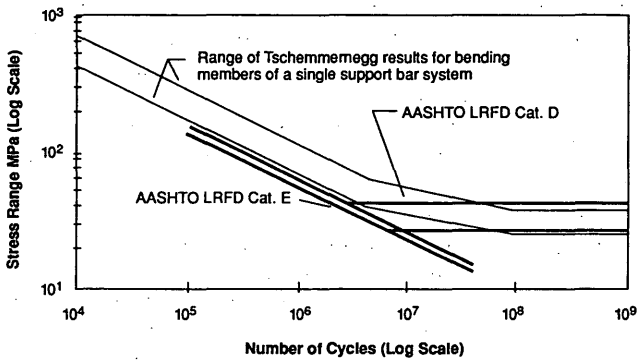

FIGURE 7 AASHTO LRFD S-N curves compared with a range of different Tschemmernegg S-N curves.

The static analysis shows larger stress ranges than those suggested by the Tschemmernegg method because of variations in the travel path of trucks across the modular joint and the alternating long and short spans of the edge centerbeams of this joint. Nearly complete stress reversals are possible because of these conditions. The Tschemmernegg method is based on application of an accumulated damage model that is based on load spectrum data from several expansion joints in Europe. There is no indication of how wheel loads vary from location to location in the United States. The fatigue behavior of modular joints may not be as simple as that proposed by Tschemmernegg.

DYNAMIC ANALYSIS OF MODULAR JOINT

The global finite element model was used to perform dynamic analyses on the modular joint. The mass of the components of the modular expansion joint were added to the model, and many modes of vibration were computed. No damping was used because of uncertainty about its magnitude. However, damping must be relatively large (20 percent of critical or more) before significant changes in the dynamic periods are noted. The dynamic modal computations required a large amount of computer time because of the broad distribution of mass and stiffness and the large number of degrees of freedom. In most modal analyses, only a few modes of vibration are required because the modes are well spaced and most of the mass is

participating in very few modes. The modes of vibration for this modular expansion joint were closely spaced with hundreds needed to include the predominate portion of the mass in three-dimensional vibration. Nevertheless, the procedure produced some general observations worth noting.

The longest period modes were associated with horizontal movement. The majority of the participating mass (98+ percent) for the two translational degrees and one in-plane rotational degree of freedom were included in modes with periods of between 0.16 and 0.035 sec (6.2 to 28 Hz). These translational degrees of freedom occurred because of deformation of the elastomeric springs. Even though the stiffness of these springs was not precisely known, a 100 percent increase in stiffness would decrease the period only by approximately 30 percent. A 50 percent decrease in elastomer stiffness would increase the period by approximately 40 percent. These variations in elastomer stiffnesses are possible, but they represent upper limits on the probable variation.

Two typical vertical modes of vibration in a centerbeam located near the edge of the joint (CB13) are shown in Figure 8. The vertical modes of vibration with significant participating mass had periods ranging from 0.05 to 0.005 sec (20 to 200 Hz). There were many similar closely spaced modes, each with a modest participating mass. However, the period of these vertical modes of vibration was about 0.015 sec (67 Hz) for most of the participating mass of the system.

In past inspections of the Third Lake Washington Bridge joints, inspectors noted that the elastomeric bearings were sometimes loose and not precompressed. A lack of precompression reduces the stiffness of these bearings because they cannot act in tension without the precompression. As a result, several analyses were performed to evaluate the effect of loose bearings. Individual loose bearing might double the period of a single critical mode but have minimal effect on most modes of vibration. An increased number of loose bearings can increase the period of a larger number of modes of vibration, but the relative magnitude of the period increase would often be smaller than that noted for a single mode.

Impact represents the dynamic amplification of the system attributable to the dynamic loading. The wheel load on any centerbeam is initially 0 until the wheel makes contact with the given beam, and it reaches its maximum value when the wheel is nearly centered over the given centerbeam. The load on a beam then decreases until the wheel separates from the beam. If the truck is traveling at a constant velocity, this translates into the linear time-dependent load function shown as an insert in Figure 9. For a tire contact length of 24 cm and a centerbeam width of 80 mm, vehicles at 33, 67, and 100 km/hr would have load durations of 0.035, 0.017, and 0.012 sec, respectively.

Figure 9 shows the maximum dynamic response divided by the static response as a function of the ratio of the duration of the ramp function loading to the period of the system. The dynamic amplification of 1.0 indicates that the structure feels the full static loading, and a factor greater than 1.0 implies impact or dynamic amplification. Figure 9 shows that the centerbeam feels the full static load and potential impact if the duration of the loading is longer than approximately 30 percent of the dynamic period of the structure. If the duration is less than 10 percent of the period, less than 30 percent of the static load is felt. The maximum duration is approximately 0.035 at a truck speed of 33 km/hr, and this duration is similar to the shortest dynamic periods associated with horizontal movement and deformation. The duration at 100 km/hr is 0.012 sec, and this is a small percentage of all but the shortest periods associated with horizontal movement. This suggests that significant amplification of horizontal forces should be expected at slower vehicle speeds. High-speed vehicles may cause the expansion joint to experience the static force or slight attenuation of horizontal loading. Therefore, this expansion joint may not experience the large horizontal loads suggested by the Tschemmernegg method (*6*). Comparison of load duration to vertical modes of vibration suggest that amplification will occur over a wide range of vehicle speeds. These observations are meaningful for this particular expansion joint because of the transverse flexibility of the system. Other modular joint systems, particularly multiple-support bar joints with a rigidly welded centerbeam to support bar connections, may be much stiffer transversely and feel a greater horizontal loading and possible dynamic amplification.

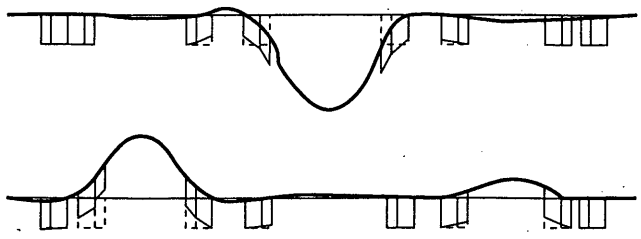

FIGURE 8 Typical vertical modes of vibration.

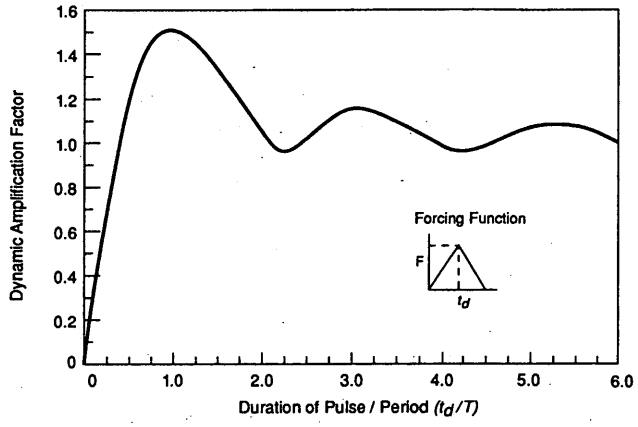

FIGURE 9 Dynamic amplification for ramp function loading.

These analyses neglect the effect of the vibration of the truck suspension systems and the additional impact caused by rough roadway surfaces. Additional amplification is possible when these factors are considered, but the maximum amplification always will occur when the duration of loading (t_d) is similar to the periods of the centerbeam and the truck suspension system.

SUMMARY

1. An analytical study of centerbeam cracking observed in the large modular expansion joints on the Third Lake Washington Bridge is described. The cracking is a result of fatigue caused by cyclic loads induced by truck wheel loads on the joint.

2. The fatigue problem is most serious in the edge centerbeams because of the larger stress range produced by the alternating long

and short spans. Residual stresses near the stirrup to centerbeam weld may cause the cyclic compressive stress to be in cyclic tension.

3. The tubular centerbeams contribute to the fatigue problem because of local deformation and through-thickness plate bending stress, but fatigue would have been a problem even if another section had been used for the centerbeams because of the centerbeam span length.

4. Wheel loads cause multiple stress cycles for a single truck passage. Therefore, the fatigue evaluation procedure of modular expansion joints must be different from that used for bridge girders. The analyses showed that a much larger stress range is possible between different trucks because the trucks do not travel over the same path across the joint. This variability may double the stress range over that computed for a single wheel load.

5. The elastomeric springs and bearings are an important element in the joint behavior. However, frequently they have been reported as being loose in the joints. The precompression or looseness of the bearings will affect local bending stress in the critical region surrounding the stirrup and may also lengthen periods of critical modes of centerbeam vibration. However, precompression is not thought to be a predominant contributor to the fatigue problems noted in the joints.

6. The Tschemmernegg design load spectrum and S-N curves are based on field measurements, analysis, and fatigue tests of modular joints in Europe. Fatigue design criteria for modular joints must consider the unique features and dynamic response of each joint system. The fatigue test must be appropriate for the loads the joint experiences, or it will lead to improper S-N curves and failure modes. The fatigue test on the as-built tubular centerbeam may not be indicative of the fatigue behavior of this joint because the fatigue test does not include the flexibility of the joint with respect to horizontal loads.

7. Welded repairs are not an effective long-term repair solution because most of those previously repaired by welding have recracked.

8. The AASHTO specifications should include fatigue design loads, allowable fatigue stress ranges, number of cycles to determine the theoretical endurance limit of fatigue critical expansion joint components, and expected design life for modular expansion joints.

9. The dynamic behavior of each type of modular joint system is strongly influenced by the dynamic response of that system. This single support bar expansion joint amplifies horizontal loads that are applied slowly, but it amplifies vertical loads through a wide range of vehicle speeds. The vertical modes of vibration with significant participating mass had periods ranging from 0.05 to 0.005 sec.

11. Single support bar expansion joints may not experience the large horizontal or lateral loads because of the transverse flexibility of the joint.

12. Dynamic analyses can be useful in determining the dynamic behavior and amplification or impact factor used in the design of modular expansion joint systems. However, the impact factor under field conditions may be significantly higher because of road roughness and the various dynamic characteristics of truck suspension systems.

13. The 1200-mm movement modular joints will require replacement before their expected design life of 25 to 30 years is achieved.

ACKNOWLEDGMENTS

The authors would like to thank Washington State Transportation Center and WSDOT, particularly A.H. Walley and M.M. Lwin, for their encouragement and support in preparing this paper.

REFERENCES

1. Brown, S., and U. Haerle. Design of a Sealed Expansion Joint for the 3rd Lake Washington Bridge. *Joint Sealing and Bearing Systems for Concrete Structures*, Vol. 2, SP-94. American Concrete Institute, Detroit, Mich., 1986, pp. 967–974.
2. Van Lund, J. A. Improving the Quality and Durability of Bridge Modular Expansion Joints. In *Transportation Research Record 1393*, TRB, National Research Council, Washington, D.C., 1993, pp. 9–16.
3. Roeder, C. W. *Fatigue Cracking in Modular Joints*. Report WA-RD 306.1. Washington State Transportation Center, March 1993.
4. Pattis, A., and F. Tschemmernegg. *Fatigue Testing and Design of Modular Expansion Joints*. University of Innsbruck and The D.S. Brown Co., Innsbruck, Austria, March 1992.
5. Fatigue Design and Testing for Expansion Joints. *Technology Bulletin for Bridge Bearings, Expansion Joints and Components*, No. 1. The D.S. Brown Co., North Baltimore, Ohio, Oct. 1991.
6. Tschemmernegg, F. The Design of Modular Expansion Joints. *Volume 1: Joints and Sealants, Third World Congress on Joint Sealing and Bearing Systems for Concrete Structures*, American Concrete Institute, Toronto, Ontario, Canada, Oct. 1991, pp. 67–86.
7. Ostermann, M. Stresses in Elastically Supported Modular Expansion Joints Under Wheel Impact Load (In German). *Bauingenieur*, Vol. 66, 1991, pp. 381–389.
8. Braun, C. Strain on Expansion Joints for Road Bridges Under Traffic Loads (In German). *Bauingenieur*, Vol. 67, 1992, pp. 229–237.
9. Frost, N. E., Marsh, K. J., and L. P. Pook. *Metal Fatigue*. Oxford University Press, 1974.
10. Koster, W. The Principle of Elasticity for Expansion Joints. *Joint Sealing and Bearing Systems for Concrete Structures*, Vol. 2, SP-94. American Concrete Institute, Detroit, Mich., 1986, pp. 675–711.
11. Agarwal, A. C. *Static and Dynamic Testing of a Modular Expansion Joint in the Burlington Skway*. Third World Congress on Joint Sealing and Bearing Systems for Concrete Structures, Toronto, Ontario, Canada, Oct. 1991.
12. Wilson, E. L., and A. Habibullah. *SAP90 Users Manual*. Computer and Structures, Inc., Berkeley, Calif., 1989.
13. Stanton, J. F., and C. W. Roeder. *NCHRP Report 248: Elastomeric Bearings—Design, Construction, and Materials*. TRB, National Research Council, Washington, D.C., 1982.
14. *Standard Specifications for Highway Bridges*, 15th ed. AASHTO, Washington, D.C., 1992.
15. *Proposed LRFD Standard Specifications for Highway Bridges*. Draft, April 17, 1992.

The opinions and conclusions expressed or implied in this paper are those of the authors and are not necessarily those of TRAC or WSDOT.

Publication of this paper sponsored by Committee on Dynamics and Field Testing of Bridges.

Measured Thermal Response of Concrete Box-Girder Bridge

K. NAM SHIU AND HABIB TABATABAI

The measured thermal behavior of the Red River Bridge in Louisiana is discussed. The Red River Bridge is a six-span continuous bridge with a main span of 113 m (370 ft) and a total length of 548 m (1,797.5 ft). The structure is a single-cell, nonprismatic concrete box-girder bridge constructed using the balanced cantilever method. A comprehensive instrumentation program was initiated during construction to monitor the bridge behavior during and after construction. Instrumentation included 42 concrete strain gauges, 93 thermocouples, and a rotation meter. Gauges were installed at three selected bridge sections in the main span, and measurements were taken over a period of 5 years. Thermal response measurements included readings taken over 24-hr periods in different seasons. Using the measured strain and temperature data, sectional restraint stresses and continuity thermal stresses were calculated. However, effects of creep and shrinkage in reducing the effective modulus of elasticity, thereby relieving the thermal continuity stresses, were not considered. Statistical analyses were used to evaluate the frequency occurrence function of the measured temperature differentials between the top and bottom of the box girder. Measured temperature distribution profiles were compared with those from current AASHTO recommendations. In addition, conventional temperature correction procedures for strain measurements were reviewed. On the basis of the temperature data, a modified temperature correction procedure is presented and its impact on strain measurements is discussed. Using the modified procedures, measured strain data were used to determine diurnal continuity strain cycles. Significance of the continuity strains is discussed.

This paper presents measured thermal response of the Red River Bridge. The Red River Bridge is the first concrete segmental box-girder bridge in Louisiana (Figure 1). Thermal investigation of the bridge was part of a research project (*1,2*) jointly sponsored by FHWA and the Louisiana Transportation Research Center. The project was undertaken by Construction Technology Laboratories, Inc., between 1982 and 1984. The research objectives were to measure and evaluate time-dependent deformations and thermal behavior of the bridge for 5 years. A comprehensive instrumentation system was installed in selected bridge segments during construction to monitor bridge behavior periodically during and after construction.

Behavioral monitoring included measurements of concrete temperatures and strains in three girder segments. Diurnal and seasonal readings were taken. Temperature differentials and temperature distribution profiles, as well as sectional restraint stresses and continuity thermal stresses, were calculated. The effects of changing effective modulus of elasticity caused by creep and shrinkage were not considered in the calculation of concrete stresses. Measured data were compared with those from the recommended AASHTO thermal design guidelines. In addition, temperature correction method for strains was investigated.

K. N. Shiu, Wiss, Janney, Elstner Associates, Inc., Northbrook, Ill. 60062. U. Tabatabai, Construction Technology Laboratories, Inc., Skokie, Ill.

RED RIVER BRIDGE

The Red River Bridge is a single-cell segmental concrete box-girder bridge located northeast of Boyce in central Louisiana. As shown in Figure 1, this bridge, 548 m (798 ft) long, consists of six spans with span lengths ranging from 69.7 m (228 ft 9 in.) to 112.8 m (370 ft). The bridge is made up of nonprismatic girder segments with depths varying from 5.3 m (17 ft 4 in.) at the pier supports to 2.2 m (7 ft 4 in.) at midspan. A typical box-girder section is shown in Figure 2. The bridge was erected by the balanced cantilever method. Bridge construction was completed in fall 1984.

The Red River Bridge was designed in accordance with the 1977 AASHTO Standard Specifications for Highway Bridges (*3*) and the 1978–1979 Interim Specifications. Bridge dimensions were based on an annual average temperature of 20°C (68°F). A linear temperature gradient of 5°C (9°F) across the depth of the bridge section was used in the design to account for temperature effects.

INSTRUMENTATION

Three segments in the 112.8-m (370-ft) span were instrumented. The instrumented segments represented segments next to the pier support, at quarter span, and at near midspan. Locations of the instrumented segments are also shown in Figure 1. Instrumentation included 42 Carlson strain meters and 93 thermocouples. The temperature and strain sensors were distributed throughout the bridge segment, as indicated in Figure 3.

Carlson strain meters were embedded in the bridge concrete during construction. This type of strain gauge has been successfully used in other projects to provide long-term concrete strains and concrete temperatures.

In addition to the Carlson meters, Type-T thermocouples were used to measure concrete temperatures. The typical arrangement of the thermocouples through the top and bottom slabs of the box girder is indicated in Figure 3. On the basis of the measurements, temperature distributions and differentials between the top and bottom of the girder were obtained. As indicated in Figure 3, thermocouples were attached on the inside surface of polyvinyl chloride (PVC) tubing. The PVC tubing was then embedded in the girder at selected positions during construction. Thermocouple lead wires were routed to a centralized switch box inside the box girder for manual readings.

During construction, strain and temperature readings were taken before and after every significant construction event that could cause stress or strain changes in the structure. After the construction was completed, readings were taken once a season for 5 years. In addition, hourly strains and temperatures were measured in four 24-hr periods. The 24-hr measurements were taken on June 24, 1987,

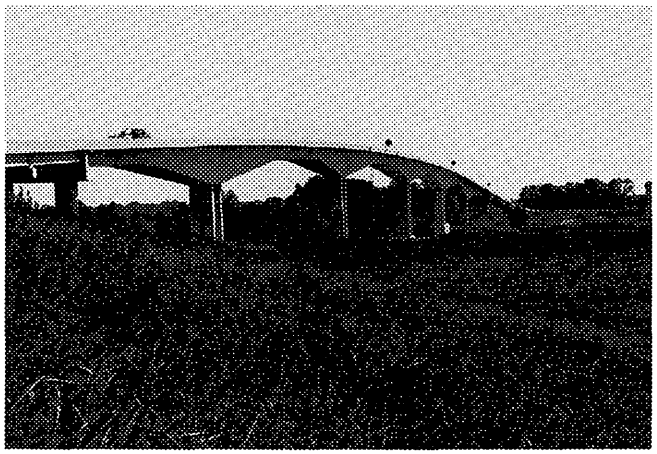

a.) Overall view

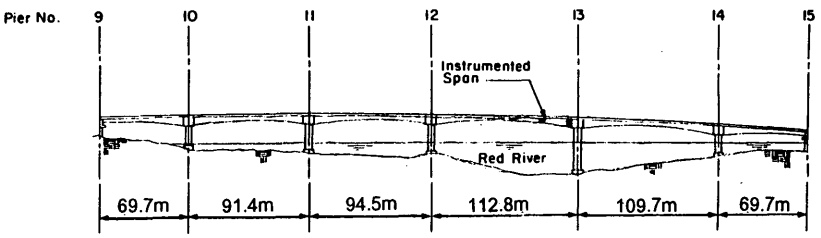

b.) Elevation

FIGURE 1 Red River Bridge.

September 23, 1987, February 1, 1988, and May 5, 1988. These dates were randomly selected to represent typical conditions in summer, fall, winter, and spring. To further supplement the data base, temperature readings were taken at 15-min intervals for 8 hr on August 5, 1986, and for 2 hr on April 1, 1987.

TEMPERATURE MEASUREMENTS

Temperature measurements are discussed in the following sections in terms of temperature differentials between the top and bottom of the girder and the temperature distributions through the bridge sections.

Temperature Differentials

Using a data sample of 89 readings, the temperature differential occurrence frequencies of the segment next to the bridge pier is shown in Figure 4. The sample included randomly selected temperature readings taken in the morning after the completion of bridge construction. The bridge structure is known to be thermally most stable in the morning. As such, the temperature differentials shown in Figure 4 reflected the seasonal variations without the daily temperature fluctuations.

The occurrence frequency of the temperature differentials resembled a lognormal distribution. Maximum positive and negative temperature differentials were measured to be 13.9°C to 16.7°C (25°F to 30°F) and –5.6° to –2.8°C (–10°F to –5°F), respectively. A positive temperature differential indicates that the top deck has a higher temperature than the box-girder bottom and vice versa.

On the basis of this limited sampling, the most frequently encountered thermal gradient was +2.8°C (+5°F), although there were a good number of occurrences with temperature differentials exceeding +5°C (+9°F). [The 1977 AASHTO design temperature differential for the Red River Bridge was +5°C (+9°F).]

Current design recommendations for temperature differentials in concrete bridges are 32°C (57.6°F) for the New Zealand Code (*5,6*), 15.4°C (27.7°F) for the British Code (*7,8*), and 10°C (18°F) for the Posttensioning Institute (*9*). The recommended AASHTO temperature differential of Imbsen et al. (*10*) for the Red River Bridge is –3.8°C (–7°F) and +17.2°C (+31°F). These recommendations are suggested for concrete girders, with depths greater than 0.61 m (2 ft) and a 51-mm (2-in.) blacktop riding surface, in the southeast region. The measured temperature differentials, between –5.6°C and +16.7°C (–10°F and +30°F), were in general agreement with the current AASHTO recommendations.

Nonlinear Temperature Distributions

Because of concrete's thermal characteristics, concrete layers beneath the surface can have substantially different temperatures than those on the surface. Figure 5 shows typical temperature vari-

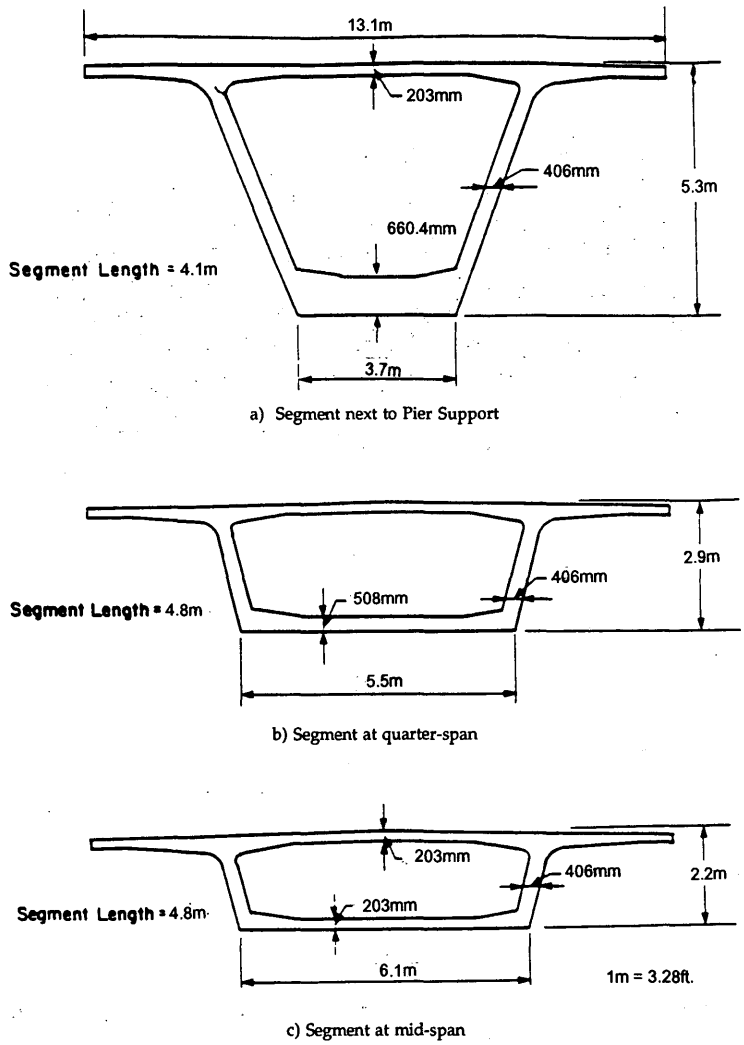

FIGURE 2 Dimensions of typical bridge segments.

ations at various layers of the top slab over an 8-hr period. Surface concrete responded much faster to the outdoor air temperatures and solar radiation than did the inner concrete layers. As a result, the temperature distributions through the bridge section were nonlinear. As indicated in Figure 5, the air temperature inside the box girder reacted very slowly to the outside temperature changes. The response lag time was about 5 to 6 hr.

Nonlinear temperature distributions through bridge sections have been well documented by several researchers (*11–16*). Hoffman et al. (*13*) have shown that temperature distribution can be adequately simulated with one-dimensional heat flow analysis. It was suggested that temperature distributions through a section (*11,14*) are best described by a parabola. Others (*10*) proposed simpler mathematical formulations such as bilinear or trilinear distributions. A comparison of the Red River Bridge measured temperature distribution with the recommended AASHTO trilinear distribution of Imbsen et al. (*10*) is indicated in Figure 6. The positive AASHTO recommended temperature distribution agreed nicely with the Red River Bridge temperature measurements, although the negative gradient did not have the same level of agreement.

THERMAL STRESSES AND STRAINS

Thermal stresses and strains are inherently different from load-induced stresses and strains. Thermal stresses or strains are closely related to the support conditions of the structural members. If a structural member is totally unrestrained, the member will respond to temperature change by expanding or contracting. Such dimensional changes represent the induced thermal strains. However, there will be no stresses induced in the member caused by the temperature changes. On the other hand, if the member is fully restrained against movement, internal stresses will be induced in the member instead. The fully restrained member will then experience neither movements nor strains. In summary, thermal stresses are primarily restrained stresses that are relieved as soon as thermal movements are allowed.

As an example, a simple beam is subjected to a linear positive temperature gradient. The beam will respond by bending upward to attain a uniform curvature. The top fibers of the beam at midspan will exhibit thermal strains but experience no thermal stresses. However, if the same beam, subjected to the same temperature gra-

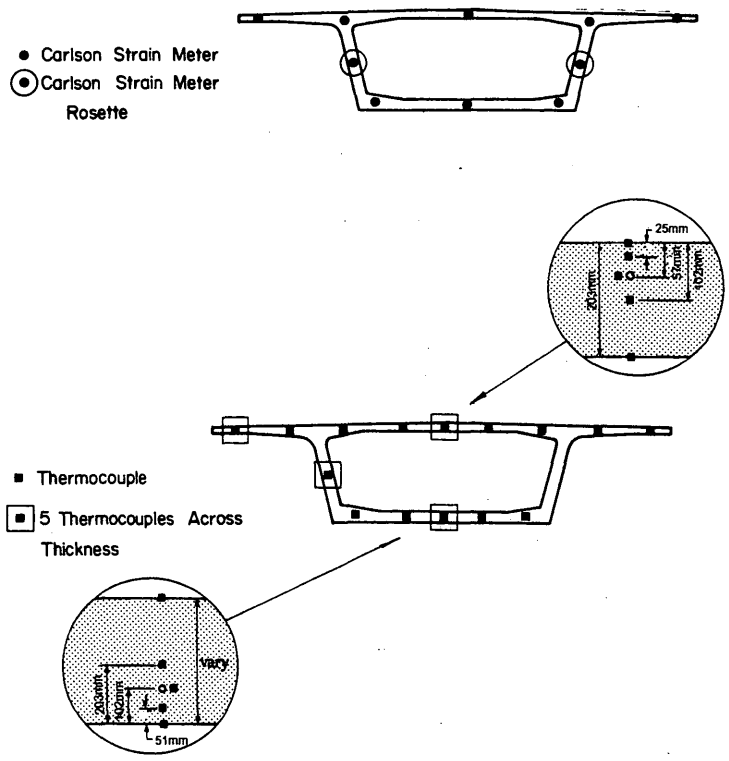

FIGURE 3 Locations of strain and temperature sensors in instrumented bridge segment.

dient, is totally restrained, the beam will have no deformations but will experience internal restrained stresses. Practically speaking, structural members are neither fully restrained nor completely free to move. This results in a combination of thermal strains and thermal stresses.

There are two types of thermal restrained stresses:

1. Sectional restrained stresses. Restraint offered by the section. Induced stresses are sometimes called self-equilibrating stresses.
2. Continuity stresses. Restraint offered by the support conditions.

Sectional Restraint Stresses

A basic assumption in the beam theory is that plane sections remain plane. In other words, strain gradients through a beam section shall be linear. If a simply supported beam (Figure 7*a*) is subjected to a linear temperature gradient, the beam will bow upward with a uniform curvature. No restrained stresses will be induced in the beam. However, if a nonlinear temperature profile is imposed across the beam section, concrete at different section depths will try to expand according to the imposed temperature profile. Assuming no restraint between concrete layers, the resulting strain profile will also be non-

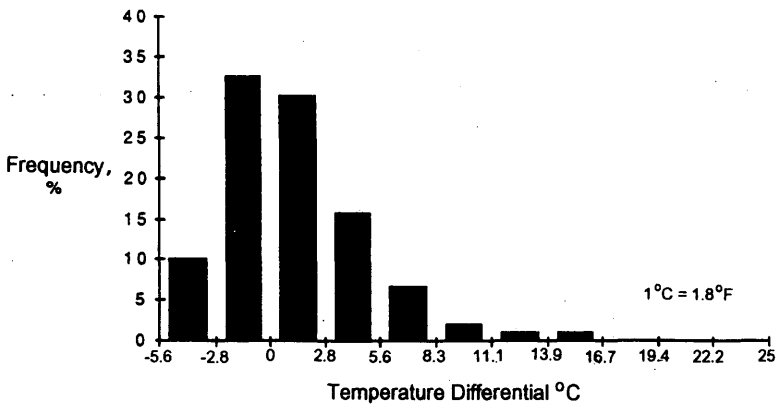

FIGURE 4 Typical frequency occurrence of temperature differentials between top and bottom of box girder.

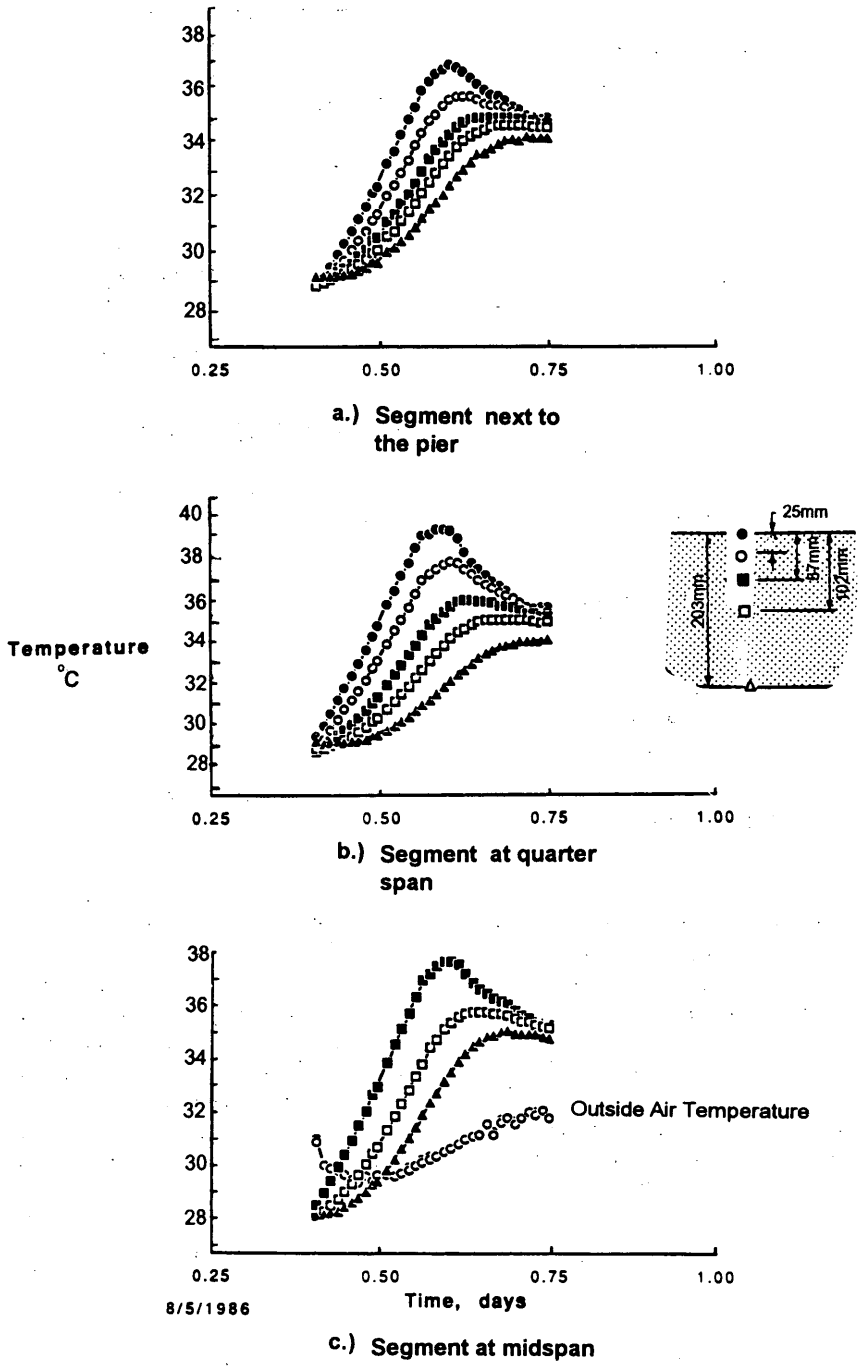

FIGURE 5 Variations of concrete temperatures in top slab of box girder, August 5, 1986.

linear, which violates the basic assumption of plane sections remaining plane. To maintain a linear strain gradient, partial restraint has to be imposed by the beam section, resulting in a combination of the thermal strains and sectional restrained stresses as indicated in Figure 7*a*.

Sectional restrained stresses occur in all sections with nonlinear temperature distributions. Some researchers (*13,15*) have indicated that such restrained stresses can be substantial and should be properly accounted for in design. However, there have been very few recorded cases of distress caused by thermal restrained stresses. As indicated in Figure 7*a*, tensile restrained stresses are induced in the midsection where very little reinforcement is normally required. Special attention has to be given to reinforcing the girder web section against unanticipated thermal cracking.

Sectional restrained stresses are internal stresses that have the characteristics of thermal stresses. As such, sectional restrained stresses cannot be measured by strain meters because strain meters measure only deformations.

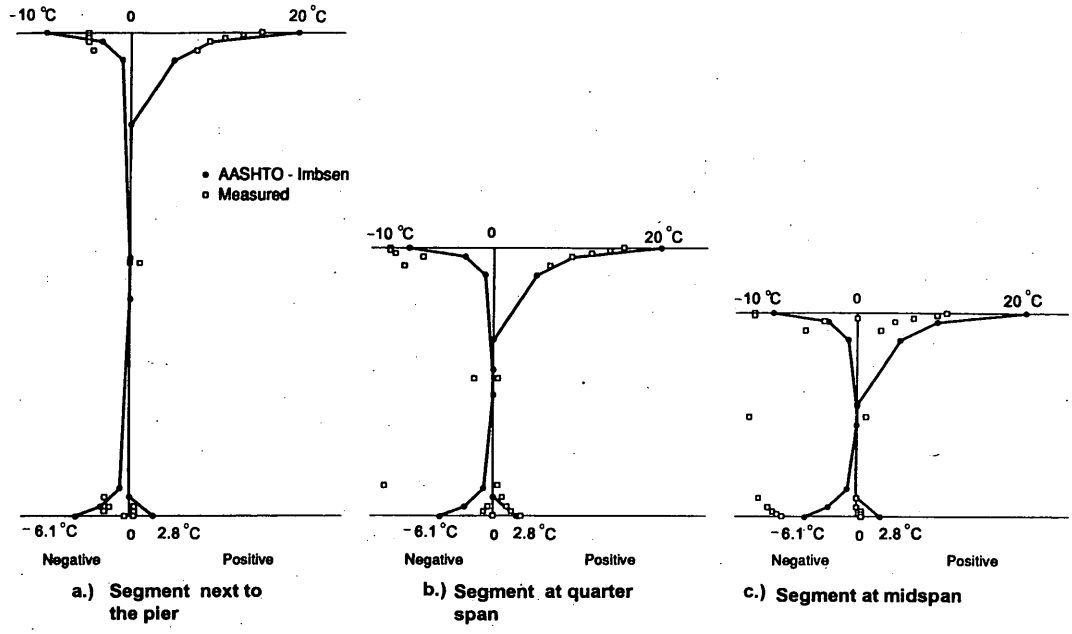

FIGURE 6 Comparison of AASHTO recommended vertical temperature gradient with measured temperature gradients with highest differentials (1°C = 1.8°F).

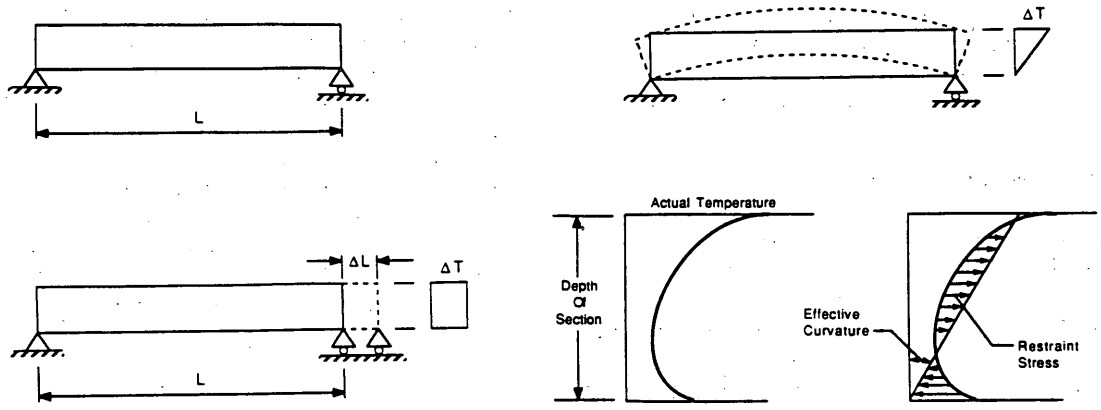

a.) Sectional restraint

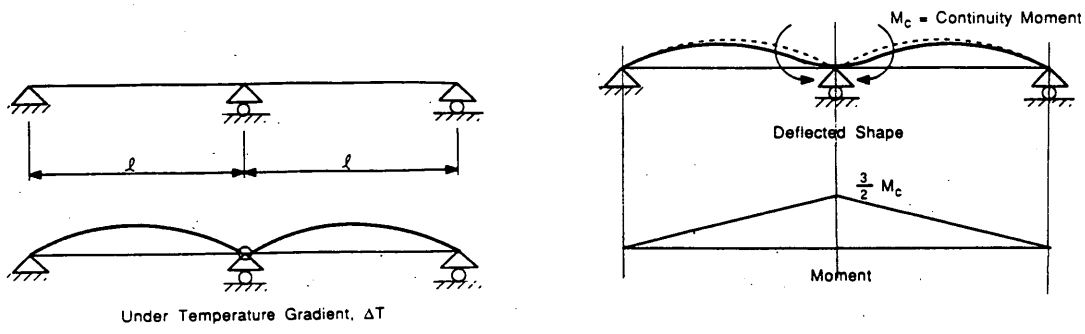

b.) Continuity restraint

FIGURE 7 Sectional restrained stresses and continuity stresses.

Continuity Stresses

When subjected to a linear temperature gradient, a simply supported beam in Figure 7*a* will be free to move and will experience no support restraint. However, support restraint will be present in multispan continuous beams. Stresses resulting from this type of restraint are called continuity stresses.

When a linear temperature gradient is imposed on two simply supported beams, each span will bow upward, as indicated in Figure 7*b* by the dotted lines. To make the two simple spans continuous over the center support, a continuity moment M_c is needed to enforce the midsupport compatibility. The moment M_c then represents the additional flexural restraint offered by the support condition. The moment M_c is called the continuity moment, and stresses resulting from this moment are the continuity stresses.

Continuity stresses are similar to the secondary stresses in prestressed concrete construction. Although they are temperature-induced stresses, continuity stresses do not have the characteristics of thermal stresses and strains. Continuity strains can be measured by strain meters. The magnitude of the continuity stresses are comparable to those of live load stresses and should be duly considered in design.

TEMPERATURE CORRECTION METHODS

All materials, including the measuring sensors, are subjected to temperature effects. To properly evaluate temperature effects in the measured strain, the strain reduction method was critically reviewed. In this section, a modified temperature adjustment procedure is proposed and its impact on strain measurements is discussed.

Conventional Temperature Correction

Usually strains are obtained by multiplying changes in strain readings before and after an event by the manufacturer's recommended gauge factor. The resulting strain values represent strain movements of the object at the temperature at which strain readings were collected. As such, the measured strains include the apparent strains from the material contraction or expansion caused by temperature changes between strain readings. To eliminate these apparent strains, the following temperature correction equation has been used.

$$\text{Temperature Correction} = (T - T_{\text{ref}}) \times \gamma_{\text{concrete}} - (T - T_{\text{ref}}) \times \gamma_{\text{meter}} \quad (1)$$

where

T = concrete temperature, °C (°F);
T_{ref} = reference temperature, 23°C (73°F);
γ_{meter} = coefficient of expansion for the strain meter; and
γ_{concrete} = coefficient of expansion for concrete.

The first term $(T - T_{\text{ref}}) \times \gamma_{\text{concrete}}$ in Equation 1 represents the apparent thermal strains of concrete, whereas the second term $(T - T_{\text{ref}}) \times \gamma_{\text{meter}}$ represents the apparent thermal strains of the strain meter. Both terms assume totally unrestrained movements.

As a basis for comparison, T_{ref} was arbitrarily chosen to be 23°C (73°F). The thermal coefficient of expansion for concrete was assumed to be 9.9 strain millionth/°C (5.5 millionth/°F). The expansion coefficient of the Red River Bridge concrete was measured to range from 8.5 to 11.5 strain millionth/°C (4.7 to 6.4 strain millionths/°F). The coefficients of thermal expansion for the strain meters were provided by the gauge manufacturer.

However, neither the concrete nor the strain meter can expand or contract freely according to the measured concrete temperature. Restraint is offered by the section to maintain a linear strain distribution through the section. To illustrate, measured concrete strain gradients of the bridge segment next to the pier support were plotted in Figure 8. Plotted strains represent strain movements between 7:00 a.m., June 24, 1987, and 11:00 a.m., June 25, 1987. Strains before and after temperature correction were presented. Strain gradients with no temperature correction were linear through the bridge segment. However, after the temperature correction was made according to Equation 1, the strain gradients became nonlinear. The nonlinear strain gradient violated the basic assumption of elastic beam theory, indicating that the temperature correction procedures are not correct and have to be modified.

On the basis of the beam theory, concrete can respond only to an equivalent linear temperature gradient instead of the actual temperature profiles. For a typical positive nonlinear temperature gradient, Equation 1 overcompensates the thermal strains at the top section and undercompensates strains at the midsection.

Modified Temperature Correction

Instead of using the measured temperatures directly for correction, a linear and correctable temperature profile was calculated. A fifth-order parabola was derived from the measured concrete temperatures in the top slab, in the midsection, and in the bottom slab to describe the nonlinear temperature distribution.

The bridge section was initially assumed to be totally restrained. As such, the nonlinear temperature distribution will induce a nonlinear stress profile. Then, the restraint is removed and the bridge section will react to the nonlinear stress profile to attain a curvature. By solving the two equilibrium equations (summation of forces and moments), the resultant curvature, ϕ, can be calculated by Equation 2.

$$\phi = \gamma/I \times \int_o^h t_y \times (y - n) \times b_y \times dy \quad (2)$$

where

ϕ = curvature,
y = vertical axis of the bridge section,
γ = coefficient of concrete expansion,
t_y = temperature distribution function,
b_y = width of concrete bridge section,
n = neutral axis of bridge section,
h = height of bridge section, and
I = bridge section moment of inertia.

The resultant curvature represents allowable sectional movements under the nonlinear temperature distribution. In fact, it represents the linear correctable temperature movements. Using the resultant curvature, an equivalent linear temperature gradient between the top and bottom of the section can be calculated by Equation 3.

$$T_e = \phi \times h/\gamma \quad (3)$$

where T_e is the equivalent linear temperature gradient.

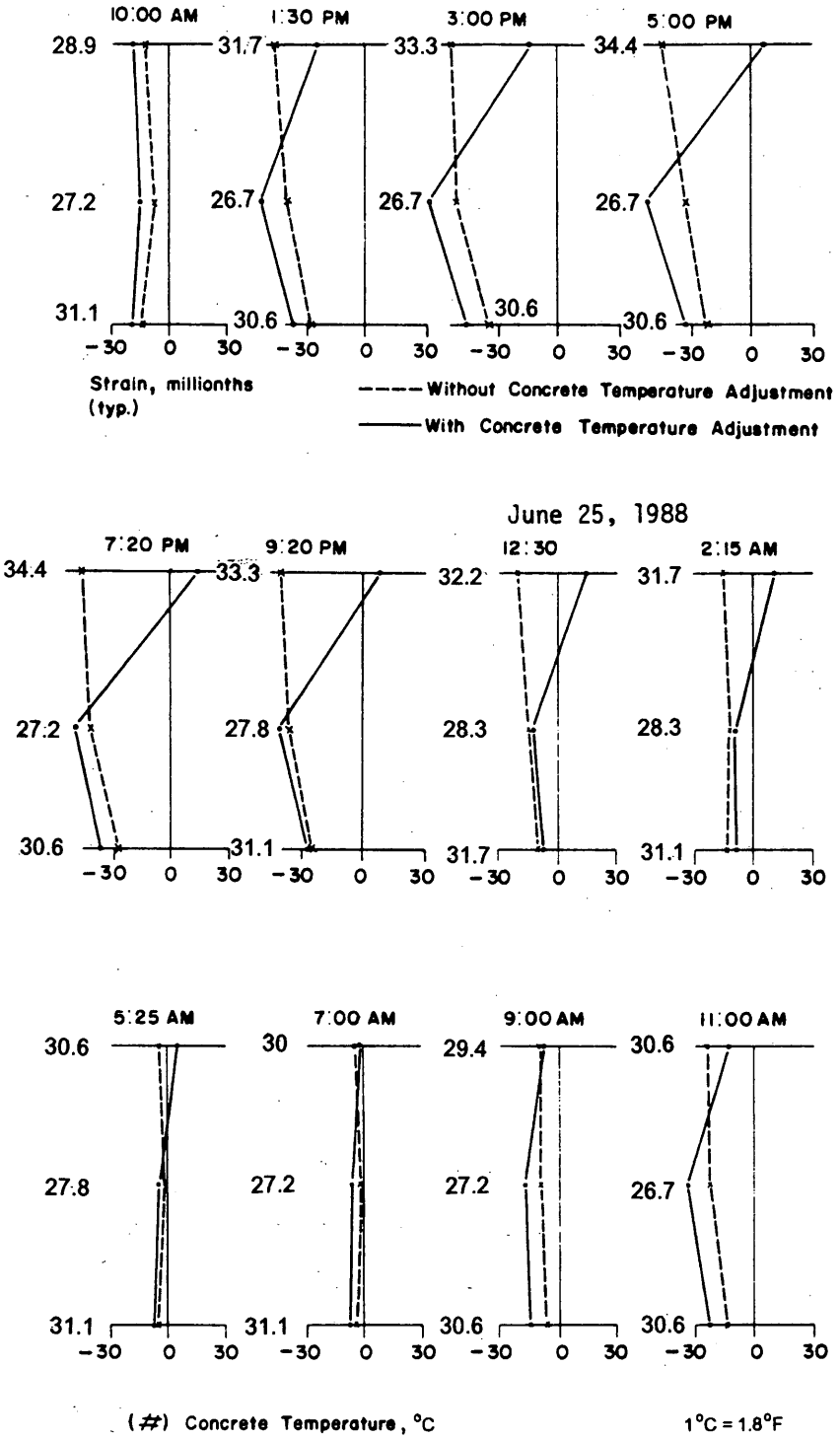

FIGURE 8 Strain gradient with and without concrete temperature correction for segment next to pier support, June 24 and 25, 1987.

With $T_e(y)$ in place of T, Equation 1 can be used to correct for the apparent temperature strains. A step-by-step procedure for the modified concrete temperature correction is summarized as follows:

1. Measured temperatures of the girder are used to derive a parabolic function to describe the temperature distribution across the girder section.
2. Curvature resulting from the parabolic temperature distribution is calculated by Equation 2.
3. With the calculated curvature, an equivalent linear temperature gradient and the correctable temperature at the location of the strain gauges are calculated by Equation 3.
4. The correctable temperature is then used as concrete temperature in Equation 1.

Comparison of Two Temperature Correction Methods

Effects of the two temperature correction methods were investigated. Twenty-four-hour strain readings measured at the top and bottom of the box girder on June 24, 1987, were reduced by the two methods. Figure 9 shows the reduced strains with no concrete temperature correction, with conventional temperature correction, and with the modified temperature correction for the top slab and the web of the box girder. On the basis of these measurements, the strain differences resulting from the two correction procedures were about 50 millionths and depend on the temperature nonlinearity through the bridge section. The strain differences represent the sectional restrained strains.

To evaluate the effects of the modified temperature correction procedure, long-term strain measurements were reduced by both the conventional and modified temperature procedures. Figure 10 compares the long-term concrete strains reduced by the conventional and modified temperature correction procedures. The strain differences were about 50 to 70 millionths. This represents about 10 percent of the maximum measured strains, which were about 600 to 800 millionths. Therefore, the long-term strain measurements were not significantly affected by the temperature correction procedures.

However, the impact will be more significant for small strain measurements, such as in a diagnostic load test, or when the temperature distribution through the section is highly nonlinear, such as in composite steel girders. Special care should also be given to the

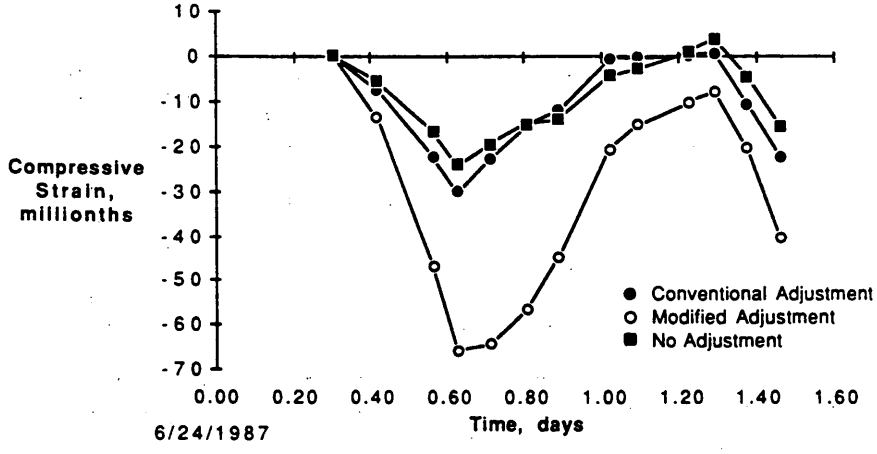

a) In the bottom slab

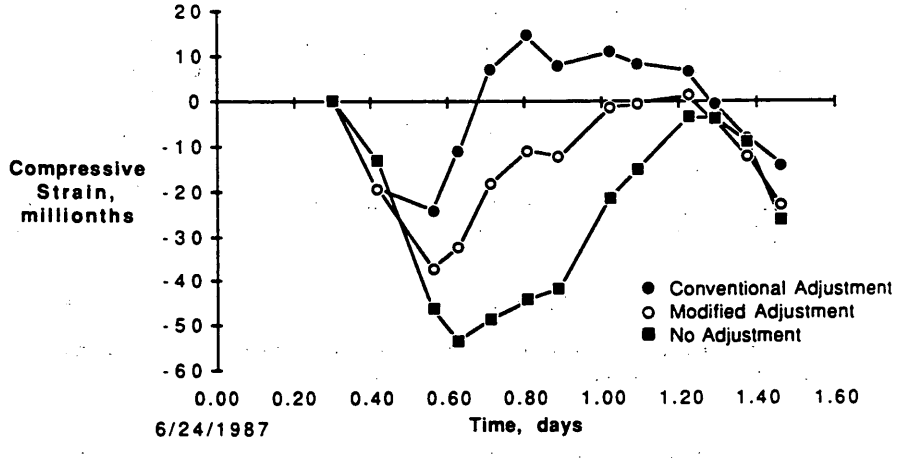

b) in the top slab

FIGURE 9 Measured concrete strains adjusted with various correction procedures for segment next to pier support.

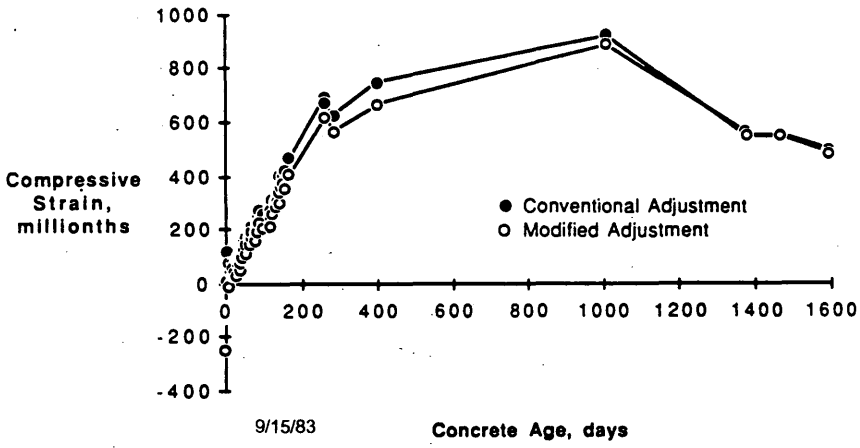

FIGURE 10 Comparison of long-term strain measurement using conventional and modified temperature correction procedures.

so-called temperature-compensating gauges, which implicitly use the conventional temperature correction method.

CONTINUITY THERMAL STRAINS

Figure 11 shows the diurnal strain variations of the bridge segment next to the pier support and at the midspan for measurements taken on June 24, 1987. The strains were temperature corrected with the modified procedures. Strain cycled 40 to 50 millionths strain in 24 hr and the magnitude of strain cycles varied with the strain locations.

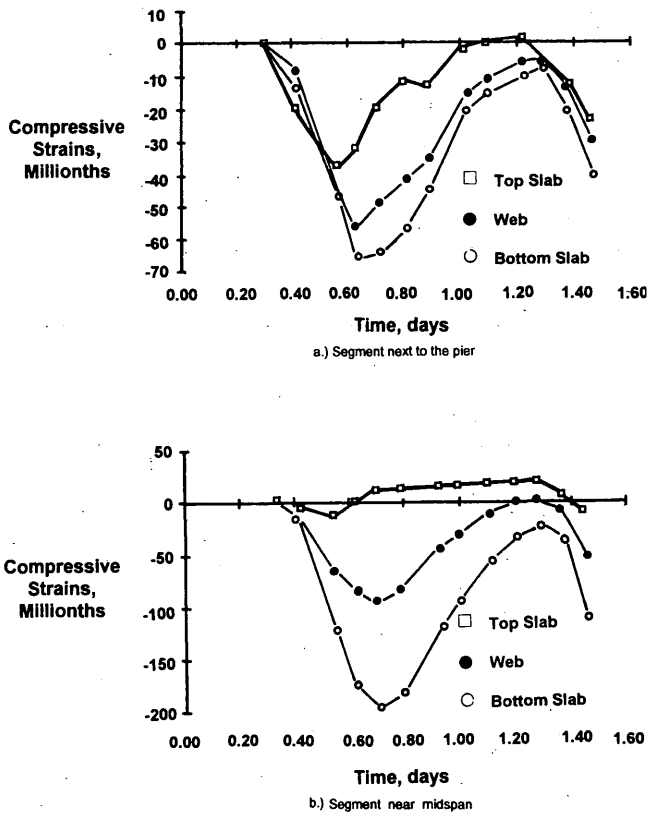

FIGURE 11 Measured daily strain cycles, June 24, 1987.

Most strain measurements were taken when there was no truck traffic on the bridge. However, even if there were trucks passing over the bridge during the diurnal readings, only isolated data points would be affected because each set of strain readings takes about 1 hr. Therefore, the measured strains essentially were free from live load stresses and represent primarily the effects of a daily temperature cycle. As previously pointed out, sectional restrained stresses are internal thermal stresses and cannot be measured by the strain sensors. Therefore, the measured daily strain cycle represented the continuity strains.

Section curvatures were calculated from the strain data. A comparison of the curvatures for the three instrumented segments on June 24, 1987, is shown in Figure 12. Distinct daily cycles indicated that the measured strains reflected diurnal temperature movements. Curvature fluctuations were found to be more significant in the midspan segment than the segment near the pier support. The reason was that the pier segments are much deeper and consequently stiffer than the midspan segments.

Some researchers (*15*) have indicated that the magnitude of the continuity thermal strains can be significant. However, the continuity strains are directly related to the continuity moments, and the continuity moments depend on the equivalent linear thermal gradients. The equivalent linear temperature gradients are in turn related to the temperature differentials and the proposed temperature distribution profile. For a measured temperature differential of 17.2°C (31°F) in the segment next to the pier with a parabolic distribution profile, the equivalent linear temperature gradient was only 8.3°C (15°F).

The continuity stresses of the bridge are affected by the following factors:

1. Temperature differentials between the top and bottom of the bridge section,
2. The temperature distribution profiles through the section,
3. The support conditions, and
4. The sectional properties.

In addition, how the continuity stresses in segmental bridges combine with the other stress conditions depends on the time when

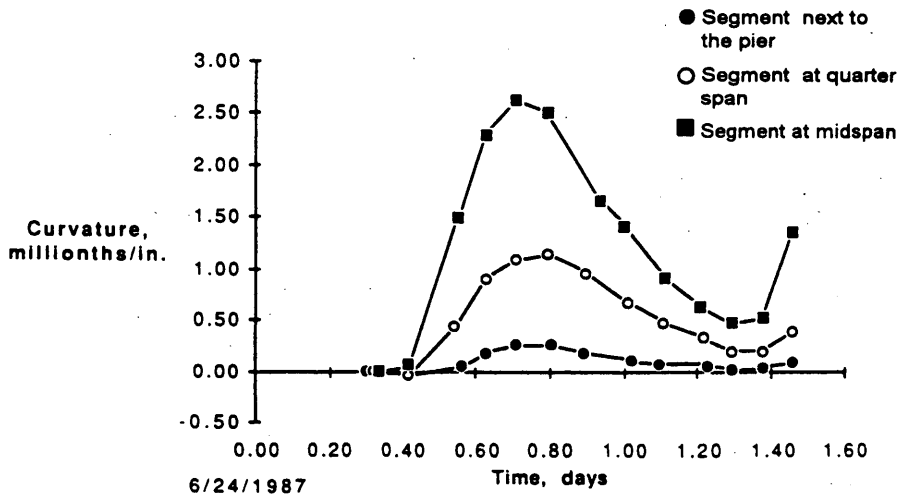

FIGURE 12 Measured diurnal curvatures for three instrumented segments, June 24 and 25, 1987.

the two mating balanced cantilevers are connected. If the cantilever spans were made continuous in the afternoon, the continuous span will subsequently experience predominantly cooling daily cycles. As such, the continuity moment counteracts the negative moments. On the other hand, if the span is made continuous in early morning, the continuity thermal stresses will be added onto the total stresses. Additional data are needed to verify the relationship of the continuity moments to the other stress-induced moments.

FINDINGS AND DISCUSSION

On the basis of the temperature and strain measurements on the Red River Bridge, the following findings were made:

1. The measured temperature differentials were in general agreement with the AASHTO recommendations and the measured temperature distributions through the bridge segments agreed with the trilinear distribution recommended by Imbsen et al (10).
2. The conventional temperature correction procedure for strain readings assumes unrestrained movements between section layers. This assumption violates the basic rule that plane sections remain plane for flexural beam elements. A modified temperature correction procedure was developed.
3. The modified temperature correction procedure does not significantly affect the long-term strain measurements. Depending on the temperature distribution profile, the strain error is approximately 50 to 100 millionths. However, temperature effects have to be carefully adjusted when measured strains are less than 200 millionths.
4. Continuity stresses depend on the imposed temperature gradient, temperature distribution, and the sectional properties. In addition, how the continuity stresses are combined with other load-induced stresses depends on the time and season when the bridge is made continuous.

ACKNOWLEDGMENTS

Work described in this paper was sponsored by the Louisiana Transportation Research Center in cooperation with FHWA. S. C. Shah and Masood Rasoulian coordinated the project for Louisiana and their contributions to the project are sincerely appreciated.

REFERENCES

1. Shiu, K. N., and M. Rasoulian. Performance Monitoring of the Red River Bridge. *Proc., 2nd International Conference on Short- and Medium-Span Bridge*, Ottawa, Ontario, Canada, Aug. 17–21, 1986.
2. Shiu, K. N., H. G. Russell, and H. Tabatabai. Instrumentation of Red River Bridge at Boyce, Louisiana. Report FHWA/LA-91/233. Louisiana Transportation Research Center, Jan. 1991.
3. *Standard Specifications for Highway Bridges*, 12th ed. AASHTO, 1977, Interim, 1978, 1989.
4. Shiu, K. N. Seasonal and Diurnal Behavior of Concrete Box-Girder Bridges. In *Transportation Research Record 982*, TRB, National Research Council, Washington, D.C., 1984, pp. 50–56.
5. Churchward, A., and Y. J. Sokal. Prediction of Temperatures in Concrete Bridges. *Journal of the Structural Division, ASCE*, Vol. 107, No. ST11, Nov. 1981, pp. 2163–2175.
6. Priestley, M. J. N. Thermal Stresses in Concrete Structures, *Proc., Canadian Structural Concrete Conference*, Toronto, Ontario, Canada, 1981, pp. 256–283.
7. Emerson, M. *Temperature Differences in Bridges, Basis of Design Requirements*. TRRL LR 765. U.K. Transport and Road Research Laboratory, Crowthorne, Berkshire, England, 1977.
8. *Steel, Concrete, and Composite Bridges, Part I, General Statement*. British Standard BS 5400. British Standard Institute, Crowthorne, Berkshire, England, 1978.
9. *Precast Segmental Box Girder Bridge Manual*. Post-tensioning Institute and Prestressed Concrete Institute, 1978.
10. Imbsen, R. A., D. E. Vandershaf, R. A. Schamber, and R. V. Nutt. *Thermal Effects in Concrete Bridge Superstructures*. NCHRP Report 276: TRB, National Research Council, Washington, D.C., Sept. 1985.
11. Priestley, M. J. N. Design of Concrete Bridges for Temperature Gradients. *Journal of the American Concrete Institute*, Vol. 75, No. 5, May 1978, pp. 209–217.
12. Wanders, S. P., D. A. Winslow, and C. D. Sutton. *Study of the Segmental Box Girder Bridge at Turkey Run: Construction, Instrumentation, and Data Collection*. FHWA/IN/JHRP-79/25. Purdue University, West Lafayette, Ind., 1979.
13. Hoffman, H. C., R. M. McClure, and H. H. West. Temperature Study of an Experimental Segmental Concrete Bridge, *PCI Journal*, Vol. 28, No. 2, March/April 1983, pp. 78–97.
14. Potgieter, I., and W. L. Gamble. *Response of Highway Bridges to Non*

linear Temperature Distributions. Report FHWA/IL-UI/201. University of Illinois, April 1983.
15. Elbadry, M., and A. Ghali. Thermal Stresses and Cracking of Concrete Bridges. *Journal of the American Concrete Institute*, Vol. 83, No. 6, Nov.–Dec. 1986, pp. 1001–1009.
16. Prakash Rao, D. S. Temperature Distributions and Stresses in Concrete Bridges. *Journal of the American Concrete Institute*, Vol. 83, No. 4, July–Aug. 1986, pp. 589–596.

Publication of this paper sponsored by Committee on Dynamics and Field Testing of Bridges.

Test Results of Fasteners for Structural Fiberglass Composites

ED (AHMED) MORSI AND J. LARRALDE

Reinforced plastic (RP) materials have been widely used for corrosion control and are rapidly gaining acceptance as the construction material of choice for a cost-effective, high-quality product. Commercially available RP materials have been developed to maximize the properties of resins and glass fiber reinforcements that characterize them: corrosion resistance, high ratio of strength to weight, and dielectric properties. Certain design aspects still need to be resolved. The technical and structural integrity of fiberglass connections have been the least understood and have caused the most concern among engineers, designers, and construction personnel. Extensive analysis of the connections should be considered when designing and selecting the material and fasteners to ensure product and structural reliability. RP connection hardware such as self-tapping screws, bolts, nuts, rivets, and adhesives are the most commonly used connection hardware in RP construction. Although steel connection design and performance are well established and well known to engineers and designers, the behavior of RP connections is not yet fully understood. The complexity of the RP material composition, such as types and ratios of fibers and resins, can greatly influence the performance of the connection. The test results of RP connection fasteners and some insight into the behavior of various types of material and fasteners are presented. The test results are compared with the allowable strengths of the various types of fasteners.

The use of reinforced plastic (RP) structural shapes has increased in the last decade, primarily in the construction of wastewater, seawater, and chemical plants and the electronic industry. RP structural material has advantages over conventional construction materials (steel, aluminum, and wood) in corrosive environments because of its high resistance to corrosion and high ratio of strength to weight. However, the most difficult part for the engineer and designer of RP structures is the connections.

Steel detailing is well established, whereas RP connection detailing is not fully understood because of several factors, such as orientation of glass fibers in the RP structural members, percentage and type of glass in the composite, creep deformations, and effect of elevated .emperatures on the viscoelastic modules. Therefore, developing efficient techniques and reliable data for RP connection fasteners is necessary. Limitations of RP connection size, shape, and number and size of bolts permitted within the connection will add to the complexity of the system (*1–3*).

There are two main types of RP connections (*4*): (a) adhesives bonding mainly for nonrigid structure joints and (b) mechanical fasteners, which are the most reliable and controlled technique for connecting RP structures. When designing RP connection systems the following must be considered: thickness of RP material to be connected, number and size of bolts required, surrounding environment, surface temperature, and accessibility to inspect the connection. Several research projects and tests have been conducted in the last decade to determine the allowable tension and shear stress for RP fasteners and connections (*5,7,9*).

The behavior of RP connection fasteners is different from that of the conventional material fasteners. In the case of RP mechanical fasteners, the RP material thickness and the orientation of fibers have been found to be the most critical aspect in the design of the connection. Furthermore, it was also found that the distance between the beam web and the fastener is important because the beams failed in bending instead of shear. The RP material also will determine the capacity and strength of the connection rather than the bolt or fastener allowable load alone.

This paper presents the results of several tests aimed at investigating the effect of various types of fasteners in RP connections where bending, pull-out, and punch-out failures may occur. The tests were conducted on three types of fasteners: standard stainless steel (SS) bolts and nuts, self-tapping screws, and flat-head screws.

TEST PROCEDURE

RP Material with Standard SS Nuts and Bolts

Wide-flange RP pultruded beams were used for testing this type of fastener. This type of beam represents the most commonly used type in RP construction. RP beams are manufactured as follows: the reinforcement materials are in continuous strands of glass fibers roving and bidirectional mats that have been wet in a resin bath and pulled through a heated die. Because most glass fibers roving is in the longitudinal direction, the beams are stronger lengthwise (30,000 psi) than crosswise (7,000 psi).

The test beams were cut into 6-in.-long sections and were tested with the fasteners at various distances from the web, and as close as possible to the web face, to determine the maximum load. The following three beam sizes were tested: W 8 × 8 × ½ in., W 6 × 6 × ⅜ in., and W 6 × 6 × ¼ in. using an SS bolt ¼ in. in diameter and 2 in. long with washer and nut, as shown in Figure 1. The beam flanges were drilled to produce holes 5/16 in. in diameter for ¼-in. bolts and at a distance indicated in Figures 1 and 2. After the bolts were fastened in the flanges, the pull-out load was applied gradually at a rate of 0.1 in./min.

RP Material with Self-Tapping Screws

RP plates cut from pultruded beam flanges were used in this test. Test specimens were 2 ½ in. wide × 6 in. long with different thicknesses: ¼, ⅜, and ½ in. each. The self-tapping screws used in the tests were of various types, that is, self tapping for steel, concrete, and wood. All the screws were ¼ in. in diameter and 1 ½ in. long.

A. Morsi, IMCO Reinforced Plastics, Inc., Moorestown, N.J. 08057. J. Larralde, Civil Engineering Department, Drexel University, Philadelphia, Pa. 19104.

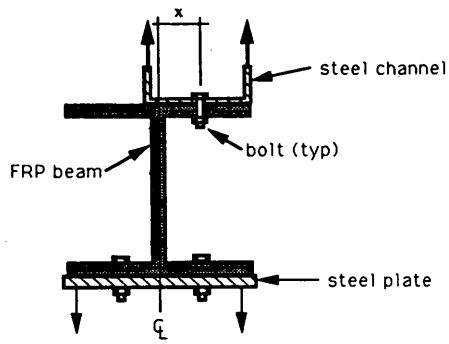

FIGURE 1 Test procedure for FRP beams with stainless steel nuts and bolts.

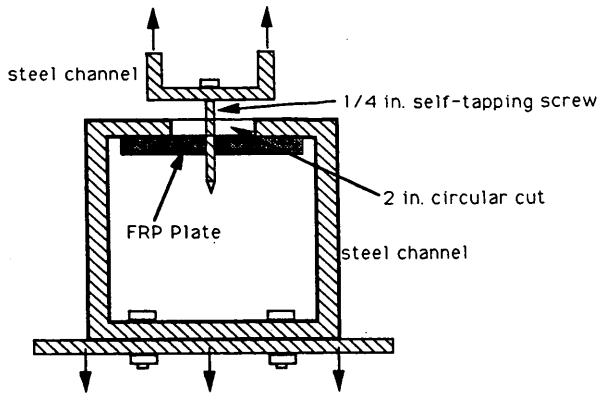

FIGURE 3 Test procedure for FRP plates with self-tapping screws.

The plates were predrilled at pilot holes 3/16 in. in diameter. The plates were held down on the test machine with steel plates, as shown in Figures 2 and 3. The load was applied gradually by pulling out the fasteners from the RP plates at a rate of 0.1 in./min. The test was repeated in three different plate thicknesses: 1/4, 3/8, and 1/2 in. using the three different types of screws.

RP Material With Flat-Head Screws

Flat-head screws can be used where the field conditions do not permit using standard nuts and bolts. The RP material used in this test was cut from pultruded flat sheets 3 in. wide × 12 in. long with various thicknesses of 1/4, 3/8, and 1/2 in. The flat-head screws used in the tests were of three different diameters: 1/4, 3/8, and 1/2 in. The plates were drilled for each screw size with countersunk holes, as indicated in Figures 2 and 4. In addition, two holes were drilled close to the main countersunk hole, about 1 1/4 in. center to center, to hold down the plate on the testing machine. The load was applied gradually at 0.1 in./min until the screw was pulled out completely from the plate.

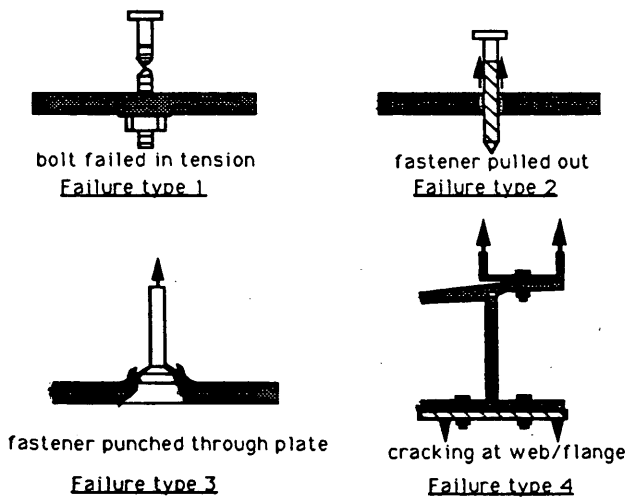

FIGURE 2 Failure types.

RESULTS AND DISCUSSION

In the first series of tests, RP beams with standard nuts and bolts, the beam flanges failed first. However, the distance between the bolt and web was kept to a minimum. In most cases, the flanges failed first at the joint between the flange and web. The failure load was proportional to the flange thickness. Failure occurred either as cracking at the flange/web joint or as bolt punching through the flange. The failure type depended on the distance from the bolt to the web (x). Test results are given in Table 1.

In the second series of tests, RP plates with self-tapping screws 1/4 in. in diameter (Figure 3), the screws failed by pulling out from the plate. The maximum pullout load for self-tapping screws for steel and concrete was very close in each test, as shown in Table 2. However, the maximum load in the self-tapping screws for wood was comparable in 1/4-in.-thick plate, but in thicker plates (3/8 and 1/2 in.), the wood screws themselves failed in tension (Figure 2, Failure Type 1). These failure loads show an increase in load-carrying capacity of RP material 1/2 in. thick at about 75 percent over 3/8 in. thick and 120 percent over 1/4 in. thick. Failure loads of the second test group are summarized in Table 2.

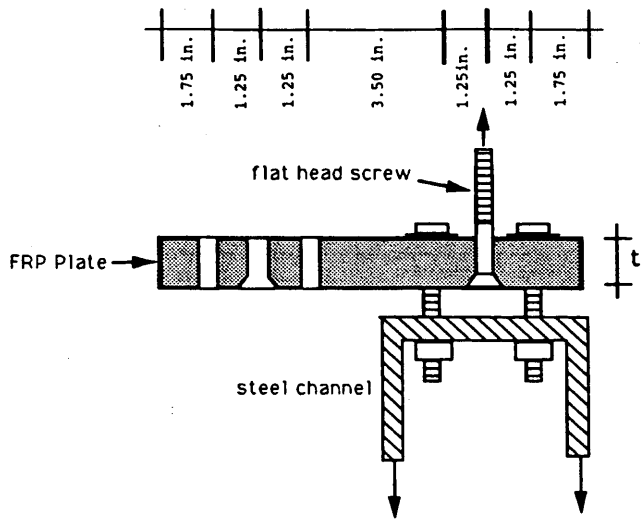

FIGURE 4 Test procedure for FRP plates with flat-head screws.

TABLE 1 Test Results of RP with Bolts

Beam Size	Test No.	Pulled Out Load	Failure Type (See Fig 2)	(x) Distance (See Fig 1)
W 8 x 8 x 1/2	G11	1,100 lb	4	1 3/4"
W 8 x 8 x 1/2	G12	3,400 lb	2	3/4"
W 6 x 6 x 3/8	G13	1,350 lb	4	5/8"
W 6 x 6 x 1/4	G14	970 lb	4	1/2"

The third series of test, RP plates with flat-head screws, the plates failed by pulling out the screws from the RP material, with the exception of the screws that were ¼ in. in diameter, which failed in tension when tested with the ½-in.-thick plate (the screw failed in tension when reaching the ultimate load of 2,400 lb). There were indications of splits occurring between the fiber layers, especially where the glass fibers run in crosswise directions. The plate thickness seemed to be the main factor for load resistance, as shown in Table 3. Also, the low ductility of RP material caused the plates to rapidly fail without advance notice. Before installation of the flat-head screw, a countersunk hole must be drilled and prepared, which will reduce the thickness of the plate to approximately 40 percent.

CONCLUSIONS AND RECOMMENDATIONS

Standard conventional bolting material is the most efficient way to connect RP structural elements. It offers a large selection of bolt sizes and types. Stiffening the flange/web area can prevent the development of cracks that reduce structural integrity.

Self-tapping screws in the RP connection provide the simplest and most economical solution to the construction technique, especially where the connections are in inaccessible locations. On the other hand, the self-tapping screws have a limited load-carrying capacity over other fasteners and limited cycles for assembly and disassembly because the screw's threads exert excessive damage to the RP holes.

The flat-head screws showed higher load capacity than the self-tapping screws. As the load increases, it tends to cause cracking in the RP material, mainly in the direction of fiber orientation. Because of the complexity of the RP connection and the wide variety of fasteners, material thickness, fastener's pattern, and spacing in the connection, the following design recommendations should be considered:

1. The anisotropic behavior of RP material limits the connection efficiency of the fiberglass composites. Therefore, to minimize stress concentration and increase connection capacities, oversize washers or combined mechanical fasteners with adhesives, or both, should be provided.
2. Connection strength can be increased by bonding RP angles to the connection members in addition to the fasteners.
3. RP materials display different strength characteristics depending on the orientation of glass fibers; thus, care should be taken when using the fasteners in directions parallel or perpendicular to the member.
4. Failure of RP material is completely different from that of other conventional materials; therefore, methods for deflection monitoring should be provided.
5. RP material can be significantly affected by elevated temperatures; thus, tight-fit fasteners and adhesive connections should be considered. In addition, engineers and designers should specify the appropriate type of fastener and resin (polyester or vinylester) as recommended on the corrosion resistance chart.
6. RP materials show a large variability because there is no RP manufacturing standardization. As a result, the designer must specify material properties and consider a large factor of safety.

ACKNOWLEDGMENTS

The authors thank the Civil Engineering Department, Drexel University, for allowing use of the laboratory equipment. Also, the au-

TABLE 2 Test Results of RP Plates with Self-Tapping Screws

RP Plate Thickness (in)	1/4" Dia Self-Tapping for Steel		1/4" Dia Self-Tapping for Concrete	
	Max Pull Out * Loads (lb)	Failure Type (See Fig 2)	Max Pull Out * Loads (lb)	Failure Type (See Fig 2)
1/4"	912	2	780	2
3/8"	1,100	2	1,130	2
1/2"	1,938	2	1,995	2

TABLE 3 Test Results of RP Plates with Flat-Head Screws

Plate Thkness	Screw Size	Test Max Pull Out (lb)	Failure Type (See Fig 2)	Nominal Ultimate Strength of Screws (*)	Screw Type
1/4"	1/4" dia	1,640	3	2,400 lb	Steel
	3/8" dia	2,000	3	6,240 lb	S.S.
	1/2" dia	2,890	3	11,760 lb	Steel
3/8"	1/4" dia	2,240	3	2,400 lb	Steel
	3/8" dia	3,265	3	6,240 lb	S.S.
	1/2" dia	4,700	3	11,760 lb	Steel
1/2"	1/4" dia	2,400	1	2,400 lb	Steel
	3/8" dia	4,390	3	6,240 lb	S.S.
	1/2" dia	5,410	3	11,760 lb	Steel

(*) From AISE Design Manual (1)

thors acknowledge appreciation to their families for their support and patience. Without these people, this report would not have been possible.

REFERENCES

1. Manual of Steel Construction, 8th ed. American Institute of Steel Construction, Inc., 1980.
2. Structural Plastics Design Manual, *Manuals and Reports on Engineering Practice 63*, ASCE, New York, 1984.
3. *Structural Plastics Selection Manual.* Task Committee on Properties of Selected Plastics and Systems, Structural Plastics Research Council, ASCE, New York, 1985.
4. Austin, R., R. Yuan, and W. Chan. *Structural Plastic Connections.* ASCE, Structures Congress, 1991.
5. Bank, L., A. Mosallam, and X. Gonsior. *Beam to Column Connections for Pultruded RP Structures.* ASCE, Materials Engineering Congress, 1990.
6. Benjamin, B. S. *Structural Design with Plastics*, 2nd ed. Van Nostrand Reinhold Co., 1982.
7. Cook, J., and A. Morsi. *Column Base Connections of Fiber Reinforced Plastics*, ASCE *Material Selection, Design, and Tooling for Structural Plastics*, 1984.
8. Fujii, S., K. Shimomura, and M. Kaneko. *High-Strength RN Bolts.* Annual Meeting of the Society of the Plastic Industry, Washington, D.C., 1986.
9. Ross, R., and A. Tuthill. Guidelines for Successful Use of Marine Fasteners, *Corrosion Science, The Journal of Science and Engineering*, Vol. 47, No. 7, July 1991.

Publication of this paper sponsored by Committee on Structural Fiber Reinforced Plastics.